MOMENTUM AND HEAT/MASS TRANSFER PHENOMENA OF CONTAMINATED BUBBLES IN POWER-LAW LIQUIDS

Submitted in partial fulfillment of the
requirements for the degree of

DOCTOR OF PHILOSOPHY

by

Venkata Swamy Nalajala

DEPARTMENT OF CHEMICAL ENGINEERING

INDIAN INSTITUTE OF TECHNOLOGY GUWAHATI

GUWAHATI, ASSAM – 781039, INDIA

JUNE 2014

CERTIFICATE

It is certified that the work contained in the thesis entitled "**Momentum and Heat/Mass Transfer Phenomena of Contaminated Bubbles in Power-law Liquids**", by Venkata Swamy Nalajala (Roll No. 09610707)**,** has been carried out under my supervision and that this work has not been submitted elsewhere for a degree.

Date: 16-06-2014

Dr. Nanda Kishore
Associate Professor
Department of Chemical Engineering
Indian Institute of Technology Guwahati
Guwahti-781 039
Assam

Dedicated to my beloved parents

Late Mr. Venkateswarlu
and
Mrs. Veeranarayanamma

Acknowledgements

This space of the thesis is as essential as any other. It is imperative, at this point, that I express my heart-felt thanks and gratitude to all the people that have direct or indirect connect in lending their warmth and support during the course of my PhD studies and also being so quintessentially related to me in my ups and downs of life. May I also state that the names of those that are not been mentioned here, for space limitation, should not feel they are unimportant to me. They mean to me as much as others and I have immense respect for them too.

Foremost, I would like to thank my supervisor Dr. Nanda Kishore for providing me with the opportunity to complete my PhD thesis at IIT Guwahati, India. I especially want to thank my supervisor, Dr. Nanda Kishore, whose support and guidance made my thesis work possible. He has been actively interested in my work and has always been available to advise me. I express sincere thanks to Prof. R.P. Chhabra for his valuable suggestions. I express sincere thanks to my doctoral committee chairman Dr. G. Pugazhenthi and other committee members Dr. Pankaj Tiwari and Dr. Amaresh Dalal for their periodic assessment of the findings of my research and their constructive suggestions that had helped a great deal in shaping the thesis in the present form. I express sincere thanks to Prof. Prabirkumar Saha, Dr. Mihir K. Purkait, Dr. Lakshmi Haobam and Dr. M. Venkata Satish Kumar for their support and valuable suggestions. Thanks to other faculty members of the department for their concern and motivation towards my endeavor.

I express thanks to all the staff members of the Department of Chemical engineering for their help in every which way. I express sincere thanks to my labmates Ravi Kiran Anjani, Rahul Ramteke, Harsaraj, Harinath, Dilleswararao, Rajasekhar reddy, Anand, Subramanyam and Vasu Kiran for their support throughout my research.

Completing this work would have been all the more difficult were it not for the support and friendship provided by Subhojit Das, Krishna Chaitanya, Santhi Raju, Praveen, Satyanarayana, Anantharaj, Monash, Murugavel, Vinoth, Vijay Singh, Bolleddu Ravi, Kishore, Kiran, Murali, Anand, Anil, Valapa Ravi, Kartick Mondal, Prashanth, Manna, Ruhit, Anup Kishore, Manohar, Srinivas, Chinna, Yadav, Kamal, Kanchapogu, Chandrasekhar, among others. I am indebted to them. Thank are also to my friends outside of IITG (Dr. T. Siva Sankar, Ganesh, Panthulu Garu, Siva Rama Krishna, Krishna, Venkatesh, N. Ashok, Srinivas, Kiran, T. Ashok, Rajesh, Gopi, Masthanaiah, Srihari, Venkata Ramana, Sandeep, Girivasu, Gouri, Ameer Basha) for their love and wishes throughout my studies.

Last, but not the least, thanks to my family members and relatives who have always been by me through thick and thin and for their help in ways not known to them. I owe sincere thanks for the selfless continued support and encouragement of my mother and younger brother toward my academic pursuit.

N. Venkata Swamy

Contents

List of Tables

List of Figures

Nomenclature

C = molar concentration, kmol m^{-3}

C_d = total drag coefficient, dimensionless

C_{df} = friction drag coefficient, dimensionless

C_{dp} = pressure drag coefficient, dimensionless

C_o = molar concentration at the cell boundary, kmol m^{-3}

C_p = specific heat, $JKg^{-1}K^{-1}$

C_s = molar concentration on the surface of the drop, kmol m^{-3}

d = diameter of sphere, m

D_o = molecular diffusivity, m^2s^{-1}

D_t = diameter of tube, m

F_D = drag force, N

h = convective heat transfer coefficient, $Wm^{-2}K^{-1}$

I_2 = second invariant of the rate of deformation tensor, s^{-2}

k = thermal conductivity, $Wm^{-1}K^{-1}$

L_d = downstream distance, m

L_R = wake length, m

L_u = upstream distance, m

m = power-law consistency index, $Pa.s^n$

n = power-law behavior index, dimensionless

Nu = Nusselt number, dimensionless

Nu_{avg} = average Nusselt number, dimensionless

p = pressure, dimensionless

Pe = Peclet number, dimensionless

Pr = Prandtl number, dimensionless

R = bubble radius, m

Re = Reynolds number, dimensionless

R_{∞} = domain radius, dimensionless

Sc = Schmidt number, dimensionless

Sh = Sherwood number, dimensionless

Sh_{avg} = average Sherwood number, dimensionless

T = temperature, K

T_o = temperature of power-law liquid, K

T_s = temperature of bubble surface, K

U_o = free stream velocity, ms^{-1}

V = velocity vector, ms^{-1}

v_r = r-component of velocity, dimensionless

v_θ = θ-component of velocity, dimensionless

v_ϕ = ϕ-component of velocity, dimensionless

We = Weber number, dimensionless

Greek symbols

α = stagnant cap angle, degree

ε_{ij} = rate of strain tensor, s^{-1}

θ_S = separation point, degree

Π_ε = second invariant of the rate of strain tensor, s^{-2}

Φ = Volume fraction of gas (bubble) phase, dimensionless

η = dynamic viscosity of fluid, Pa s

ρ = density of fluid, kg m^{-3}

τ = extra stress, Pa

λ = wall factor, dimensionless

$\dot{\gamma}$ = shear rate, s^{-1}

ABSTRACT

The presence of impurities or contaminants or surface active materials is unavoidable in many industrial applications in which bubbles play important role. The momentum and heat/mass transfer from bubbles can also be affected by wall confinement, neighboring bubbles and rheology of surrounding continuous liquid. Thus, in this dissertation, the momentum and heat/mass transfer phenomena of unconfined and confined single contaminated bubbles and those of swarms of contaminated bubbles in Newtonian and power-law liquids are numerically elucidated. The non-diffusing surfactant effects are incorporated using the spherical stagnant cap model whereas the effect of volume fraction of contaminated bubble swarms is studied by the use of free surface cell model. The flow behavior and heat/mass transfer phenomena of unconfined single contaminated bubbles in power-law fluids are studied using both in-house solver and Ansys Fluent. The momentum and heat/mass transfer phenomena of confined contaminated bubbles in power-law fluids are studied using Ansys Fluent. The momentum and mass transfer phenomena of swarms of contaminated bubbles is studied using in-house solver. In the in-house solver, a finite difference method based simplified marker and cell (SMAC) semi implicit algorithm used with convective terms being discretized using the quadratic interpolation for convective kinematics (QUICK) scheme; while the diffusive terms discretized using central differencing scheme. In Ansys Fluent, the conservation equation of mass and momentum are solved using the semi-implicit method for pressure-linked equations (SIMPLE) algorithm along with QUICK scheme for convective terms. Furthermore, the contamination effects on the drag coefficients, streamline patterns, surface pressure, surface vorticity, surface viscosity, isotherm contours, surface Nusselt number and average Nusselt number of confined and unconfined single contaminated bubbles and of swarms of contaminated bubbles in power-law fluids are

extensively discussed as functions of the Reynolds number, Prandtl number, stagnation cap angle, power-law index, wall factor and holdup. In summary, for the case of unconfined single contaminated bubbles, for $Re \leq 20$, there is no flow separation for all cap angles and power-law index in the present range of investigation. Regardless of value of the Reynolds number, there is no flow separation for all values of power-law index provided the cap angle is $\leq 30°$. For $\alpha > 30°$ and $Re > 20$, the recirculation wake length increases with increasing Reynolds number and/or cap angle and/or decreasing wall factor and/or holdup. Further a crossover Reynolds number (at $Re \approx 5$) is found on C_d versus Re curve for all values of the index; however, this crossover Reynolds number is found to be weak function of the cap angle. Regardless of the values of the cap angle, below this crossover Reynolds number, the drag coefficients increases with the decreasing power-law index, while the opposite trend is observed above this crossover Reynolds number. In case of confined bubbles this crossover Reynolds number is not found, and the drag coefficient decreased with decreasing power-law indices. Furthermore the drag coefficient of bubbles in a swarm increased with increasing Reynolds number and/or cap angle and/or bubble holdup. The thermal boundary layer becomes thinner with increasing Reynolds number and/or Prandtl number and/or decreasing wall factor and/or cap angle and/or power-law index. The average Nusselt number increases with increasing Reynolds number and/or Prandtl number and/or bubble holdup and/or decreasing cap angle and/or wall factor and/or power-law index.

Chapter 1

INTRODUCTION

1.1. General Introduction

Presence of bubbles is ubiquitous in many chemical, biochemical and processing industries. Some applications include bubble columns, aeration, pollution cleaning systems, purification of materials and extraction of materials from mixtures, production of polymeric alloys and ceramics via liquid route, emulsions, paints, food processing and preservation, pharmaceutical products, wastewater treatment, floatation, etc. Some industrial applications include removal of inorganic contaminants from fuel gas using gas bubbles (Yang and Li 2012), removal of mineral ores using froth flotation (Ghosal *et al.*, 1993), removal of oil and other impurities from water using bubbles, separation of bitumen from oil sand pulp by using bubbles (Drelich *et al.*, 1994), removal of sediment fraction containing heavy metals from river sediment by flotation (Abd-El-Rahman *et al.*, 1999) etc. The motion of a bubble or a droplet in an immiscible fluid medium differs from that of a solid particle because of mobile surface of bubbles/droplets and the internal circulations inside bubbles/droplets. Furthermore, the rate of mass transfer from circulating bubbles/droplets can be greatly affected by the intensity of the internal circulations inside the bubbles/drops. However, it is difficult to maintain clean conditions and the presence of surfactants or contaminants or impurities is unavoidable in multiphase flows. The effect of surface contamination on the hydrodynamics of and mass transfer from bubbles can effectively be handled by the use of spherical stagnant cap model. According to this model, the insoluble contaminants can be adsorbed on the surface of a bubble and move towards the rear end of the bubble because of surface advection caused by the main flow. Further these contaminants

accumulate at the rear end of the bubble forming an immobile stagnant cap while the rest of the bubble surface remains mobile. As the concentration of contaminants gradually increases, the surface of the bubble is increasingly covered by contaminants and ultimately in the limit of the fully covered by contaminants the bubble behaves as a solid particle. The angle of surface contamination is a measure of the fraction of the bubble surface covered by the contaminants and is referred to as the stagnant cap angle (α). The stagnant cap angle is measured from the rear stagnation point and in the limits of $\alpha = 0$ and $\alpha = \pi$, the partially contaminated bubble represents completely clean spherical bubble and fully contaminated immobile spherical solid particle, respectively. This phenomenon is perhaps first explained by Frumkin and Levich (1947); and later on well supported by several other studies in the literature (Savic, 1953; Garner and Skelland, 1955; Elzinga and Banchero, 1961; Horton, *et al*., 1965; Huang and Kintner, 1969; Beitel and Heideger, 1971; McLaughlin, 1996; Cuenot *et al.*, 1997; Ponoth and McLaughlin, 2000; Liao and McLaughlin, 2000; Liao *et al*., 2004). However, Sadhal and Johnson (1983) generalized this model to the case of droplets as well; and reported closed form expressions for the drag force of contaminated bubbles and drops as function of the stagnant cap angle (α). The steps involved in the stagnant cap formation process are shown in **Figure 1.1**. Initially, bubbles are free from contaminants, then during the process of bubble rise the contaminants in bulk solution diffuse towards the bubble surface and these contaminants are adsorbed on to the surface of the bubble. The adsorbed contaminants move to the rear end because of the surface convection and form a spherical stagnant cap at the rear end of the bubble. The kinetics of stagnant cap formation depends on the adsorption/desorption kinetics of surfactant and convection over the bubble interface (Krzan *et al.*, 2004; Krzan *et al.*, 2007). The rates of either kinetic adsorption of contaminants or diffusive transport of contaminants to the bubble surface

are low compared to the surface convection; and the surface diffusion should be low for the formation of stagnant cap (Palaparthi *et al.*, 2006).

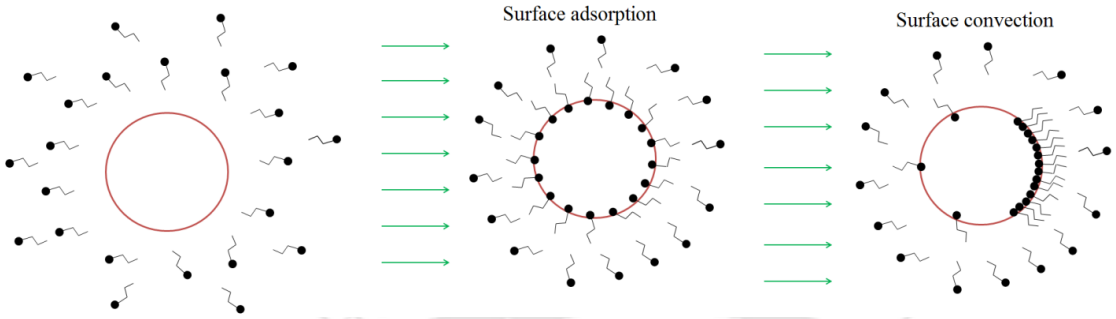

Figure 1.1: Schematic diagram of stagnant cap formation.

Furthermore, notwithstanding the valuable physical insights gained from the study of single bubble dynamics, the presence of the neighboring bubbles modifies the flow field around each bubble which, in turn, impinges on the resulting momentum, heat and mass transfer rates in such systems. From a theoretical standpoint, a mathematical framework is needed to describe the inter-bubble interactions which can be combined with the momentum and species continuity equations to obtain the velocity and concentration fields for bubble swarms rising in surfactant-laden fluids. Thus, the combination of spherical stagnant cap model and spherical cell approach can be advantageous. In the spherical cell model, which is somewhat less rigorous, the inter-particle interactions are approximated by postulating the each spherical particle to be surrounded by a hypothetical concentric envelope of continuous phase. The size of the envelope is chosen such that the volume fraction of the dispersed phase of the cell is equal to the overall mean volume fraction of the system. Thus, the radius of the hypothetical envelope is related to the size of an individual sphere via the mean volume fraction of the dispersed phase. Furthermore, over the years, many boundary conditions on the hypothetical envelope have been proposed (Chhabra,

2006; Zholkovskiy *et al.*, 2007a,b); however, zero shear stress (Happel, 1958) and zero vorticity (Kuwabara, 1959) conditions are extensively used in hydrodynamic studies of bubbles, drops and particles in Newtonian and non-Newtonian continuous fluids. Though, both models prescribe free stream velocity for normal component of the velocity; however, the second boundary condition along the hypothetical envelope is different. Because of the extra energy dissipation in the zero vorticity cell model, the resulting values of drag are larger than those obtained by the free surface cell model. While it is difficult to theoretically justify either of these conditions, both have been used to treat scores of situations involving flow of Newtonian and non-Newtonian fluids through multiple bubbles, drops and particles over wide range of Reynolds numbers (Chhabra, 2006). Furthermore, these cell models have also been extensively used in other real life applications such as electrophoresis (Hsu *et al.*, 2004; Lee *et al.*, 2004), heterogeneous catalytic reaction, etc. (Mao *et al.*, 2007; Lee *et al.*, 1998). Recently Zholkovskiy *et al.* (2007a,b) have extensively reviewed the literature on the use of spherical cell approach for a range of systems such as pure multiparticle-fluid hydrodynamics to electrokinetic phenomena in concentrated dispersed systems; and provided comparative information on the merits and demerits of different boundary conditions used along the spherical cell boundary. However, in regard to multiparticle-fluid interactions (such as in the case of flow through packed and fluidized beds, etc.), the superiority of free surface cell model over other cell models has been extensively demonstrated (Chhabra, 2006). The main advantage of free surface cell model is to provide information on the effect of volume fraction on the overall drag and mass transfer coefficients of dispersed two phase system without investigating the flow behavior around each individual particle (fluid particle or solid particle) in the ensemble. Thus, in this dissertation work free surface cell model has been adopted for the case of swarms of contaminated bubbles.

On the other hand, many materials encountered in several industrially important applications (polymers, food, fermentation, effluent treatment, emulsions, etc.) display a range of non-Newtonian characteristics including shear-thinning, shear-thickening, yield stress and viscoelastic characteristics (Chhabra and Richardson, 2008). Heavy oil, fracturing fluids, drilling muds, high density polyethylene, high impact polystyrene, poly propylene, nylon, poly carbonate and silica nanoparticles in polyethylene glycol are some examples of power-law fluids (Chhabra and Richardson, 2008; Escobar *et al.*, 2012; Yu *et al.*, 2012). Furthermore, the motion and heat/mass transfer phenomena of contaminated bubbles to surrounding surfactant-laden liquids can also be affected by the confining wall of the contacting equipment.

Therefore, not only the contamination (surfactants) affect the motion and heat/mass transfer of bubbles but also the presence of surrounding bubbles (swarms of bubbles), the wall retardation due to the confining container wall and the rheology of the surrounding continuous liquid affect the overall momentum and heat/mass transfer characteristics of the bubble motion. Thus, the rate of bubble rise and the rate of mass transfer from single and multiple contaminated bubbles in surfactant-laden power-law fluids is a good approximation of many industrially important multiphase flow applications. For instant, the knowledge of the bubble rise velocity facilitates the sizing of the contacting equipment if the desired residence time is known from other considerations, or conversely, for existing contacting equipment, it is used to calculate the mean contacting time. Similarly, the rate of bubble motion also helps in ascertaining the stability of an emulsion or the ease of separation by gravity depending upon the envisaged application. Furthermore, the rate of mass transfer is enhanced in the case of multiple bubbles because of the bending of the streamlines and the corresponding sharpening of the velocity and concentration gradients in the vicinity of the bubble in a swarm as compared to the case of an isolated bubble

in an unconfined continuous liquid. Therefore, an adequate knowledge of the rise velocity and the rate of mass transfer from unconfined and confined single and swarms of partially contaminated bubbles moving in surfactant-laden power-law fluids is a prerequisite to understanding, designing and rationalizing the overall efficiency of gas-liquid contacting system. This information can be conveniently presented in terms of the pertinent dimensionless parameters such as the Reynolds number (Re), power-law behavior index (n), volume fraction of the dispersed phase (Φ), degree of stagnant cap (α), wall factor (λ) and Schmidt number (Sc). Thus, this dissertation aims to numerically investigate the momentum and heat/mass transfer phenomena of single and multiple contaminated bubbles in an unconfined and confined flow of surfactant-laden power-law fluids as functions of aforementioned dimensionless parameters. The swarms of multiple bubbles cases are numerically investigated using in-house finite difference method based solver whereas the case of confined bubble is investigated using ANSYS Fluent commercial solver and the case of unconfined contaminated single bubble in surfactant-laden power-law fluids is solved by the use of both Fluent and in-house solver. However, before proceeding to other chapters, classification of fluids and an overview of the present dissertation are presented below.

1.2. Classification of Fluids

A substance which undergoes a continuous deformation under the action of external shear force is known as fluid (liquid or gas). Depending on their response to the externally applied pressure, fluids can be classified as compressible and incompressible fluids. Most of the gases are compressible whereas liquids are incompressible whose response to shearing forces is of great importance. In this study, by default, all fluids are regarded as incompressible fluids. Based on the response to the externally applied shear action, fluids can be classified as purely viscous,

purely elastic and visco-elastic fluids. A purely viscous fluid dissipates all the energy as heat due to the viscous resistance. The deformation in purely viscous fluids is irreversible. A purely elastic fluid is capable of storing all the energy and release it as soon as the external shearing force is removed. Thus, the deformation in purely elastic fluids is reversible. On the other hand, a large number of fluids show a combination of both viscous and elastic characteristics which are known as visco-elastic or elastico-viscous fluids depending on the contributions of viscous and elastic effects. These fluids are capable to store part of the energy while the rest, they dissipate as the heat due to viscous resistance because of the shearing action.

1.2.1. Newtonian fluids

Newton's law of viscosity states that the shearing force per unit area is proportional to the negative of the velocity gradient. The proportionality constant of this relation is defined as the dynamic viscosity of the fluid. A fluid which obeys this law is called as a Newtonian fluid. The rheogram or flow curve (i.e., shear stress versus shear rate curve) of a Newtonian fluid is a straight line passing through the origin as shown in **Figure 1.2** and the slope of this line is the viscosity of the fluid. The viscosity of a Newtonian fluid is independent of the shear rate and the shear stress at a given temperature and pressure. Some of examples include many gases, water, simple organic liquids, solutions of low molecular weight inorganic salts, molten metals, etc.

1.2.2. Non-Newtonian fluids

For a non-Newtonian fluid, the flow curve or rheogram is non-linear and/or does not pass through origin i.e., the ratio of the shear stress and the shear rate is not constant at a given temperature and pressure. These non-Newtonian fluids can further be classified as follows:

a. Time-independent fluids for which the relation between shear stress and shear rate is independent of duration of shearing and its kinematic history. These fluids are also known as “purely viscous”, “inelastic”, “generalized Newtonian” fluids.

b. Time-dependent fluids for which the relation between shear stress and shear rate depends upon the duration of shearing and its kinematic history.

c. Visco-elastic fluids which exhibit characteristics of both ideal fluids and elastic solids i.e., they exhibit the recovery upon release of the external force.

1.1.2.1. Time-independent fluids

For these fluids, the shear stress is purely a function of shear rate only and depending on the type of functionality these fluids may further divided into the following subgroups. Qualitative flow curves on linear scales for these fluids are shown in **Figure 1.2**.

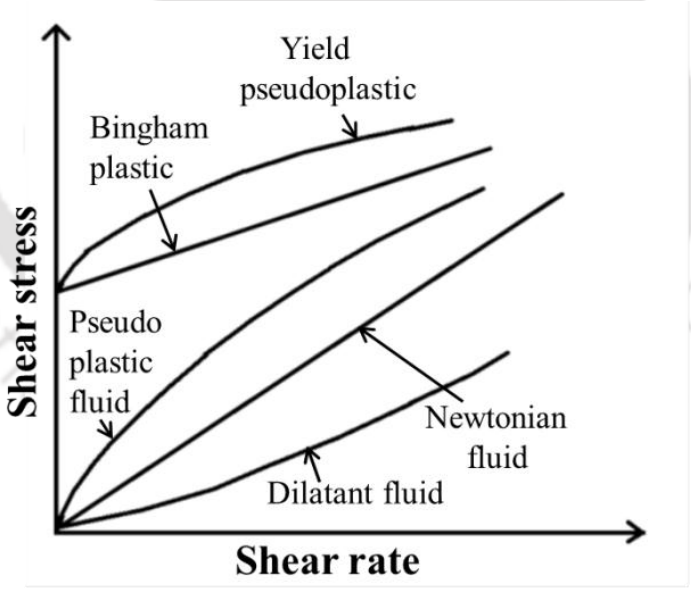

Figure 1.2: Rheogram of time-independent non-Newtonian fluids.

Shear-thinning or pseudoplastic fluids: The apparent viscosity of these fluids decreases with the shear rate and the flow curve is concave downwards. Both at very low and very high shear rates, most of shear-thinning fluids exhibits Newtonian behavior. For intermediate shear rates the slope of the curve at any point is < 1 and depending on the type of polymer this may vary from just < 1 to close to zero. Suspensions, emulsions, high molecular weight solutions, blends, melts, etc. exhibit this behavior. Only a selection of more widely used models for these fluids are presented here.

- *The power law or Ostwald de Waale model*: In the intermediate shear rate region, the non-linear flow curve of shear-thinning and shear-thickening fluids can be represented as a straight line on double logarithmic coordinates. Thus, the following expression is appropriate to represent these fluids:

$$\tau_{yx} = m\dot{\gamma}^{n} \tag{1.1}$$

Thus the apparent viscosity of a power law fluid is given by

$$\eta_{app} = m\left|\dot{\gamma}\right|^{n-1} \tag{1.2}$$

For $n < 1$, $n = 1$ and $n > 1$, this model exhibits shear-thinning, Newtonian and shear-thickening behaviors, respectively.

- *The Carreau viscosity model*: This model also accounts for viscosities in the low and high shear rate regions i.e, η_0 and η_∞ as compared to the power law model. Based on molecular network considerations, Carreau proposed the following expression for these fluids

$$\frac{\eta-\eta_\infty}{\eta_0-\eta_\infty} = \left[1+\left(\lambda_c\dot{\gamma}\right)^2\right]^{(n-1)/2} \tag{1.3}$$

Where λ_c is relaxation time, for $n < 1$, this model represents shear-thinning fluids, whereas, for $\eta = \eta_0$, $n = 1$ and $\lambda = 0$, this model reduces to Newtonian fluid behavior.

- *Ellis fluid model*: When the deviations from the power-law model are significant only at low shear rates, then Ellis model is more appropriate to be considered.

$$\eta = \frac{\eta_0}{1 + \left(\tau_{yx} / \tau_{1/2} \right)^{\alpha_E - 1}} \tag{1.4}$$

Where index α_E is a measure of the degree of shear-thinning behavior (the greater the value of α_E, greater is the extent of shear-thinning), $\tau_{1/2}$ is the shear stress at which the apparent viscosity drops to half of its zero viscosity, η_0. This model reduces to Newtonian behavior for $\tau_{1/2} \to \infty$.

Shear-thickening or dilatants fluids: The rheological behavior of these fluids is exactly opposite to that of shear-thickening fluids. The flow curve for these fluids is concave upward and their apparent viscosity increases with the shear rate. In the intermediate region of shear rates the slope of the curve at any point is > 1 and it follows the Newtonian fluid behavior in the low and very high shear rate regions. Examples of such fluids are rare like high concentrated suspensions of corn syrup, kaolin in water, china clay, titanium in suspensions, beach sand, PVC in dioctylphthalate, etc. For $n > 1$, equation (1.2) represents the shear-thickening behavior.

Viscoplastic fluids: These fluids require a certain additional amount of stress before they flow which is known as a yield stress. Once the magnitude of the external force exceeds this yield stress, the flow curve may be linear or non-linear. A fluid with a linear curve after exceeding the yield stress is called as a Bingham plastic, whereas, a fluid with non-linear flow curve after exceeding the yield stress is known as a yield-pseudoplastic material. Some of examples include

carbonal solutions, meat extract, chocolates, paints, foams, blood, drilling muds, etc. Some models related to viscoplastic fluids are presented.

- *Bingham plastic model*: This model represents the viscoplastic fluids for which the flow curve in the intermediate shear rate region is linear.

$$\tau_{yx} = \tau_0 + \eta_0\left(\dot{\gamma}_{yx}\right) \quad for \ |\tau_{yx}| > |\tau_0| \tag{1.5}$$

where

$$\dot{\gamma}_{yx} = 0 \qquad for \qquad |\tau_{yx}| < |\tau_0|$$

- *Herschel- Bulkley fluid model*: This model represents the viscoplastic fluids for which the flow curve is non-linear after exceeding the yield stress.

$$\tau_{yx} = \tau_0 + m\left(\dot{\gamma}_{yx}\right)^n \quad for \ |\tau_{yx}| > |\tau_0| \tag{1.6}$$

where $\dot{\gamma}_{yx} = 0 \qquad for \qquad |\tau_{yx}| < |\tau_0|$

- *Casson fluid model*: Many biological materials are described by this model.

$$|\tau_{yx}|^{1/2} = |\tau_0|^{1/2} + \left(\eta\left|\dot{\gamma}_{yx}\right|\right)^{1/2} \quad for \ |\tau_{yx}| > |\tau_0| \tag{1.7}$$

where $\dot{\gamma}_{yx} = 0 \qquad for \qquad |\tau_{yx}| < |\tau_0|$

1.1.2.2. Time-dependent fluids

The relation between shear stress and shear rate of these fluids depend on the duration of the shearing and its kinematic history. Based on the time dependent nature of the viscosity of these fluids, they are classified as follows:

Thixotropic fluids: When these fluids are subjected to constant shear rate then the shear stress and apparent viscosity of these fluids will decrease with the time. Thixotropic fluids are essentially pseudoplastic type where the orientation of molecules at a particular shear rate is a time dependent process as compared to being instantaneous as in the case of pseudoplastic fluids. Some of examples include concentrated suspensions, emulsions, protein solutions, food stuffs, etc.

Rheopectic or negative thixotropic fluids: As the time of shearing progress, the apparent viscosities of these fluids increase. Rheopectic fluids are dilatants type fluids where the dilatancy is time dependent. Colloidal suspensions, coal slurries, aqueous gypsum paste etc. display this behavior. The deformation of both thixotropy and rheopexy fluids form hysteresis loop.

1.1.2.3. Viscoelastic fluids

These fluids display characteristics of both ideal fluids and elastic solids. They deform upon application of external stress and show partial recovery upon the removal of external stress, and remaining portion, they dissipate as energy due to viscous friction. Polymer melts, polymer and soap solutions, synovial fluid, etc. display both viscous and elastic characteristics. The fraction of viscous and elastic characteristics can be characterized by well-known Deborah number, *De*, defined as the ratio of characteristic time of the substance to the time scale of the process. Small and large values of Deborah number imply to viscous and elastic behaviors respectively.

1.3. Organization of Thesis

This dissertation work dealing with the numerical investigation of momentum and heat/mass transfer phenomena of single and swarms of partially contaminated bubbles in unconfined and confined power-law fluids is organized into seven chapters as follows:

- Chapter 2 deals with literature available for single and swarms of clean bubbles, partially contaminated bubbles and fully contaminated bubbles in Newtonian and non-Newtonian fluids. Literature on wall retardation effects on clean and fully contaminated bubbles are also critically reviewed thereby facilitating to setup the goals for this work.

- Chapter 3 deals with problem statement and mathematical formulation for the momentum and heat/mass transfer phenomena of partially contaminated single and swarms of spherical bubbles in Newtonian and non-Newtonian fluids. This chapter also presents the underlying assumptions, field equations, appropriate boundary conditions and the dimensionless parameters associated with the present study. Further this chapter also presents the post processing of results to infer the values of the derived parameters like drag coefficients, Nusselt and/or Sherwood numbers, streamlines, concentration contours, etc. as functions of pertinent kinematic and rheological parameters.

- Chapter 4 deals with the numerical methodology for studying momentum and heat/mass transfer phenomena of partially contaminated single and swarms of spherical bubbles in Newtonian and non-Newtonian fluids in-house solver and ANSYS Fluent. This chapter also presents discretization of governing equations and boundary conditions.

- Chapter 5 presents choice of numerical parameters by means of domain and grid independence studies. Further this chapter also presents the reliability and accuracy of present numerical solver by comparing present results with literature counterparts.

- Chapter 6 deals with results and discussion of different cases considered in this study. To be specific, the momentum transfer behavior of partially contaminated single bubbles in unconfined Newtonian and power-law fluids is investigated by using both in-house solver

and ANSYS Fluent; whereas the associated heat/mass transfer phenomena has been investigated using ANSYS Fluent only. The drag and heat/mass transfer phenomena of confined partially contaminated spherical bubbles in Newtonian and power-law fluids are investigated using ANSYS Fluent. Finally the drag and heat/mass transfer phenomenon of swarms of partially contaminated bubbles in Newtonian and power-law fluids are studied using the in-house solver. The streamline patterns, vorticity contours, surface pressure distribution, surface vorticity distribution, drag coefficient, drag ratio, isotherm contours, surface Nusselt number and average Nusselt number for wide range of Reynolds number, Prandtl number, wall factor, volume fraction, power-law indices and stagnant cap angle are delineated and discussed in details.

- Chapter 7 summarizes the major findings of this dissertation work along with the possible scope for future work.

Chapter 2

LITERATURE REVIEW

The literature pertaining to the momentum and heat/mass transfer phenomena of fully clean bubbles ($\alpha = 0$) and fully contaminated bubbles ($\alpha = \pi$) in Newtonian and non-Newtonian fluids have been thoroughly reviewed by Clift *et al.* (1978), Soo (1990), Michaelides (2006) and Chhabra (2006). Further developments on fully contaminated spherical bubbles (immobile surface) in confined Newtonian and non-Newtonian fluids are thoroughly reviewed in Reddy and Kishore (2012, 2013). Thus this chapter presents brief recount of analogous literature for the case of partially contaminated bubbles in Newtonian and non-Newtonian fluids. However, the literature on the swarms of partially contaminated bubbles in Newtonian fluids is virtually non-existent even in the creeping flow regime, let alone for intermediate to large Reynolds numbers, thus the previous work for two extreme cases of the stagnant cap angles, i.e. $\alpha = 0$ (swarms of clean bubbles) and $\alpha = 180^{o}$ (assemblages of fully contaminated bubbles or assemblages of solid spheres) are presented.

2.1. Partially Contaminated Bubbles

2.1.1. Flow phenomena

2.1.1.1. Newtonian fluids

The literature pertaining to effects of contaminants on drag coefficients of bubbles and drops in Newtonian continuous liquids is available at least in the steady axisymmetric flow regime using the so–called stagnant cap model. The formation of stagnant cap is probably first explained by

Frumkin and Levich (1947); and later on well supported by several other studies in the literature (Savic, 1953; Garner and Skelland, 1955; Elzinga and Banchero, 1961; Horton *et al*., 1965; Huang and Kintner, 1969; Beitel and Heideger, 1971; McLaughlin, 1996; Cuenot *et al.*, 1997; Ponoth and McLaughlin, 2000; Liao and McLaughlin, 2000; Liao *et al*., 2004). The experimental literature on effects of surfactants (contaminants) on rise velocity and associated mass transfer of bubbles show significant variations from those of clean bubbles. Some of the key findings are presented here. From experimental studies it appear that surfactants are distributed in such a way to form an immobile cap over the rear of a globule while surface flow is not obstructed on the forward surface (Cullen and Davidson, 1957; Griffith, 1962). Davis and Acrivos (1966) predicted the cap size and associated bubble drag as a function of the surface pressure at which the contaminant stagnant film collapses. Skelland *et al.* (1987) studied effects of surface active agents on the drop size, terminal velocity and droplet oscillation in liquid-liquid systems. They found that the terminal velocity not affected by the type of surfactant and furthermore the effect of surfactant on the onset of droplet oscillation was also small.

The stagnant spherical cap model was first generalized by Sadhal and Johnson (1983) for both bubbles and drops in the creeping flow limit. They proposed following analytical expression for drag forces of contaminated bubbles and drops.

$$C_d = \frac{16}{\mathrm{Re}}\left\{\frac{1}{2\pi\left(1+k_\mu\right)}\left(2\left(\pi-\theta_{cap}\right)+\sin\left(\theta_{cap}\right)+\sin\left(2\theta_{cap}\right)-\frac{1}{3}\sin\left(3\theta_{cap}\right)\right)+\frac{2+3k_\mu}{2+2k_\mu}\right\} \qquad (2.1)$$

Where, k_μ is the ratio between viscosity of dispersed bubble/drops phase and the continuous phase. This correlation reduces to Levich (1962) solution for the case of clean spherical bubbles; reduces to Hadamard (1911) and Rybczynski (1911) solution for the case of clean spherical

droplets; and reduces to Stokes drag for fully contaminated bubbles (i.e., rigid sphere). Their expression for drag force of contaminated bubbles/drops shows that the drag force of contaminated bubble is almost equal to those of clean bubble for $\alpha \leq 40$; and is very close to those of rigid particles for $\alpha \geq 140$. Between these two limits the drag force of contaminated bubbles is strongly increasing with increasing value of cap angle. However, the analytical expression of Sadhal and Johnson (1983) is valid for a very small concentration of surfactants because they considered linear relation for surfactant surface pressure. Thus He *et al.* (1991) concluded that the results of Sadhal and Johnson (1983) leads to under-prediction of cap angle and drag coefficient; and revisited the same problem by taking account of non-linear effects. Fdhila and Duineveld (1996) carried out experiments and numerical simulations to obtain the rising velocity of small bubbles (organic and inorganic materials) in quiescent contaminated solutions in the range of Reynolds numbers 50 – 200. They found that the benchmarking between experimental results and simulation values by stagnant cap model is satisfactory. Leppinen *et al*. (1996a, b) numerically calculated the complete Navier – Stokes equations inside and around the spherical and deforming droplet coupled with surfactants concentration along the interface. Leppinen *et al.* (1996a) observed that when the droplet is spherical, effect of contamination on the drag of the fluid sphere is small; while, when the droplet is allowed to deform (Leppinen *et al*., 1996b), significant effect of surfactants concentration is found on the amplitude of the droplet oscillations. McLaughlin (1996) numerically investigated the effect of surfactants on a deforming bubble rising in water at Reynolds numbers ranging up to 600. McLaughlin and coworkers (Ponoth and McLaughlin, 2000; Liao and McLaughlin, 2000; Liao *et al*., 2004) carried out extensive experimental and numerical studies; and provided support for the accuracy of stagnant cap model for the case of bubble rise in a Newtonian liquid diluted with

surfactants over wide range of conditions. Cuenot *et al*. (1997) numerically investigated the effects of contamination (weekly soluble surfactants) on bubble rise velocity at higher Reynolds numbers. Their results also provide numerical support to the reliability of the stagnant cap model even at high Reynolds number. Takemura and Yabe (1999) experimentally and numerically investigated the rising velocity and dissolution rate of carbon dioxide bubbles in slightly contaminated water. They found that their drag coefficients and Sherwood numbers obtained by stagnant cap model are in excellent agreement with their own experimental counterparts. Thus this study also infers ability of the stagnant cap model to explain the mechanism of transient process where the bubble behavior changes from that of a fluid sphere to that of a solid sphere. Further Takemura and Matsumoto (2000) conducted experiments on dissolution rate of spherical carbon dioxide bubbles in strong alkaline solutions of sodium hydroxide with simultaneous chemical reactions. In the same paper, under the assumption of stagnant cap model, they also reported numerical results by solving complete Navier – Stokes equations and convection – diffusion equations for bubble dissolving in alkaline solution with simultaneous nonequilibrium reaction at the bubble surface. The agreement between their experimental and numerical values of drag coefficients and Sherwood numbers are found to be satisfactory. Zholkovskij *et al.* (2000) reported the physico-chemical hydrodynamics of rear stagnation cap formation at low Reynolds numbers and found that the bubble velocity depends on time because of non-stationary process of surface stagnant zone formation. Zhang and Finch (2001) experimentally investigated the unsteady rising of contaminated bubbles and observed that the transient distance to reach the steady state can be order of few meters at low concentrations of surfactants. Zhang *et al*. (2001) studied bubble velocity profile and surfactant mass transfer to bubble surface. They found that simulated and experimental velocity profiles shown stagnant cap model and boundary layer mass

transfer control are valid for adsorption of Triton X-100 onto rising bubble diameter of 0.8mm. Zhang *et al.* (2003) studied temperature effect on single bubble velocity profile in water and surfactant solution. They found that time to reach constant velocity decreased with increasing temperature. In surfactant solution, temperature has no effect for $Re > 130$. Krzan *et al.* (2002) studied local velocity profiles of bubbles in *n*-butanol, *n*-hexanol and *n*-nonanol solutions. The degree of deformation (ratio between horizontal and vertical diameters) found to be larger in clean water than in *n*-alkanol solutions with the corresponding horizontal and vertical diameter ratios of 1.5 and 1.05-1.03. Alves *et al.* (2005) experimentally investigated the effect of bubble contamination on its rise velocity and mass transfer by using simplified stagnant cap model. The stagnant cap model is modified to account for the dissolution of surfactants by diffusion mode. The experimental results are found to be consistent with simple relationship of Takemura and Yabe (1997) under very different conditions from those in Alves *et al.* (2005). Recently, Palaparthi *et al.* (2006) conducted experiments and numerical simulations for glycerol – water system with a polyethylene – oxide surfactant under the assumption of spherical stagnant cap model. They also obtained a good agreement between experimental and numerical results. Saboni *et al.* (2010) numerically investigated effects of the contamination on flow and drag behavior of fluid spheres at Reynolds number ranging up to 400 using the spherical stagnant cap model. They used the stream function – vorticity approach with exponential transformation in the radial direction so that to tackle the finer grid requirement around the fluid sphere in a larger computation domain of unconfined flow. They proposed following correlation for drag coefficient of contaminated fluid sphere as function of drag coefficients of clean fluid sphere and fully contaminated fluid sphere and the normalized drag coefficient of Sadhal and Johnson (1983).

$$C_D = C^*_{D,Sadhal\&Johnson}\left(C_D^{rigid} - C_D^{mobile}\right) + C_D^{mobile} \qquad (2.2)$$

Their correlation reproduces their own numerical results within ±15% of difference. Finally, on the basis of extensive experimental and numerical literature cited above, it is thus safe to conclude that a coherent picture has arrived on the flow and drag behavior of partially contaminated bubbles in Newtonian liquids at least in the steady axisymmetric flow regime.

2.1.1.2. Non-Newtonian fluids

On the other hand, pertaining to the flow and drag phenomena of partially contaminated bubbles/drops in power-law fluids, the available literature is very limited. Rodrigue *et al*. (1996) experimentally investigated the rising velocity of contaminated bubbles in Carreau model non-Newtonian fluids. Rodrigue *et al*. (1997) employed perturbation technique to theoretically investigate the drag force of a contaminated bubble in Carreau model fluids in the limit of small Carreau number. Rodrigue *et al*. (1999) further extended their study for power-law and Carreau model fluids using thermodynamic approach (which assumes linear difference in the surface tension from the equilibrium value) and a physical approximation (based on geometry and boundary conditions) in the limit of small Reynolds number. Tzounakos *et al*. (2004) experimentally investigated the effect of surfactant concentration on the terminal velocity, shape and drag coefficient of bubbles in power-law liquids. They found that the bubble shape is independent of the surfactant concentration used in their study; however, the rise velocity and surface mobility of bubbles are strong functions of the concentration of the surfactants. Thus, the reliable information on the flow and drag behavior of partially contaminated bubbles in unconfined and confined power-law (and other types of) non-Newtonian fluids within the framework of spherical stagnant cap model is not available in the open literature.

2.1.2. Heat/mass transfer phenomena

Garner and Hale (1953) studied effect of surface active agents in liquid extraction processes. They found that addition of only 0.015% of Teepol to water phase causes reduction in the rate of extraction of diethylamine from toluene drops. Garner and Skelland (1955) studied factors effecting droplet behavior in liquid-liquid systems. They found that presence of surfactants inhibit internal circulation inside drops which causes to decrement in mass transfer. Similar observations were also made by several other researchers (Elginga and Banchero, 1961; Horton *et al.* 1965; Boye-Christensen and Terjesen, 1959; Huang and Kintner, 1969). Lindland and Terjesen (1956) studied the effect of surface active agents on mass transfer in falling drop extraction. They found 68% reduction in overall mass transfer coefficient when 6×10^{-5} g of sodium oleyl-p-anisidinesulphonate added to 100 ml of water. With increasing surfactant concentration further, its effect on mass transfer coefficient was found to be insignificant. Boye-Christensen and Terjesen (1959) studied the effect of surface active agents on extraction of o-nitrophenol and iodine from aqueous solutions by single drops of carbon tetrachloride. They found that surface active agents decrease terminal velocities, and rate of mass transfer from drops. Huang and Kintner (1969) developed mass transfer model based on the spherical cap assumption by allowing reduction in interfacial area and changes in internal circulation. In the presence of surface active agents, the internal circulations, oscillations, and zig-zag path of drops were found to be completely eliminated**.** Takemura and Yabe (1999) studied the dissolution rate of gas bubbles at Reynolds numbers below 100 both experimentally and numerically using the spherical stagnant cap model. Ponoth and McLaughlin (2000) studied the effect of surfactants on the dissolution rate of carbon dioxide, methane and helium bubbles using finite difference

method and stochastic Lagrangian approach and developed following correlation to their results which relates the Sherwood number of bubble to its size and Reynolds number.

$$Sh = y\left(Sh_m - Sh_{im}\right) + Sh_{im} \tag{2.3}$$

Where

$$y = x^{0.434} \tag{2.4}$$

$$x = \frac{\mathrm{Re} - \mathrm{Re}_{im}}{\mathrm{Re}_m - \mathrm{Re}_{im}} \tag{2.5}$$

$$\mathrm{Re}_m = -255 + 516 d_e \tag{2.6}$$

$$Sh_m = 1.13\left[1 - \frac{2.96}{\mathrm{Re}_m^{1/2}}\right]^{1/2} Pe^{1/2} \tag{2.7}$$

$$\mathrm{Re}_{im} = \frac{Ar}{18}\left[1 + \frac{Ar/96}{\left(1 + 0.079 Ar^{0.749}\right)^{0.755}}\right]^{-1} \tag{2.8}$$

$$Sh_{im} = 0.725\,\mathrm{Re}_{im}^{1/2}\, Sc^{1/3} \tag{2.9}$$

Here subscripts "im" and "m" stands for immobile and mobile surfaces respectively. Vasconcelos *et al.* (2002) studied the dissolution of single bubbles of low solubility gases in a downward stream of water by adapting stagnant cap model and predicted transition point of mobile to immobile for various range of conditions including different gases with various concentrations and a wide range of bubble diameters. Alves *et al.* (2004) studied the gas-liquid mass transfer in stirred tanks interpreted through bubble contamination kinetics and found that bubbles in PEG solution behave as rigid bubbles (k_L^{rigid}), bubbles in tap water behaving closer to

mobile (k_L^{mobile}), bubbles in salt solution are with intermediate values of k_L. Alves *et al.* (2005) have also studied the effect of bubble contamination on its rise velocity and mass transfer and reported that their theoretical predictions of mass transfer coefficients are consistent with their own experimental mass transfer coefficients. Painmanakul *et al.* (2005) found that the liquid-side mass transfer coefficient is same for all bubble diameters; and Higbie (1935) and Frossling (1938) theories not applicable for the presence of small amount of surfactants. They proposed a model on the basis of surface coverage ratio to predict the liquid side mass transfer coefficient. Sardeing *et al.* (2006) predicted that the liquid-side mass transfer coefficient depends on bubble diameter. For bubble diameter < 1.5 mm, the liquid-side mass transfer coefficient found to be constant and presence of surfactants does not affect the liquid-side mass transfer coefficient, however, for bubble diameter > 3.5 mm, the liquid-side mass transfer coefficient depends on the concentration of surfactants. Dani *et al.* (2006) studied the effect of interface contamination on the mass transfer from spherical bubbles at low Reynolds numbers using dynamic numerical simulation. The obtained results of average Sherwood number are proportional to $Pe^{1/3}$ and $Pe^{1/2}$ for fully contaminated and clean bubbles respectively. Dani (2007) studied contamination effects on mass transfer from bubble in the range of Reynolds number ($0.01 \leq Re \leq 300$), Schmidt number ($1 \leq Sc \leq 10^5$) and contamination angle ($0^o < \alpha < 180^o$) by solving Navier-Stokes equation and diffusion-advection for a scalar. Dani *et al.* (2007) studied the effect of interface contamination on the mass transfer from single spherical bubble with the presence of chemical reaction by solving the equations using COMSOL software and concluded that Sherwood number increases with the Peclet number, contamination angle and Damkohler number. Madhavi *et al.* (2007) studied reactive bubble system of CO_2^- aqueous solutions of NaOH for various concentrations of NaOH (4%, 6% and 10% (w/v)) and found that the size reduction of bubbles in

more concentrated solutions is faster because of chemical reaction and reduction in shrinking rate of bubble after certain time due to accumulation of surfactants on bubble surface. Maceiras *et al.* (2008) studied the effect of bubble contamination on CO_2 absorption in amine solutions experimentally, and found that the mass transfer coefficient decreases mainly due to the reduction in mobile surface with the increase in contamination. Francois *et al.* (2011) compared their experimental results of Sherwood number with theoretical predictions of Frossling (1938) and Higbie (1935) models for fully contaminated and clean bubbles, and found that their experimental results are in between theoretical predictions of Frossling (1938) and Higbie (1935). In a recent study, Saboni *et al.* (2011) numerically investigated the effect of contamination on the mass transfer from contaminated fluid sphere to a Newtonian liquid using the spherical stagnant cap model in the range of Reynolds number *(0 < Re < 200)*, Peclet number *(0 < Pe < 10^5)*, viscosity ratio between the dispersed phase and continuous phase (*0 < k_μ < 10*) and the stagnant cap angle *(0^o < α < 180^o)*.; and proposed following correlation:

$$Sh = \frac{3}{3+k_\mu}\left\{\begin{array}{l}\left(1.65+0.67\left(\sqrt{Pe}+\frac{0.67\,\mathrm{Re}}{\mathrm{Re}+15}(\sqrt{Pe}-1\right)\right)0.01\theta_{cap}+ \\ \frac{1}{3}\left(\left(3+k_\mu\right)\left(1-0.01\theta_{cap}\right)+k_\mu 0.01\theta_{cap}\right)\left(1-0.12\,\mathrm{Re}^{1/3}+(1+Pe)^{1/3}\left(1+0.12\,\mathrm{Re}^{1/3}\right)\right)\end{array}\right\} \quad (2.10)$$

Therefore, on the basis aforementioned literature, it can be safely concluded that the reliable information on heat/mass transfer phenomena of partially contaminated bubbles/drops in Newtonian fluids is now available at least in the steady axisymmetric flow but for the case of power-law liquids analogous information is not available even in the limit of small Reynolds and large Peclet numbers.

2.2. Swarms of Bubbles, Drops and Particles

Since the literature on the swarms of contaminated bubbles in Newtonian fluids is virtually non-existent beyond the creeping flow regime, it is instructive to briefly review the previous work for two extreme cases of the stagnant cap angles, i.e. $\alpha = 0$ (swarms of clean bubbles) and $\alpha = 180^{o}$ (assemblages of fully contaminated bubbles or assemblages of solid spheres).

2.2.1. Flow phenomena

2.2.1.1. Swarms of spherical bubbles in Newtonian and power-law fluids

Gal-Or and Waslo (1968) used free surface cell model to obtain analytical closed form solution for the terminal velocity of ensembles of bubbles and drops with or without the presence of the surfactants in viscous Newtonian fluids under the creeping flow conditions. Their results supplemented by those of Marucci (1965) who has employed the free surface cell model to analyse the rise velocity of bubble swarms in Newtonian media at high Reynolds number by using the inviscid flow approximation. In the intermediate range, LeClair and Hamielec (1971) numerically investigated the free rise velocity of swarms of spherical bubbles using free surface cell model in the range of Reynolds number up to 100 and bubble volume fraction up to 0.6. They made extensive calculations on individual and total drag coefficients along with vorticity and pressure distributions along surface of the bubbles in swarms. They also extensively validated their results with other analytical and experimental results and are in good agreement for various cases. Manjunath *et al.* (1994) numerically studied the steady rise of swarms of bubbles through a quiescent Newtonian liquid within the framework of the free surface cell model and proposed a correlation for the total drag coefficient as a function of the bubble hold-

up (Φ) and the Reynolds number in the range of $8 \times 10^{-6} \leq \Phi \leq 0.6$ and $0.001 \leq Re \leq 100$ respectively.

In addition to these intrinsic problems in modeling such as multi-body flow systems, for the case of non-Newtonian fluids, further difficulties arises from the non-linearity of the viscous terms which preclude the possibility of an analytical treatment even in the creeping flow regime, akin to that Gal-Or and Waslo (1968) for ensembles of bubbles and drops in Newtonian liquids. Therefore, many investigators have employed velocity and stress variational principles to obtain approximate upper and lower bounds on drag coefficient (and hence on the free rise velocity) for swarms of spherical bubbles rising in power-law liquids (Gummalam and Chhabra, 1987; Jarzebski and Malinowski, 1986; Zhu and Deng, 1994; Sun and Zhu, 2004) and in Carreau model fluids (Jarzebski and Malinowski, 1987a,b; Gummalam *et al.*, 1988; Zhu, 1995, 2001). Suffice it to add here that not only these two bounds diverge increasingly as the value of the power-law index decreases below unity, but the variational principles are applicable only to shear-thinning fluids and in the absence of inertial effects. Furthermore, this approach yields the true upper and lower bounds only for Newtonian and power-law liquids and resulting bounds are only approximate for other generalized Newtonian fluid models. Notwithstanding these limitations, when these predictions are plotted in the form of ratio between the free rise velocity of swarms and single bubbles as a function of gas hold-up and the power law index, this ratio shows a monotonic decrease with the increasing value of the gas hold-up in moderately shear thinning fluids ($n \approx 0.5 - 0.6$), but this ratio can go through a maximum value in highly shear-thinning fluids and this behavior is qualitatively consistent with the scant experimental results available in the literature (Deckwer, 1992; Chhabra, 2006). Similarly, in another approach, the non-linear viscous terms have been approximated either by using the corresponding flow field

for Newtonian fluids or the flow variables are expanded in the form of a series with (n-1) as the perturbation parameter. Due to the nature of these approximations, obviously both these approaches yield the results which are valid only for weakly shear-thinning fluids. These results are also restricted to the low Reynolds number regime only. The works of Bhavaraju *et al.* (1978) demonstrated the utility of the cell model approach for swarms of spherical bubbles rising freely in power-law fluids. Beyond the creeping flow regime, Manjunath and Chhabra (1992) solved the field equations within the framework of free surface cell model to obtain numerical predictions of the drag on bubble swarms rising in unconfined power-law fluids in the range of conditions: $1 \leq Re \leq 50$, $0.4 \leq n \leq 1$ and $0.1 \leq \Phi \leq 0.6$. Recently, Kishore *et al.* (2006, 2007, 2008a, 2008b, 2008c) numerically studied the drag behavior and mass transfer from bubble swarms and ensembles of droplets in Newtonian and power-law liquids at moderate Reynolds numbers in the range of conditions: $0.6 \leq \Phi \leq 10^{-6}$, $1 \leq Re \leq 200$, $1 \leq Sc \leq 1000$ and $0.6 \leq n \leq 1.6$. Therefore, based on a combination of theoretical and numerical results, reliable information is now available on the free rise velocity of swarms of completely clean spherical bubbles rising in Newtonian and power-law liquids in the wide range of conditions.

2.2.1.2. Assemblages of fully contaminated bubbles in Newtonian and power-law fluids

Ever since the pioneering work of Happel (1958) and Kuwabara (1959), the cell model approaches are extensively used to investigate the Newtonian fluid flow through multiparticle assemblages in the wide ranges of Reynolds number and the bed porosity. Most of these studies have been thoroughly reviewed by Happel and Brenner (1983) and Chhabra (2006). Although, many investigators considered the creeping motion through assemblages, Leclair and Hamielec

(1968) numerically solved the complete Navier-Stokes equations in conjunction with the free surface cell model to predict the flow behavior of a Newtonian fluid through assemblages of solid particles at intermediate Reynolds numbers. Their numerical results are comparable with experimental results up to Reynolds number of approximately Re = 30. El-Kaissy and Homsy (1973) carried out a regular perturbation analysis for both i.e., the free surface and zero vorticity cell models, and provided theoretical expressions for friction factor as a function of bed voidage ($0.3 \leq \varepsilon \leq 0.6$) and Reynolds number. As the interparticle distance increases (i.e., the voidage increases), the maximum value of Reynolds number up to which their analysis is applicable decreases. Nishimura and Ishii (1980a) employed the free surface cell model together with the boundary layer assumptions to study the Newtonian flow through packed and distended beds at high Reynolds numbers ($10 \leq Re \leq 10^5$) and reported extensive results on friction factor as functions of bed voidage and Reynolds number. They compared their theoretical results with experimental friction factors of packed and distended beds; and were in good agreement. However, it is unlikely that the boundary layer approximation will be valid in such confined flows, especially at low voidages. Further examination of their results suggests several unusual features such as their calculated values of form drag are independent of the value of the Reynolds number in the range of $10 \leq Re \leq 10^5$; and also their results, in the limit of the voidage approaching unity, differ appreciably from the literature values of drag coefficient for a single sphere (Jaiswal *et al.*, 1991a). Further they extended their study for the case of mass transfer (Nishimura and Ishii, 1980b). Jaiswal *et al.* (1991a) solved the complete Navier-Stokes equations describing the flow of incompressible Newtonian fluids relative to beds of particles using finite element technique in the range of parameters $0.001 \leq Re \leq 100$ and $0.3 \leq \varepsilon \leq 0.9$. They also compared their results with available experimental results and provided the range of applicability

of the free surface cell model (up to $Re \approx 10 - 20$), and its performance has contrasted with that of zero vorticity cell model. Prasad *et al.* (1990) analytically obtained the creeping flow solution of a Newtonian fluid relative to an assemblage of composite spheres within the framework of the free surface cell model. They derived an analytical expression for the drag force experienced by assemblages embracing wide ranges of combinations of size, thickness of porous region, permeability of porous medium and the concentration of the assemblage. Recently, Mao *et al.* (2007) extended the cell model approach to the catalytic reaction over a spherical catalyst pellet and the effects of several parameters on the effectiveness factor are numerically obtained. It was observed that the voidage of the particle assemblage shows more recognized influence than the Peclet and Reynolds numbers of particles. They also proposed set of cell model equations for catalytic reaction in particle assemblages to account for the overall effect of external mass transfer and the cell configuration in dense suspensions.

The flow of generalized Newtonian fluids through assemblages of solid particles has also acquired great interest amongst many investigators and are thoroughly reviewed by (Chhabra *et al.*, 2001; Chhabra, 2006). Several researchers employed the well-known variational principles to obtain approximate upper and lower bounds on drag coefficient for flow past multiparticle assemblages using free surface cell model. Mohan and Raghuraman (1976a,b) obtained such bounds for the creeping flow of power-law and Ellis model fluids, while Chhabra and Raman (1984) carried out a similar analysis for a Carreau model fluid. In spite of their wide spread utility, the results based on variational principles suffer from the drawback and the predictions are sensitive to the choice of trail functions used in the analysis and it is not possible to estimate a priori the error inherent in the predicted bounds. Experience also shows that both the bounds diverge for higher degree of non-Newtonian behaviour, therefore, not very useful for strongly

non-Newtonian fluids (Chhabra, 2006). Thus, numerical techniques emerge as only alternate and accurate methods for the non-Newtonian flow behaviour in complex flow geometries. On the other hand, Kawase and Ulbrecht (1981a) developed a closed form solution for the creeping flow of power-law fluids by linearizing the governing equations. Their analysis, however, is limited to mildly shear-thinning fluids. Using the results obtained by this approach combined with the results of Acharya *et al.* (1976) for the case when the voidage approached unity, Kawase and Ulbrecht (1981c) obtained the relative sedimentation velocity of assemblages and single sphere in the creeping flow regime using the free surface cell model. Kawase and Ulbrecht (1985) obtained a new model for non-Newtonian fluids (power-law, Carreau, Ellis model fluids flow through fluidized beds by extending the concept of Richardson and Zaki (1954)**.** In this model, they used the existing correlations for an isolated sphere and extended to those for a fluidized bed by incorporating a voidage function. The model is in good agreement with other correlations for flow of non-Newtonian fluids in the creeping flow range. In the high Reynolds number range, Hua and Ishii (1981) and Kawase and Ulbrecht (1981b) employed the boundary layer approximations to study the flow of power-law fluids through particulate beds. However, the validity of boundary layer approximations appears questionable especially for dense assemblages. Moreover, when the bed void approaches unity, the predictions of Hua and Ishii (1981) do not reduce to the corresponding limiting case of a single solid sphere. Satish and Zhu (1992) obtained finite difference solutions for a power-law fluid flow through assemblages of solid spheres at low Reynolds numbers within the framework of zero shear stress and zero vorticity cell models. They presented their results in the closed form which compare favorably with variational bounds and the modified Blake-Kozney equations. Zhu and Satish (1992) extended it for the case of a Carreau model fluid using the free surface cell model. In series of

papers, Jaiswal *et al.* (1991a,b, 1992, 1993, 1994) reported numerical results of Newtonian and power-law fluid flow through assemblages of solid spheres in the range of parameters $0.3 \leq \varepsilon \leq 0.9999$, $0.001 \leq Re \leq 20$ and $0.2 \leq n \leq 2$. Recently, Dhole *et al.* (2004) contrasted both the cell models by numerically obtaining the friction factors for the power-law fluid flow through assemblages of solid particles up to Reynolds number of 500, $0.4 \leq \varepsilon \leq 0.6$ and $0.5 \leq n \leq 1.8$. Therefore, in summary, based on a combination of theoretical and numerical results, reliable information is now available on the steady and incompressible flow of Newtonian and power law liquids through assemblages of mono-size solid spheres up to Reynolds number of 200.

2.2.2. Heat/mass transfer phenomena

2.2.2.1. Swarms of spherical bubbles in Newtonian and power-law fluids

Ruckenstein (1964) obtained an expression for the mass transfer coefficient of swarms of spherical bubbles and drops using the free surface cell model in the creeping and potential flow regimes for large values of Peclet numbers, i.e., within the framework of a thin concentration boundary layer. LeClair and Hamielec (1971) obtained corresponding results for swarms of bubbles rising in Newtonian liquids using the zero vorticity cell model for finite values of the Reynolds and Peclet numbers. In a series of publications, Gal-Or and co-investigators (Waslo and Gal-Or, 1971; Yaron and Gal-Or, 1971; Gal-Or and Yaron, 1973; Yaron and Gal-Or, 1973) obtained the drag and mass transfer coefficients of ensembles of fluid spheres in Newtonian continuous media using free surface cell model in the limit of vanishingly small Peclet numbers. Gal-Or and Resnick (1964) proposed a model based on the average residence time of the gas bubbles in the continuous phase which permits the prediction of total mass transfer rates for a sparingly soluble gas in a gas-liquid contactor. Lee *et al.* (1999) contrasted the predictions of the

zero shear stress and zero vorticity cell models for convective mass transfer rates of swarms of circulating bubbles in a Newtonian medium in the creeping flow regime. Kishore *et al.* (2007) numerically studied the mass transfer from ensembles of Newtonian fluid spheres to surrounding immiscible Newtonian continuous fluids at moderate Reynolds and Peclet numbers over the range of conditions: $1 \leq Re \leq 200$, $0.2 \leq \Phi \leq 0.6$, $0.1 \leq k_{\mu} \leq 50$ and $1 \leq Sc \leq 10000$.

Similarly, for mass transfer from freely rising swarms of spherical bubbles to power-law or any other generalized Newtonian fluids, the adequate literature is available. For instance, Bhavaraju *et al.* (1978) obtained an approximate solution of the rate of mass transfer from swarms of bubbles to a power-law liquid using the approach of Hirose and Moo-Young (1969) together with the free surface cell model and thin concentration boundary layer approximation. Jarzebski and Malinowski (1986, 1987a,b) predicted the mass transfer from swarms of bubbles and drops to power-law and/or Carreau model fluids by using the thin concentration boundary layer approximation together with the free surface cell model. Kishore *et al.* (2008) studied the mass transfer from ensembles of fluid spheres to surrounding immiscible power-law continuous liquids at moderate Reynolds and Peclet numbers in the range of conditions: $1 \leq Re_o \leq 200$, $1 \leq Sc \leq 10000$, $0.6 \leq n_o \leq 1.6$, $0.1 \leq k \leq 50$ and $0.2 \leq \Phi \leq 0.6$. Further Kishore *et al.* (2008) extended their study to numerically investigate the drag behavior and mass transfer from bubble swarms in power-law liquids at moderate Reynolds numbers in the range of conditions: $0.6 \leq \Phi \leq 10^{-6}$, $1 \leq Re \leq 200$, $1 \leq Sc \leq 1000$ and $0.6 \leq n \leq 1.6$.

2.2.2.2. Assemblages of fully contaminated bubbles in Newtonian and power-law fluids

Pfeffer (1964) seems to be the first one to use the free surface cell model to predict the rate of heat/mass transfer in assemblages of solid spheres. In the limit of $Re \rightarrow 0$ and $Pe \rightarrow \infty$, Pfeffer (1964) obtained following expression for the Sherwood number by making use of free surface cell model together with thin boundary layer solution of the diffusion equation due to Levich (1962)

$$Sh_{avg} = 1.26\left[\frac{1-(1-\varepsilon)^{5/3}}{2-3/R_{\infty}+3/R_{\infty}^{5}-2/R_{\infty}^{6}}\right]Pe^{1/3} \tag{2.11}$$

In the limit of $\varepsilon \rightarrow 0$, the above expression reduces to the familiar Levich-Lighthill solution for single solid spheres. Nishimura and Ishii (1980b) numerically solved the diffusion equation for heat/mass transfer in assemblages of solid spheres within the framework of the free surface cell model at high Reynolds numbers using the velocity profiles obtained in Nishimura and Ishii (1980a). They proposed the following correlation for the average Sherwood number

$$Sh_{avg} = \frac{2}{1-(1-\varepsilon)^{1/3}} + 0.6Re^{1/2}Sc^{1/3}\varepsilon^{-1/2} \tag{2.12}$$

They observed that their results are in good agreement with experimental data of single solid spheres, and packed and particulate fluidized beds. Recently, Coutelieris *et al.* (2005) numerically obtained the mass transfer from a moving Newtonian fluid to assemblages of spherical solid absorbers using zero vorticity cell model for Peclet number less than 100. They observed that the higher efficiencies correspond to lower porosity, whereas increasing Peclet numbers lead to lower the efficiency. The adsorption/reaction/desorption mechanism provided a

reasonable estimation of the adsorption efficiency tendency compared to available experimental measurements.

Adequate information is also available about the analogous problem in non-Newtonian fluids at least up to *Re* = 200 and *Pr* = 1000. For instance, Kawase and Ulbrecht (1981a,b) combined thin concentration boundary layer approximation with free surface cell model to elucidate the role of power-law index on the rate of mass transfer for the creeping motion of power-law liquids in fixed and fluidized beds of spherical particles in the limit of large Peclet numbers. Satish and Zhu (1992) employed a finite difference method to contrast the predictions of two cell models in terms of the average Sherwood number at high Peclet numbers under the creeping flow conditions. They observed that a decrease in the flow behavior index leads to a slight increase in the mass transfer rate for assemblage of solid spheres, however, this increase is found to be small compared to with that for a single solid sphere. Shukla and Chhabra (2004a) and Shukla *et al.* (2004b) numerically solved the convective heat transfer in fixed and fluidized beds of solid spheres to power-law liquids at intermediate Reynolds and Peclet numbers using both cell models. Most of these studies predict a slight enhancement in the value of Sherwood number in shear-thinning fluids which is consistent with the scant experimental results (Chhabra *et al.*, 2001). Kishore *et al.* (2009) extended the studies of Shukla and Chhabra (2004a) for the case of assemblages of solid spheres of moderate to large void fractions (0.7 – 0.999999) using free surface cell model at Reynolds number up to 200, Prandtl number up to 1000 and power-law index between 0.6 – 1.6.

Therefore, based on aforementioned discussion, it is safe to conclude that reliable information is now available on the rate of heat/mass transfer from swarms of clean spherical bubbles (α = 0) and from assemblages of fully contaminated spherical bubbles ($\alpha = \pi$) to

Newtonian and power-law liquids in the moderate range of Reynolds and Peclet numbers. However, analogous information is not available in the case of partially contaminated bubbles.

2.3. Objective of Thesis

The detailed literature review presented in the aforementioned subsection indicate that a coherent picture is available for the momentum and heat/mass transfer phenomena of contaminated single spherical bubbles in unconfined Newtonian fluids. On the other hand, literature is very scarce for both drag and mass transfer phenomena of contaminated single spherical bubbles in unconfined and confined non-Newtonian fluid flows. Furthermore, for the case of swarms of partially contaminated bubbles, analogous literature is not available even in Newtonian fluids, let alone power-law and other types of non-Newtonian fluids. Therefore, the present dissertation is aimed to numerically investigate following objectives over the wide range of pertinent dimensionless parameters:

- Momentum and heat/mass transfer phenomena of unconfined single spherical bubble in contaminated power-law fluids within the framework of spherical stagnant cap model.
- Momentum and heat/mass transfer phenomena of confined single spherical bubble in contaminated Newtonian and power-law fluids within the framework of spherical stagnant cap model.
- Momentum and heat/mass transfer characteristics of swarms of spherical bubbles in contaminated Newtonian and power-law fluids within the frameworks of spherical stagnant cap model and free surface cell model.

Chapter 3

PROBLEM STATEMENT AND DESCRIPTION

Depending on relative contribution of hydrodynamic and interface tension forces, bubbles/drops may tend to deform during their rise/fall in another immiscible fluid. Hydrodynamic forces tend to deform the surface of bubbles/drops while the surface tension forces act as resisting force to deformation. The relative contribution of hydrodynamic and surface tension forces fluctuate until a steady shape has been attained by bubbles/drops denoting establishment of equilibrium between these forces. Thus bubbles/drops can retain their spherical shape if the surface tension forces are of greater magnitude compared to hydrodynamic forces. Further Wellek *et al.* (1966), Fdhila and Duineveld (1996) experimentally obtained the quantitative relation between the Weber number (*We*, ratio between viscous and surface tension forces) and shape eccentricity of bubbles/drops in Newtonian fluids. They concluded that for $We \leq 0.1$, the deviation of the drop eccentricity from spherical shape is negligible. Furthermore, according to Winnikow and Chao (1966) and Winnikow (1968), for $We < 4$ (which corresponds to Reynolds number in the range of 300-1000), the drop oscillations are negligible during their rise/fall in Newtonian liquids. On the other hand, analogous information is not available when the continuous phase obey non-Newtonian behavior; however, the scant experimental literature on rise/fall of bubbles/drops in non-Newtonian fluids suggest that the viscoelasticity causes much greater shape deformation than the shear dependent viscosity of the continuous liquid (Chhabra, 2006). Thus, in this work, motion of single and swarms of spherical bubbles in contaminated inelastic power-law liquids with significantly large surface tension forces (so that Weber number remains too small to avoid deformation) are considered. Furthermore, the momentum and mass transfer phenomena of

single and swarms of contaminated bubbles in surfactant-laden Newtonian (n = 1) and shear-thinning type power-law liquids (n = 0.6 and n = 0.8) are numerically investigated by using an in-house solver. This solver is a finite difference method based SMAC semi-implicit algorithm implemented on a staggered grid in spherical coordinates. However, this solver faces convergence difficulty with the increasing non-linearity of governing equations as the power-law index deviates increasingly from unity; and this convergence difficulty magnifies with the decreasing Reynolds number (Re < 10). Nevertheless, this kind of convergence difficulty in numerical studies on highly shear-thinning or highly shear-thickening fluids is not at all uncommon and many other researchers have also experienced such convergence problems (Butcher and Irvine, 1990; Graham and Jones, 1994; D'Alessio and Pascal, 1996; Dhole *et al.*, 2006, 2007). Furthermore, in many real-life applications, often one encounter highly shear-thinning or highly shear-thickening type power-law fluids interacting with dispersed bubbles/droplets at small but finite Reynolds numbers. Thus for the case motion of and heat transfer from partially contaminated unconfined and confined single bubbles in highly shear-thinning (up to n = 0.2) and highly shear-thickening (up to n = 1.8) fluids, ANSYS Fluent is used which is a robust and reliable computational fluid dynamics based software for this kind of flow problems. However, for the case of swarms of partially contaminated bubbles in power-law liquids, only in-house solver is used.

3.1. Single and Swarms of Bubbles in Contaminated Power-law Liquids using In-house Solver

Consider a spherical bubble of radius, R, steadily translating (with a constant velocity U_0) in an infinite expanse of power-law fluid contaminated with surfactants. During the course of bubble

translation, the insoluble surfactants accumulate in the rear of the bubble forming a spherical cap with immobile surface, while the rest of the bubble surface remains mobile (**Figure 3.1**). Within the framework of the spherical stagnant cap model, the degree of contamination is expressed by the cap angle "α" measured from the rear stagnation point.

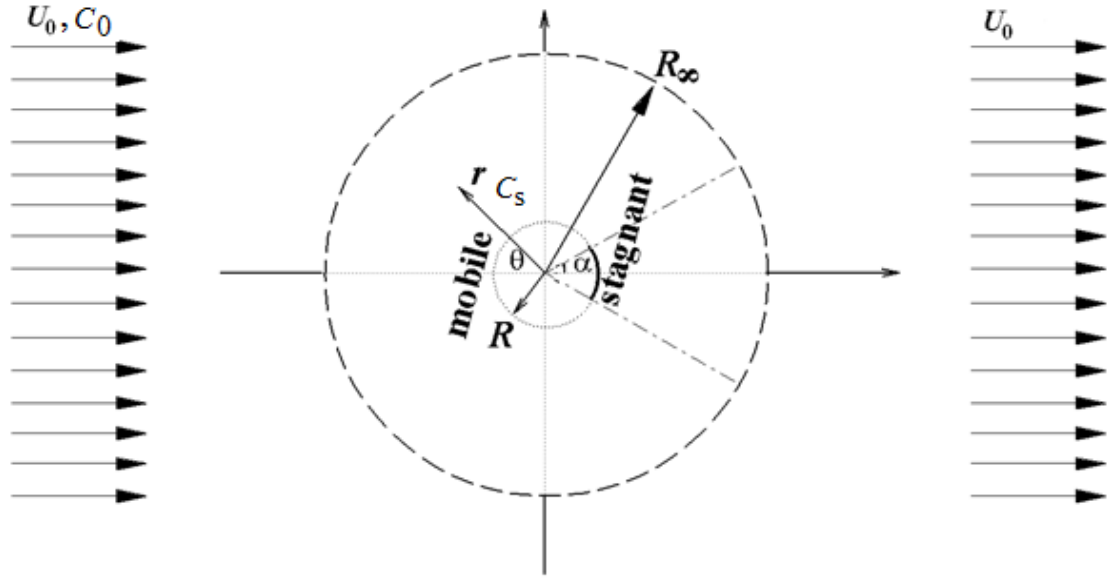

Figure 3.1: Schematic representation of uniform flow past a spherical bubble with immobile stagnant cap of surfactants at the rear end.

Similarly consider a relative velocity between a swarm of mono-size spherical bubbles (of radius R) and a contaminated power-law fluid as shown schematically in **Figure 3.2(a)**. In the swarms, these bubbles are equidistant from each other. Within the framework of the cell model, the hydrodynamic interactions are approximated by postulating each bubble to be surrounded by a hypothetical envelope of continuous fluid of radius R_∞ as shown in **Figure 3.2(b)**. The size of the envelope is chosen such that the volume fraction of the dispersed phase of each cell is equal to the overall mean volume fraction of the dispersed phase in the system, i.e., $R_\infty = \Phi^{-1/3}$. Thus, the multi-bubble system (**Figure 3.1(a)**) is converted into an equivalent single bubble (**Figure**

3.2(b)) problem yet counting for the volume fraction of the bubble swarm. Further it is assumed that during the course of the rise of bubble swarms, the insoluble surfactants are adsorbed uniformly on the surface of each bubble in the swarm and gradually these surfactants migrate towards the rear end of the bubble. Furthermore, it is assumed that the so-adsorbed surfactants form stagnant caps on all bubbles with equal degree of contamination.

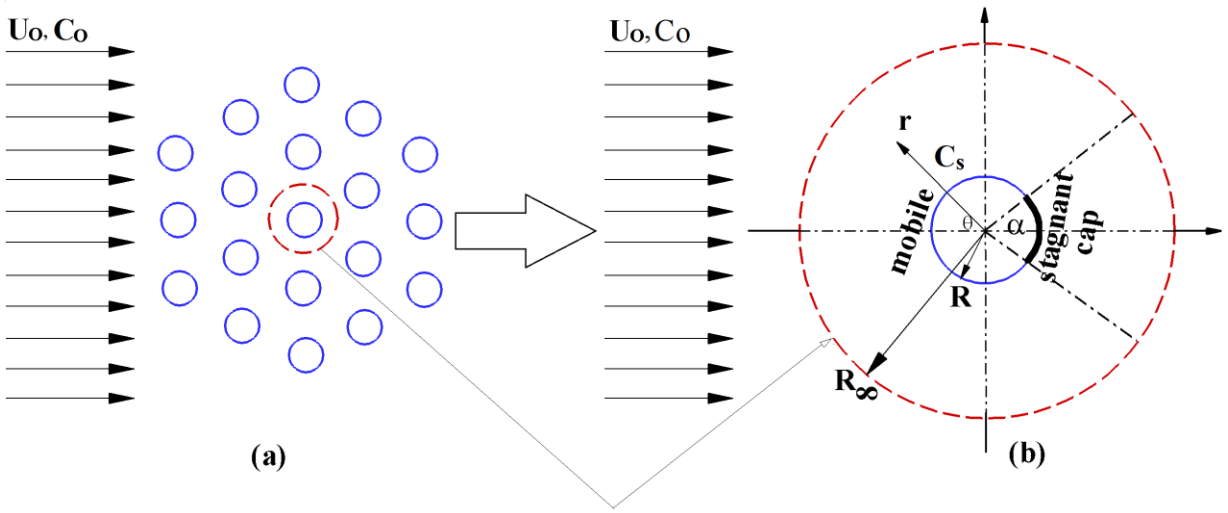

Figure 3.2: Flow of contaminated fluids through bubble swarms within the framework of cell model and spherical stagnant cap model.

Because of the presence of insoluble surfactants along the surface of the bubble, portion of the surface becomes immobile, thus, the bubble retains spherical shape even at large Reynolds numbers. Furthermore, under these conditions, the Weber number is small enough so that bubble can retain its spherical shape in a Newtonian continuous phase; however, there is no analogous information for a non-Newtonian continuous phase. Therefore, it is difficult to suggest critical values of the Reynolds number under which the bubble remains spherical in surfactant-laden power-law fluids.

3.1.1. Governing equations

Over the range of conditions spanned in this work, the flow is assumed to be axisymmetric and a sphere-in-sphere computational domain is chosen. Thus a spherical coordinate system (r, θ, ϕ) with its origin located at the center of the bubble is employed and the polar axis ($\theta = 0^o$) is directed along the direction of flow. Due to axisymmetry the velocity component in the ϕ-direction (v_ϕ) and derivatives with respect to ϕ are zero. Assuming the flow to be incompressible, the continuity, momentum and mass transfer equations in their dimensionless forms are written as follows:

- Continuity equation

$$\frac{1}{r^2}\frac{\partial}{\partial r}\left[r^2 v_r\right]+\frac{1}{r\sin\theta}\frac{\partial}{\partial\theta}\left[v_\theta \sin\theta\right]=0 \tag{3.1}$$

- r – component of momentum equation

$$\frac{\partial v_r}{\partial t}+\frac{1}{r^2}\frac{\partial}{\partial r}\left[r^2 v_r^2\right]+\frac{1}{r\sin\theta}\frac{\partial}{\partial\theta}\left[v_r v_\theta \sin\theta\right]-\frac{v_\theta^2}{r}=-\frac{\partial p}{\partial r}+\frac{2^{n+1}}{\mathrm{Re}}\left[\varepsilon_{rr}\frac{\partial\eta}{\partial r}+\frac{\varepsilon_{r\theta}}{r}\frac{\partial\eta}{\partial\theta}\right]$$
$$+\frac{2^n\eta}{\mathrm{Re}}\left[\frac{1}{r^2}\frac{\partial^2}{\partial r^2}\left(r^2 v_r\right)+\frac{1}{r^2\sin\theta}\frac{\partial}{\partial\theta}\left(\sin\theta\frac{\partial v_r}{\partial\theta}\right)\right] \tag{3.2}$$

- θ – component of momentum equation

$$\frac{\partial v_\theta}{\partial t}+\frac{1}{r^2}\frac{\partial}{\partial r}\left[r^2 v_r v_\theta\right]+\frac{1}{r\sin\theta}\frac{\partial}{\partial\theta}\left[v_\theta^2\sin\theta\right]+\frac{v_r v_\theta}{r}=-\frac{1}{r}\frac{\partial p}{\partial\theta}+\frac{2^{n+1}}{\mathrm{Re}}\left[\varepsilon_{r\theta}\frac{\partial\eta}{\partial r}+\frac{\varepsilon_{\theta\theta}}{r}\frac{\partial\eta}{\partial\theta}\right]$$
$$+\frac{2^n\eta}{\mathrm{Re}}\left[\frac{1}{r^2}\frac{\partial}{\partial r}\left(r^2\frac{\partial v_\theta}{\partial r}\right)+\frac{1}{r^2}\frac{\partial}{\partial\theta}\left(\frac{1}{\sin\theta}\frac{\partial}{\partial\theta}\left[v_\theta\sin\theta\right]\right)+\frac{2}{r^2}\frac{\partial v_r}{\partial\theta}\right] \tag{3.3}$$

- Mass transfer equation

$$\frac{\partial C}{\partial t}+\frac{1}{r^2}\frac{\partial}{\partial r}\left[r^2 v_r C\right]+\frac{1}{r\sin\theta}\frac{\partial}{\partial\theta}\left[v_\theta C\sin\theta\right]=\frac{2}{Pe}\left[\frac{1}{r^2}\frac{\partial}{\partial r}\left(r^2\frac{\partial C}{\partial r}\right)+\frac{1}{r^2\sin\theta}\frac{\partial}{\partial\theta}\left(\sin\theta\frac{\partial C}{\partial\theta}\right)\right] \tag{3.4}$$

In equations (3.1) - (3.4), velocity terms are scaled using free stream velocity U_o, radial coordinate *r* using bubble radius R, pressure using ρU_o^2, components of rate of deformation tensor by $\left(U_o / R\right)$, viscosity by a reference viscosity $\eta_{ref}\left(=m\left(U_o / R\right)^{(n-1)}\right)$, stress components by $\eta_{ref}\left(U_o / R\right)$, concentration difference (C-C_o) by (C_s-C_o) and time by $\left(R/U_o\right)$. Further, although the main interest is to obtain the steady state solution, the transient terms are retained in equations (3.2) – (3.4) because the false-transient scheme is used here to obtain the steady state solution. In order to obtain fully converged velocity, pressure and concentration profiles, segregated approach has been used, i.e., first momentum equations are solved for fully converged velocity and pressure profiles, and then the so-obtained velocity profile is used as input to solve the mass transfer equation.

Furthermore, in the case of swarms of bubbles within the framework of the cell model, the non-dimensional radius of the hypothetical fluid envelope R_∞ can be related to the overall mean volume fraction of the dispersed phase (Φ) as follows:

$$R_\infty = \Phi^{-1/3} \tag{3.5}$$

Therefore, by simply varying the value of R_∞, one can simulate systems of various volume fractions of the dispersed phase including the limiting case of single bubble by setting $R_\infty \rightarrow \infty$, i.e., $\Phi \rightarrow 0$. Conversely, one can readily calculate the value of R_∞ for known values of the volume fraction of the dispersed phase and radius of the bubble.

For an incompressible liquid, the components of the extra stress tensor are related to the rate of deformation tensor as follows:

$$\tau_{ij} = 2\eta\varepsilon_{ij}; \quad \text{where i,j = r, } \theta, \phi \tag{3.6}$$

The power-law viscosity is given by:

$$\eta = \left(\frac{\Pi_{\varepsilon}}{2}\right)^{(n-1)/2} \tag{3.7}$$

Where, Π_{ε} is second invariant of rate of deformation tensor which can be expressed in terms of velocity components and their derivatives e.g., see Bird *et al*. (2002).

The dimensionless numbers appearing in above equations are defined as follows:

- Reynolds number: $\mathrm{Re} = \dfrac{\rho U_o^{(2-n)} (2R)^n}{m}$ (3.8)

- Schmidt number: $Sc = \dfrac{m}{\rho D_0}\left[\dfrac{U_0}{2R}\right]^{n-1}$ (3.9)

- Peclet number: $Pe = \mathrm{Re} \times Sc = \dfrac{U_0(2R)}{D_0}$ (3.10)

where, ρ is the density of the fluid, m is the power-law fluid consistency index, n is the power-law behavior index and D_0 is the molecular diffusivity.

3.1.2. Boundary conditions

The boundary conditions for single and swarms of contaminated bubbles differ from each other only pertaining to one of the boundary conditions at the cell boundary and all other boundary conditions are identical in both cases as given below:

- At the outer cell boundary ($r = R_{\infty}$):

$$v_r = -\cos\theta\ ; \qquad v_\theta = \sin\theta\ ; \qquad C = 0 \qquad \leftarrow \text{For single bubbles} \tag{3.11}$$

$$v_r = -\cos\theta\ ; \qquad \tau_{r\theta} = 0\ ; \qquad C = 0 \qquad \leftarrow \text{For swarms of bubbles} \tag{3.12}$$

- Along the axis of symmetry ($\theta = 0, \pi$):

$$v_\theta = 0\,; \quad \frac{\partial v_r}{\partial \theta} = 0\,; \; \frac{\partial C}{\partial \theta} = 0 \tag{3.13}$$

- Along the mobile surface of bubble ($r = 1, \theta = 0, \alpha$):

$$v_r = 0\,; \quad \tau_{r\theta} = 0\,; \quad C = 1 \tag{3.14}$$

- Along the immobile surface of bubble ($r = 1, \theta = \alpha, \pi$)

$$v_r = 0\,; \quad v_\theta = 0\,; \quad C = 1 \tag{3.15}$$

Suffice it to add here that for the case of single bubble, the outer cell boundary condition should obey the uniform velocity field due to the imposed unbounded nature of the flow (Eq. 3.11). On the other hand for the case of swarms of bubbles the normal velocity component along the cell boundary is same as that of the free stream velocity (Eq. 3.11); however, the zero shear stress condition (Eq. 3.12) indicates the non-interacting nature of the cells within the frame work of the free surface cell model (Happel, 1958). Equation (3.13) is simply a statement of the axisymmetric flow condition; while equations (3.14) – (3.15) refer to the mobile and immobile portions of the bubble surface in the context of the spherical stagnant cap model.

Furthermore, in the case of single bubbles, because the thickness of the momentum boundary layer on the bubble surface progressively decreases as the Reynolds number gradually increases, a very fine grid is required in the vicinity of the bubble surface. Thus, a logarithmic $\left(y = \ln r\right)$ transformation is used in the radial direction of the continuous phase to circumvent

this difficulty. Equations (3.1) – (3.4), subject to the boundary conditions outlined in equations (3.11) – (3.15) provide the theoretical framework to map the entire computational domain ($1 \leq r \leq R_\infty$) in terms of the primitive variables, i.e., v_r, v_θ, p and C.

3.1.3. Individual and total drag coefficients

Once the fully converged velocity and pressure profiles are known, individual and total drag coefficients can be evaluated as follows (for derivation, see Appendix A):

Total drag coefficient is defined as:

$$C_d = \frac{2F_d}{\rho_o U_o^2 A_p} = C_{dp} + C_{df} \tag{3.16}$$

The pressure component (C_{dp}) is evaluated as:

$$C_{dp} = 2\int_0^\pi \left[p \sin 2\theta \right]_{r=1} d\theta \tag{3.17}$$

and the frictional component (C_{df}) is evaluated as:

$$C_{df} = \frac{2^{n+2}}{\mathrm{Re}} \int_0^\pi \left\{ \eta \left[\left(\frac{\partial v_\theta}{\partial r} - \frac{v_\theta}{r} \right) \sin^2 \theta - \left(\frac{\partial v_r}{\partial r} \right) \sin 2\theta \right] \right\}_{r=1} d\theta \tag{3.18}$$

3.1.4. Local and average Sherwood numbers

Once the fully converged concentration profile is known, by equating the rates of mass transfer by diffusion and by convection at the surface of the bubbles, the local Sherwood number (Sh_θ) can be seen as follows (for derivation, see Appendix B):

$$Sh_\theta = \frac{k_c (2R)}{D_0} = -2\left[\frac{\partial C}{\partial r}\right]_{r=1} \tag{3.19}$$

Where, k_c is the inter-phase mass transfer coefficient in the continuous phase. The value of the local Sherwood number will vary with position on the surface of the bubble and thus it is customary to define average Sherwood number (Sh_{avg}) as follows:

$$Sh_{avg} = \frac{1}{2}\int_0^\pi Sh_\theta \sin\theta d\theta \tag{3.20}$$

From the scaling of field equations and boundary conditions, it can be seen that the local and average Sherwood numbers are functions of the Reynolds and Peclet numbers, power-law index, volume fraction and the stagnant cap angle.

3.1.5. Streamlines and vorticity profiles

Further insights about the detailed flow kinematics can be gained from the streamlines, vorticity and concentration contours around the bubble. The vorticity in spherical coordinates can be calculated as follows:

$$\omega_{r\theta} = \frac{\partial v_\theta}{\partial r} + \frac{v_\theta}{r} - \frac{1}{r}\frac{\partial v_r}{\partial \theta} \tag{3.21}$$

The stream function in spherical coordinates can be calculated using the following expression:

$$E^2(\psi) = \frac{\partial^2 \psi}{\partial r^2} + \frac{\sin\theta}{r^2}\frac{\partial}{\partial \theta}\left(\frac{1}{\sin\theta}\frac{\partial \psi}{\partial \theta}\right) = \omega_{r\theta} r \sin\theta \tag{3.22}$$

where the stream function is related to velocity components as follows:

$$v_r = \frac{-1}{r^2 \sin\theta}\frac{\partial \psi}{\partial \theta} \quad ; \quad v_\theta = \frac{1}{r \sin\theta}\frac{\partial \psi}{\partial r} \tag{3.23}$$

Suffice it to add here that the vorticity and streamline profiles are computed from the fully converged velocity profiles as a post-processing procedure to display results, and not as primary means of solution (through stream function – vorticity formulation). The "primitive variable" approach for solving velocity components directly is used. Finally, the concentration contours are plotted from the concentration field obtained by solving the mass transfer equation.

Finally, it is important to develop a relation to measure the stagnant cap angle for a given amount of surfactants for different values of Reynolds numbers in the power-law index because measuring spherical stagnant cap angle experimentally is the cumbersome task. However, along the spherical stagnant cap the surface contaminants are usually distributed in such a way that the surface tension gradient balances the shear stress. By making the use of these balance for the case of spherical bubble rising contaminated Newtonian fluids in creeping flow limit, Davis and Acrivos (1966) developed approximate results between the surface tension gradient and the cap angle. They have grouped the difference between maximum and minimum surface tensions and the viscosity of the fluid along with bubble rise velocity in the definition of Capillary number. Further, in the limit of Re $\rightarrow$ 0, they have developed approximate results between the degree of contamination and the inverse of the Capillary number. Furthermore, for the case of translation of spherical droplets in contaminated Newtonian fluids in the creeping flow limit, this approach was adapted by Sadhal and Johnson (1983) and reported a closed form of expression between the amount of surfactant at the interface and the cap angle. However, in the literature, there is no analogous information between the amount of surfactant and the stagnant cap angle in the range of finite to large Reynolds numbers even in contaminated Newtonian fluids, let alone surfactant-

laden power-law fluids. Therefore, in this work, for the case of spherical bubbles rising in contaminated power-law liquids, a similar approach is adapted to obtain the following relation:

$$Ca^{-1} = \left(\frac{\sigma_{max} - \sigma_{min}}{mU_o}\right)\left(\frac{2R}{U_o}\right)^{n-1} = m\,\mathrm{Re}\int_{\alpha}^{\pi}\left(\frac{I_2}{2}\right)^{(n-1)/2}\varepsilon_{r\theta}\,d\theta \qquad (3.24)$$

where Ca is the capillary number for the power-law fluids, and σ_{max} and σ_{min} are the maximum and minimum surface tensions respectively. Since, the integration in the right hand side of the equation (3.24) becomes highly non-linear with the power-law index deviating from unity; it is not possible to obtain closed form relation between the surface tension gradient and the cap angle of spherical bubble rising in contaminated power-law liquids even in the limit of Re → 0. Therefore, the closed form expression of Sadhal and Johnson (1983) can be used as a first order approximation for the case of spherical bubbles rising in contaminated power-law liquids as well.

3.2. Unconfined Single Bubble in Contaminated Power-law Liquids Using ANSYS Fluent

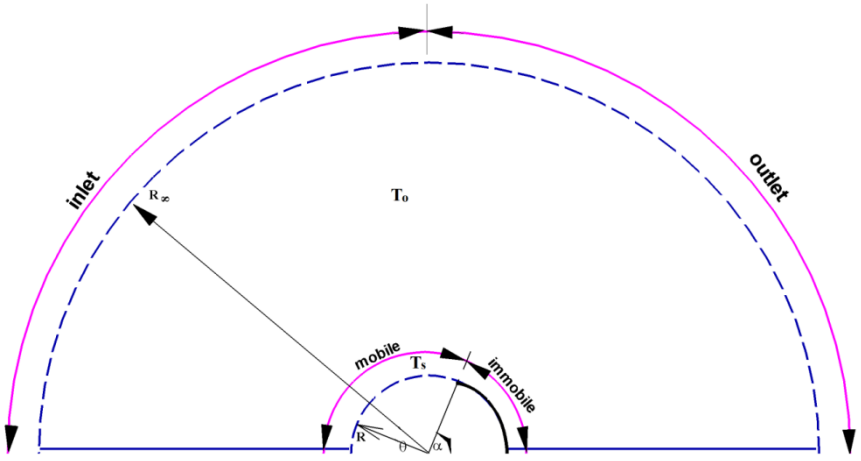

Figure 3.3: Schematic representation of computational domain of flow over contaminated bubbles.

Consider unconfined relative motion between spherical bubbles (of radius, R) and surfactant-laden power-law liquids. The assumptions and limitation are same as in the case of in-house solver. For the computational simplicity, sphere-in-a-sphere domain has been chosen as shown in **Figure 3.3**. The outer sphere represents the size of the computational domain and its radius is R_∞. The inner sphere represents the bubble (of radius, R). The front half of the outer sphere is treated as inlet whereas the rear half of the outer sphere is outlet. The temperature on bubble surface and in free stream power-law liquid are T_s and T_o, respectively. The heat transfer takes place between heated bubble surface to surrounding contaminated power-law liquid. Furthermore, in the present framework of numerical simulations, the Biot number for heat transfer is assumed to be small enough so that the inside and on the surface of the bubble, uniform temperature is maintained at T_s. Thus, the present flow and heat transfer problem can be described by the conservation equations of the mass, momentum and energy as written below:

- Continuity equation: $\nabla \cdot V = 0$ (3.25)
- Momentum equation: $\rho\left[(V \cdot \nabla)V\right] = -\nabla P + \nabla \cdot \tau$ (3.26)
- Energy equation: $\rho C_p \left(V \cdot \nabla \mathrm{T}\right) = k\nabla^2 T$ (3.27)

Further, the boundary conditions used to solve momentum equations are inlet velocity and pressure outlet boundary conditions at inlet and outlet, respectively; zero shear stress and no-slip conditions along the mobile and immobile portions of the bubble, respectively; and axisymmetry boundary condition along the central axis of the computational domain. In order to solve the energy equation, uniform inlet temperature T_o at the inlet, constant temperature T_s along the surface of bubble and axisymmetry condition along the central axis are used. Here too, segregated approach is used to obtain the temperature field in the computational domain, that is,

first the momentum equations are solved to obtain the steady velocity profile, and then by using so obtained velocity profile, the energy equation is solved for the temperature profile. Once fully converged velocity, pressure and temperature fields are obtained, they are further used to evaluate streamlines, vorticity patterns, surface viscosity distributions, individual and total drag coefficients, isotherm contours along with local and average Nusselt numbers of contaminated bubbles as functions of the pertinent parameters such as the Reynolds number (*Re*), Prandtl number (*Pr*), power-law index (*n*) and the stagnant cap angle (α).

3.3. Confined Single Bubble in Contaminated Power-law Liquids using ANSYS Fluent

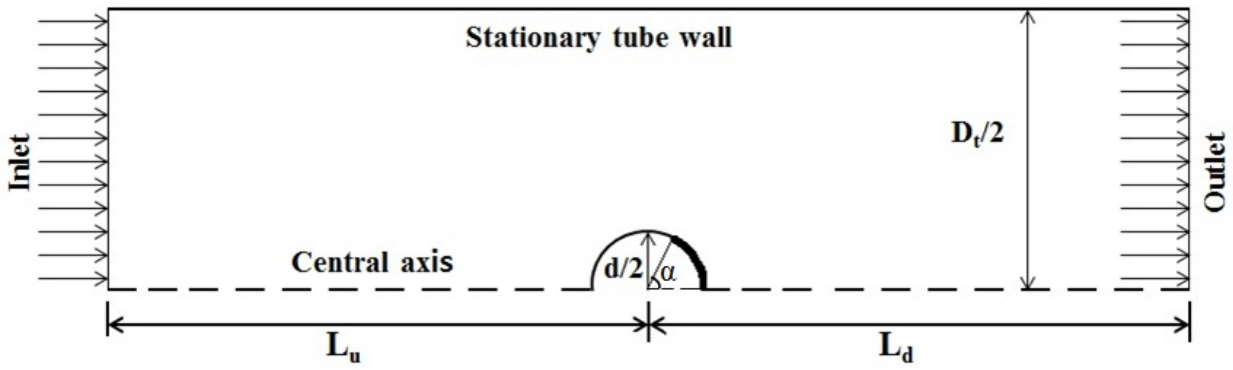

Figure 3.4: Schematic representation of flow past a confined partially contaminated bubble.

Consider the relative motion between a bubble (of radius, $R=d/2$) and a contaminated power-law fluid in a confined container. The relative motion is schematically represented in **Figure 3.4**. The bubble is located along the central axis of a long cylindrical tube of length L, and diameter D_t. With reference to the location of the bubble, the upstream distance is L_u and the downstream distance is L_d. Further an incompressible surfactant-laden power-law fluid is flowing in the tube with an inlet velocity V_o, temperature T_o and pressure P_o. During the course of surfactant-laden

power-law fluid flow around the bubble, the contaminants (or surfactants) adsorbed along the surface of the bubble and due to the main convection flow these contaminants further dragged towards the rear of the bubble to form a stagnant cap. Furthermore, in order to account for wall retardation effects, the diameter of the tube is varied according to the value of wall factor (λ) which is defined as the ratio between the diameters of the tube to that of spherical bubble. Here too segregated approach is used to obtain the velocity and temperature profiles. The assumptions and governing equations are same as in the case of unconfined bubble case. However, appropriate boundary conditions are the standard velocity inlet and the pressure outlet at the inlet and outlet respectively; symmetry boundary condition along the central axis; no-slip wall along the tube wall; and zero shear stress and no-slip velocity boundary conditions along the mobile and immobile (stagnant cap zone) portions of the bubble surface, respectively. In order to solve the heat transfer equation, the appropriate boundary conditions are constant temperature on bubble surface (T_s), along the tube wall a constant temperature (T_o) and inlet fluid temperature (T_o). The heat transfer takes place between heated bubble surface to surrounding contaminated power-law liquid. Once the fully converged velocity, pressure and temperature profiles are known, the streamline profiles, vorticity contours, drag coefficients, isotherm contours, and local and average Nusselt numbers are obtained in a similar method as in the case of unconfined partially contaminated bubbles.

Chapter 4

NUMERICAL METHODOLOGY

4.1. In-House SMAC Solver

Briefly, the non-dimensional momentum equations segregated from species continuity equation, subject to the boundary conditions (as described in previous chapter) have been numerically solved on a sphere-in-sphere type concentric spherical computational domain. A finite difference method based SMAC-implicit algorithm has been implemented on a staggered grid arrangement in spherical coordinates. This algorithm is a simplified version of marker and cell (MAC) method due to Harlow and Welch (1965). The modification is introduced here to handle the non-Newtonian viscosity of the fluid effectively and semi implicit formulation is used. The diffusive and non-Newtonian terms of the momentum equations are discretized using a second order central difference scheme. The convective terms are discretized using quadratic upstream interpolation for convective kinematics (QUICK) scheme due to Leonard (1979). The final steady-state solution is obtained by using a false-transient time stepping method and this is why the time-dependent terms are retained in the momentum equations. This procedure involves three steps: in the first step, the non-Newtonian viscosity equation is used to evaluate the dimensionless non-Newtonian viscosity field over the entire flow domain using the previous time-step values of the velocity field. In the next step, the unknown velocity field is predicted using the previous time-step pressure field. Finally, the pressure field is corrected using the predicted velocity field which is further used to correct the velocity field. For the next time-step calculations, the sum of the predicted and corrected velocity fields are used as new values of the

velocity field. This sequence of time-stepping is continued until the velocity field satisfies the equation of the continuity within a prescribed level. The stopping criterion for simulations is fixed as the maximum difference of any quantity between the two consecutive time-steps divided by the time step (Δt) should be below 10^{-3}. The fully converged steady velocity and pressure profiles are used to evaluate individual and total drag coefficients as functions of pertinent dimensionless parameters.

4.1.1. Staggered grid arrangement

The convergence of predictor-corrector kind of solvers is poor on normal collocated grids. The collocated grid may also cause checkerboard velocity-pressure distribution. To overcome this problem the staggered grid system is used in this work. Another important advantage of a staggered grid is that the transport rates across the faces of control volume can be computed without interpolation of velocity components. The computational domain is divided into a number of cells, which are shown in **Figure 4.1** as a two-dimensional section of a sphere. This figure shows a spherical staggered grid arrangement for a 2-D axisymmetric spherical computational flow domain, where the dependent variables (v_r(i,j), v_θ(i,j) and p(i,j)) with same indices staggered to one another. In this arrangement, the scalars are located at the center of the cell, whereas, velocity vectors will be located at the center of the cell faces to which they are normal. Thus, the location of the velocity components are at the center of the cell faces to which they are normal and the grid points for the pressure and species concentrations are at the center of the cell. In such an arrangement, the pressure difference between the two adjacent cells is the driving force for the velocity component located at the interface of these cells during the numerical iterations. Thus the pressure-velocity corrections are directly related to each other, and the pressure-velocity iterative loops converge quickly. As shown in **Figure 4.1** cells are labeled

as (i,j), where i and j denote the cell number as counted in θ- and r - directions respectively. The pressure is defined at the center of the cell and is denoted by p(i,j). The r-component velocity of cell (i,j) is defined at the cell face in r-direction i.e., at the center of the cells (i,j) and (i,j+1), and is denoted by v_r(i,j+1/2). The θ-component velocity of cell (i,j) is defined at the cell face in θ-direction i.e., at the center of the cells (i,j) and (i+1,j), and is denoted by v_θ(i+1/2,j). In a staggered grid arrangement, velocities are not defined at the cell centers, so whenever needed these are calculated by interpolation.

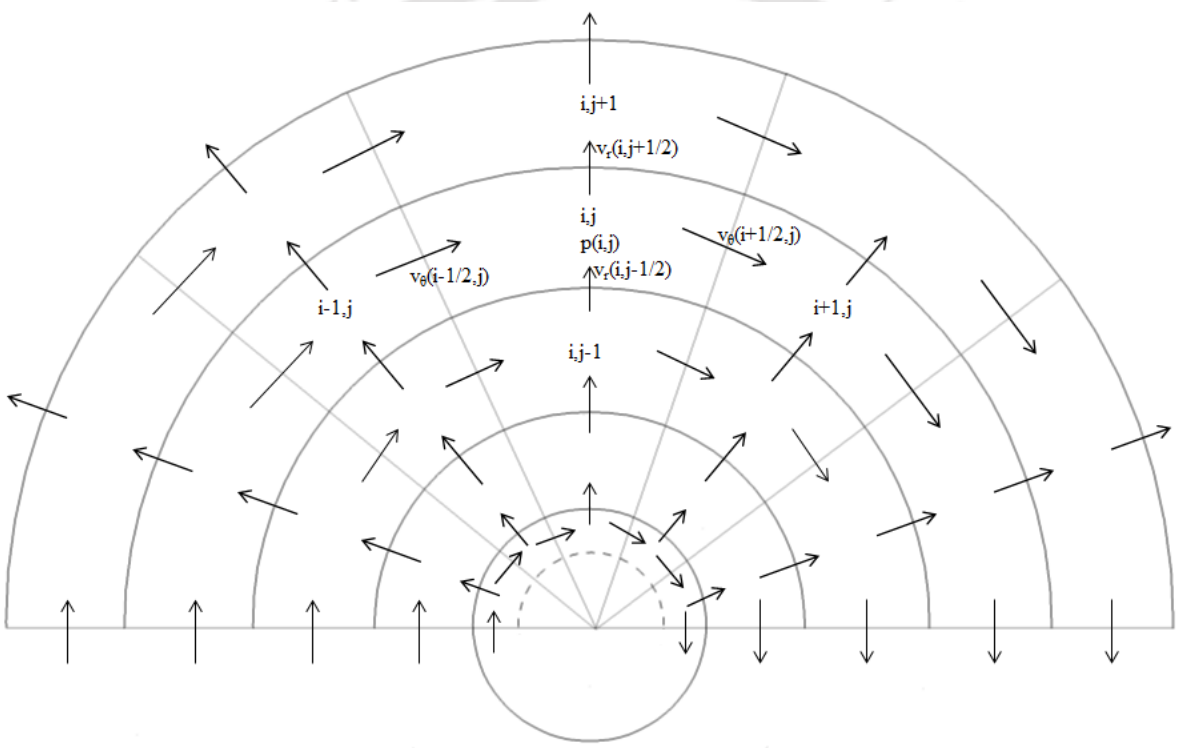

Figure 4.1: Two dimensional staggered grid arrangement in spherical coordinate system.

All computations are performed in half-domain assuming the axisymmetry in φ - direction, i.e., $v_\phi = 0$ and no variables depend on ϕ-coordinate. **Figure 4.2** shows the physical and computational domains appropriately divided into many small cells (or grids). The domain with solid lines represent the physical domain, whereas, the domain enclosed by dashed lines represents the computational domain. The cells with dashed lines also serve as boundary cells or

fictitious cells. A solid line denoted by "s" represents the interface between bubble and outside continuous fluid flow field. Two dashed lines along θ-direction on the either side of $\theta = 0$ and $\theta = \pi$ serves as fictitious cells for computations. When we solve for the continuous flow field, the dashed line denoted by (s-1) serves as the boundary for the continuous fluid flow field.

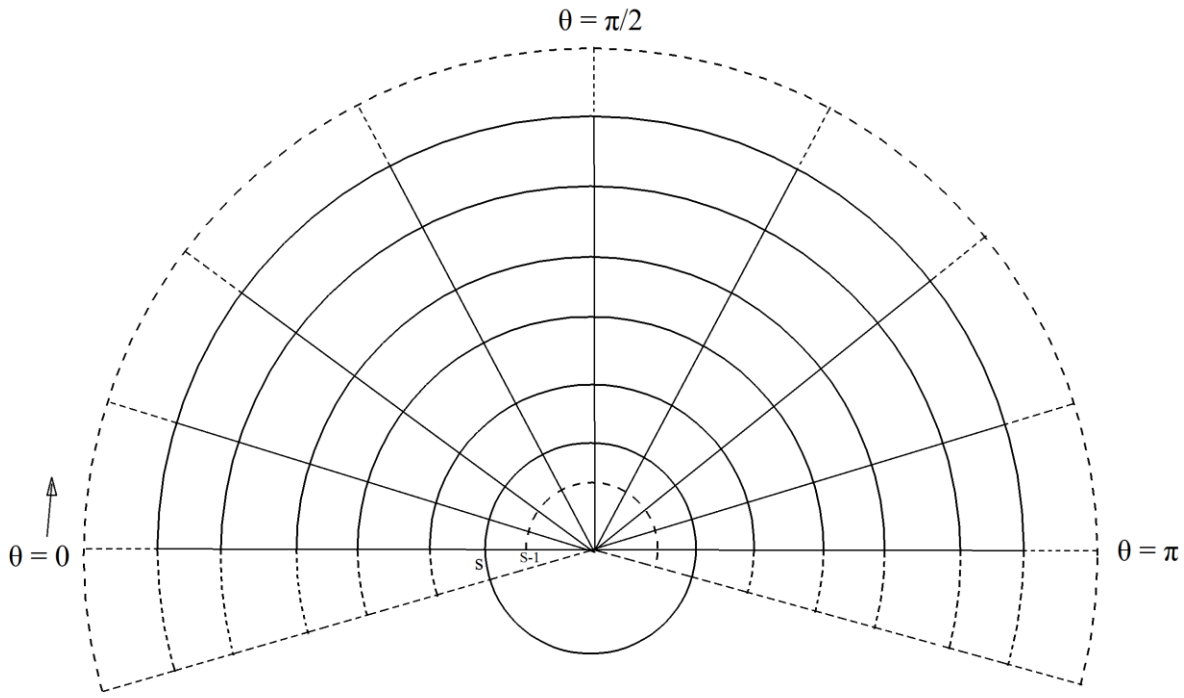

Figure 4.2: Grid arrangement in computational domain.

4.1.2. Discretization of governing equations

The diffusive and non-Newtonian terms of *r*- and *θ*- momentum equations have been discretized by second order central difference scheme. But convective terms have been discretized using the QUICK scheme for better accuracy and to avoid numerical instabilities. In convective schemes, each convective term is divided as two parts; a variable and a coefficient depending on which component of momentum equation is considered. Then, the coefficient will be averaged and the convective scheme will be employed on the variable term depending on whether the coefficient is positive or negative. For example, in the *r*-momentum equation the variable is v_r and

coefficient can be v_θ or v_r depending on the term being discretized. Similarly, in θ-momentum equation the variable is v_θ and coefficient can be v_θ or v_r. The detailed discretization of r- and θ-momentum equations and equation of continuity, Poisson's equation for pressure correction, non-Newtonian viscosity, vorticity equation, vorticity transport equation, etc. have been shown in Appendix-C.

4.1.3. SMAC-implicit algorithm

The major difficulty encountered in obtaining the solution of incompressible fluid flow using primitive variables based momentum equation is the non-availability of any obvious equation for calculating the pressure field. SMAC-semi implicit scheme is implicit for diffusion and non-Newtonian terms while explicit in convective term (pressure terms are explicit in predictor step but in combined predictor-corrector scheme pressure terms are implicit). An advantage of the SMAC-semi implicit scheme over SMAC-explicit (which is explicit in convective and diffusion terms) scheme is that one can use larger values of time-step. This numerical scheme mainly consists of three steps, velocity prediction, pressure correction and finally velocity correction. All these steps are solved by the Gauss-Seidel iteration procedure. In the first step, we assume the pressure field at the $(t_s)^{th}$ time-step and "predict"' the velocity field at the $(t_s+1)^{th}$ time-step by using the Gauss-Seidel iterations. In the second step, this predicted velocity field is used to solve the Poisson's equation which yields pressure correction. This pressure correction is then used to calculate the velocity corrections. Finally, all the predictor and corrector quantities are added to estimate the modified velocity and pressure field for the next time-step. These steps are repeated until a fully converged steady-state solution is obtained. The predictor and corrector equations used in this work are derived below.

4.1.3.1. Velocity prediction

Consider *r*- and θ- components of momentum equation in the following form (the complete discretization of equations is given in Appendix-C):

$$\left[\frac{\partial v_r}{\partial t}\right]_{i,j+1/2} + [CONVR]_{i,j+1/2} = -\left[\frac{\partial p}{\partial r}\right]_{i,j+1/2} + [DIFFR]_{i,j+1/2} + [NONR]_{i,j+1/2}$$

$$\left[\frac{\partial v_\theta}{\partial t}\right]_{i+1/2,j} + [CONV\theta]_{i+1/2,j} = -\left[\frac{1}{r}\frac{\partial p}{\partial \theta}\right]_{i+1/2,j} + [DIFF\theta]_{i+1/2,j} + [NON\theta]_{i+1/2,j}$$

Discretizing the above equations we get

$$\frac{v_r^{t_s+1}(i,j+1/2) - v_r^{t_s}(i,j+1/2)}{\Delta t} + [CONVR]_{i,j+1/2}^{t_s} = -\left[\frac{\partial p}{\partial r}\right]_{i,j+1/2}^{t_s+1} + [DIFFR]_{i,j+1/2}^{t_s+1} + [NONR]_{i,j+1/2}^{t_s+1} \quad (4.1)$$

$$\frac{v_\theta^{t_s+1}(i+1/2,j) - v_\theta^{t_s}(i+1/2,j)}{\Delta t} + [CONV\theta]_{i+1/2,j}^{t_s} = -\left[\frac{1}{r}\frac{\partial p}{\partial \theta}\right]_{i+1/2,j}^{t_s+1} + [DIFF\theta]_{i+1/2,j}^{t_s+1} + [NON\theta]_{i+1/2,j}^{t_s+1} \quad (4.2)$$

where the superscript (t_s) represents the current time-step at which the variable values are known and (t_s+1) indicates the next time-step at which the variables are unknown. Here the convective term is explicit while the diffusion, non-Newtonian and pressure terms are implicit. The pressure at the (t_s+1)th step is unknown and there is no equation for pressure which can be used to obtain it. So we assume an approximate pressure field at the (t_s+1)th time-step by its previous time-step value. Therefore here we predict velocity field v_r* and v_θ* at the (t_s+1)th time-step by using an assumed pressure field (and obviously will not satisfy continuity). Hence equations (4.1) and (4.2) lead to give prediction equations which can be written as follows:

$$\frac{v_r^{*}(i,j+1/2) - v_r^{t_s}(i,j+1/2)}{\Delta t} + [CONVR]_{i,j+1/2}^{t_s} = -\left[\frac{\partial p}{\partial r}\right]_{i,j+1/2}^{t_s+1} + [DIFFR]_{i,j+1/2}^{*} + [NONR]_{i,j+1/2}^{*} \quad (4.3)$$

$$\frac{v_\theta^{*}(i+1/2,j) - v_\theta^{t_s}(i+1/2,j)}{\Delta t} + [CONV\theta]_{i+1/2,j}^{t_s} = -\left[\frac{1}{r}\frac{\partial p}{\partial \theta}\right]_{i+1/2,j}^{t_s} + [DIFF\theta]_{i+1/2,j}^{*} + [NON\theta]_{i+1/2,j}^{*} \quad (4.4)$$

where v_r* and v_θ* are predicted velocities. In Eq. 4.3 and Eq. 4.4, all variables are at $(t_s)^{th}$ time-step are known, while variables with an asterisk (*) are unknown. Thus Eq. 4.3 and Eq. 4.4 are solved to get v_r* and v_θ* by using Gauss-Seidel iterations. In Eq. 4.3, [DIFFR]* is a function of v_r* only, but [NONR]* is function of v_r* and v_θ*. So to predict v_r*, the value of v_θ*, which is unknown is required. So for computations, v_θ* is lagged to v_θ^{ts}. But in Eq. 4.4, where too [DIFFθ]* and [NONθ]* are functions of both v_r* and v_θ*, however, there is no need of lagging here, since v_r* is computed before predicting v_θ*, since in the prediction-step usually first v_r* will be predicted before predicting v_θ*. (It may be noted that, this kind of lagging is not required in case of Newtonian calculations, since [NONR]* and [NONθ]* drops to zero for the case of Newtonian fluids).

4.1.3.2. Velocity correction

In order to estimate the velocity corrections at $(t_s+1)^{th}$ time-step, the velocity correction should be added to the velocity prediction to count as final values for the next time-step calculations. In this section, the formulation of the velocity correction equations is presented. Subtracting Eq. 4.3 and Eq. 4.4 from Eq. 4.1 and Eq. 4.2 respectively we get expressions for the velocity correction which can be written as follows

$$\frac{v_r'(i,j+1/2)}{\Delta t} = -\left[\frac{\partial p}{\partial r}\right]'_{i,j+1/2} + [DIFFR]'_{i,j+1/2} + [NONR]'_{i,j+1/2} \tag{4.5}$$

$$\frac{v_\theta'(i+1/2,j)}{\Delta t} = -\left[\frac{1}{r}\frac{\partial p}{\partial \theta}\right]'_{i+1/2,j} + [DIFF\theta]'_{i+1/2,j} + [NON\theta]'_{i+1/2,j} \tag{4.6}$$

where

$$\frac{v_r'(i,j+1/2)}{\Delta t} = \frac{v_r^{t_s+1}(i,j+1/2) - v_r^*(i,j+1/2)}{\Delta t}$$

$$\frac{v_\theta^{/}(i+1/2,j)}{\Delta t}=\frac{v_\theta^{t_s+1}(i+1/2,j)-v_\theta^{*}(i+1/2,j)}{\Delta t}$$

$$\left[\frac{\partial p}{\partial r}\right]^{/}_{i,j+1/2}=\left[\frac{\partial p}{\partial r}\right]^{t_s+1}_{i,j+1/2}-\left[\frac{\partial p}{\partial r}\right]^{t_s}_{i,j+1/2}$$

$$\left[\frac{1}{r}\frac{\partial p}{\partial \theta}\right]^{/}_{i+1/2,j}=\left[\frac{1}{r}\frac{\partial p}{\partial \theta}\right]^{t_s+1}_{i+1/2,j}-\left[\frac{1}{r}\frac{\partial p}{\partial \theta}\right]^{t_s}_{i+1/2,j}$$

$$[DIFFR]^{/}_{i,j+1/2}=[DIFFR]^{t_s+1}_{i,j+1/2}-[DIFFR]^{*}_{i,j+1/2}$$

$$[DIFF\theta]^{/}_{i+1/2,j}=[DIFF\theta]^{t_s+1}_{i+1/2,j}-[DIFF\theta]^{*}_{i+1/2,j}$$

$$[NONR]^{/}_{i,j+1/2}=[NONR]^{t_s+1}_{i,j+1/2}-[NONR]^{*}_{i,j+1/2}$$

$$[NON\theta]^{/}_{i+1/2,j}=[NON\theta]^{t_s+1}_{i+1/2,j}-[NON\theta]^{*}_{i+1/2,j}$$

In all above expressions, primed variables indicate correction quantities. Eq. 4.5 and Eq. 4.6 can be solved using Gauss-Seidel iterations but the difficulty is the non-availability of $p_{ij}^{/}$; the pressure corrector. Therefore, before calculating the velocity correction, pressure correction should be known which can be obtained as explained below.

4.1.3.3. Pressure correction

The quantities v_r^{ts+1} and v_θ^{ts+1}, the velocity components at $(t_s+1)^{th}$ time-step, must satisfy the continuity equation i.e.,

$$\frac{1}{r^2}\frac{\partial\left(r^2 v_r^{t_s+1}\right)}{\partial r}+\frac{1}{r\sin\theta}\frac{\partial\left(v_\theta^{t_s+1}\sin\theta\right)}{\partial\theta}=0 \qquad (4.7)$$

where v_r^{ts+1} and v_θ^{ts+1} are given as:

$$v_r^{t_s+1}=v_r^{*}+v_r^{/},\qquad v_\theta^{t_s+1}=v_\theta^{*}+v_\theta^{/} \qquad (4.8)$$

From the continuity equation

$$\Rightarrow \nabla.V^{t_s+1} = \nabla.V^{*} + \nabla.V^{/} = 0 \Rightarrow \nabla.V^{*} = -\nabla.V^{/}$$

Now by expanding the term $\nabla.V^{/}$, we get

$$\nabla.V^{/} = \frac{1}{r^2}\frac{\partial\left(r^2 v_r^{/}\right)}{\partial r} + \frac{1}{r\sin\theta}\frac{\partial\left(v_\theta^{/}\sin\theta\right)}{\partial\theta}$$

Here $v_r^{/}$ and $v_\theta^{/}$ given by Eq. 4.5 and Eq. 4.6 respectively. Thus by using Eqs. 4.5 and Eq. 4.6; and considering these two equations only for *Newtonian case* we get:

$$\nabla.V^{/} = \frac{1}{r^2}\frac{\partial}{\partial r}\left[r^2\left(-\left[\frac{\partial p}{\partial r}\right]^{/}_{i,j+1/2} + \left[DIFFR\right]^{/}_{i,j+1/2}\right)\Delta t\right] + \frac{1}{r\sin\theta}\frac{\partial}{\partial\theta}\left[\sin\theta\left(-\left[\frac{1}{r}\frac{\partial p}{\partial\theta}\right]^{/}_{i+1/2,j} + \left[DIFF\theta\right]^{/}_{i+1/2,j}\right)\Delta t\right]$$

$$\Rightarrow \frac{\nabla.V^{/}}{\Delta t} = \frac{1}{r^2}\frac{\partial}{\partial r}\left[r^2\left(-\left[\frac{\partial p}{\partial r}\right]^{/}_{i,j+1/2} + \left[DIFFR\right]^{/}_{i,j+1/2}\right)\right] + \frac{1}{r\sin\theta}\frac{\partial}{\partial\theta}\left[\sin\theta\left(-\left[\frac{1}{r}\frac{\partial p}{\partial\theta}\right]^{/}_{i+1/2,j} + \left[DIFF\theta\right]^{/}_{i+1/2,j}\right)\right]$$

$$\Rightarrow \frac{\nabla.V^{/}}{\Delta t} = \frac{1}{r^2}\frac{\partial}{\partial r}\left(-\left[r^2\left[\frac{\partial p}{\partial r}\right]^{/}_{i,j+1/2}\right]\right) + \frac{1}{r\sin\theta}\frac{\partial}{\partial\theta}\left[\left(-\sin\theta\left[\frac{1}{r}\frac{\partial p}{\partial\theta}\right]^{/}_{i+1/2,j}\right)\right] + \frac{1}{r^2}\frac{\partial}{\partial r}\left(r^2\left[DIFFR\right]\right)^{/}_{i,j+1/2} + \frac{1}{r\sin\theta}\frac{\partial}{\partial\theta}\left(\sin\theta\left[DIFF\theta\right]\right)^{/}_{i+1/2,j}$$

By simplifying the right hand side term of the above expression and writing in conservative from, the resulting expression can be represented as follows

$$\frac{\nabla.V^{/}}{\Delta t} = -\nabla^2 p^{/} + \frac{2^n\eta}{\mathrm{Re}}\nabla^2\left(\nabla.V^{/}\right) \qquad (4.9)$$

where the operator ∇^2 is given by

$$\nabla^2 = \frac{1}{r^2}\frac{\partial}{\partial r}\left(r^2\frac{\partial}{\partial r}\right) + \frac{1}{r\sin\theta}\frac{\partial}{\partial\theta}\left(\frac{\sin\theta}{r}\frac{\partial}{\partial\theta}\right)$$

Since we know that $\nabla.V^{*} = -\nabla.V^{/}$ and by making use of this expression in Eq. 4.9, we get

$$\nabla^2 p^{/} = \frac{\nabla.V^{*}}{\Delta t} - \frac{2^n\eta}{\mathrm{Re}}\nabla^2\left(\nabla.V^{*}\right) \qquad (4.10)$$

Eq. 4.10 is solved for $p^{/}_{i,j}$ with appropriate boundary conditions and using the predicted velocity V^{*}. Then with the resultant pressure correction, Eq. 4.5 and 4.6 are solved for $v_r^{/}$ and $v_\theta^{/}$

respectively. (In the Eq. 4.10, the viscosity and power-law index terms appear because the radial distances have been normalized using the radius of the drop, however, this term would have not appeared in the pressure corrector equation if the radial distances were normalized using the diameter of the fluid sphere). Finally we get the corrected velocity and pressure fields by $v_r^{t_s+1} = v_r^* + v_r^1$, $v_\theta^{t_s+1} = v_\theta^* + v_\theta^1$ and $p_{ij}^{t_s+1} = p_{ij}^* + p_{ij}^/$. The Eq. 4.10 is for Newtonian case only, however, in the present study, the same equation has been used for non-Newtonian systems to avoid further complications. However, this is justified since the Eq. 4.10 ensures that the velocity field satisfies the continuity equation, which is the same for both Newtonian and non-Newtonian flows. The momentum equations ensure that the correct non-Newtonian solution is obtained.

Finally, the fully converged velocity and pressure fields can be used to evaluate the derived quantities such as the individual and total drag coefficients, streamlines and vorticity contours, distributions of viscosity, pressure, vorticity and tangential velocity on the surface of the drop, etc., as discussed in the previous chapter as functions of the pertinent dimensionless parameters.

4.1.4. Segregated algorithm for species heat/mass transfer

In the numerical study of heat and mass transfer problems, sometimes scalars like temperature and species concentration are solved along with the momentum equations. However, how the solutions of the flow equations and the energy/concentration equations are sequenced is determined by the kind of flow and mass transfer problem being solved. In this work, it is assumed that the flow field is steady and independent of the temperature/concentration being solved. Such situations would arise in steady forced convective problems, say, when the temperature field is not strong enough to cause substantial changes in the density so as to affect the flow by buoyancy. In such cases, the momentum equations can be solved independent of

temperature/concentration equations. Thus, in this study, the steady velocity field in the entire flow domain is obtained by numerically solving the momentum equations segregated from the species concentration equation.

The fully converged velocity field was used as the input for the species mass transfer equation to obtain the concentration field by using a time-stepping procedure applied to the species continuity equation. Because an implicit scheme is used each time-step solution is obtained by Gauss-Seidel iterations. The concentration profile in the continuous phase is obtained with a similar implicit algorithm which uses the QUICK and second order central differencing schemes, respectively, for the convective and diffusive terms of the species mass transfer equation. The detailed discretization of the mass transfer equation has been shown in Appendix-C. After obtaining the steady concentration field for the continuous phase, one can readily calculate the values of the local and average Sherwood numbers, as explained in the previous chapter as functions of pertinent dimensionless parameters.

4.2. Solution Methodology Using Fluent Software

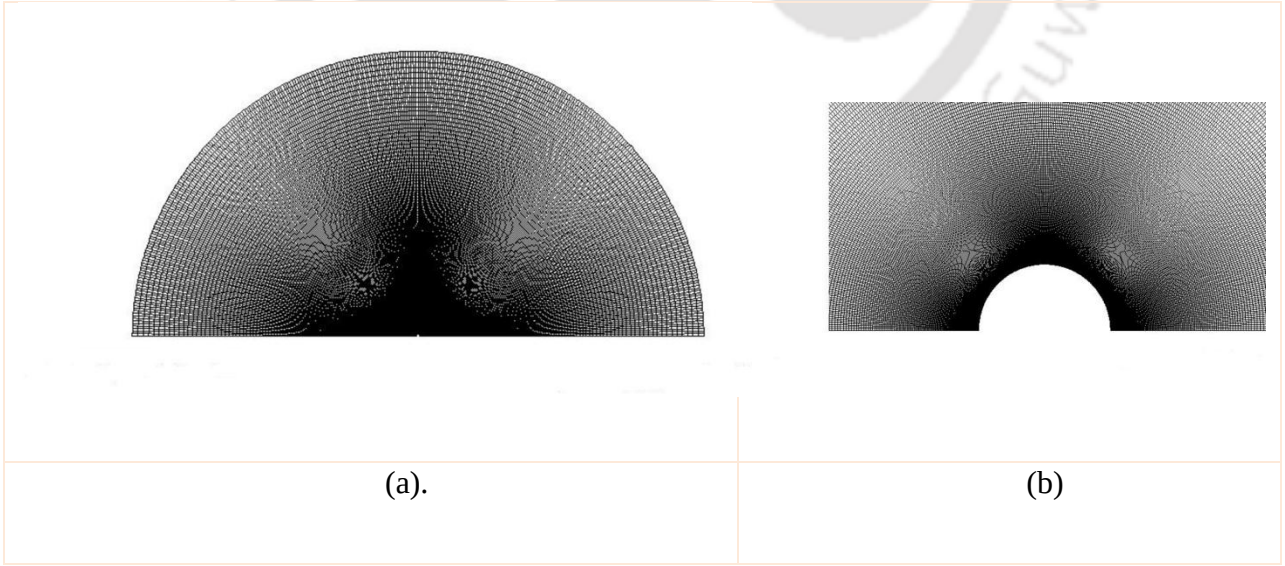

(a). (b)

Figure 4.3: Schematic representation of computational grid: (a) full domain and (b) near bubble.

The governing conservation equations of the mass and momentum along with appropriate boundary conditions are solved using a commercial solver, Ansys Fluent, in conjunction with mesh generating software Gambit. In the Gambit, two half circles (inner one for bubble of radius, R, and the outer one for the computational domain of radius R_∞) and a central axis connecting two circles are generated. These edges are joined together to form complete computational domain. In order to generate grid in the computational domain, along each of these edges, specified number of node points are designated. Then quadrilateral mesh has been generated in the sphere-in-a-sphere computational domain as shown in **Figure 4.3(a).** In order to cluster the grid in the vicinity of the bubble surface as shown in **Figure 4.3(b)**, along the central axis of the computational domain, node points are used with a specified aspect ratio. Thus generated mesh has been exported to the Ansys Fluent to obtain the steady velocity and pressure fields in the entire domain by choosing axisymmetric laminar viscous flow solver. In the Fluent, the boundary conditions are set as described in the previous section. The semi-implicit method for pressure-linked equations (SIMPLE) algorithm along with quadratic upstream interpolation for convective kinematics (QUICK) scheme for momentum terms are chosen. In order to obtain the fully converged velocity and pressure fields, the residual tolerance for the continuity and momentum equations are set to as 10^{-8}. The fully converged velocity and pressure fields are further utilized to evaluate the streamlines, vorticity contours, surface viscosity distributions and drag coefficients. The fully converged velocity field is also utilized to solve the energy equation using similar algorithm to obtain the temperature profile in the entire computational domain. The residual tolerance for the energy equation set to as 10^{-10}.However, before presenting new results, it is mandatory to benchmark the solver for numerical artifacts such as the domain and grid independence of the solver.

Chapter 5

CHOICE OF NUMERICAL PARAMETERS

In this chapter, numerical details such as optimum domain, optimum grid and validity and reliability of solution methodology are established for transport phenomena of unconfined and confined partially contaminated bubbles in power-law fluids and swarms of partially contaminated bubbles in Newtonian and power-law liquids. Because of domination of viscous forces domain independence studies carried at small Reynolds numbers, whereas because of domination of convective forces, grid independence study has been carried out at higher Reynolds numbers.

5.1. Drag Behavior of Unconfined Single Bubble using In-house Solver

5.1.1. Domain and grid study

Table 5.1: Effect of grid on C_d of fully clean ($\alpha = 0$) and fully contamianted bubbles ($\alpha = \pi$) in shear-thinning fluid of $n = 0.6$ at $Re = 200$.

Grid	$\alpha = 0$	$\alpha = \pi$
60×150	0.138	0.508
90×200	0.133	0.508
120×240	0.134	0.509

For the case of unconfined partially contaminated bubbles in Newtonian and power-law liquids, a domain of size R_∞ = 150 is chosen which is consistent with other numerical studies related to Newtonian and power-law flow past bubbles, drops and particles (Saboni *et al*., 2010; Dhole *et al*. 2006, 2007). For this domain, a detailed grid study is carried out at *Re* = 200 for *n* = 0.6 when the bubble is fully clean ($\alpha = 0$) and completely contaminated ($\alpha = \pi$) and presented in **Table 5.1**. From this table it can be seen that the improvement in C_d is within ± 0.4-0.5 by refining the grid from 90×200 (r-×θ-) to 120×240 but at an expanse of several folds larger CPU time; hence grid 90×200 is used.

5.1.2. Validation

Table 5.2: Comparison of C_d of clean spherical bubble in Newtonian fluids.

Re	Brabston and Keller (1975)	Feng and Michaelides (2001)	Dhole *et al.* (2007)	Present
1	17.59	17.57	-	17.17
10	2.35	2.441	2.464	2.392
20	1.362	1.404	1.434	1.397
100	-	0.379	0.383	0.374
200	0.197	0.206	0.212	0.206

The comparison of present C_d values of clean bubble and fully contaminated bubble with literature counterparts are shown in **Table 5.2** and **Table 5.3**. From these tables it can be seen that the present values are in good agreement with literature counterparts. **Table 5.4** shows the comparison of present C_d values of clean bubble, partially contaminated bubble and fully

contaminated bubble in Newtonian fluids with literature counterparts. From this table it can be seen that the present values are in good agreement with literature counterparts.

Table 5.3: Comparison of C_d of fully contaminated spherical bubbles in Newtonian fluids.

Re	LeClair *et al.* (1970)	Saboni *et al.* (2004)	Dhole *et al.* (2006)	Present
1	27.37	27.55	26.13	27.71
10	4.337	4.424	4.281	4.344
20	2.736	2.768	2.692	2.739
100	1.096	1.084	1.062	1.094
200	0.772	0.776	0.744	0.779

Table 5.4: Comparison of C_d of partially contaminated spherical bubble in Newtonian liquids.

α	Takemura and Yabe (1999)	Saboni *et al*. (2010)	Present
		Re = 10	
0	2.37	2.47	2.391
56	2.88	2.92	2.915
90	3.76	3.86	3.741
116	4.19	4.33	4.316
180	4.22	4.42	4.341
		Re = 100	
0	0.38	0.37	0.374
56	0.51	0.50	0.507
90	0.83	0.88	0.930
116	1.02	1.07	1.091
180	1.09	1.09	1.094

5.2. Drag Behavior of Unconfined Single Bubble using Ansys Fluent

5.2.1. Domain and grid study

Table 5.5: Effect of domain size on C_d of clean and fully contaminated bubbles at Re = 0.1.

R_∞	No. of nodes on			$\alpha = 0^o$			$\alpha = 180^o$		
	Bubble Surface	Outer sphere	Central axis	n = 1.6	n = 1	n = 0.2	n = 1.6	n = 1	n = 0.2
50	100	100	160	84.7164	160.41	223.15	113.8204	250.44	342.89
100	100	200	320	83.281	158.73	223.05	111.1063	246.18	342.28
150	100	300	480	83.1089	158.52	223.29	110.6745	245.15	342.22

Table 5.6: Effect of grid on C_d of clean and fully contaminated bubbles at Re = 200.

Grid	No. of nodes on			$\alpha = 0^o$			$\alpha = 180^o$		
	Bubble Surface	Outer sphere	Central axis	n = 1.6	n = 1	n = 0.2	n = 1.6	n = 1	n = 0.2
G1	250	250	200	0.3155	0.3324	0.42	0.7365	0.4987	0.4708
G2	350	350	200	0.2917	0.3185	0.4269	0.7292	0.4808	0.4935
G3	350	350	400	0.329	0.1955	0.1345	1.1245	0.7737	0.3526
G4	350	350	600	0.3453	0.1996	0.1239	1.1255	0.7704	0.3501
G5	350	350	700	0.3483	0.2008	0.1238	1.1256	0.7704	0.3416
G6	350	350	800	0.3497	0.2015	0.1240	1.1256	0.7704	0.3403

The domain independence study has been carried out at *Re* = 0.1 for extreme values of the power-law index and the cap angle for three different values of the domain size (**Table 5.5**). This **Table 5.5** also shows the grid size used for the domain independence study. Along the surface of the bubble, the constant interval size (0.01) of the grid is maintained for all three values of the domain size. Though two domains of size 100 and 150 times the bubble size produce almost identical C_d values for all combinations of the power-law index and cap angle, for safer side, a large domain size (i.e., R_∞ = 150) has been chosen. Further, it is mandatory to find out optimum grid for this domain. A detailed grid independence has been carried out at *Re* = 200 for extreme values of the power-law index and the cap angle and presented in **Table 5.6**. Although grids G4, G5 and G6 produce almost identical results, finer grid G6 has been chosen for all other computations.

5.2.2. Validation

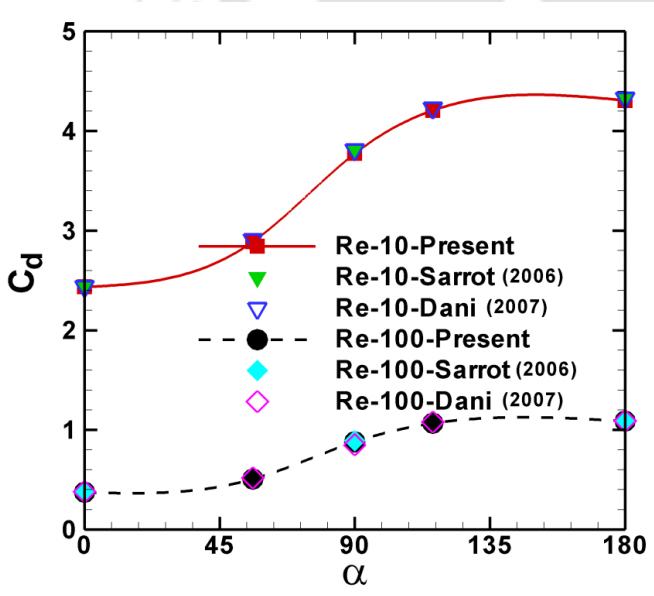

Figure 5.1: Comparison of drag C_d of contaminated bubbles in Newtonian liquids with numerical literature values.

The present C_d values of partially contaminated bubbles in Newtonian liquids are compared with literature counterparts and are in excellent agreement (**Figure 5.1**). Similarly present C_d values of fully contaminated and completely clean bubbles in power-law liquids are compared with literature values; and the agreement is satisfactory (**Figure 5.2**).

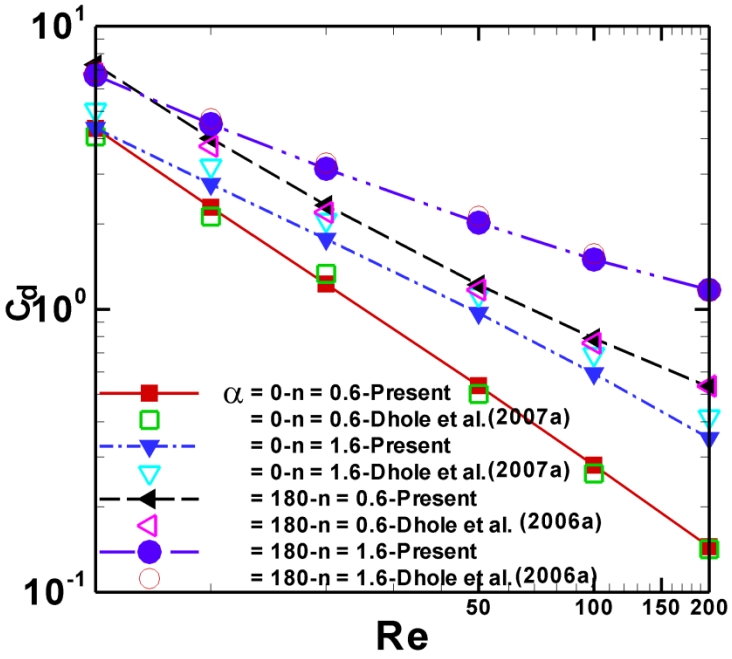

Figure 5.2: Comparison of C_d of clean and fully contaminated bubbles in power-law liquids with numerical literature values.

5.3. Heat Transfer Phenomena of Unconfined Single Bubble using Ansys Fluent

5.3.1. Grid study

For the heat transfer problem, same domain (R_∞ = 150) has been chosen as in the case of momentum transfer. However, thermal boundary layer can be thinner than the momentum boundary layer; and hence grid study has been carried out in the case of heat transfer problem as

well. The grid independence study has been carried out at Re = 200 for extreme values of power-law indices, i.e., n = 0.2 and n = 1.6 and cap angle $\alpha = 0^o$ and $\alpha = 180^o$ with an optimum domain of R_∞ = 150 (**Table 5.7**). It can be seen from this **Table 5.7** that grids G5 and G6 produce almost identical results with maximum error not more than 0.4%; however, for safer side, the finer grid G6 has been chosen for all other computations. The fully converged velocity and pressure fields of momentum study are used to solve the energy equation using similar algorithm to obtain the temperature profile in the entire computational domain.

Table 5.7: Effect of grid on Nu_{avg} of clean and fully contaminated spherical bubbles at Re = 200.

Grid	No. of nodes on			$\alpha = 0^o$		$\alpha = 180^o$	
	Bubble Surface	Free stream sphere	Central axis	n = 0.2	n = 1.6	n = 0.2	n = 1.6
G1	250	250	200	7.86	7.86	7.86	7.86
G2	350	350	200	7.86	7.86	7.86	7.85
G3	350	350	400	66.87	66.67	64.33	61.47
G4	350	350	600	362	337.81	198.81	86.66
G5	350	350	700	479.87	427.82	206.11	85.95
G6	350	350	800	482.09	428.2	205.34	85.92

5.3.2. Validation

Table 5.8: Comparison of Nu_{avg} of contaminated bubbles in Newtonian liquids at Pr = 500.

		Contamination angle (α)				
		180^o	116^o	90^o	56^o	0^o
Re = 10	Takemura and Yabe (1999)	20	30	40	51	56
	Dani (2007)	21	29	40	53	58
	Saboni *et al.* (2011)	21	30	42	55	60
	Present Results	21	29.4	40.6	53	57.7
Re = 100	Takemura and Yabe (1999)	58	110	155	197	214
	Dani (2007)	60	116	164	205	218
	Saboni *et al.* (2011)	60	108	163	206	220
	Present Results	56.6	106.4	156.1	203.9	218.3

Table 5.9: Comparison of Nu_{avg} of completely clean bubbles and fully contaminated bubbles in power-law liquids at Pr = 100.

	Completely clean bubble ($\alpha = 0^o$)			
n	Re = 10		Re = 100	
	Dhole *et al.* (2007)	Present work	Dhole *et al.* (2007)	Present work
0.8	27.247	27.71	103.162	100.61
1.6	25.055	23.93	94.862	91.92
	Fully contaminated bubble ($\alpha = 180^o$)			
n	Re = 10		Re = 100	
	Dhole *et al.* (2006)	Present work	Dhole *et al.* (2006)	Present work
0.8	13.637	13.62	34.95	36.08
1.6	11.874	11.21	27.598	28.04

The present heat transfer results are compared with the literature values for the case of contaminated bubbles in Newtonian fluids (**Table 5.8**) and the agreement between two values is excellent (within the range of discrepancy is ± 2-3%). Furthermore, the present values of the average Nusselt numbers of completely clean (fully mobile, $\alpha = 0$) and fully contaminated (fully immobile, $\alpha = \pi$) bubbles in power-law liquids are also compared with the literature values (**Table 5.9**) and the agreement is found to be satisfactory.

5.4. Wall Retardation Effect on Drag Behavior and Heat Transfer Phenomena of Single Bubble using Ansys Fluent

5.4.1. Entry and exit effects

In the case of confined transport phenomena, one of the dimensions of computational domain (i.e., diameter of the tube) is prefixed based on the value of wall factor; however, other two dimensions, i.e., entry and exit lengths (or upstream and downstream distances) with reference to the location of bubble are needed to be optimized through numerical experiments. **Table 5.10** shows the effect of upstream and downstream distances on the drag experienced by both clean and fully contaminated bubbles at $Re = 0.1$ for extreme values of the power-law fluid behavior index. It can be seen from this table that all L_u and L_d distances reproduce almost identical results, however for safer side larger values, i.e., $L_u = L_d = 75$ are chosen for all other computations.

Table 5.10: Entry and exit effects on C_d of confined clean spherical bubbles (α = 0°) and fully contaminated spherical bubbles (α = 180°) in power-law fluids at Re = 0.1.

L_u and L_d Lengths	Number of nodes on					Drag coefficient			
	Inlet / Outlet	Bubble surface	Tube wall	L_u	L_d	$\alpha = 0^o$		$\alpha = 180^o$	
						n = 0.2	n = 1.6	n = 0.2	n = 1.6
					λ = 2				
25	20	300	200	150	150	260.1344	2879.5302	428.2707	8619.4112
50	20	300	400	300	300	259.9691	2888.0408	427.8084	8660.8443
75	20	300	600	450	450	260.0078	2894.3561	427.7554	8677.5311
					λ = 3				
25	30	300	200	150	150	237.3004	1288.6478	369.147	2781.1595
50	30	300	400	300	300	237.2283	1288.7034	369.103	2782.3781
75	30	300	600	450	450	237.2034	1288.6931	368.8479	2783.6449
					λ = 5				
25	50	300	200	150	150	236.1435	748.3045	355.956	1283.2913
50	50	290	400	300	300	235.0154	748.0796	355.7499	1283.6982
75	50	300	600	450	450	234.8756	748.0965	355.588	1283.8732

5.4.2. Grid study

Table 5.11: Grid effects on C_d of confined clean spherical bubbles (α = 0°) and fully contaminated spherical bubbles (α = 180°) in power-law fluids at *Re* = 200.

Grid no.	Number of nodes on					Drag coefficient			
	Inlet / Outlet	Bubble surface	Tube wall	L_u	L_d	$\alpha = 0^o$		$\alpha = 180^o$	
						n = 0.2	n = 1.6	n = 0.2	n = 1.6
				λ = 2					
1	20	200	600	450	450	0.2046	1.7628	0.7337	6.2905
2	20	300	600	450	450	0.201	1.7781	0.738	6.3144
3	20	300	600	550	550	0.231	1.7688	0.7711	6.2921
4	20	300	600	650	650	0.2365	1.7672	0.7555	6.2888
5	20	300	600	700	700	0.1985	1.7896	0.751	6.3383
6	20	300	800	700	700	0.2002	1.7729	0.7595	6.3063
7	20	300	1002	700	700	0.2414	1.7683	0.7602	6.3054
8	20	300	1200	700	700	0.2288	1.7646	0.761	6.3029
				λ = 5					
9	50	200	600	450	450	0.1344	0.7613	0.4502	2.6922
10	50	300	600	450	450	0.1319	0.7683	0.4344	2.6949
11	50	300	600	550	550	0.132	0.7685	0.4424	2.6954
12	50	300	600	650	650	0.1329	0.77	0.4395	2.7006
13	50	300	600	700	700	0.1318	0.7698	0.436	2.6982
14	50	300	800	700	700	0.1331	0.7702	0.4477	2.7
15	50	300	1000	700	700	0.1332	0.7699	0.4482	2.6995
16	50	300	1200	700	700	0.1337	0.77	0.4536	2.6997

Table 5.11 presents effect of grid resolution on total drag coefficients of clean and fully contaminated bubbles at *Re* = 200 for extreme values of power-law index and wall factor. From this table it can be seen that 20 nodes along the inlet/outlet, 300 nodes along the surface of the bubble, 1200 nodes along the tube wall and 700 nodes along the upstream and downstream lengths are found to be optimum. This optimum grid chosen for all other computations of momentum and heat transfer study.

5.4.3. Validation

Table 5.12: Comparison of C_d of confined fully contaminated spherical bubbles in Newtonian fluids with no-slip wall boundary condition.

Re	$\lambda = 3$			$\lambda = 5$		
	Wham *et al.* (1996)	Kishore and Gu (2010)	Present work	Wham *et al.* (1996)	Kishore and Gu (2010)	Present work
1	126.934	120.681	120.257	81.854	79.775	79.337
10	14.235	13.648	13.469	11.412	11.031	10.996
20	8.252	7.959	7.848	7.266	6.938	6.999
50	4.574	4.374	4.331	4.349	3.965	3.904

Table 5.12 shows the comparison for the drag coefficients of fully contaminated bubble (α = 180°)) with literature values in Newtonian fluids with no-slip tube wall condition. **Table 5.13** shows the comparison for the drag coefficients of fully contaminated bubble (α = 180°)) with literature values in shear-thinning fluids with moving tube wall condition. **Table 5.14** shows the comparison of average Nusselt number for fully contaminated bubble in Newtonian and shear-thinning with moving tube wall condition. From these three tables, it can be seen that the presented results are in excellent agreement with literature results and inspires confidence to

produce new results on the drag behavior and heat transfer characteristics of confined partially contaminated bubbles in power-law type non-Newtonian fluids and the present results are believed to be accurate and reliable within ±4-5%.

Table 5.13: Comparison of C_d of confined fully contaminated spherical bubbles in Newtonian and shear-thinning fluids with moving wall boundary condition.

Re	$n = 1$		$n = 0.6$		$n = 0.2$	
	Song *et al.* (2009)	Present work	Song *et al.* (2009)	Present work	Song *et al.* (2009)	Present work
			$\lambda = 2$			
1	142.8	142.6	77.68	76.99	40.48	40.86
5	28.42	28.66	15.79	15.58	8.39	8.42
10	14.62	14.53	8	8.02	4.37	4.4
50	3.603	3.62	2.13	2.14	1.14	0.97
100	2.35	2.32	1.42	1.41	0.82	0.86
			$\lambda = 5$			
1	40.57	40.53	38.592	39.08	35.407	36.73
5	8.88	8.81	8.154	8.16	7.214	7.05
10	5.02	4.98	4.379	4.4	3.754	3.66
50	1.73	1.7	1.31	1.29	0.889	0.89
100	1.18	1.16	0.84	0.83	0.538	0.54

Table 5.14: Comparison of Nu_{avg} of fully contaminated bubble in power-law fluids with moving wall boundary condition.

n	*Re*	*Pr*	Song *et al.* (2010)	Reddy and Kishore (2013)	Present work
			$\lambda = 2$		
0.6	5	1	3.208	3.876	3.88
		100	15.17	15.213	15.22
	100	1	9.814	9.785	9.798
		40	35.349	35.905	35.584
1	5	1	3.152	3.844	3.16
		100	13.879	13.827	13.833
	100	1	8.834	8.864	8.868
		40	29.278	29.288	29.2064
			$\lambda = 5$		
0.6	5	1	3.1873	3.2423	3.2422
		100	12.084	12.162	12.1543
	100	1	8.762	8.737	8.7321
		40	30.404	30.698	30.6723
1	5	1	3.141	3.128	3.1268
		100	10.469	10.453	10.4476
	100	1	7.752	7.792	7.7881
		40	25.059	25.05	25.0366

5.5. Drag Behavior and Mass/Heat Transfer Phenomena of Bubble Swarms using In-house Solver

5.5.1. Grid study

Table 5.15: Effect of grid on C_d of swarms of bubbles of Φ = 0.1 at *Re* = 200 in Newtonian fluids.

Stagnant cap angle (α)	Grid – 1 (30×30)	Grid – 2 (60×30)	Grid – 3 (90×60)
0°	0.284	0.285	0.288
180°	1.459	1.498	1.492

Table 5.16: Effect of grid on drag of swarms of contaminated bubbles of Φ = 0.1 at *Re* = 200 in power-law fluid of *n* = 0.6.

Stagnant cap angle (α)	Grid – 1 (30×30)	Grid – 2 (60×30)	Grid - 3 (60×60)	Grid – 4 (90×60)
0°	0.1731	0.1869	0.1944	0.1942
180°	1.0153	0.9777	1.023	1.0055

In the case of bubble swarms, as per the cell model, the size of the domain is fixed for a given value of bubble holdup through $R_\infty = \Phi^{-1/3}$; hence only grid study is required. The grid independence study is carried out for bubble swarms of holdup = 0.1 in Newtonian fluids at *Re* = 200 and shown in **Table 5.15**. It can be seen that two grids i.e., Grid - 2 and Grid – 3 produced almost identical results. Grid – 2 chosen for all other computations of momentum study of bubble swarms in Newtonian fluids. Similarly, the grid independence study has also been carried

out for bubble swarms of holdup = 0.1 in power-law liquids of n = 0.6 at Re = 200 and shown in **Table 5.16**. In this case, Grid - 3 and Grid – 4 produced almost identical results; and thus Grid – 3 has been chosen for all other computations of momentum study of bubble swarms in power-law fluids of n = 0.8 and n = 0.6. For heat/mass transfer phenomena of swarms of contaminated bubbles, same grid as in the case of momentum transfer has been used.

5.4.2. Validation

Table 5.17: Comparison of drag of swarms of clean spherical bubbles (α = 0°) of Φ = 0.4 in Newtonian fluids.

Re	Manjunath and Chhabra (1992)	Kishore *et al*. (2008b)	Present
1	60.7	60.212	60.153
10	6.16	6.129	6.122
20	3.19	3.212	3.205
50	1.48	1.549	1.540

Table 5.18: Comparison of drag of swarms of fully contaminated bubbles (α = 180°) of Φ = 0.5 in Newtonian fluids.

Re	Jaiswal *et al*. (1991)	Dhole *et al*. (2004)	Kishore *et al*. (2006)	Present
1	911.1	919.6	910.7	910.095
10	91.22	93.39	91.68	91.532
50	18.72	21.82	20.93	20.739

Table 5.19: Comparison of average Nusselt number of fully contaminated bubble swarms of holdup = 0.2 at *Re* = 1 in Newtonian fluids.

Pe	Pfeffer (1964)	Kishore *et al.* (2007)	Present
100	7.9506	8.7719	8.4512
200	10.0171	10.8158	10.4015
500	13.5933	14.3594	13.7896
1000	17.129	17.8598	17.1428
2000	21.5812	22.2636	21.3678

The present numerical solver is solved for extreme cases of contamination i.e., clean bubble swarms and assemblages of fully contaminated bubbles at low to moderate Reynolds numbers. **Table 5.17** shows a comparison between drag coefficients of swarms of completely clean bubbles (α = 0°) of holdup 0.4 rising in a Newtonian liquid at different Reynolds numbers; and the agreement between present and literature values is excellent. Similarly, **Table 5.18** shows a comparison between present values of drag coefficients of assemblages of fully contaminated bubbles (α = 180°) in Newtonian liquids at different Reynolds numbers. Here too, the agreement between present and literature results is excellent. **Table 5.19** shows comparison of average Nusselt number of fully contaminated bubble swarms (α = 180°) of holdup = 0.2, and the agreement between present and literature values is satisfactory.

Finally, this extensive domain, grid and validation studies for variety of cases gives confidence in the accuracy and reliability of present solver. Thus, it is now safe to use present in-house and Ansys Fluent solvers to study the respective objectives as mentioned earlier of this dissertation.

In view of extensive validation shown above, the present results are believed to be reliable and accurate to within ± 2-4%.

Chapter 6

RESULTS AND DISCUSSION

6.1. Drag Behavior of Contaminated Single Bubble in Power-law Fluids

6.1.1. Using in-house solver

In order to delineate effects of surface contamination on the rise velocity of spherical bubbles, following range of conditions are considered: Reynolds number, Re = 10, 20, 50, 100, 200; power-law index, n = 0.6, 0.8, 1; and cap angle, α = 0°, 30°, 60°, 90°, 120°, 150°, 180°.

6.1.1.1. Flow Patterns

Figure 6.1 shows effect of stagnant cap angle (α) on streamline patterns (upper half) and iso-vorticity contours (lower half) around bubbles rising in Newtonian fluids (n = 1) at Re = 200. For completely clean bubbles ($\alpha = 0^o$) and slightly contaminated bubbles (α = 30°), the streamlines are symmetric fore and aft the bubble. Although at Re = 200, the convection forces dominate over viscous forces, because of mobile nature of the bubble surface, enough amount of stresses cannot be accumulated around the bubble surface to form a recirculation wake as opposed to the case of solid sphere. This behavior is consistent with the observations of Ryskin and Leal (1984) for a clean spherical bubble. Similarly, because of mobile nature of surface of the bubble, small amount of vorticity is created on its surface and is being carried away along the flow direction because of convection effect of the main flow. However, as the concentration of surfactants increases to form a stagnant cap of angle α = 60° (**Figure 6.1(c)**), a small recirculation wake is observed in the rear end of the bubble. Since one third of the mobile surface is immobile because

of surfactants presence, considerable amount of stresses are accumulated in the rear half of the bubble and a small recirculation is formed.

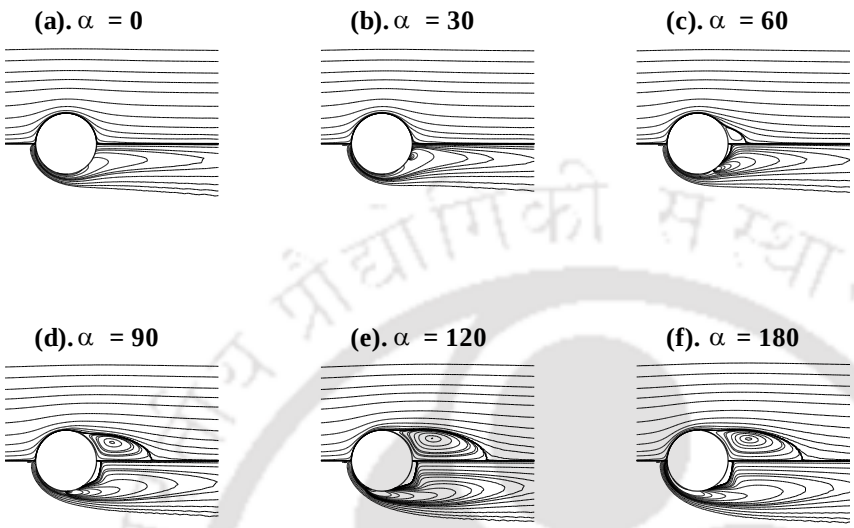

Figure 6.1: Streamline and vorticity patterns around contaminated bubbles in a Newtonian fluid (n = 1) at Re = 200.

Further increase in surfactant concentration to form bigger stagnant cap has increased the length of the recirculation wake (L_R) and eventually for fully contaminated bubble (α = 180°), a recirculation wake is formed which is equal to the case of solid sphere in Newtonian fluids at Re = 200. However, for α = 120° and α = 180°, the lengths of the recirculation wake are almost equal to each other. The reason can be the amount of mobile surface for α = 120° is small and not adequate enough to transmit the stresses through this mobile part of the surface of bubble. Further the amount of vorticity being created on the surface of the bubble also increases with increasing the stagnant cap angle. This vorticity behavior is also consistent with literature on spherical bubbles and particles in Newtonian fluids at Re = 200.

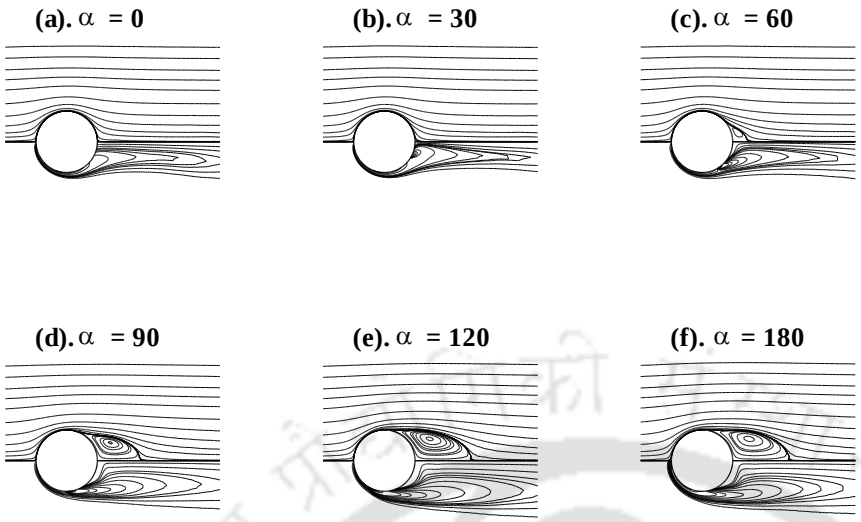

Figure 6.2: Streamline and vorticity patterns around contaminated bubbles in a shear-thinning fluid (n = 0.8) at Re = 200.

Figure 6.2 shows effect of stagnant cap angle on streamline and vorticity patterns around spherical bubbles at Re = 200 in shear-thinning fluids of power-law index n = 0.8. For a given value of the stagnant cap angle, and qualitatively similar trend can be seen as in the case of Newtonian fluids (**Figure 6.1**). However, the length of recirculation wake (L_R) and separation angle (θ_S, measured from rear stagnation point) are clearly affected by the shear-thinning nature of the surrounding fluid. The recirculation wake length decreases with a decrease in power-law index from n = 1 to n = 0.8. This behavior is consistent with numerical simulations of Dhole *et al*. (2006) for the case of power-law fluid flow past solid spheres. The reason can be attributed to the fact that as the power-law index decreases, the apparent viscosity of surrounding fluid decreases with increasing shear stress. Therefore, it is easier for the bubble to rise in shear-thinning fluids as compared to Newtonian liquids.

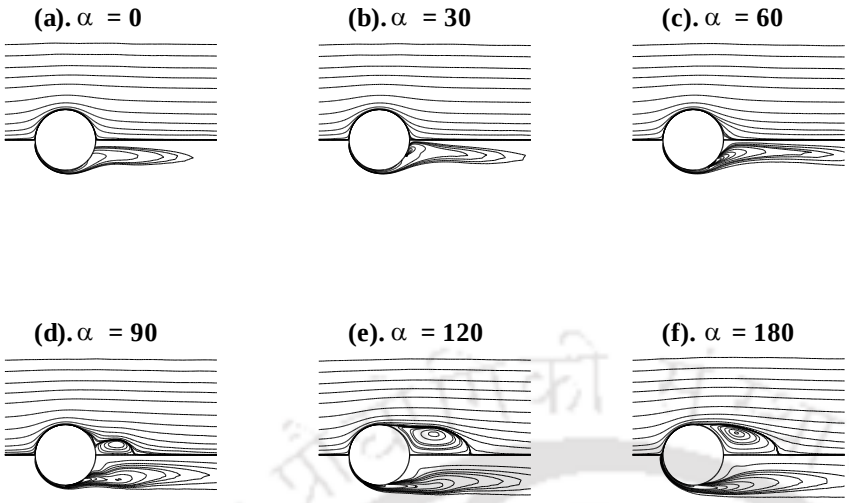

Figure 6.3: Streamline and vorticity patterns around contaminated bubbles in a shear-thinning fluid (n = 0.6) at Re = 200.

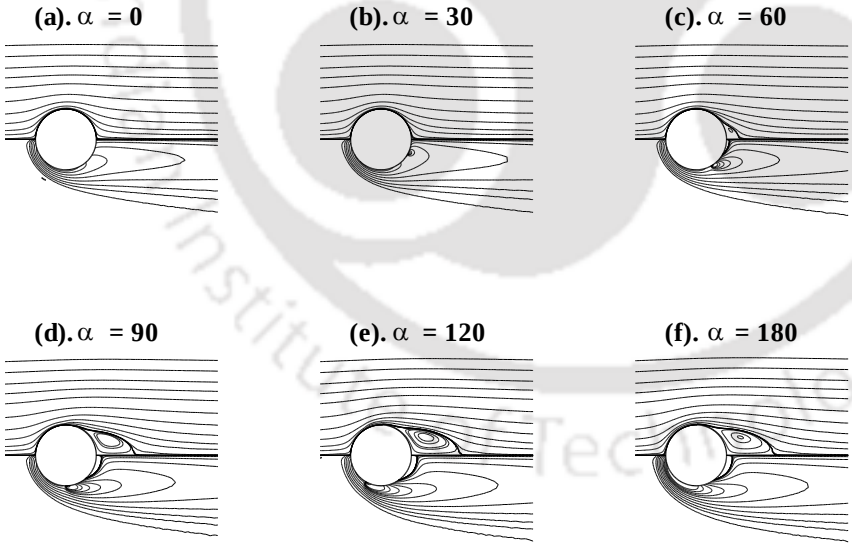

Figure 6.4: Streamline and vorticity patterns around contaminated bubbles in a Newtonian fluid (n = 1) at Re = 100.

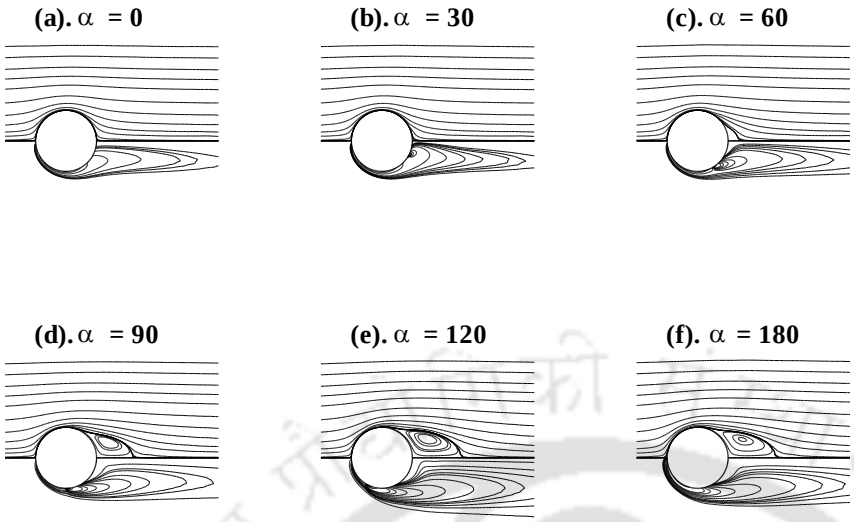

Figure 6.5: Streamline and vorticity patterns around contaminated bubbles in a shear-thinning fluid (n = 0.8) at Re = 100.

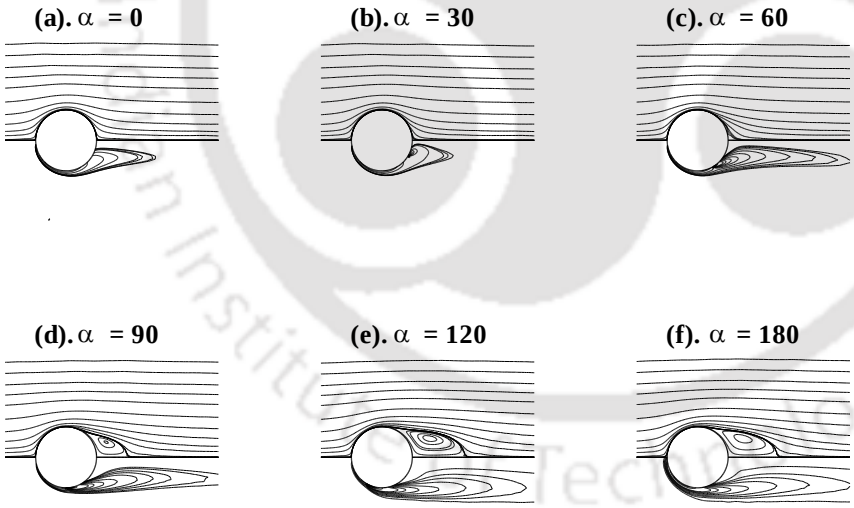

Figure 6.6: Streamline and vorticity patterns around contaminated bubbles in a shear-thinning fluid (n = 0.6) at Re = 100.

Figure 6.3 shows similar effects of stagnant cap angle and shear-thinning nature of fluid on streamlines and vorticity patterns of spherical bubbles in a shear-thinning fluid of power-law index n = 0.6 at Re = 200. **Figures 6.4-6.6** shows qualitatively similar effects of stagnant cap angle and shear-thinning viscosity nature of the fluid on streamlines and vorticity patterns around spherical bubbles at Re = 100 for n = 1 (**Figure 6.4**), for n = 0.8 (**Figure 6.5**) and for n = 0.6 (**Figure 6.6**). However, clearly because of reduction in Reynolds number, the convection forces are lowered; and thus, the lengths of recirculation wakes and angles of flow separation decrease as compared to respective counterparts when Re = 200 (**Figures 6.1-6.3**). Qualitatively similar observations on streamline and vorticity patterns are made for other combinations of the Reynolds number and the power-law index.

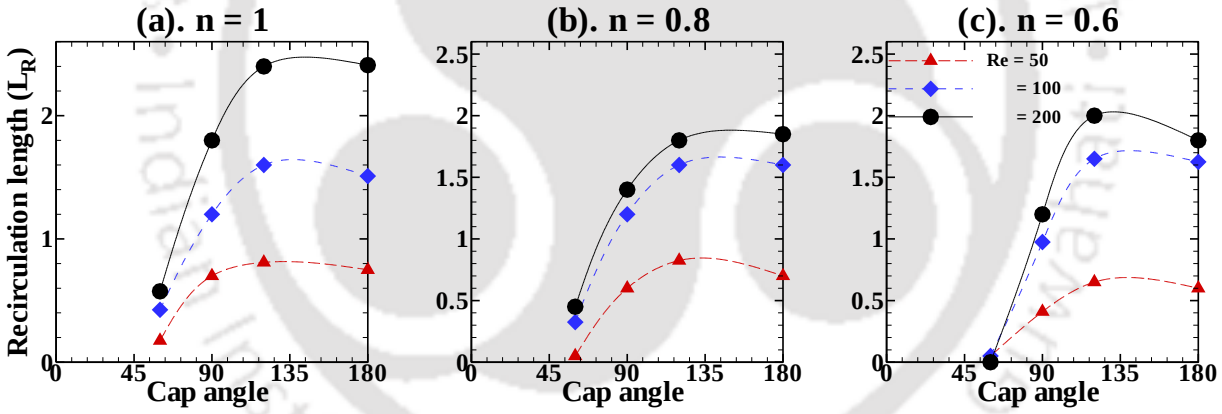

Figure 6.7: Lengths of recirculation wakes as function of the stagnant cap angle for different values of the Reynolds number and power-law index.

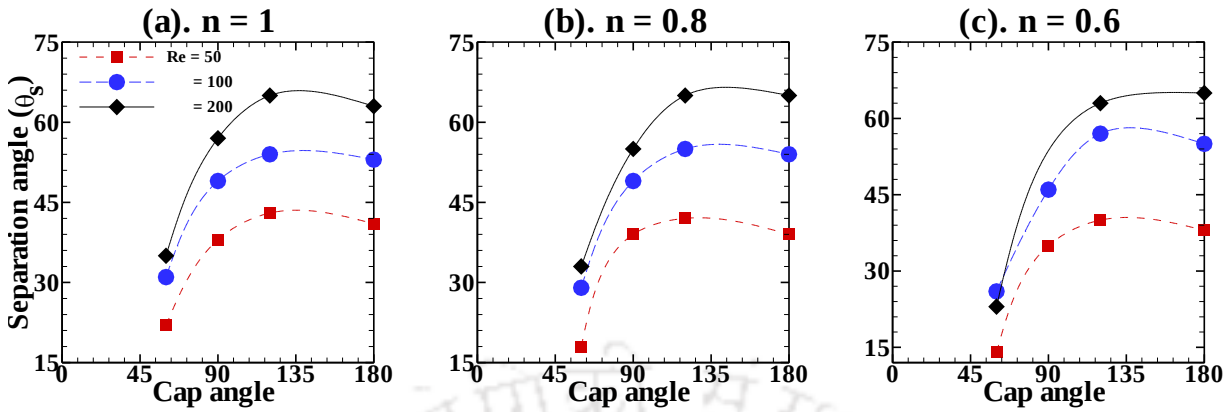

Figure 6.8: Flow separation angle as function of the stagnant cap angle for different values of the Reynolds number and power-law index.

Furthermore, the effects of shear-thinning viscosity behavior of fluid and stagnant cap angle on lengths of recirculation wakes and the angle at which flow separation occurs behind contaminated bubbles are shown in **Figures 6.7 and 6.8** for different values of the Reynolds number and the power-law index. Broadly, the length of the recirculation wake increases with increasing Reynolds number; however mixed trend is observed with respect to the power-law index and cap angle (particularly for $\alpha \geq 120°$). Further, the flow separation angle moves forward from rear end with increase in Reynolds number; and mixed trend is observed with the power-law index and cap angle.

6.1.1.2. Surface pressure distribution

Figure 6.9 shows the distribution of dimensionless pressure along the surface of contaminated bubble in Newtonian and shear-thinning fluids at *Re* = 50. Regardless of value of the power-law index, for completely clean bubbles (α = 0°) and fully contaminated bubbles (α = 180°), the pressure along the surface of the bubble decreases as one traverses from front stagnation point to

the top of the bubble (around equator), and then it increases up to the rear stagnation point because of the pressure recovery.

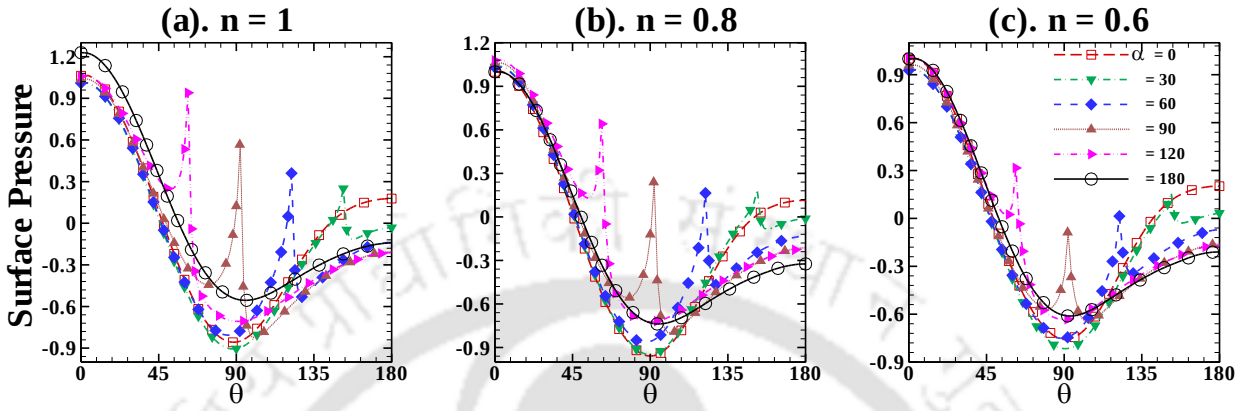

Figure 6.9: Surface pressure distribution on surface of contaminated bubbles as function of stagnant cap angle at *Re* = 50.

However, the pressure recovery is large for clean bubbles compared to fully contaminated bubbles; thus, pressure drag is low for clean bubbles. Further, for both $\alpha = 0°$ and $\alpha = 180°$, the pressure recovery in the rear half the bubble decreases with decreasing power-law index. On the other hand, for partially contaminated bubbles (i.e., for $\alpha = 30, 60, 90, 120$) settling in Newtonian liquids (**Figure 6.9(a)**), there is a discontinuity at the leading edge of the stagnant cap because of sudden change of nature of bubble surface from mobile to immobile. Because of this sudden discontinuity of the pressure, there is sudden local rise in drag coefficient compared to the case of clean bubble. Also, because of this sudden rise in pressure coefficient at the leading edge of the stagnant cap, there is sudden drop in the rise velocity of the bubble. Further, the sudden increase in the pressure at the leading edge of the stagnant cap is found to be maximum when $\alpha = 90°$; while it is small for other values of the cap angle. This observation is also consistent with literature (Fdhila and Duineveld, 1996) observations when the surrounding

liquid obeys Newtonian behavior. For the shear-thinning fluids (**Figure 6.9(b,c)**), qualitatively similar behavior is observed compared to Newtonian liquids (**Figure 6.9(a)**); however, the height of pressure rise at the leading edge of the stagnant cap decreases with decreasing power-law index. Furthermore, for a given value of the power-law index, as the value of the Reynolds number increases, for completely clean and fully contaminated bubbles the pressure recovery in the rear of the bubble increases; while for partially contaminated bubbles the sudden rise in pressure at the leading edge of the stagnant cap decreases. Qualitatively similar observations made for other combinations of the Reynolds number and power-law index.

6.1.1.3. Surface vorticity distribution

Figure 6.10 shows effect of the shear-thinning viscosity behavior and stagnant cap angle on the distribution of the vorticity along the surface of the bubble at Re = 50. For clean bubbles (α = 0°), the vorticity increases from its zero value at the front stagnation point and gradually reaches its maximum in the vicinity of the top of the bubble (around equator) and finally decreases to zero value at the rear stagnation point. There is no negative value of vorticity in the rear half of the bubble because there is no recirculation wake formation for any value of the Reynolds number of a completely clean bubble; this observation is also consistent with literature both for Newtonian (Ryskin and Leal, 1984; Fdhila and Duiveneld, 1996) and shear-thinning fluids (Dhole *et al*. 2007). On the other hand, for other extreme when the bubble is completely covered by surfactants (behaves likes solid particle), there is a recirculation wake in the rear end; and thus, the vorticity reaches negative value in the recirculation zone. This behavior is also consistent with solid sphere (α = 180°) results available in the literature for Newtonian fluids (Leal, 1989) and power-law fluids (Graham and Jones, 1994; Dhole *et al*., 2006).

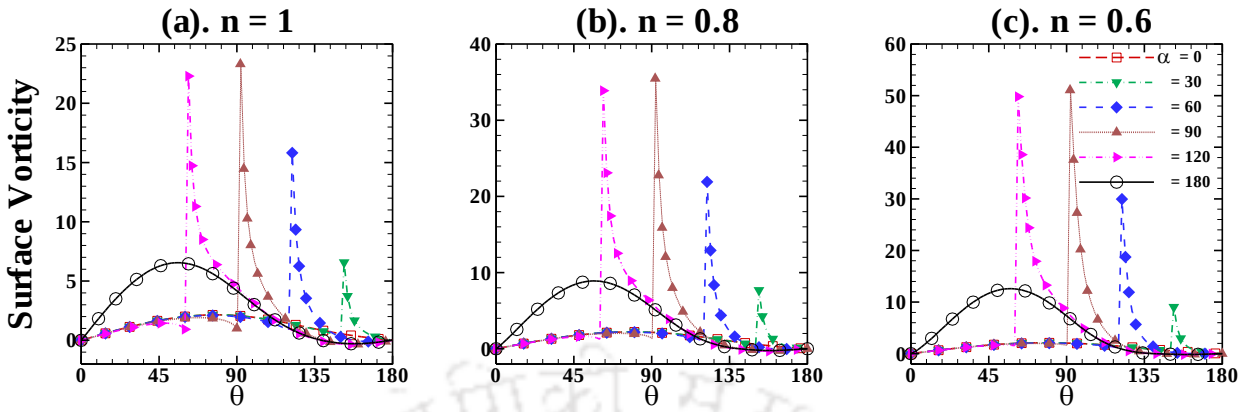

Figure 6.10: Surface vorticity distribution on surface of contaminated bubbles as function of stagnant cap angle at *Re* = 50.

For contaminated bubbles in Newtonian liquids (**Figure 6.10(a)**), the vorticity distribution follows the clean bubble vorticity curve in the upstream mobile surface until the leading edge of the stagnant cap, and then goes through a sudden rise in its value at the leading edge of the stagnant cap i.e., detaches from the vorticity curve of the clean bubble. During relaxation of vorticity in the stagnant cap immobile region, the vorticity of contaminated bubble asymptotically decreases and reattaches the vorticity curve of fully contaminated bubble (solid sphere) along the downstream immobile surface (i.e., along the stagnant cap). The sudden rise in the value of vorticity at the leading edge of the stagnant cap induces drastic decrease in the rise velocity of the contaminated bubble (Fdhila and Duiveneld, 1996). Furthermore, the rise in vorticity at the leading edge of the stagnant cap is large for α = 90° while it is low for other values of the stagnant cap angle. For shear-thinning fluids of power-law index, *n*= 0.8 (**Figure 6.10(b)**) and *n* = 0.6 (**Figure 6.10(c)**), the vorticity distributions along the surface of bubbles are qualitatively similar to the case of Newtonian fluids (**Figure 6.10 (a)**). However, the maximum value of the vorticity increases with decreasing power-law index both for a clean bubble (occurs at around equator, i.e., in the vicinity of top of the bubble); and for a fully contaminated bubble

(occurs at around $\theta \approx 45$ - 60°). Further, the maximum rise in the vorticity value at the leading edge of the stagnant cap of a contaminated bubble surface also increases with decreasing power-law index. Finally, for fixed values of the power-law index, as the value of the Reynolds number increases, the maximum value of the vorticity that clean, partially contaminated and fully contaminated bubbles could attain increases. Here too, qualitatively similar trends are observed for other combinations of the Reynolds number and power-law index.

6.1.1.4. Drag phenomena

Figure 6.11 shows effect of surface contamination on total drag coefficients of bubble against the stagnant cap angle in Newtonian and shear-thinning fluids. The characteristic C_d versus *Re* curve recovered for all values of the power-law index and stagnant cap angle. Furthermore, regardless of the value of the power-law index and Reynolds number, as the cap angle increases the total drag coefficient increases because the surface of bubble transforms from completely mobile to completely immobile as the value of cap angle gradually increases from 0° to 180°. Thus, the amount of stresses that can pass through the mobile surface of bubble gradually decreases; hence the drag coefficient gradually increases as the stagnant cap angle increases. However, for fixed values of the Reynolds number and cap angle, as the value of the power-law index decreases, the drag coefficient decreases because of decrease in apparent viscosity, hence the viscous forces decreases compared to Newtonian fluids under identical conditions. Finally, the total drag coefficients decreases with decreasing cap angle and/or with decreasing power-law index and/or with increasing Reynolds numbers.

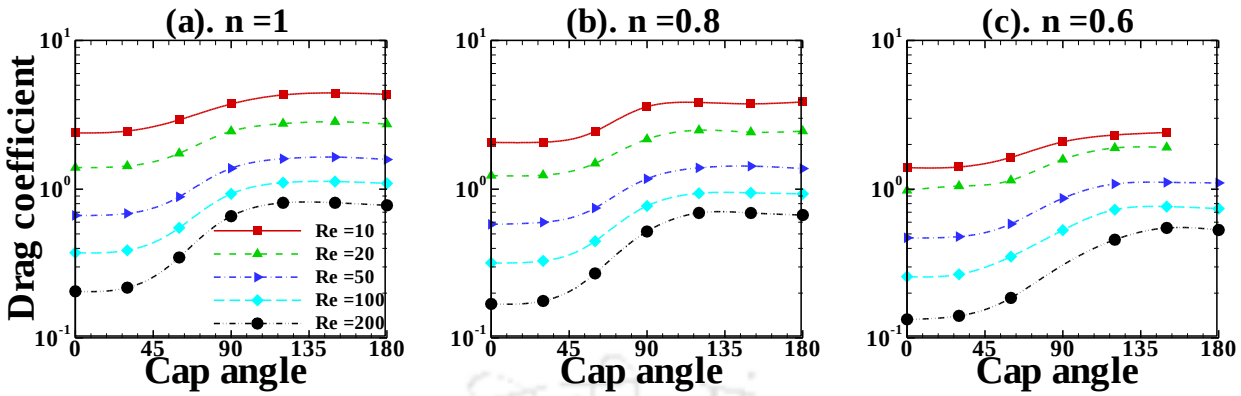

Figure 6.11: Drag coefficients of contaminated bubbles in Newtonian and shear-thinning fluids.

Figure 6.12 shows effect of surface contamination on the ratio between the pressure and friction drag coefficients (C_{dp}/C_{df}) of the bubble with respect to the stagnant cap angle in Newtonian and shear-thinning fluids. In the case of Newtonian fluids, as the cap angle increases up to 30°, the change in drag ratio is negligible and very weakly dependent on the value of the Reynolds number. Same trend is also observed for the case of shear-thinning fluids; however, the value of the drag ratio increases with decreasing power-law index. For both Newtonian and shear-thinning fluids, the drag ratio decreases for $Re \leq 20$ as the cap angle increases. However, for $Re \geq 50$, for cap angle between 60°-120°, the drag ratio increases for all fluids; and beyond 120° it decreases. The reasons are not understood at this stage for aforementioned behavior of drag ratio with respect to the Reynolds number and cap angle. For all values of the Reynolds number and the stagnant cap angle, the drag ratio increases with power-law index.

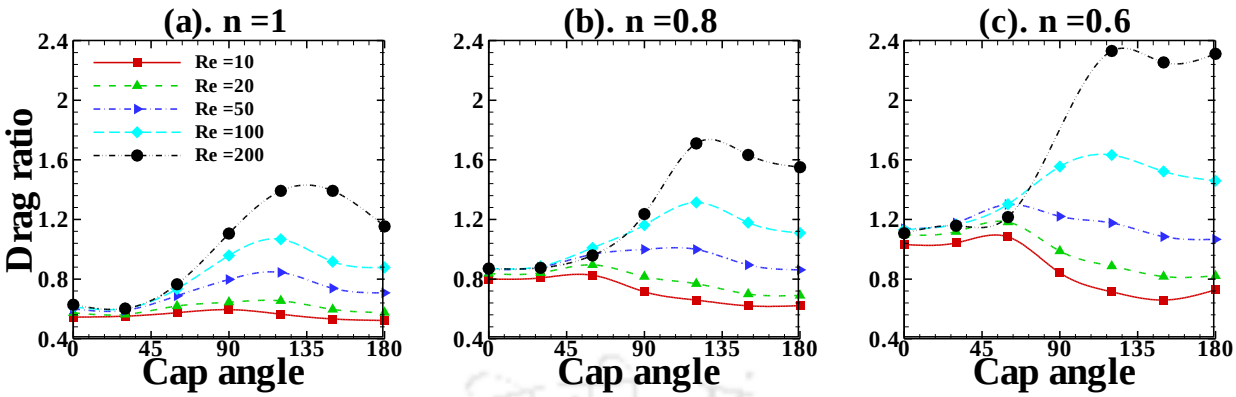

Figure 6.12: Ratio between pressure and friction drag coefficients of contaminated bubbles in Newtonian and shear-thinning fluids.

6.1.2. Drag behavior of partially contaminated single bubble using Ansys Fluent

In order to delineate effects of surface contamination on the flow and drag characteristics of the bubble. The following range of conditions are considered: *Re* = 0.1, 1, 5, 10, 20, 50, 100, 200, α = 0, 30, 60, 90, 120, 150, 180 and *n* = 0.2, 0.4, 0.6, 0.8, 1, 1.2, 1.4 and 1.6. Since the streamlines, vorticity contours, surface pressure and surface vorticity distributions are same as in the case of in-house solver; only drag behavior over extended Reynolds number and power-law indices are presented herein.

6.1.2.1. Drag phenomena

Figure 6.13 shows drag coefficients of spherical bubbles with various degrees of contamination in power-law fluids of wide range of power-law indices at *Re* = 0.1 – 200. For all values of the power-law index, the total drag coefficient is found to decrease with decreasing cap angle and with the increasing Reynolds number. For a clean bubble ($\alpha = 0^o$), because of complete mobile

surface, the stresses acting on its surface can easily transmit to the interior to decrease the drag of the bubble as compared to a fully contaminated bubble which behaves as a solid particle (α = 180°) settling under identical conditions. Thus, for partially contaminated bubbles, the drag is in between the two limits of the spherical bubble drag and that of a solid sphere. On the other hand, the C_d versus *Re* curve exhibits a crossover Reynolds number with respect to the power-law index at $Re \approx 5$. In other words, below the crossover Reynolds number, the total drag coefficient decreases with the increasing power-law index whereas the reverse is true for the Reynolds number above the crossover Reynolds number. However, this crossover Reynolds number is found to be independent of the degree of contamination. The existence of this crossover Reynolds number seems to be possible according to experimental investigation of Velez-Cordero and Zenit (2011) for clean bubbles and numerical studies for solid spheres (fully contaminated bubbles) (Tripathi *et al.* 1994). As per these studies, below this crossover Reynolds number, the C_d values of shear-thinning fluids can be larger compared to their Newtonian counterparts at lower Reynolds numbers; and reverse is true for shear-thickening fluids (Tripathi and Chhabra, 1995). In another numerical study (Dhole *et al.* 2006), drag coefficient of rigid sphere found to be smaller for shear-thickening fluids as compared to the Newtonian counterparts at $Re = 1$.

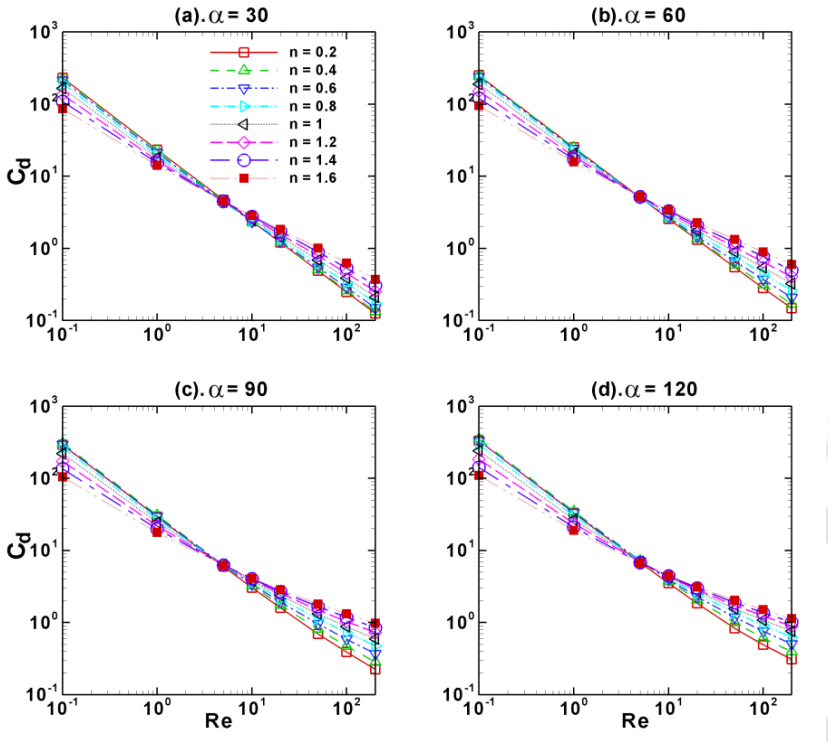

Figure 6.13: Drag coefficient of contaminated bubbles in power-law fluids.

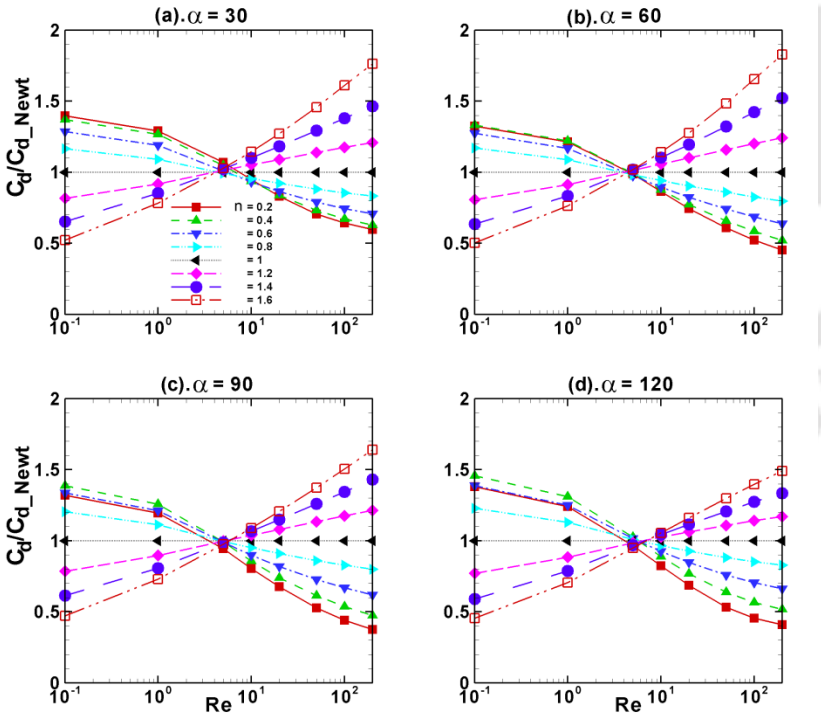

Figure 6.14: Normalized drag cofficient of partially contaminated bubbles in power-law fluids.

Figure 6.14 shows the ratio between C_d of power-law fluids and C_d of Newtonian fluids (normalized drag coefficient) as function of the Reynolds number for different values of the cap angle. The normalized drag coefficient for shear-thinning fluids ($n < 1$) decreases with increasing Reynolds number, whereas, the reverse trend is observed for shear-thickening fluids ($n > 1$). The normalized drag coefficient reaches to unity at $Re \sim 5$ for both shear-thinning and shear-thickening fluids for all cap angles which referred to as the crossover Reynolds number and it is clearly found to be independent of the cap angle. For all values of the cap angle, below this crossover Reynolds number, the normalized drag coefficient is large for a shear-thinning fluid while opposite trend is true for a shear-thickening fluid. Regardless of the values of the cap angle, above this crossover Reynolds numbers, normalized drag coefficients of shear-thickening fluids are large compared to those of Newtonian fluids whereas reverse is true for shear-thinning fluids.

6.1.2.2. Surface viscosity distribution

Figure 6.15 shows the distribution of the viscosity along the surface of contaminated bubble in different power-law fluids at $Re = 50$. For a clean bubble in shear-thinning fluids (**Figures 6.15(a)** and **6.15(b)),** i.e., for $\alpha = 0°$, the surface viscosity is minimum at front stagnation point, it gradually increases to certain maximum value at around equator of the bubble surface and then again gradually decreases to certain intermediate value at rear stagnation point. For a clean bubble in shear-thickening fluids (**Figures 6.15(c)** and **6.15(d)**), viscosity distribution is quite opposite to the case of shear-thinning fluids, i.e., the surface viscosity decreases from its finite value at front stagnation point to a minimum value at around equator of the bubble and again rises gradually to a certain value at the rear stagnation point. On the other hand, for a fully contaminated bubble in shear-thinning fluids (**Figures 6.15(a)** and **6.15(b)**), i.e., for $\alpha = 180°$,

the surface viscosity is certain large value at front stagnation point, it gradually decreases up to almost $\theta \approx 50°$ or so and then gradually increases further to a maximum value at the point of flow separation, and finally it decreases in the recirculation region before relax with a maximum value at the rear stagnation point.

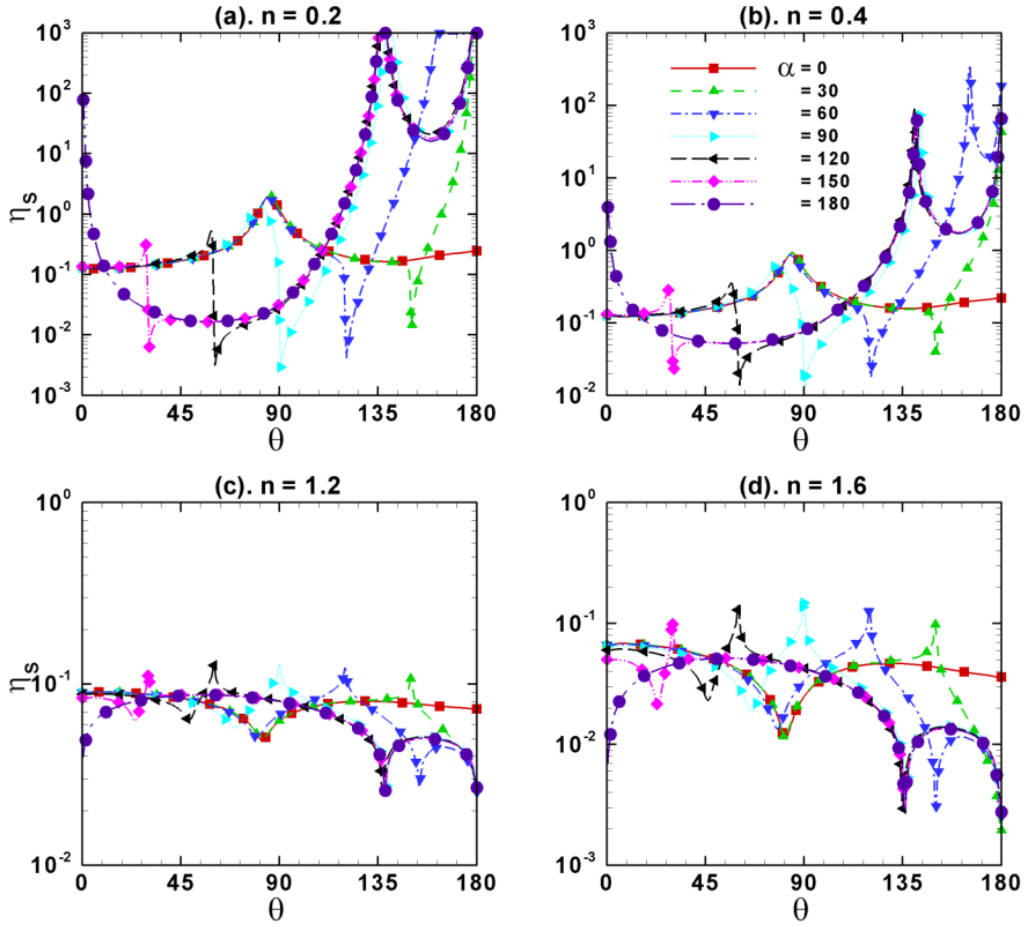

Figure 6.15: Distribution of viscosity along the surface of contaminated bubble at *Re* = 50.

For a fully contaminated bubble in shear-thickening fluids (**Figures 6.15(c)** and **6.15(d)**), opposite trends are seen as compared to shear-thinning fluids. On the other hand, for contaminated bubbles in shear-thinning fluids (**Figures 6.15(a)** and **6.15(b)**), the surface viscosity follows the surface viscosity curve of a clean bubble along the mobile portion of the

bubble, and then it drops to certain minimum value before rejoining the surface viscosity curve of solid sphere. For shear-thickening fluids (**Figures 6.15(c)** and **6.15(d)**), the trends of surface viscosity along the contaminated bubbles are followed that of clean bubble and then rejoins that of fully contaminated bubble, however, at the leading edge of stagnant cap, the surface viscosity experience sudden rise unlike sudden fall in the case of shear-thinning fluids (**Figures 6.15(a)** and **6.15(b)**).

6.2. Heat Transfer Phenomena of Unconfined Partially Contaminated Single Bubble in Power-law Fluids using Ansys Fluent

In order to delineate the effects of the Reynolds number (*Re*), the Prandtl number (*Pr*), the contamination angle (α) and the power-law index (n) on the isotherm contours and on the Nusselt numbers (*Nu*), the following ranges are considered: *Re*: 0.1, 1, 5, 10, 20, 50, 100, 200, *Pr*: 1, 10, 100, 1000, $\alpha = 0^o, 30^o, 60^o, 90^o, 120^o, 150^o, 180^o$ and n = 0.2, 0.4, 0.6, 0.8, 1.2, 1.4, 1.6.

6.2.1. Isotherm contours

Figure 6.16 shows the distribution of isotherm contours around clean and contaminated bubbles (α: 0 - 180°) in power-law fluids of n = 0.2 at *Re* = 20 (upper half) and *Re* = 200 (lower half) for *Pr* = 100. At *Re* = 20, for α = 0°, the isotherm contours are carried away in the flow direction without any distortion; and the boundary layer is moderately thin. As the value of the cap angle increases, at *Re* = 20, though there is no distortion of isotherms; however, the boundary layer has gradually increased with increasing cap angle. At *Re* = 200 and $\alpha \leq 30^o$ (**Figures 6.16(a)** and **6.16(b))**, the isotherm contours are uniform and thermal boundary layer is thinner than in the case of *Re* = 20. However, for $\alpha \geq 60^o$, the distortion of isotherm contour appeared because of the recirculation wake formation in the rear half of the bubble and this distortion of isotherm

contours increase with the increasing cap angle. Further, for fixed values of the Reynolds/Prandtl numbers and power-law index, the thermal boundary layer become thicker with the increasing cap angle and hence the rate of the heat transfer reduces with the increasing cap angle.

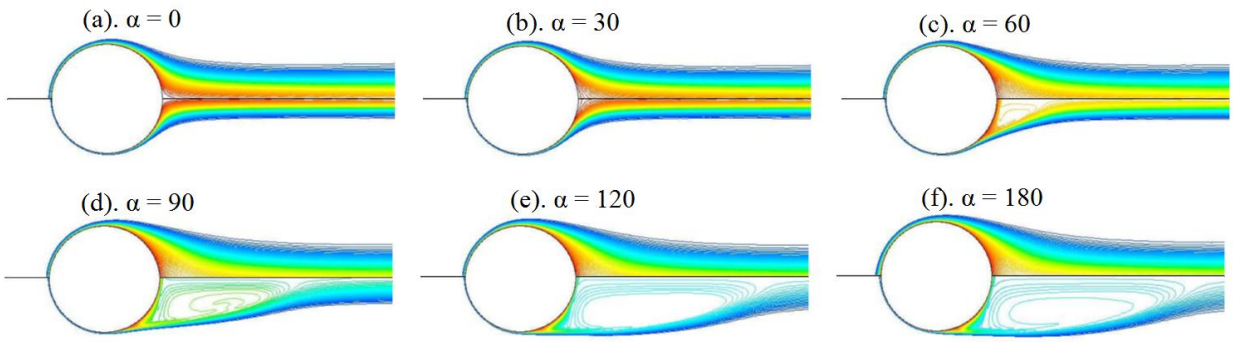

Figure 6.16: Isotherm contours around contaminated bubble for n = 0.2 at Pr = 100 with Re = 20 (upper half) and Re = 200 (lower half).

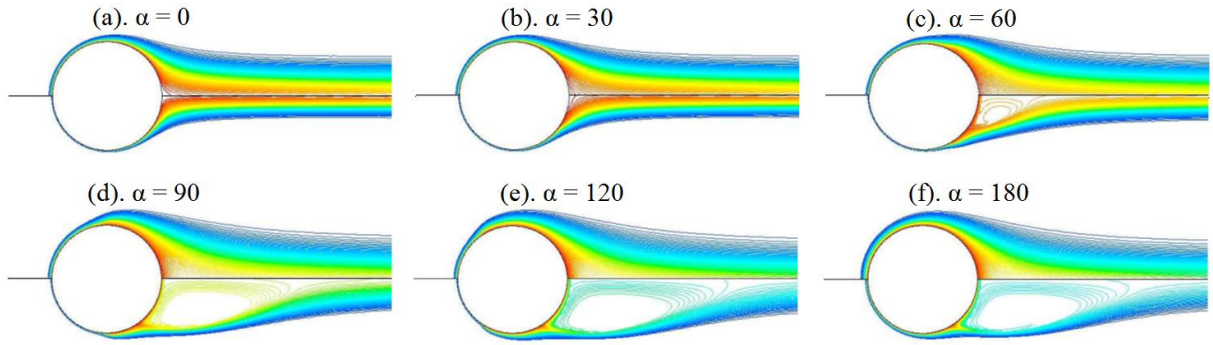

Figure 6.17: Isotherm contours around contaminated bubble for n = 1.6 at Pr = 100 with Re = 20 (upper half) and Re = 200 (lower half).

Figure 6.17 shows the distribution of isotherm contours for n = 1.6 at Re = 20 (upper half) and Re = 200 (lower half) for different values of cap angles at Pr = 100; and qualitatively similar trends has been observed as in the case of n = 0.2 (**Figure 6.16**). However, for fixed values of the Reynolds/Prandtl numbers and cap angles, the thickness of thermal boundary layer

comparatively increased for power-law fluid of n = 1.6 as compared to that of n = 0.2 and thus the heat transfer is dominant in shear-thinning fluids followed by the Newtonian and shear-thickening fluids. In other words, the rate of heat transfer from the bubble surface to the surrounding fluid increases with the decreasing power-law index (n). Furthermore, for fixed values of the cap angle and Reynolds number (Re > 20), the degree of distortion of isotherm contours decreases with the increasing power-law index. Finally, the thermal boundary layer becomes thinner with the increasing Reynolds and/or Prandtl numbers and/or with the decreasing cap angle and/or power-law index.

6.2.2. Surface Nusselt number

Figure 6.18 shows the variations of the Nusselt number along the surface of contaminated bubbles in power-law liquids of n = 0.2 (**Figures 6.18a** and **6.18b**) and n = 1.6 (**Figures 6.18c** and **6.18d**) at Re = 1 for different values of the stagnant cap angle and Prandtl number. For clean bubbles, regardless of the values of the power-law index and Prandtl number, the surface Nusselt number decreases from the front stagnation point to the rear stagnation point without any rise in the rear of the bubble. For fully contaminated bubbles, the surface Nusselt number decreases from the front stagnation point to the rear stagnation point, except for power-law fluids of n = 0.2 at Pr = 1000 (**Figure 6.18b**). In this case, the surface Nusselt number increases from front the stagnation point to around equator $\theta \sim 90^{o}$, and decreases as traversing towards the rear stagnation point. For partially contaminated bubbles, the surface Nusselt number follows the surface Nu trends of the clean bubbles as traversing from front stagnation point to leading edge of stagnant cap, and then there is a sudden decrease in surface Nusselt number at the leading edge of the stagnant cap. This reduction is strong function of the Reynolds/Prandtl numbers and the power-law index. As traversing from the leading edge of the stagnant cap to the rear

stagnation point, the surface Nusselt number of partially contaminated bubbles follows the surface Nu trends of fully contaminated bubble trends. Furthermore, for fixed values of the cap angle and Prandtl number, as the power-law index decreases, the local value of the surface Nu increases and the sudden decrease in the value of the surface Nu at the leading edge of the cap increases.

Figure 6.19 shows the variation of the Nusselt number along the surface of the contaminated bubbles in the power-law liquids of n = 0.2 (**Figures 6.19a** and **6.19b**) and n = 1.6 (**Figures 6.19c** and **6.19d**) at Re = 100. For clean bubbles, the trends are similar to the case of **Figure 6.18**; however, for fully contaminated bubbles in the power-law liquids of n = 0.2, the surface Nusselt number increases from the front stagnation point to $\theta \sim 30^{o}$, and then decreases to minimum value in the rear half of the bubble and it further increases as traversing towards the rear stagnation point (because of the formation of the recirculation wake in the rear half of the bubble), whereas no such rise in the value of the surface Nu in the front half of the contaminated bubbles is observed in the case of the power-law liquid of n = 1.6. For partially contaminated bubble, the surface Nusselt number follows the path of the clean bubbles as traversing from the front stagnation point to the leading edge of stagnant cap, and then experiences sudden reduction in the surface Nusselt number at leading edge of stagnant cap and from the leading edge of the stagnant cap, the surface Nu of contaminated bubble follows the path of fully contaminated bubbles (solid spheres). This sudden reduction in the value of the surface Nu of the contaminated bubble at the leading edge of the stagnant cap increases with the increasing Reynolds number and/or Prandtl number and/or with the decreasing power-law index.

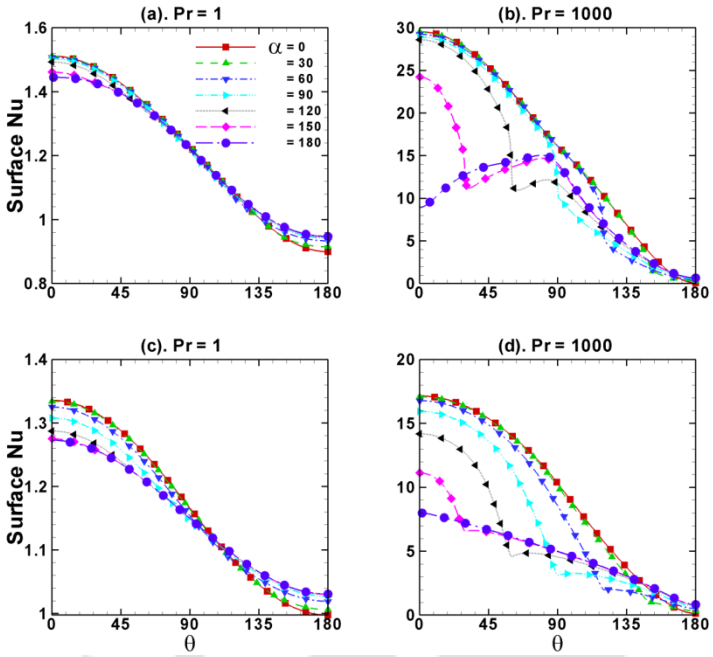

Figure 6.18: Surface Nusselt number of contaminated bubbles in power-law liquids of n = 0.2 (a-b) and n = 1.6 (c-d) at Re = 1.

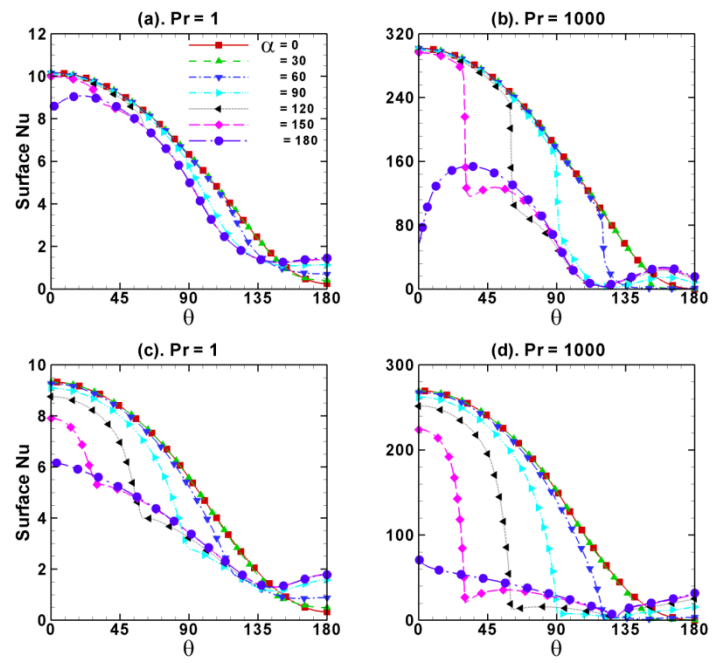

Figure 6.19: Surface Nusselt number of contaminated bubbles in power-law liquids of n = 0.2 (a-b) and n = 1.6 (c-d) at Re = 100.

6.2.3. Average Nusselt number

Figure 6.20 shows the variation of the average Nusselt numbers of contaminated spherical bubbles in power-law liquids of n = 0.2 (**Figures 6.20(a-c)**) and n = 1.6 (**Figures 6.20(d-f)**) at different values of the Reynolds numbers and the stagnant cap angles. The average Nusselt number increases with the increase in the Peclet number for all cap angles, Reynolds numbers and power-law indices. This is due to temperature wake becomes larger with the increase in Reynolds number and/or Prandtl number which leads to increase in convection. Further the average Nusselt number decreases with the increase in the cap angle for all Reynolds numbers, Peclet numbers and power-law indices. This is due to convection near the bubble surface decreases as bubble surface becomes immobile (Takemura and Yabe, 1999).

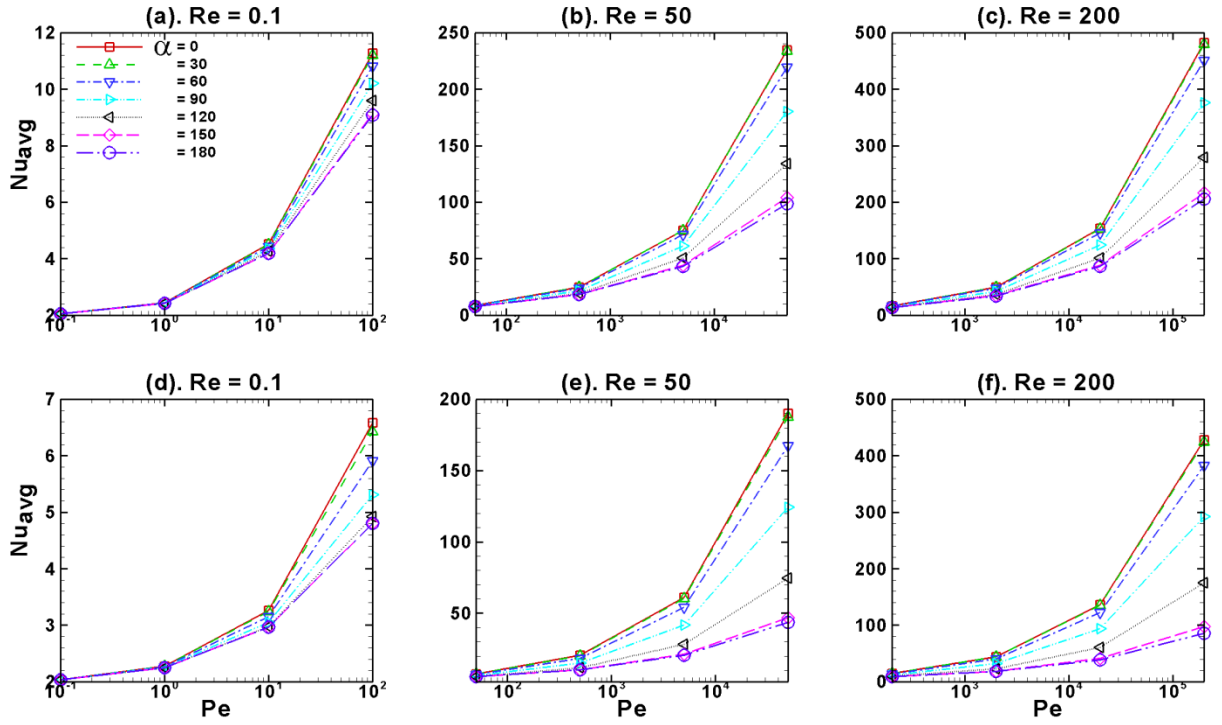

Figure 6.20: Average Nusselt number of contaminated bubbles in power-law liquids of n = 0.2 (a-c) and n = 1.6 (d-f).

The average Nusselt number increases with the decreasing power-law index for all Reynolds numbers, Peclet numbers and cap angles. As the value of power-law index (n) decreases, the apparent viscosity of the fluid around the bubble surface decreases which results in higher velocity gradients, which enhances the rate of the heat transfer and thus the average Nusselt number is higher for shear-thinning fluids followed by the Newtonian and shear-thickening fluids. Finally, regardless of values of the Reynolds/Prandtl numbers and the power-law index, as the degree of contamination increases, the rate of the heat transfer from the surface of the bubble to the surrounding power-law liquid decreases.

6.3. Wall Retardation Effect on Drag Behavior of Contaminated Spherical Bubble in Power-law Fluids

In order to delineate the combined effects of the wall retardation and power-law type non-Newtonian fluid rheology on the momentum characteristics of the partially contaminated bubbles, the following range of conditions are considered: Re: 0.1, 1, 5, 10, 20, 50, 100, 200; λ = 2, 3, 5; α = 0, 30, 60, 90, 120, 150, 180 and n = 0.2, 0.4, 0.6, 0.8, 1, 1.2, 1.4, 1.6.

6.3.1. Flow patterns

Figure 6.21 shows the streamline patterns around partially contaminated bubbles in shear-thinning (n = 0.2) **Figure 6.21 (a-d)** and shear-thickening (n = 1.6) **Figure 6.21 (e-h)** fluids with confinement λ = 2 at Re = 20 (upper half) and Re = 200 (lower half). At Re = 20, regardless of the value of the power-law index and degree of contamination, there is no recirculation wake formation at the rear of the bubble. Further the fore and aft symmetry of the streamlines around the contaminated bubbles is not maintained as in the case of small Reynolds number flow. At Re = 200, for both shear-thinning and shear-thickening fluids, a significant size of the recirculation

wake is formed for contaminated bubbles with α = 60° and the size of the recirculation wake significantly increases with the increase in the degree of contamination because of decreasing mobility of the surface. Furthermore, for all $\alpha \geq 60°$, the size of the recirculation wake increases with the decreasing power-law index.

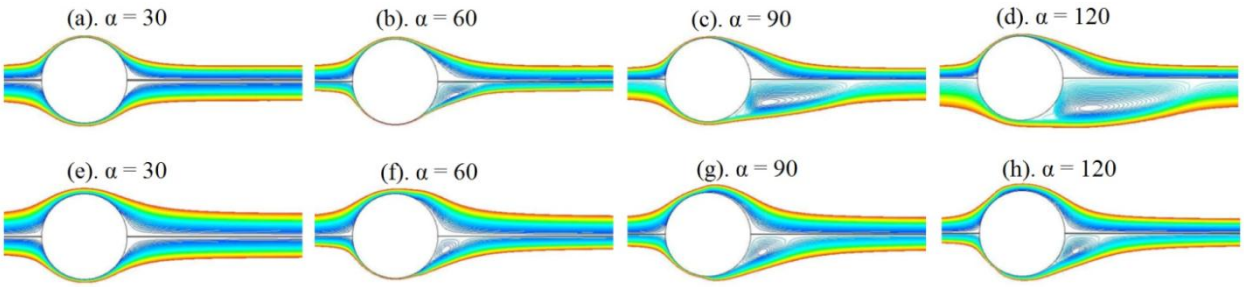

Figure 6.21: Streamline patterns around contaminated bubbles in power-law fluids of n = 0.2 (a-d) and n = 1.6 (e-h) at Re = 20 (upper half) and Re = 200 (lower half) for λ = 2.

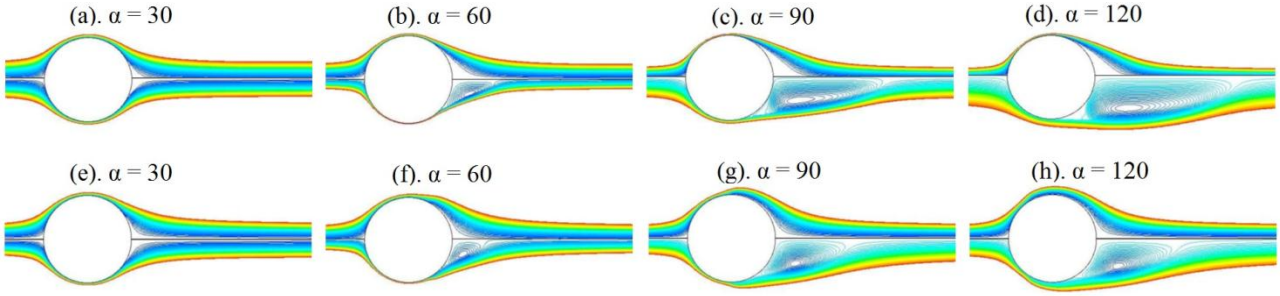

Figure 6.22: Streamline patterns around contaminated bubbles in power-law fluids of n = 0.2 (a-d) and n = 1.6 (e-h) at Re = 20 (upper half) and Re = 200 (lower half) for λ = 3.

Figures 6.22 and **6.23** shows the streamline patterns around partially contaminated bubbles in shear-thinning (n = 0.2) and shear-thickening (n = 1.6) fluids at Re = 20 (upper half) and Re = 200 (lower half) with confinement λ = 3 and λ = 5, respectively, and qualitatively similar trends are seen as in the case of λ = 2 (**Figure 6.21**). However, regardless of the values of the power-law index and the Reynolds number, with the increase in the wall factor, the size of

the recirculation wake increased because of decreasing retardation effects. Finally, the physical significance of these results indicate that the motion of contaminated bubble increases with the increasing wall factor (i.e., decreasing retardation) and/or with the decreasing power-law index and/or with the decreasing cap angle.

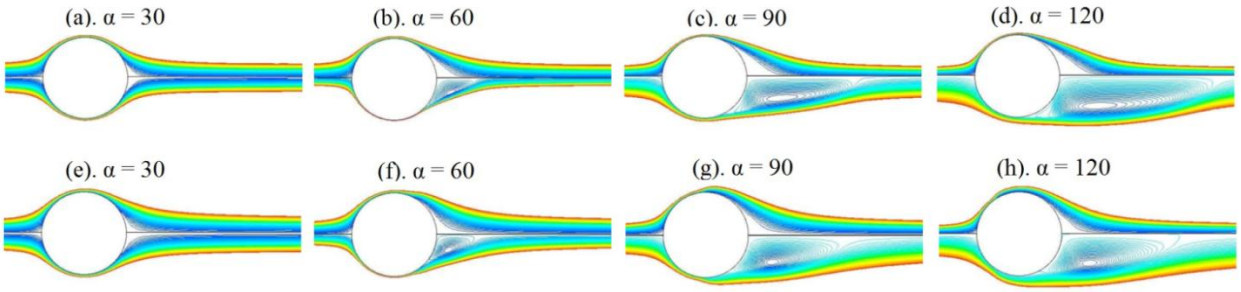

Figure 6.23: Streamline patterns around contaminated bubbles in power-law fluids of n = 0.2 (a-d) and n = 1.6 (e-h) at Re = 20 (upper half) and Re = 200 (lower half) for λ = 5.

6.3.2. Surface pressure and shear stress distribution

Figure 6.24 shows the combined effects of the cap angle, power-law index and the wall factor on the distribution of the pressure coefficient along the surface of the contaminated bubbles at Re = 50. In the case of Newtonian (n = 1) and shear-thickening fluids (n = 1.6), for all values of the cap angle and the wall factor, at the leading edge of the stagnant cap, a sudden rise in the value of the pressure coefficient is observed due to the sudden change of the bubble surface from completely mobile to fully immobile nature. However, for shear-thinning fluids (n = 0.2), for all values of the wall factor, the sudden rise in pressure coefficient at the leading edge of the stagnant cap is not observed which is contrast (in unconfined case also trend is almost similar) to the case of unconfined partially contaminated bubbles in shear-thinning fluids. For the case of unconfined contaminated bubbles in shear-thinning fluids as well such sudden rise in pressure

coefficient at the leading edge of the stagnant cap is observed. This may be ascribed to the reason that the effect of the wall retardation is very high in the case of highly shear-thinning fluids (n = 0.2) such that the wall retardation suppresses the sudden rise in the pressure at the leading edge.

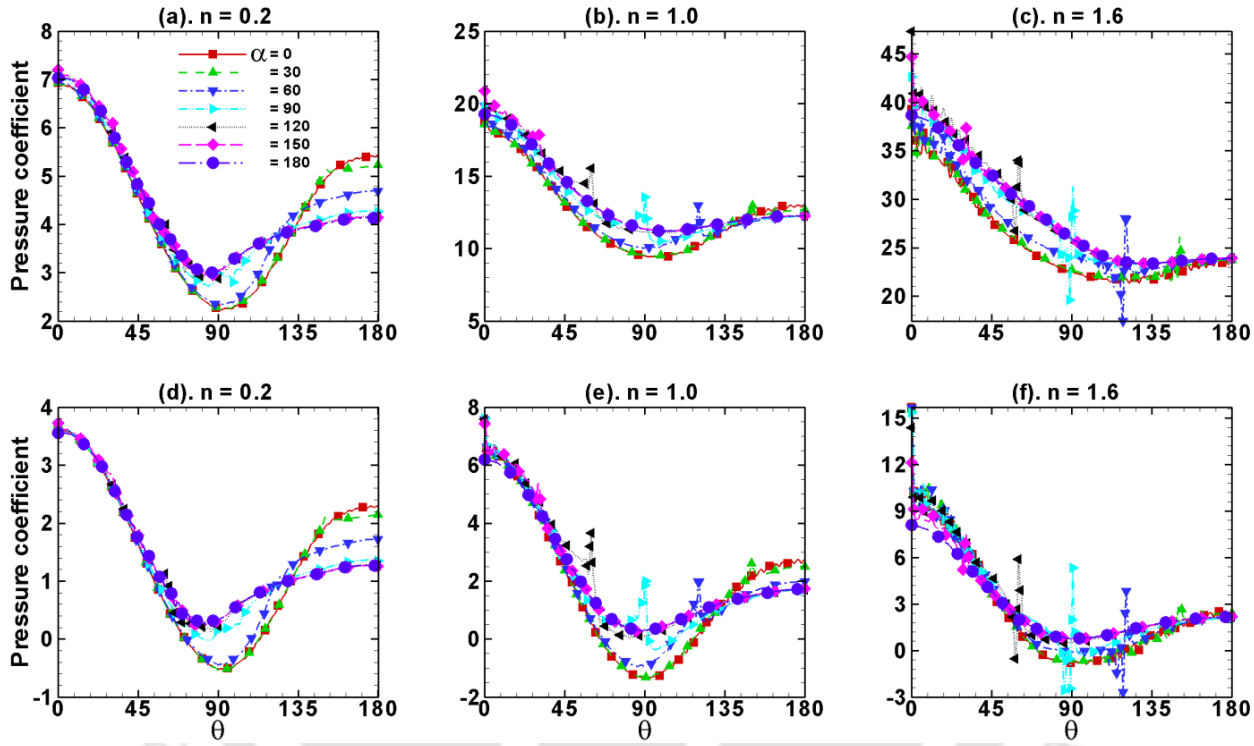

Figure 6.24: Pressure coefficient distribution along the surface of partially contaminated bubbles at Re = 50 for λ = 2 (a-c) and λ = 5 (d-f).

Figure 6.25 shows the effects of the stagnant cap angle, power-law index and the wall factor on the distribution of the shear stress along the surface of the partially contaminated bubbles confined in tubes at Re = 50. Similar to the case of unconfined partially contaminated bubbles, here too the shear stress curve for α = 0° and α = 180° follows those of clean spherical bubbles and solid spheres, respectively. For intermediate values of the stagnant cap, the shear stress curve follows that of a clean bubble up to the leading edge of the stagnant cap and follows that of a completely contaminated bubble (solid sphere) along the stagnant cap. Regardless of the

values of the power-law index and the wall factor, at the leading edge of the stagnant cap a sudden rise in the shear stress is observed. The magnitude of this sudden jump decreases with the increasing wall factor and mixed trends observed with respect to power-law index. Furthermore, for $\alpha \geq 60°$, the size of the secondary curve in the rear half of the bubble (because of the presence of the recirculation wake) increases with the increasing cap angle and/or increasing wall factor and/or decreasing power-law index.

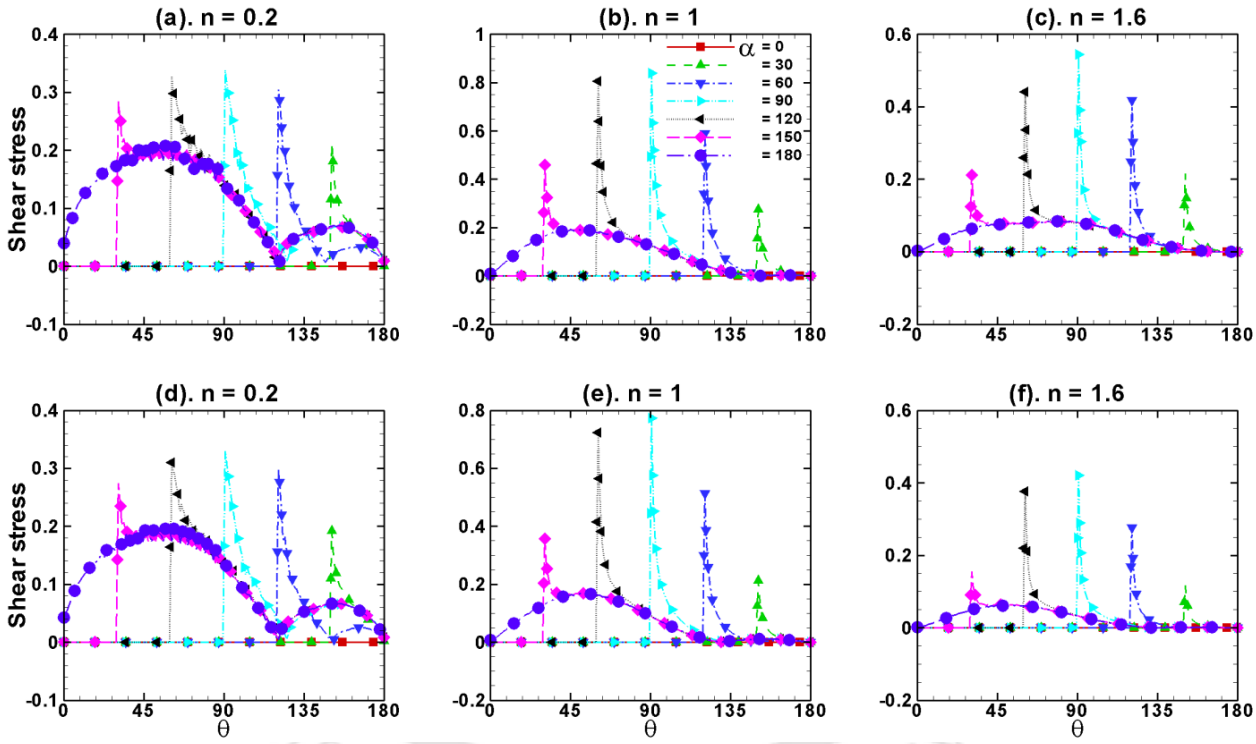

Figure 6.25: Shear stress distribution along the surface of partially contaminated bubbles at *Re* = 50 for λ = 2 (a-c) and λ = 5 (d-f).

6.3.3. Drag phenomena

Figure 6.26 shows the Reynolds number, the stagnant cap angle and the power-law index on the drag coefficients of partially contaminated bubbles for λ = 2. The characteristic drag curve, i.e.,

decreasing drag coefficient with the increasing Reynolds number, has been recovered for all values of the cap angle and the power-law index. For fixed value of the power-law index and the Reynolds number, the drag coefficient increases with the increasing stagnant cap angle because the portion of the bubble surface which becomes immobile due to contaminants increases with the cap angle. For fixed values of the cap angle and the Reynolds number, as the value of the power-law index increases, the total drag coefficient increases.

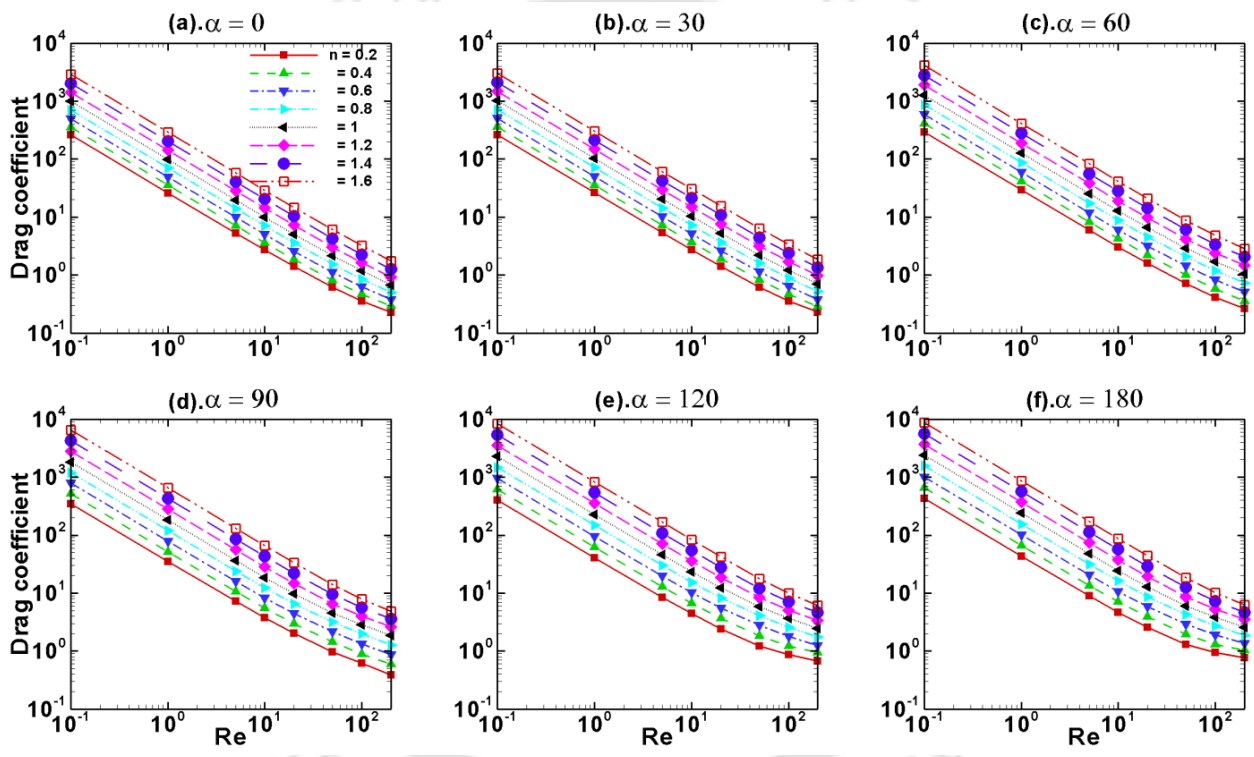

Figure 6.26: Total drag coefficients of partially contaminated bubbles in power-law fluids for λ = 2.

Figures 6.27 and **6.28** shows the qualitatively similar effects on the drag coefficients of confined contaminated bubbles for λ = 3 and λ = 5, respectively, however, with the increasing wall factor, the drag coefficient decreases because of the decreasing retardation effects. Furthermore, unlike in the case of the motion of unconfined bubble in power-law fluids,

regardless of the values of the cap angle and the wall factor, in the present case of the motion of confined bubbles there is no crossover Reynolds number in C_d versus *Re* curves with respect to the power-law index. Thus, it can be concluded that the retardation effects are much stronger than the non-Newtonian effects of the power-law fluids. The wall confinement suppresses these non-Newtonian effects and hence there is no crossover Reynolds number in the case of confined bubbles.

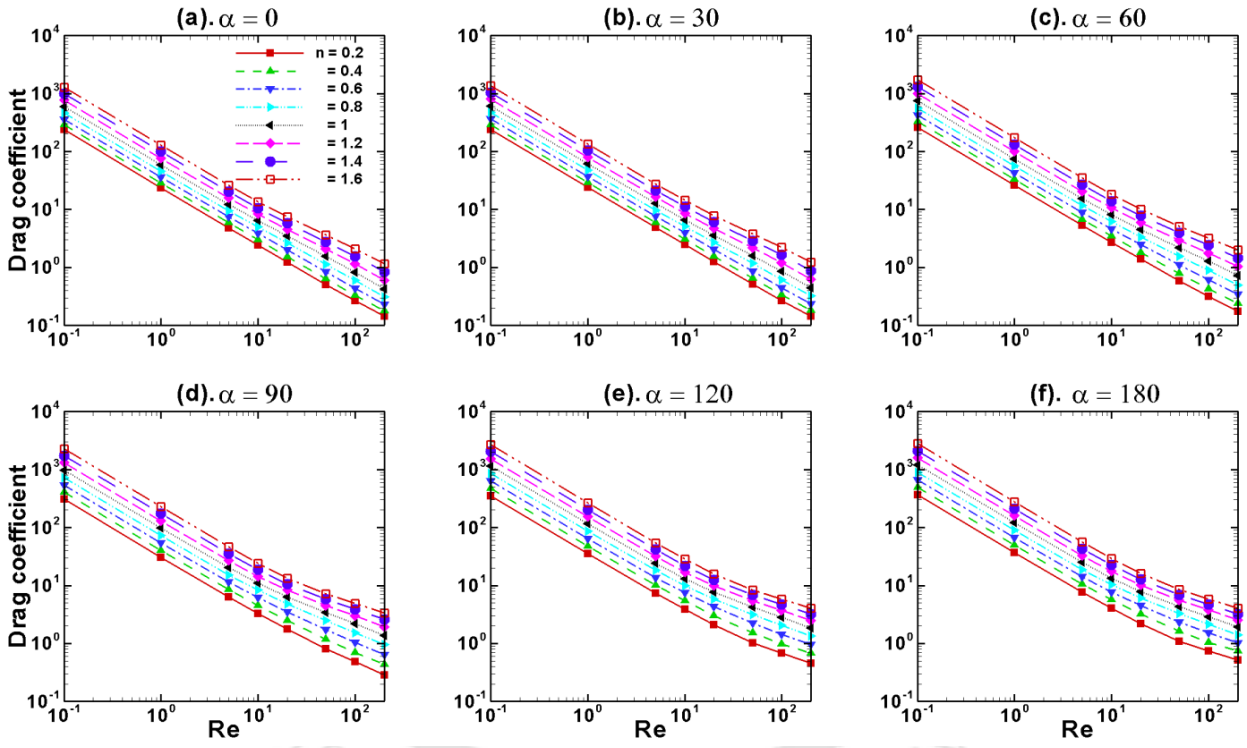

Figure 6.27: Total drag coefficients of partially contaminated bubbles in power-law fluids for λ = 3.

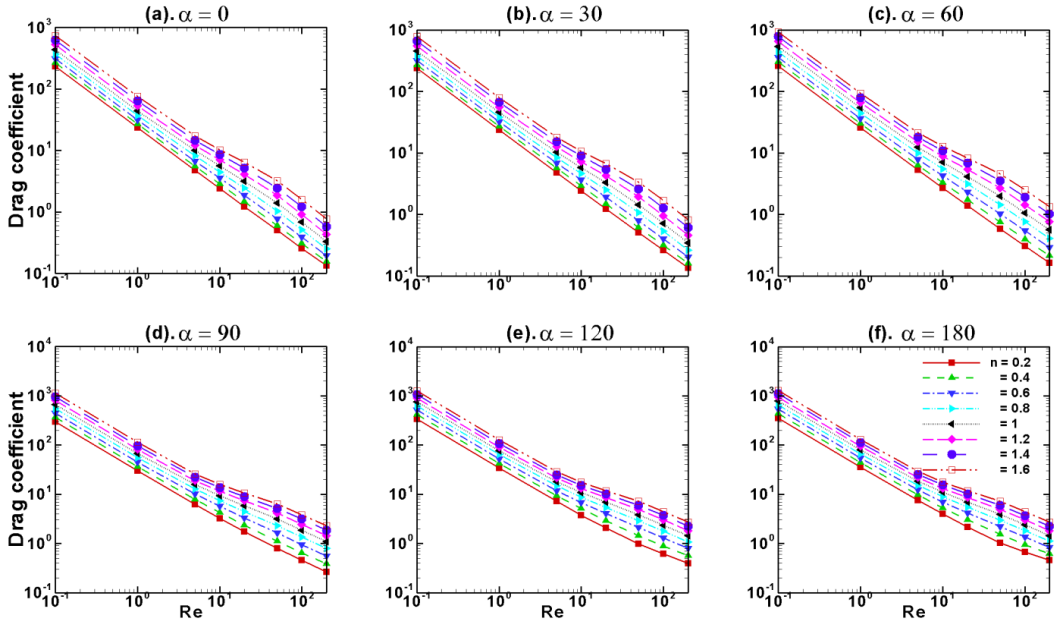

Figure 6.28: Total drag coefficients of partially contaminated bubbles in power-law fluids for λ = 5.

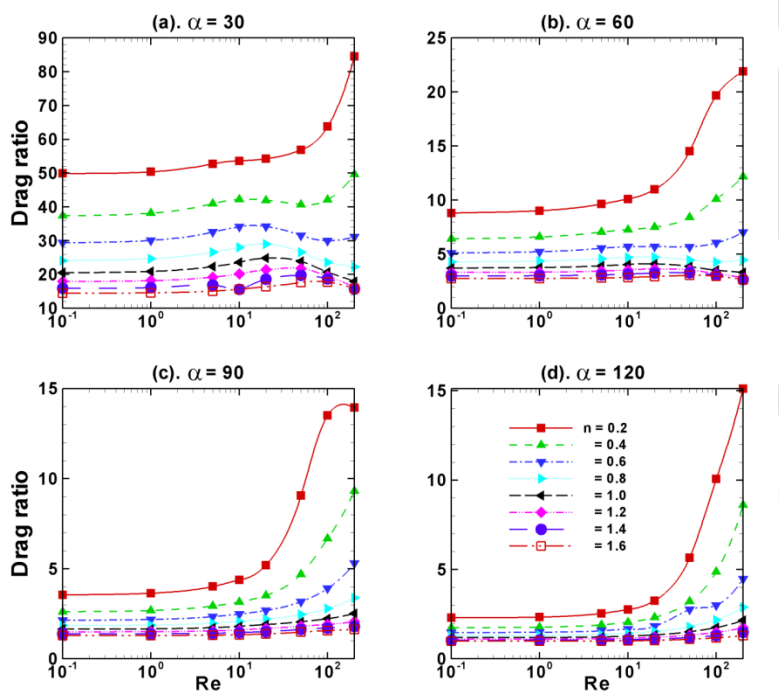

Figure 6.29: Ratio between pressure and friction drag coefficients of partially contaminated bubbles in power-law fluids for λ = 2.

Figure 6.29 shows the effects of the cap angle, Reynolds number and the power-law index on the ratio between pressure to friction drag coefficients of partially contaminated bubbles with wall factor $\lambda = 2$. Regardless of the values of the power-law index and the Reynolds number, the drag ratio decreases with the increasing cap angle because with the increasing contaminants the contribution from the friction drag coefficient increases. For all values of the Reynolds number and the cap angle, the drag ratio decreases with the increasing power-law index. For $\alpha \leq 60°$, up to $Re \approx 10$, the drag ratio is approximately independent of the Reynolds number; however, beyond $Re = 10$, a mixed trend is observed. For $\alpha > 60°$ and $Re > 10$, the drag ratio gradually increases with the increasing Reynolds number in the case of shear-thinning fluids ($n < 1$); however, for the case of shear-thickening fluids ($n > 1$), the drag ratio is more or less independent of the value of the Reynolds number.

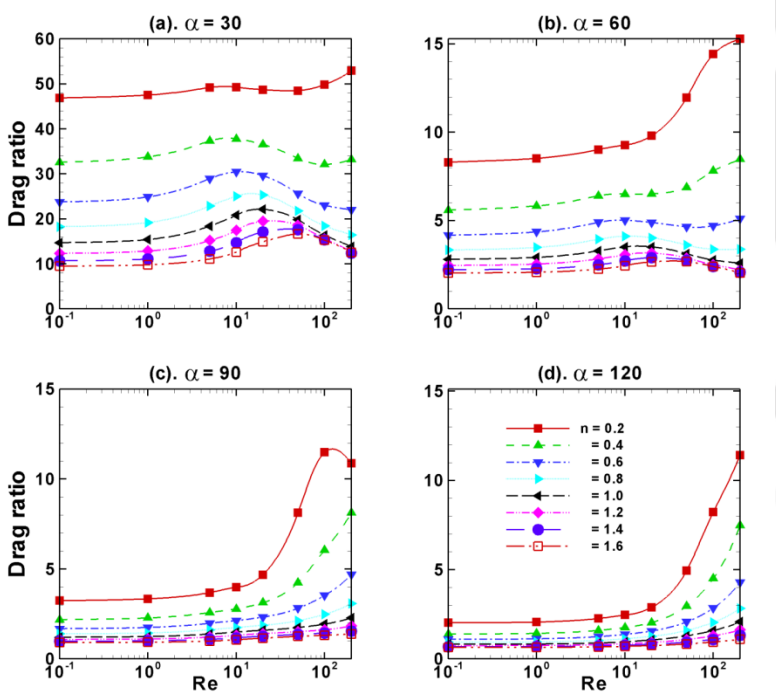

Figure 6.30: Ratio between pressure and friction drag coefficients of partially contaminated bubbles in power-law fluids for $\lambda = 3$.

Figures 6.30 and **6.31** shows the qualitatively similar trends for the case of $\lambda = 3$ and $\lambda = 5$ respectively, however, with the increasing wall factor, the drag ratio decreases for all values of the cap angle and the power-law index.

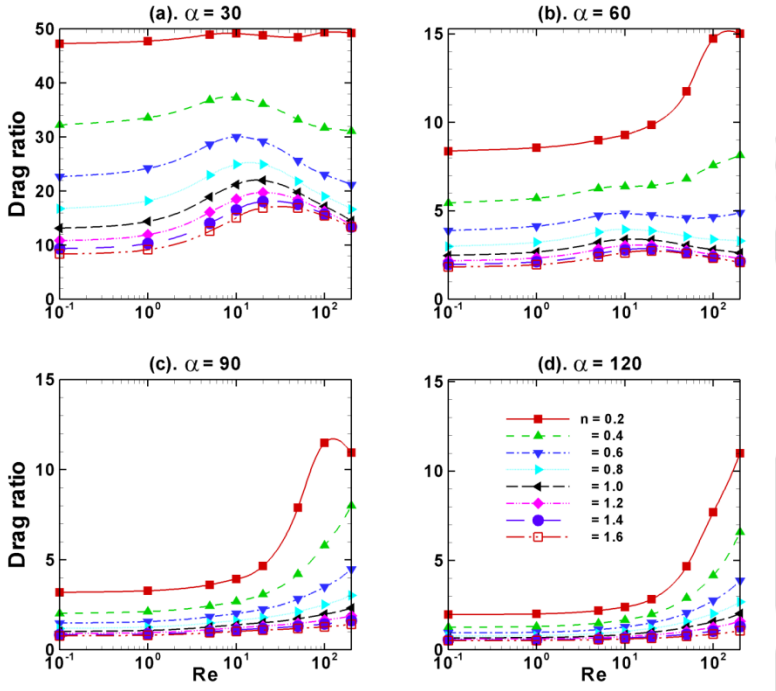

Figure 6.31: Ratio between pressure and friction drag coefficients of partially contaminated bubbles in power-law fluids for $\lambda = 5$.

6.4. Wall Retardation Effect on Heat Transfer Phenomena of Confined Contaminated Spherical Bubble in Power-law Fluids using Ansys Fluent

In order to delineate effects of the Reynolds number (*Re*), the Prandtl number (*Pr*), the wall factor (λ), the contamination angle (α) and the power-law index (n) on the isotherm contours and on the Nusselt numbers (*Nu*), the following ranges are considered: *Re*: 0.1, 1, 5, 10, 20, 50, 100, 200, *Pr*: 1, 10, 100, 1000, λ: 2, 3, 5, $\alpha = 0^o$, 30^o, 60^o, 90^o,120^o, 150^o, 180^o and n = 0.2, 0.4, 0.6, 0.8, 1.2, 1.4, 1.6.

6.4.1. Isotherm contours

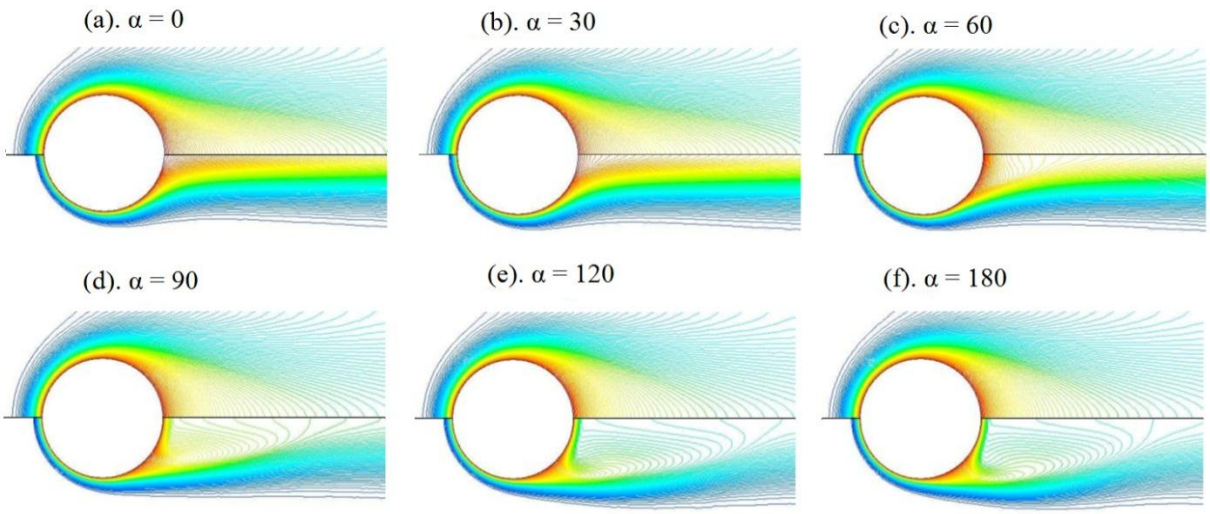

Figure 6.32: Isotherm contours around contaminated bubble for n = 0.2 at Pr = 1 with Re = 20 (upper half) and Re = 200 (lower half) for λ = 2.

Figure 6.32 shows the distribution of isotherm contours around clean and contaminated bubbles (α: 0 - 180°) in power-law fluids of n = 0.2 at Re = 20 (upper half) and Re = 200 (lower half) for Pr = 1. At Re = 20, the isotherm contours are uniformly distributed around the contaminated bubble for all cap angles. At Re = 200, for $\alpha \leq 30^{o}$, the isotherm contours are carried away in the flow direction without any distortion. For $\alpha \geq 60^{o}$, the distortion of isotherm contour appeared because of recirculation wake formation and it increases with increasing cap angle. The thermal has boundary layer become thinner with increasing Reynolds number for all cap angles. Further, thickness of thermal boundary layer increases with increasing cap angle for all Reynolds numbers. **Figures 6.33** and **6.34** shows the distribution of isotherm contours around clean and contaminated bubbles (α: 0 - 180°) in power-law fluids of n = 0.2 at Re = 20 (upper half) and Re = 200 (lower half) for Pr = 100 (**Figure 6.33**) and Pr = 1000 (**Figure 6.34**) with wall factor λ = 2. Thermal boundary layer become thinner with increasing Prandtl number for all cap angles and

Reynolds numbers. At *Re* = 200, for $\alpha \geq 60^{o}$, the distortion of isotherm contour appeared because of recirculation wake formation in the rear half of the bubble and it increases with increasing Prandtl number. Remaining all other trends are similar to **Figure 6.32**.

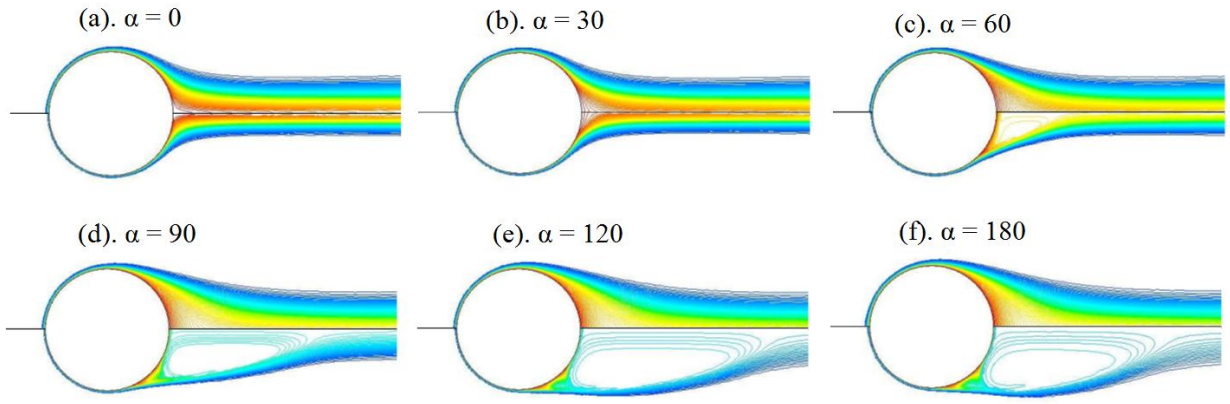

Figure 6.33: Isotherm contours around contaminated bubble for *n* = 0.2 at *Pr* = 100 with *Re* = 20 (upper half) and *Re* = 200 (lower half) for λ = 2.

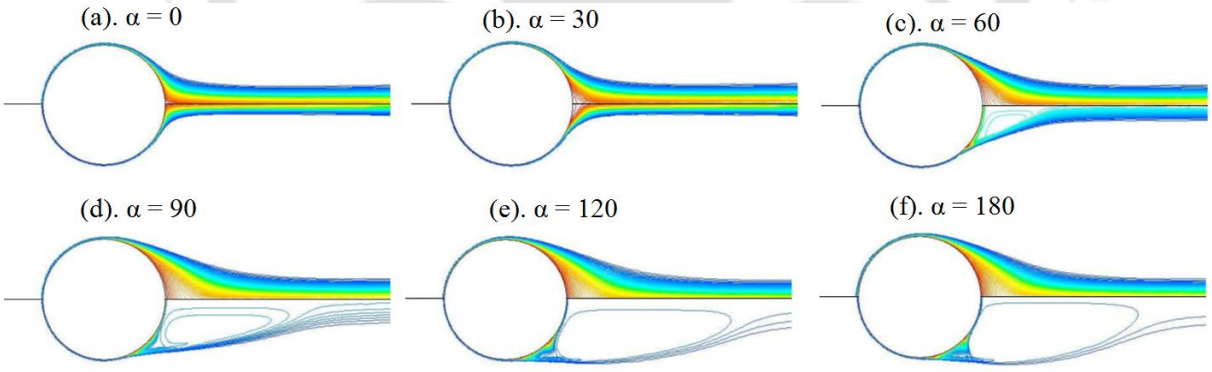

Figure 6.34: Isotherm contours around contaminated bubble for *n* = 0.2 at *Pr* = 1000 with *Re* = 20 (upper half) and *Re* = 200 (lower half) for λ = 2.

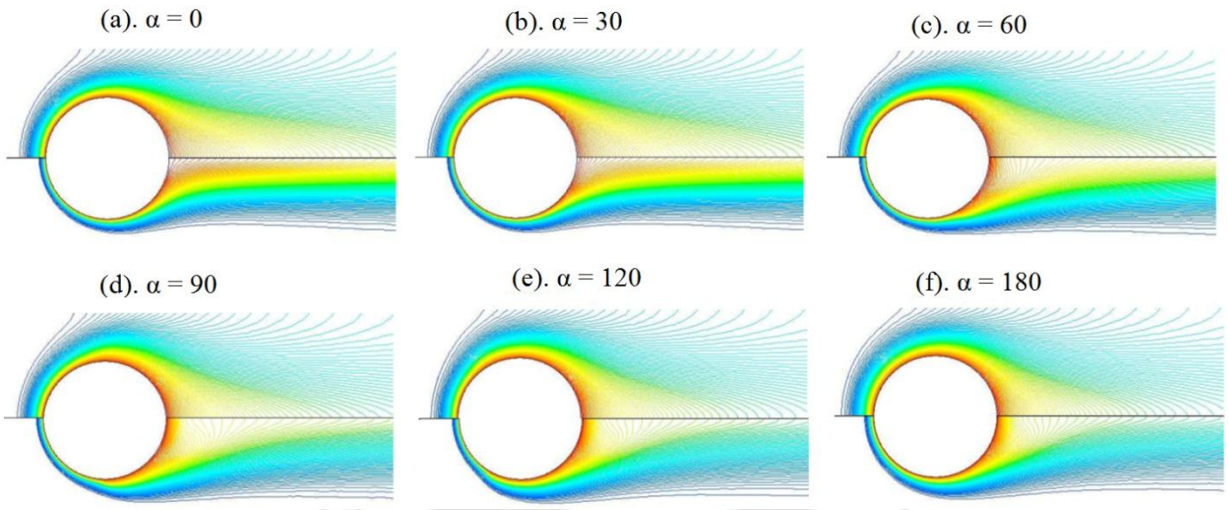

Figure 6.35: Isotherm contours around contaminated bubble for n = 1.6 at Pr = 1 with Re = 20 (upper half) and Re = 200 (lower half) for λ = 2.

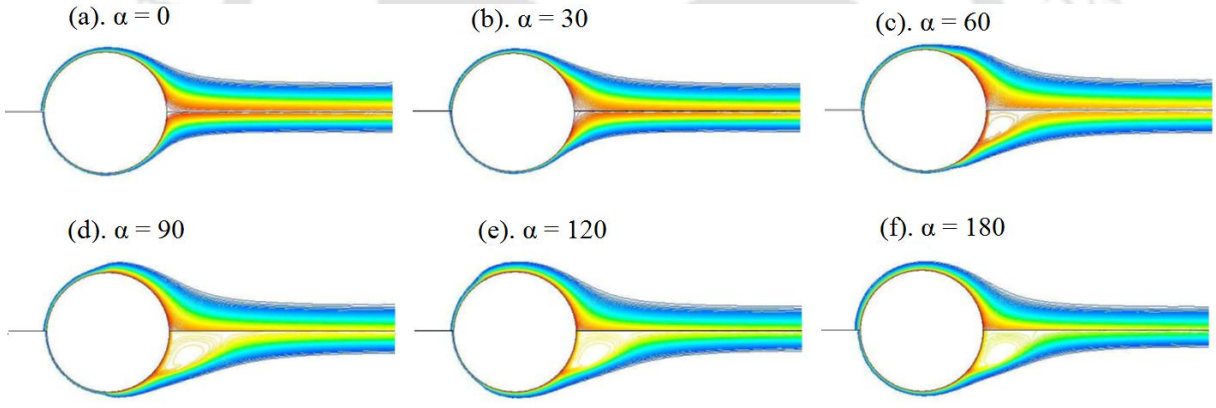

Figure 6.36: Isotherm contours around contaminated bubble for n = 1.6 at Pr = 100 with Re = 20 (upper half) and Re = 200 (lower half) for λ = 2.

Figures 6.35, 6.36 and **6.37** shows the distribution of isotherm contours around clean and contaminated bubbles (α: 0 - 180°) in power-law fluids of n = 1.6 at Re = 20 (upper half) and Re = 200 (lower half) for Pr = 1 (**Figure 6.35**), Pr = 100 (**Figure 6.36**) and Pr = 1000 (**Figure 6.37**). At Re = 20, trends are similar to **Figures 6.32, 6.33** and **6.34**. At Re = 200 for $\alpha \leq 30^{o}$, trends are similar to **Figures 6.32, 6.33** and **6.34**. For $\alpha \geq 60^{o}$, the distortion of isotherm contour

appeared because of recirculation wake formation is not intense compared to shear-thinning fluids. Remaining all other trends are similar to **Figures 6.32, 6.33** and **6.34**.

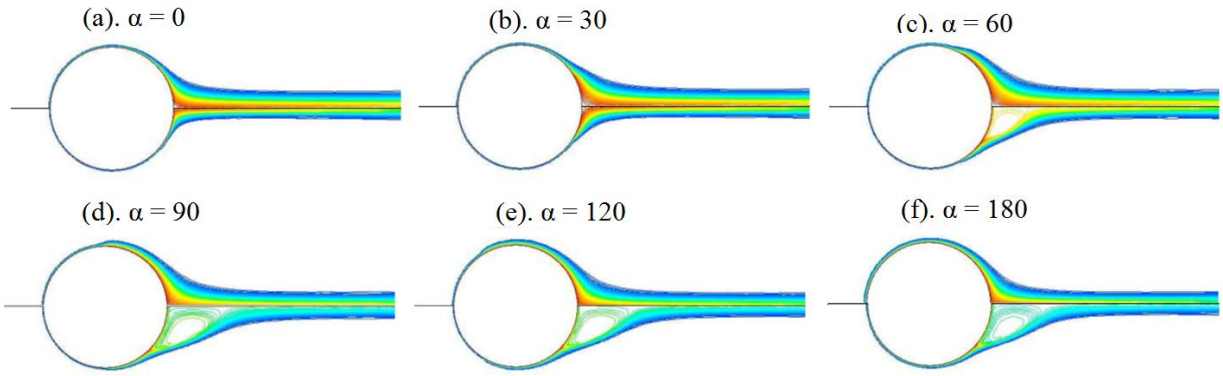

Figure 6.37: Isotherm contours around contaminated bubble for n = 1.6 at Pr = 1000 with Re = 20 (upper half) and Re = 200 (lower half) for λ = 2.

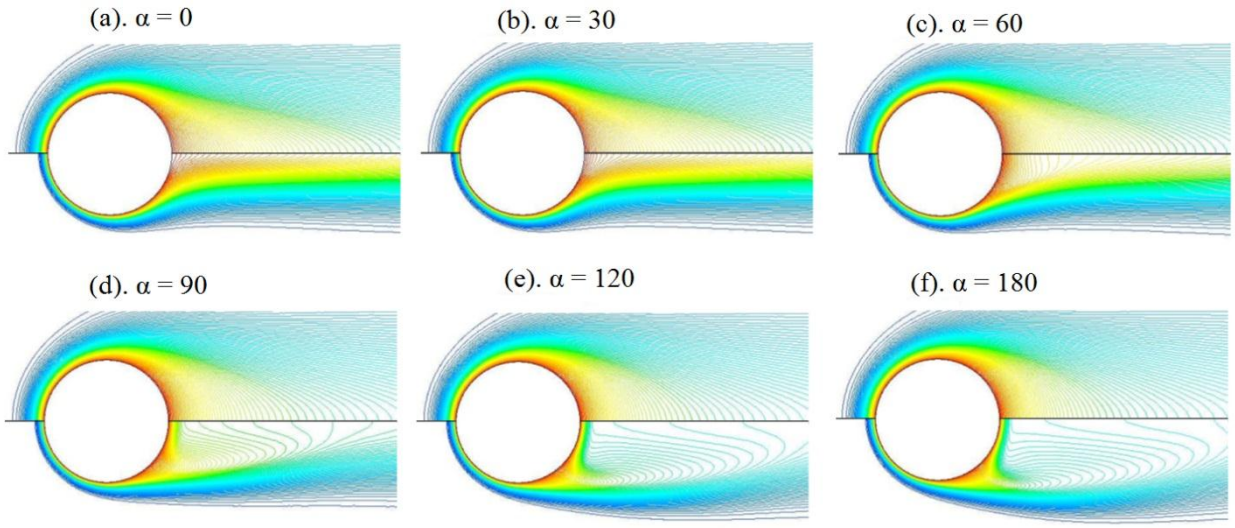

Figure 6.38: Isotherm contours around contaminated bubble for n = 0.2 at Pr = 1 with Re = 20 (upper half) and Re = 200 (lower half) for λ = 5.

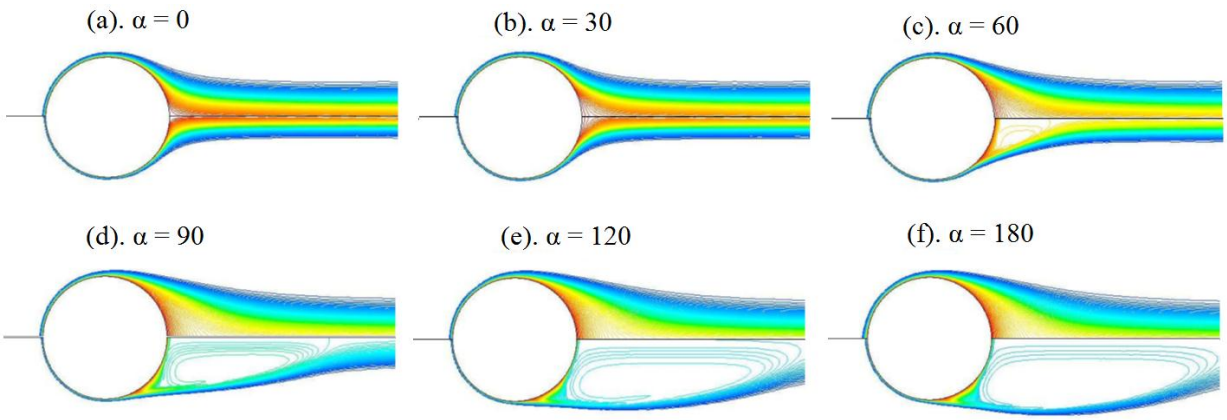

Figure 6.39: Isotherm contours around contaminated bubble for n = 0.2 at Pr = 100 with Re = 20 (upper half) and Re = 200 (lower half) for λ = 5.

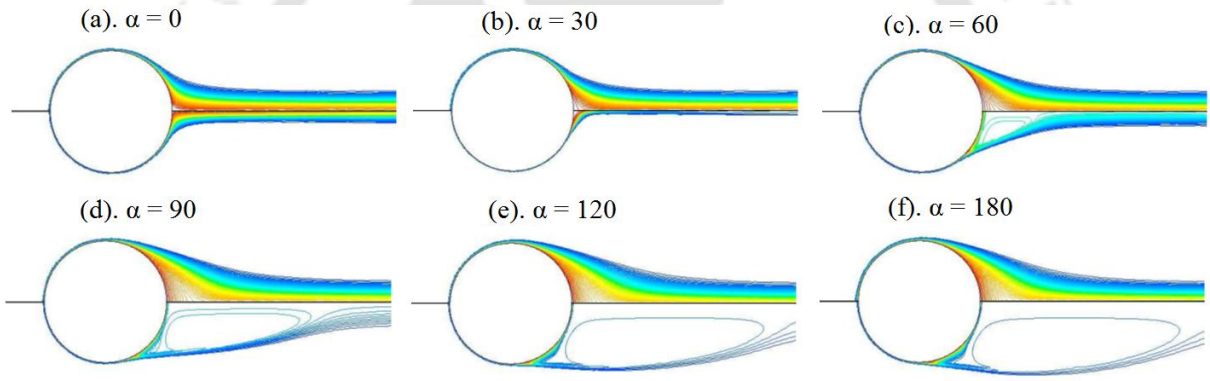

Figure 6.40: Isotherm contours around contaminated bubble for n = 0.2 at Pr = 1000 with Re = 20 (upper half) and Re = 200 (lower half) for λ = 5.

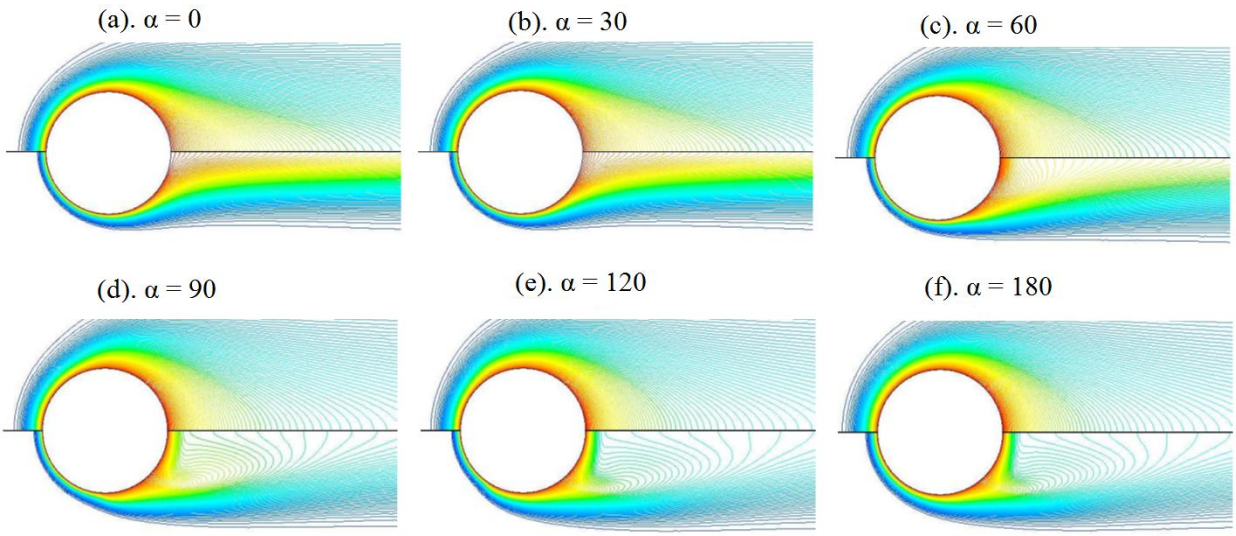

Figure 6.41: Isotherm contours around contaminated bubble for n = 1.6 at Pr = 1 with Re = 20 (upper half) and Re = 200 (lower half) for λ = 5.

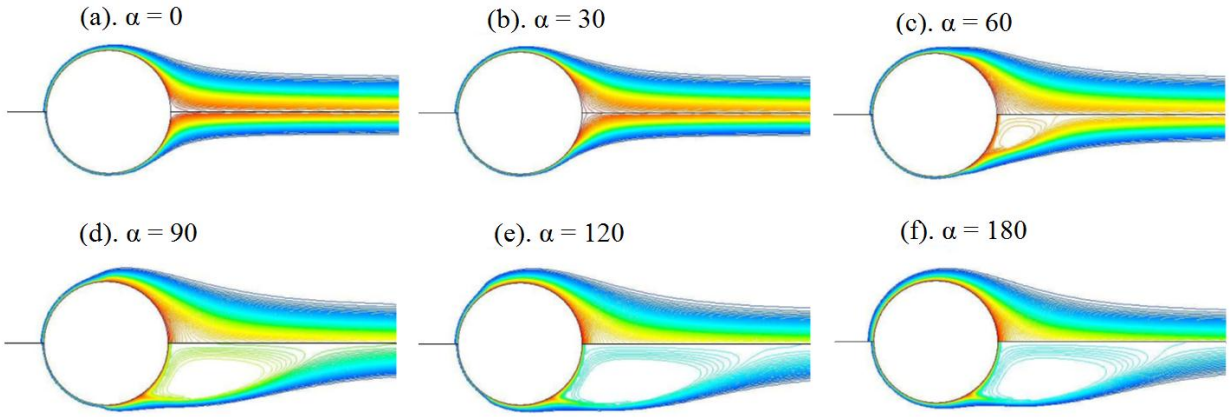

Figure 6.42: Isotherm contours around contaminated bubble for n = 1.6 at Pr = 100 with Re = 20 (upper half) and Re = 200 (lower half) for λ = 5.

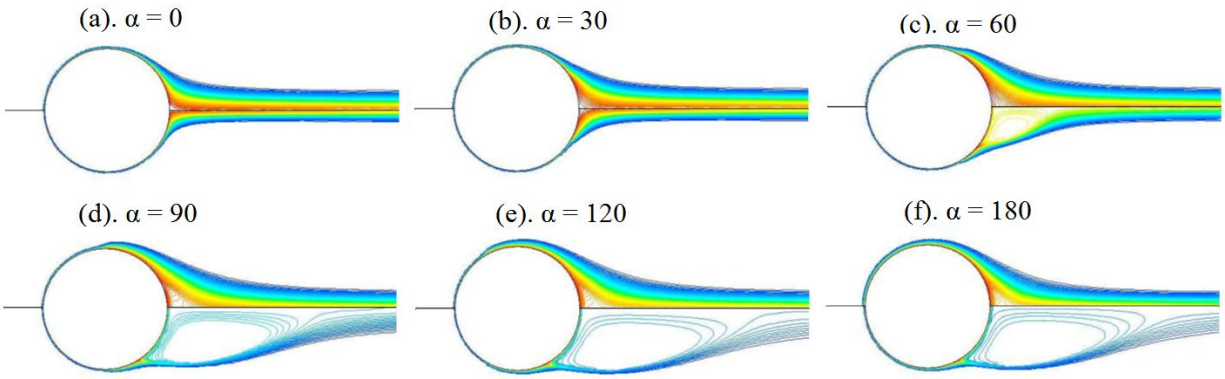

Figure 6.43: Isotherm contours around contaminated bubble for n = 1.6 at Pr = 1000 with Re = 20 (upper half) and Re = 200 (lower half) for λ = 5.

Figures 6.38-6.43 are isotherm contours for λ = 5 with Re = 20 (upper half) and Re = 200 (lower half) for Pr = 1, 100 and 1000 for power-law fluid of n = 0.2 (**Figures 6.38-6.40**) and n = 1.6 (**Figures 6.41-6.43**). Qualitatively, similar trends can be seen as in the case of λ = 2; however, for λ = 5, the boundary layer has become thicker to decrease the rate of heat transfer.

6.4.2. Average Nusselt number

Figure 6.44 shows the variation of the average Nusselt numbers of contaminated spherical bubbles in power-law liquids of n = 0.2 (**Figures 6.44(a-c)**) and n = 1.6 (**Figures 6.44(d-f)**) for λ = 2 at different values of the Reynolds numbers and the stagnant cap angles. The average Nusselt number increases with the increase in the Peclet number for all cap angles, Reynolds numbers and power-law indices. This is due to temperature wake becomes larger with the increase in Reynolds number and/or Prandtl number which leads to increase in convection. Further the average Nusselt number decreases with the increase in the cap angle for all Reynolds numbers, Peclet numbers and power-law indices. This is due to convection near the bubble surface decreases as bubble surface becomes immobile (Takemura and Yabe, 1999).

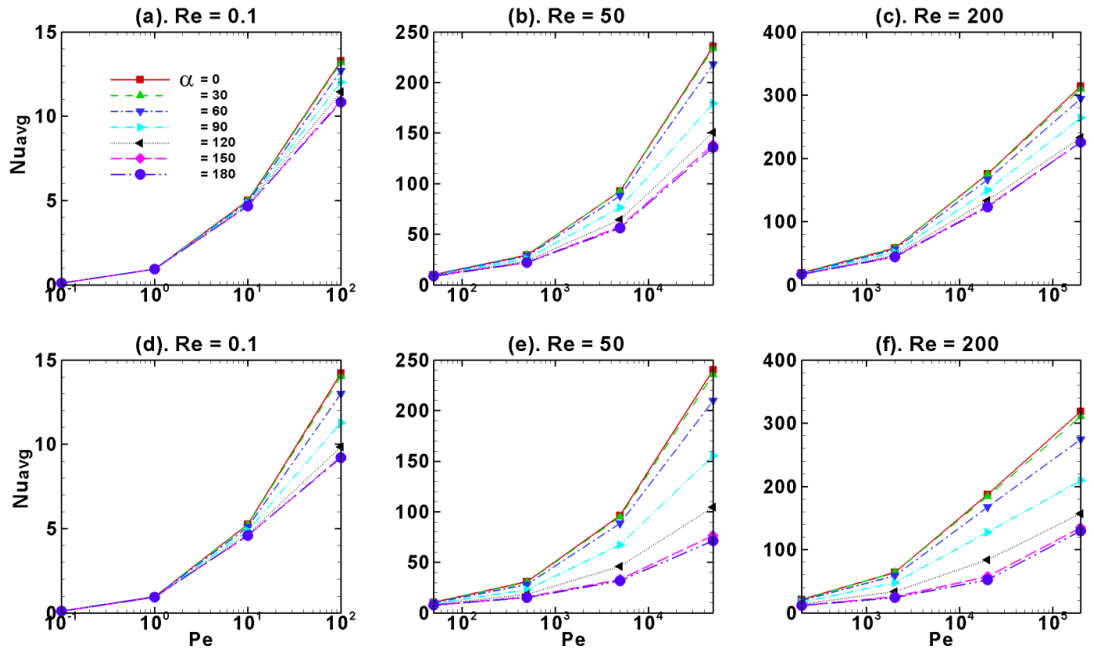

Figure 6.44: Average Nusselt number of contaminated bubbles in power-law liquids of n = 0.2 (a-c) and n = 1.6 (d-f) for λ = 2.

At lower Reynolds numbers ~ Re = 0.1 and $Pr \leq 10$, the average Nusselt number is independent of power-law indices and cap angle. For $Pr \geq 100$, average Nusselt number increases with increasing power-law indices for $\alpha \leq 60^o$ and decreases with increasing power-law indices for $\alpha \geq 90^o$. At higher Reynolds numbers ~ Re = 50, average Nusselt number increases with increasing power-law indices for all Prandtl numbers at $\alpha \leq 60^o$ and decreases with increasing power-law indices for all Prandtl numbers at $\alpha \geq 90^o$. With increasing Reynolds number further to Re = 200, trends are similar to Re = 50.

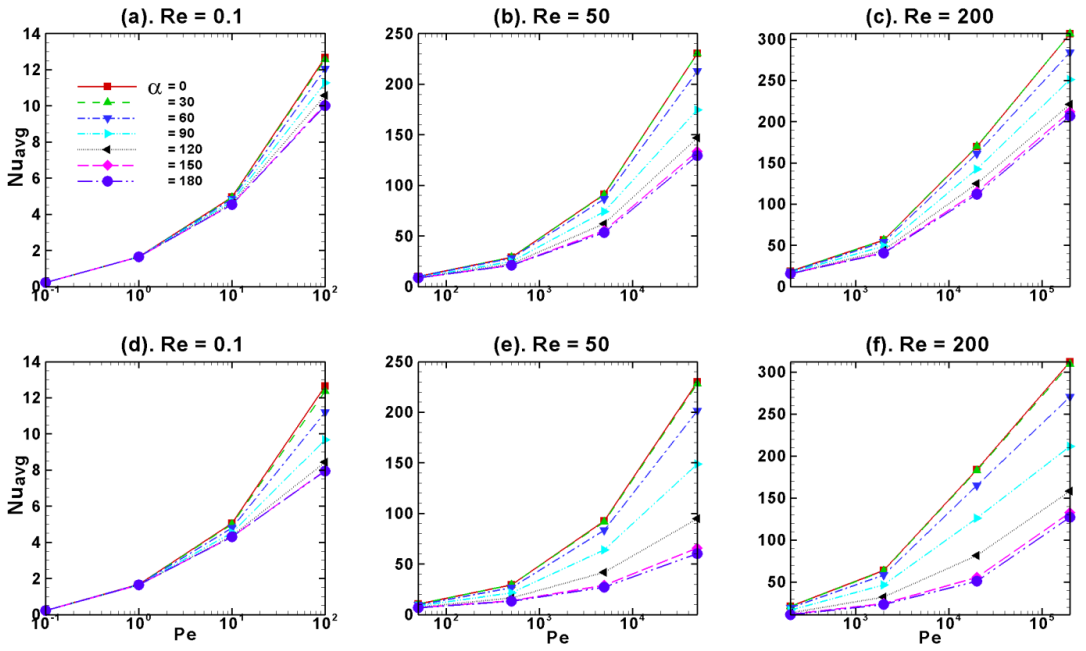

Figure 6.45: Average Nusselt number of contaminated bubbles in power-law liquids of n = 0.2 (a-c) and n = 1.6 (d-f) for λ = 3.

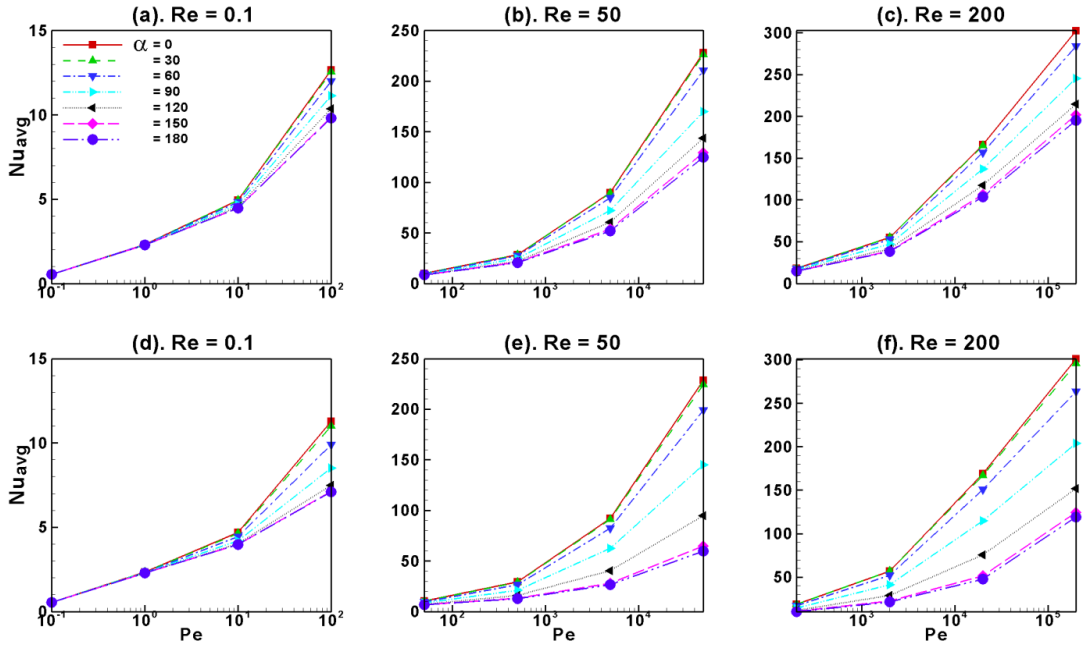

Figure 6.46: Average Nusselt number of contaminated bubbles in power-law liquids of n = 0.2 (a-c) and n = 1.6 (d-f) for λ = 5.

Figures 6.45 shows the variation of the average Nusselt numbers of contaminated spherical bubbles in power-law liquids of n = 0.2 (**Figures 6.45(a-c)**) and n = 1.6 (**Figures 6.45(d-f)**) for λ = 3 at different values of the Reynolds numbers and the stagnant cap angles. At lower Reynolds numbers ~ Re = 0.1 for $Pr \leq 10$, average Nusselt number is almost independent of power-law indices and cap angle as in the case of λ = 2. For $Pr \geq 100$, average Nusselt number decreases with increasing power-law indices for all cap angles. At higher Reynolds numbers ~ Re = 50 and for $Pr \leq 10$, average Nusselt number increases with increasing power-law indices for $\alpha \leq 60^o$ and decreases with increasing power-law indices for $\alpha \geq 90^o$. For $Pr \geq 100$, average Nusselt number decreases with increasing power-law indices for all cap angles. At Pr = 1, the average Nusselt number increases with increasing wall factor for $Re \leq 5$ and the average Nusselt number increases with decreasing wall factor for $Re \geq 10$. At $Pr \geq 10$, the average Nusselt number increases with increasing wall factor for $Re \leq 0.1$ and the average Nusselt number increases with decreasing wall factor for $Re \geq 1$. That means the increase in the average Nusselt number with increasing wall retardation will occur at moderate Reynolds and Prandtl numbers only (Song *et al.*, 2010). Remaining all other trends is similar to **Figure 6.44**. **Figures 6.46** shows the variation of the average Nusselt numbers of contaminated spherical bubbles in power-law liquids of n = 0.2 (**Figures 6.46(a-c)**) and n = 1.6 (**Figures 6.46(d-f)**) for λ = 5 at different values of the Reynolds numbers and the stagnant cap angles. Qualitatively, all trends are similar to **Figure 6.45**. The average Nusselt number increases with increasing Peclet numbers and/or decreasing cap angle. The average Nusselt number increases with increasing wall retardation at moderate Reynolds and Prandtl numbers. Mixed trends observed with respect to power-law indices for different Reynolds numbers, Prandtl numbers and cap angles.

6.5. Drag Behavior of Contaminated Bubble Swarms in Newtonian and Power-law Fluids

In order to delineate effects of the pertinent dimensionless parameters on hydrodynamics of bubble swarms in contaminated power-law fluids, following range of conditions are considered: the Reynolds numbers, *Re*: 1, 10, 20, 50, 100, 200; the bubble holdup, Φ = 0.1, 0.2, 0.3, 0.4, 0.5; power-law indices, *n*: 0.6, 0.8, 1 and the stagnant cap angle, α = 0°, 30°, 60°, 90°, 120°, 150°, 180°. However, before presenting new results, it is customary to validate the accuracy and reliability of the present numerical solver.

6.5.1. Flow patterns

Figure 6.47 shows the effects of the surface contamination on streamlines (upper half) and iso-vorticity contours (lower half) around contaminated bubble swarms with holdup 0.1 at *Re* = 50 in Newtonian fluids. Though at *Re* = 50, the convection effects are significant, because of the mobile nature of clean and moderately contaminated bubbles maintain fore and aft symmetry of streamlines. Thus, for $\alpha \leq 30°$, the streamlines around the target bubble are symmetric and there is no wake formation. However, for α = 60°, a small wake has appeared at the rear of the bubble surface which increases with the increasing stagnant cap angle. Furthermore, because of the mobile nature of the bubble surface, only moderate amount of vorticity is created around the bubble surface which is carried away along the flow direction. The amount of vorticity created increases with the increasing cap angle. The wake formation for $\alpha \geq 60°$ is mainly due to two reasons: firstly when the Reynolds number is *Re* = 50, the fluid inertia is significant which leads to the formation of a wake; secondly, when the major portion of the bubble surface becomes stagnant, only small amount of stresses can be transmitted through the remaining small mobile

portion of the surface which eventually causes the accumulation of vorticity at the rear end. Thus the size of the recirculation wake increases with the increasing contamination angle. **Figure 6.48** shows the streamlines and iso-vorticity contours for the bubble swarm of holdup = 0.5 at *Re* = 50 in Newtonian fluids and the trends are qualitatively similar to the case of very dilute system of bubble holdup 0.1 as seen in **Figure 6.47**. Qualitatively similar trends seen as in **Figure 6.47** but only variation observed is wake length suppressed with increasing holdup. **Figures 6.49** and **6.50** shows the streamlines and isotherm contours around contaminated bubble swarms of holdup = 0.1 and holdup = 0.5, respectively, in power-law fluid of *n* = 0.6. Here too qualitatively similar trends seen as in **Figures 6.47** and **6.48**, but the wake length increased with decreasing power-law indices. Qualitatively similar trends observed for other combinations of the Reynolds number, bubble holdup, power-law indices and contamination angle; hence are not repeated.

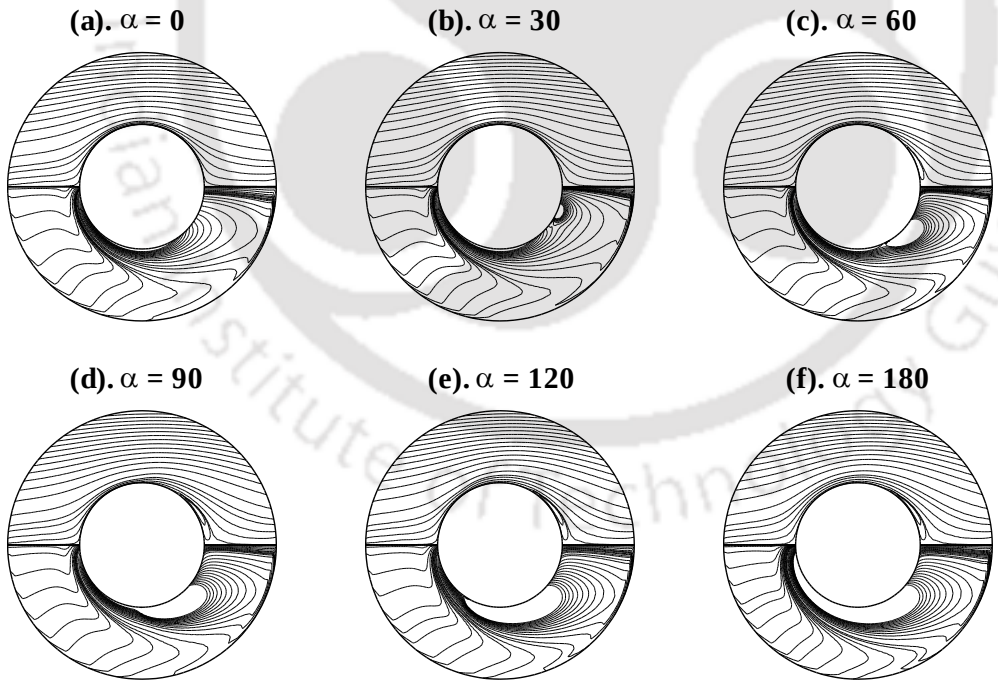

Figure 6.47: Streamlines (upper half) and iso-voticity (lower half) contours in swarms of contaminated bubbles of holdup 0.1 in Newtonian fluids at *Re* = 50.

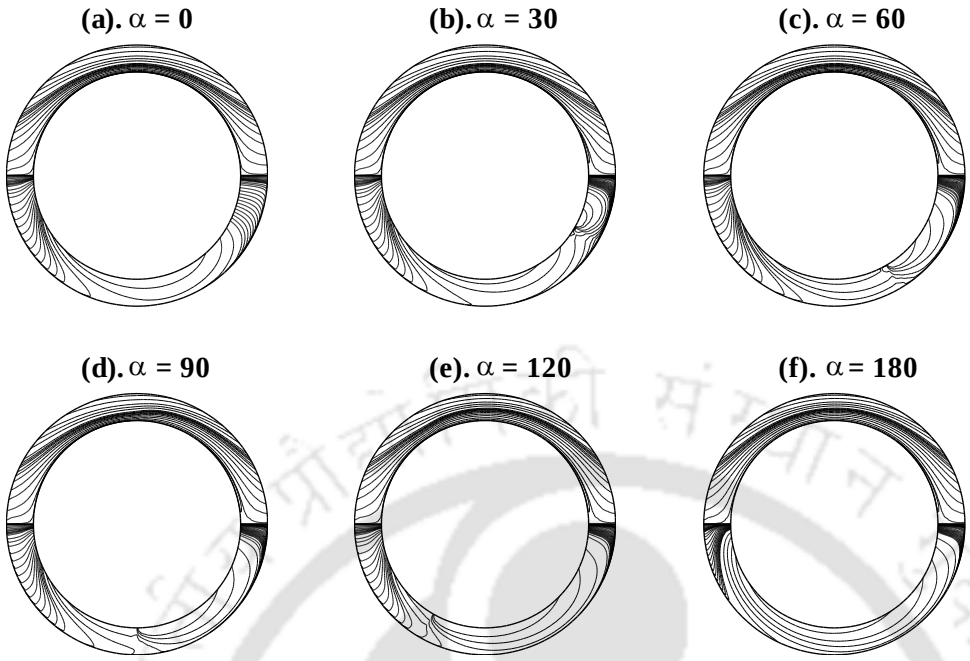

Figure 6.48: Streamlines (upper half) and iso-voticity (lower half) contours in swarms of contaminated bubbles of holdup 0.5 in Newtonian fluids at *Re* = 50.

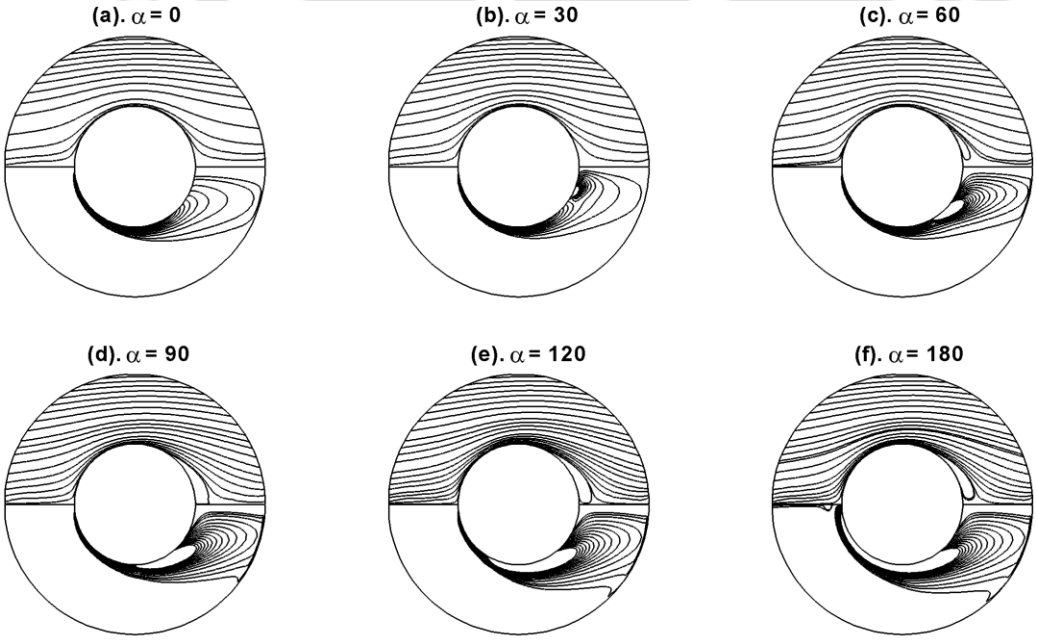

Figure 6.49: Streamlines (upper half) and iso-voticity (lower half) contours in swarms of contaminated bubbles of holdup 0.1 in power-law fluid of *n* = 0.6 at *Re* = 50.

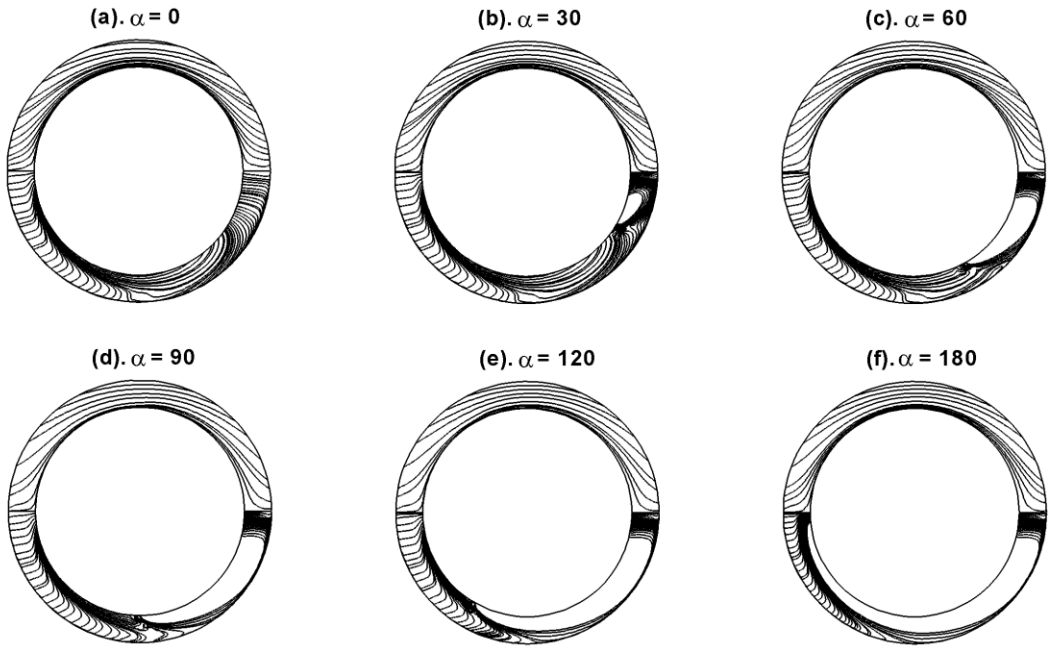

Figure 6.50: Streamlines (upper half) and iso-voticity (lower half) contours in swarms of contaminated bubbles of holdup 0.5 in power-law fluid of n = 0.6 at Re = 50.

6.5.2. Surface pressure distribution

Figure 6.51 show distributions of the pressure coefficient along surface of contaminated bubbles in swarms of holdup 0.1 (**Figure 6.51(a-c)**) and 0.5 (**Figure 6.51(d-f)**) at Re = 1, 50, 200 for different contamination angles in Newtonian fluids. For holdup of 0.1 and at Re = 1 (**Figure 6.51(a)**), for both completely clean bubbles (α = 0°) and completely contaminated bubbles (α = 180°), the pressure coefficient is maximum at front stagnation point (θ = 0°) and it gradually decreases along the surface of bubble to a minimum value at rear stagnation point (θ = 180°) without any pressure recovery. However, for intermediate values of the stagnant cap angle, at the leading edge of the stagnant cap, there is a sudden rise in the value of the pressure coefficient and then asymptotically decreases because the surface of bubble is suddenly changing from mobile to immobile because stagnant cap formation. Further because of this sudden rise in

pressure coefficient at the leading edge of the stagnant cap, there is sudden drop in rise velocity of bubble swarm. Furthermore, this sudden rise in surface pressure coefficient at the leading edge of the stagnant cap is maximum for α = 90° as compared to other values of the stagnant cap angle.

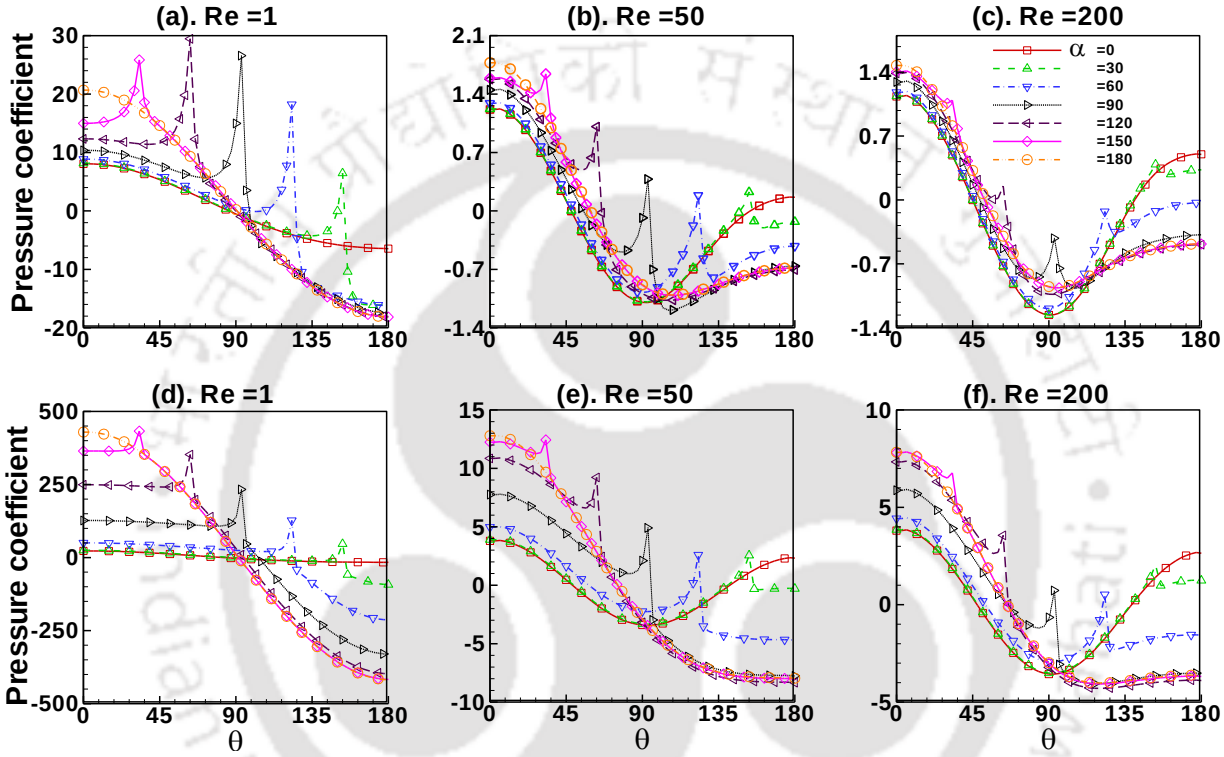

Figure 6.51: Surface pressure coefficient on surface of contaminated bubble in swarms of holdup 0.1 (a-c) and 0.5 (d-f) in Newtonian liquids.

As the Reynolds number increased to *Re* = 50 (**Figure 6.51(b)**), there is significant recovery of pressure in the rear half of the bubble because of recirculation wake formation as shown in **Figure 6.47**. Further the effect of surface contamination angle is similar to the case of *Re* = 1 with only two differences, the first one is the additional recovery of pressure at rear end and the second one is the value of sudden jump at the leading edge of the stagnant cap is small as compared to the case of *Re* = 1. Further increasing Reynolds number to 200 (**Figure 6.51(c)**),

qualitatively similar trends can be seen as in the case of Re = 50 (**Figure 6.51(b)**); however, the sudden rise in the value of pressure coefficient at the leading edge of the stagnant cap is very small such that it can be neglected for $\alpha \leq 45°$ and $\alpha \geq 135°$. From **Figure 6.51(d-f)** similar observations can be made for contaminated bubble swarms of holdup 0.5. However, the values of pressure coefficient are very large compared to the case of holdup 0.1 because of increased hindrance from neighboring particles. Further, regardless of values of the Reynolds number and stagnant cap angle, as the value of the holdup increases, the maximum value of the pressure coefficient at the leading edge decreases. For the case of shear-thinning fluids of n = 0.6 and n = 0.8, the trends of surface pressure are qualitatively similar as in the case of **Figure 6.51**; hence are not repeated.

6.5.3. Surface vorticity distribution

Figure 6.52 shows effects of the surface contamination and Reynolds number on vorticity distribution on the surface of bubbles in swarms of holdup 0.1 (**Figure 6.52(a-c)**) and 0.5 (**Figure 6.52(d-f)**) in Newtonian fluids. For clean bubbles (α = 0°), there is no flow separation at any value of Reynolds number up to 200; thus, the vorticity increases from its zero value at the front stagnation point (θ = 0°) to maximum value at around equator of the bubble then again gradually decreases to zero value at the rear stagnation point (θ = 180°). However, for fully contaminated bubbles (α = 180°), for Re > 20, because of recirculation wake formation, the vorticity decreases from its maximum value (at around θ = 40° - 70°) to certain negative value at the point of flow separation and finally recovers to its zero value at the rear stagnation point (θ = 180°) because of the recirculation wake formation. However, for contaminated bubbles altogether different trends are observed because of the sudden change of the surface boundary condition from fully slip to no-slip condition at the leading edge of the stagnant cap.

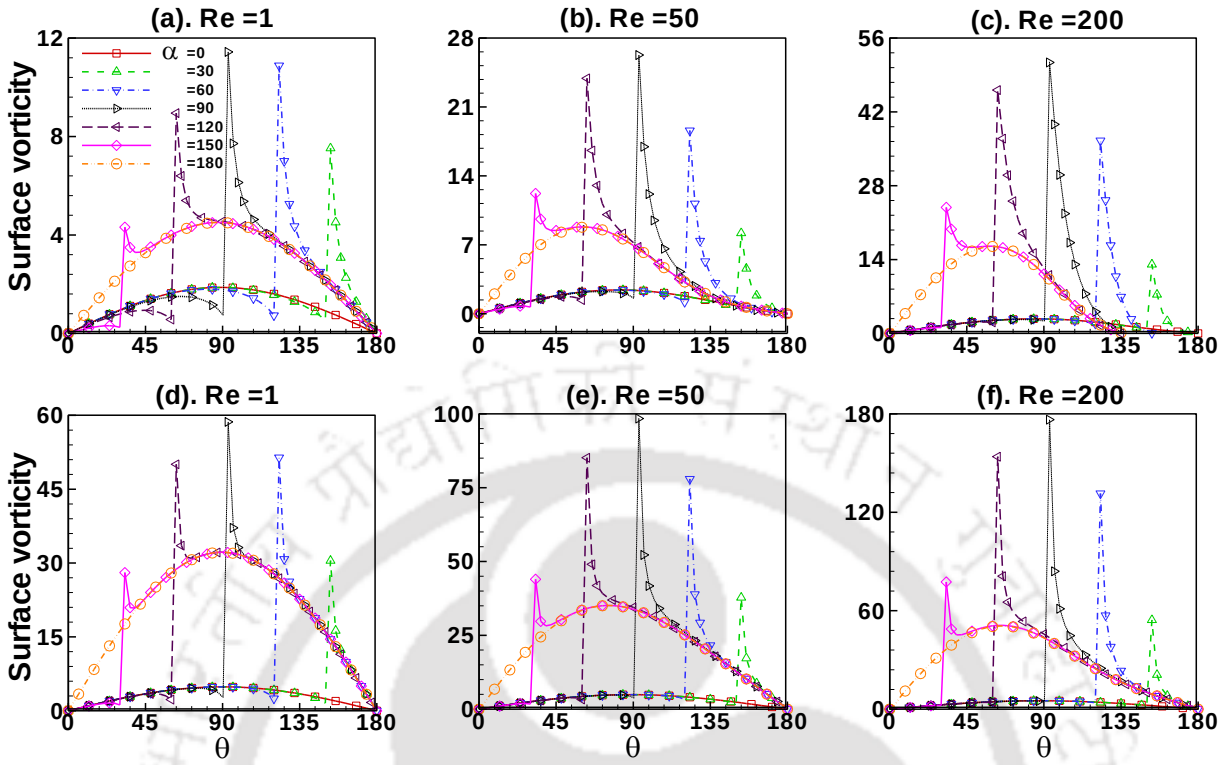

Figure 6.52: Surface vorticity on surface of contaminated bubble in swarms of holdup 0.1 (a-c) and 0.5 (d-f) in Newtonian liquids.

Further, in the mobile portion of the bubble surface, the vorticity follows the vorticity path of clean bubbles, then detaches from the vorticity path of clean bubble because of a sudden rise in vorticity at the leading edge of the stagnant cap and asymptotically decreases to reattach the vorticity path of fully contaminated bubble. This observation is consistent with the case of single contaminated bubble in Newtonian liquids (Fdhila and Duiveneld, 1996); however, the magnitudes of vorticity are higher in the case of bubble swarms because of hindrance from neighboring bubbles. Furthermore, for fixed value of bubble holdup, as the value of the Reynolds number increases, the rise in vorticity value at the leading edge of the stagnant cap increases. Qualitatively, similar trends observed for other combinations of the Reynolds number, bubble holdup, power-law index and stagnant cap angles; hence are not repeated. However, regardless

of values of the Reynolds number, power-law indices stagnant cap angle, as the value of the bubble holdup increases, the vorticity increases because of increased hindrance from neighboring bubbles.

6.5.4. Drag phenomena

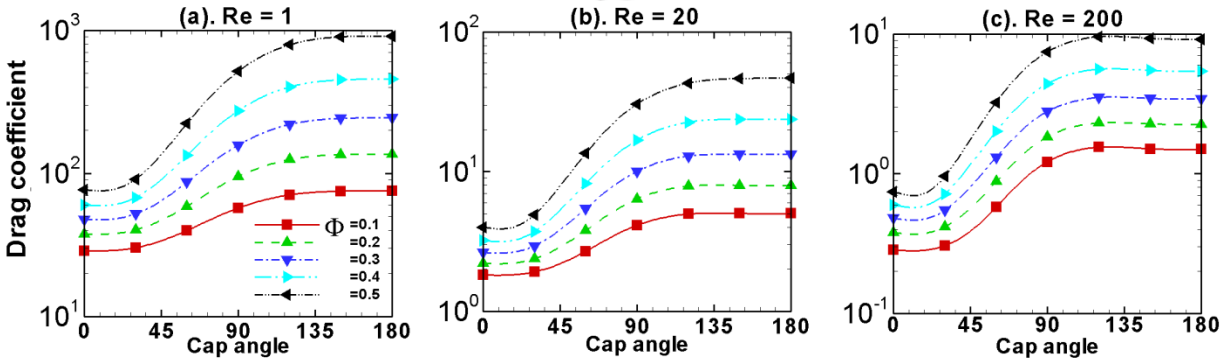

Figure 6.53: Drag coefficients of contaminated bubble swarms of different hold up in Newtonian fluids.

Figure 6.53 shows the combined effects of the Reynolds number, bubble holdup and the stagnant cap angle on drag coefficient of contaminated bubble swarms in Newtonian fluids. Regardless of values of the bubble holdup and cap angle, the characteristic drag behavior is recovered, i.e., the drag coefficient decreases with increasing Reynolds number. For fixed values of the Reynolds number and bubble holdup, the drag coefficient increases with increasing cap angle because the bubble surface gradually becomes immobile with gradual increase in the cap angle. Irrespective of values of the Reynolds number and the cap angle, the drag coefficient increases with increasing bubble holdup due to increased resistance from neighboring bubbles. **Figure 6.54** represents the combined effects of the Reynolds number, bubble holdup and the stagnant cap angle on drag coefficient of contaminated bubble swarms in power-law fluid of n =

0.8 **Figure 6.54(a-c)** and n = 0.6 **Figure 6.54(d-f).** The drag coefficient trends were same with respect to Reynolds number, holdup and cap angle as shown in F**igure 6.54**. However, the drag coefficient decreased with decreasing power-law index for all values of Reynolds number, holdup and cap angle.

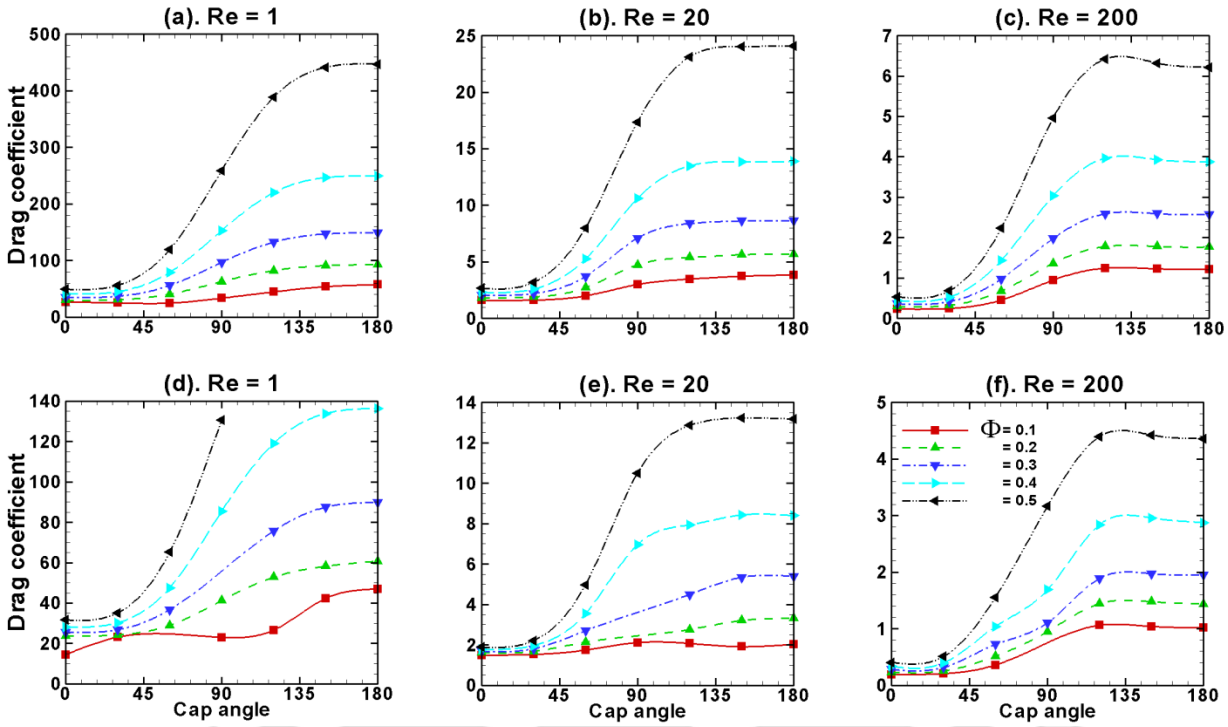

Figure 6.54: Drag coefficients of contaminated bubble swarms in power-law fluid of n = 0.8 (a-c) and n = 0.6 (d-f).

6.6. Mass Transfer Phenomena of Contaminated Bubble Swarms in Power-law Fluids

In order to delineate the effects of the Reynolds number (*Re*), the Schmidt number (*Sc*), the contamination angle (α) and the power-law index (n) on the concentration contours and on the

Sherwood numbers (*Sh*), the following ranges are considered: *Re*: 1, 10, 20, 50, 100, 200; *Sc*: 1, 10, 50, 100; $\alpha = 0^o$, 30^o, 60^o, 90^o,120^o, 150^o, 180^o and $n = 0.6, 0.8, 1$.

6.6.1. Concentration contours

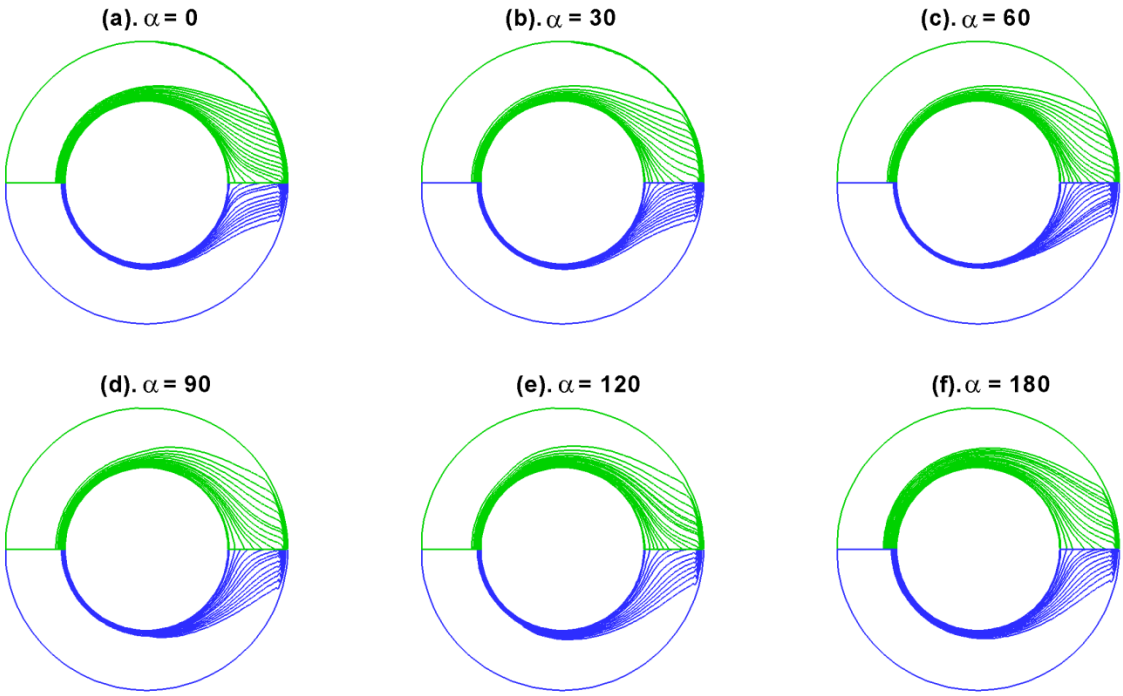

Figure 6.55: Concentration contours around contaminated bubble swarms of holdup = 0.2 in Newtonian fluids with *Re* = 20 (upper half) and *Re* = 200 (lower half) at *Sc* = 10.

Figure 6.55 shows the concentration contours around contaminated bubble swarms of holdup = 0.2 in Newtonian fluids with *Re* = 20 (upper half) and *Re* = 200 (lower half) at *Sc* = 10. At small Schmidt numbers, the concentration contours are generally uniformly distributed around the bubble; however depending on value of Reynolds number, they may be carried in the flow direction because of convection effects. Thus at *Re* = 20 (upper half), these concentration contours are partially carried away in the flow direction, but at *Re* = 200 (lower half), large

amount of concentration contours are carried away in the flow direction to increase the rate of mass transfer. However, unlike in the case of single contaminated bubble, the distortion in these contours are almost negligible for both values of Reynolds numbers, because of no flow recirculation (for *Re* = 20) and negligible flow recirculation (for *Re* = 200) in the case of bubble swarms of holdup 0.2. The thickness of concentration boundary layer has increased with increasing cap angle for all Reynolds numbers and thus the rate of mass transfer decreased with increasing cap angle. However, the concentration boundary layer thickness has decreased with increasing Reynolds number to improve the rate of mass transfer.

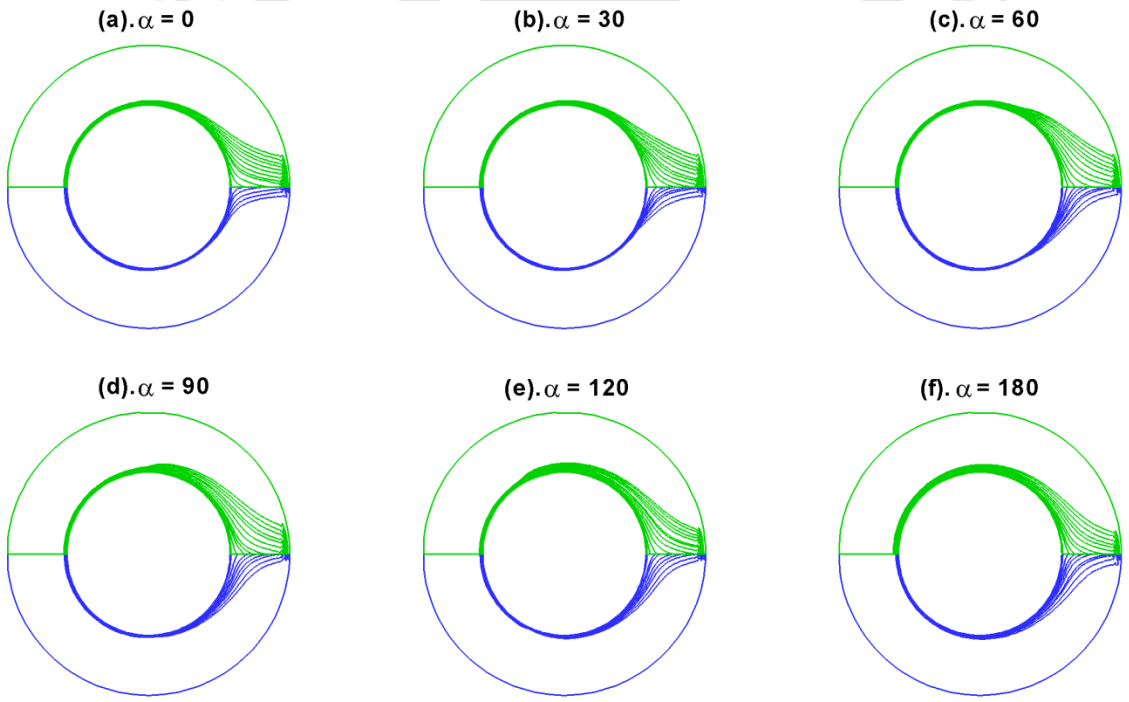

Figure 6.56: Concentration contours around contaminated bubble swarms of holdup = 0.2 in Newtonian fluids with *Re* = 20 (upper half) and *Re* = 200 (lower half) at *Sc* = 100.

Figure 6.56 shows the concentration contours around contaminated bubble swarms of holdup = 0.2 in Newtonian fluids with *Re* = 20 (upper half) and *Re* = 200 (lower half) at *Sc* =

100. In the case of *Sc* = 100, because of increased rate of convective mass transfer, for both values of Reynolds numbers, good amount of concentration contours are carried in the flow direction. Further thickness of boundary layer has also become thinner for both values of Reynolds numbers, but for *Re* = 200, it is very thin.

Figures 6.57 and 6.58 shows the concentration contours around contaminated bubble swarms of holdup = 0.2 in power-law fluid of *n* = 0.6 with *Re* = 20 (upper half) and *Re* = 200 (lower half) at *Sc* = 10 and *Sc* = 100 respectively. Qualitatively similar trends are seen as in the case of Newtonian fluid (**Figures 6.55-6.56**) but, for fixed combinations of Reynolds number, Schmidt number and cap angle, the concentration boundary layer thickness has decreased with the decreasing power-law index.

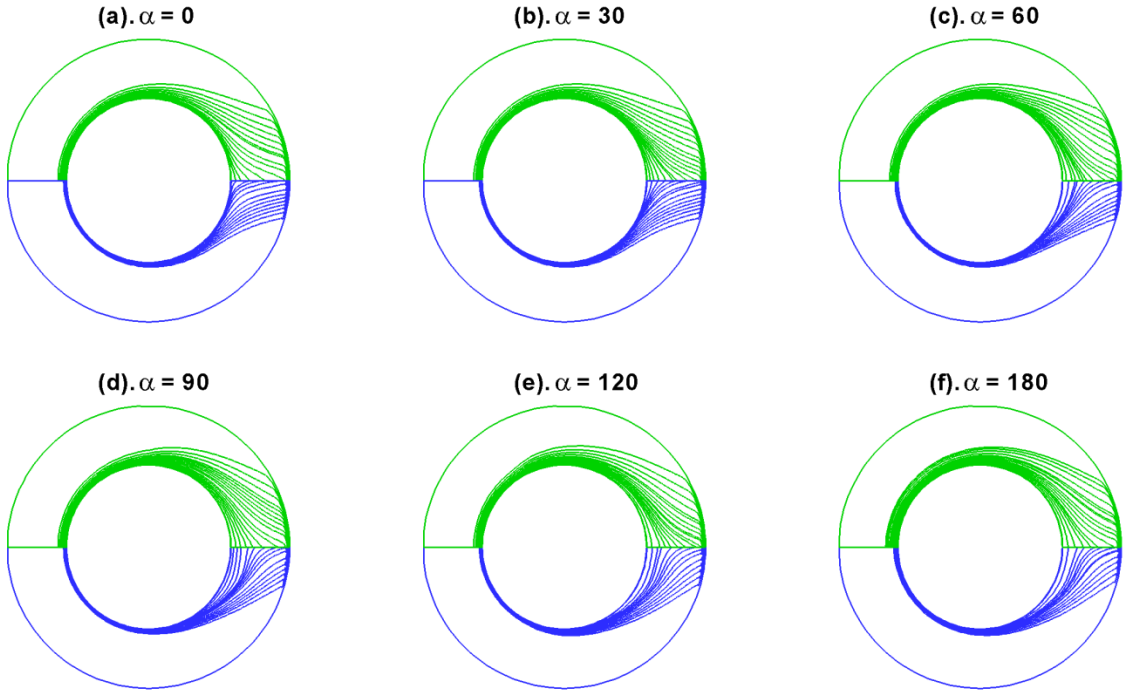

Figure 6.57: Concentration contours around contaminated bubble swarms of holdup = 0.2 in power-law fluid of *n* = 0.6 with *Re* = 20 (upper half) and *Re* = 200 (lower half) at *Sc* = 10.

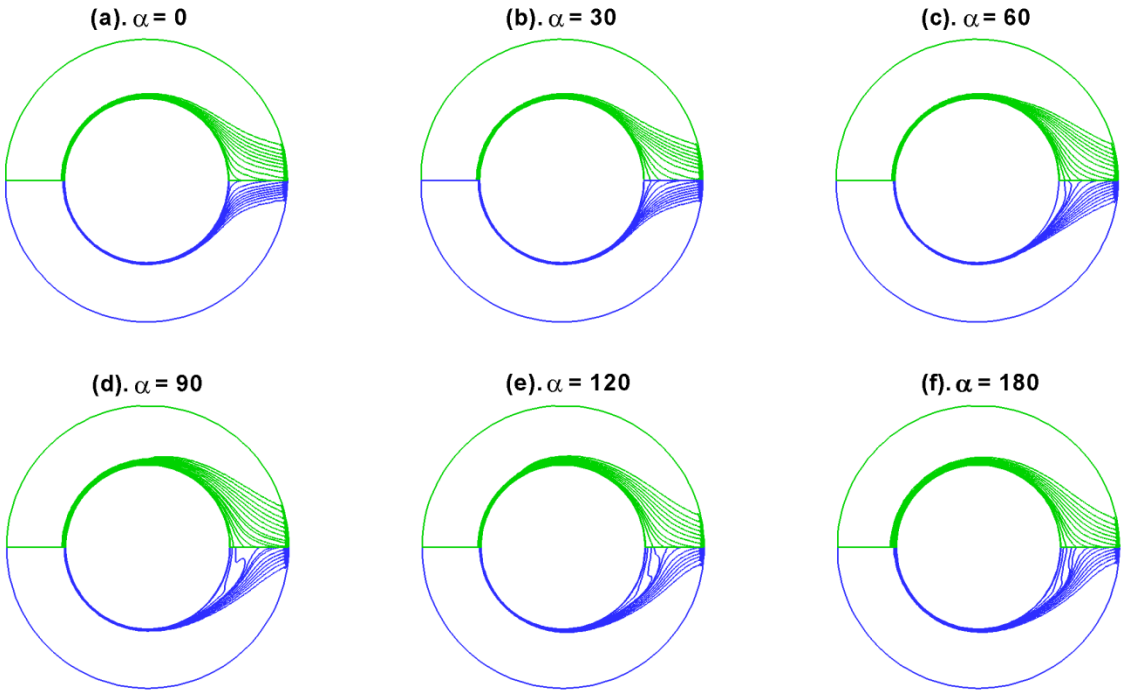

Figure 6.58: Concentration contours around contaminated bubble swarms of holdup = 0.2 in power-law fluid of n = 0.6 with Re = 20 (upper half) and Re = 200 (lower half) at Sc = 100.

Figures 6.59, 6.60, 6.61, 6.62 shows the concentration contours for holdup = 0.5 with Re = 20 (upper half) and Re = 200 (lower half) in Newtonian (n = 1) and power-law fluid of n = 0.6 for Sc = 10 and 100. Qualitatively similar trends are seen as in **Figures 6.55-6.58**; however, with increased holdup, the concentration boundary layer has become thinner due to the increased hindrance because of presence of neighbouring bubbles. Thus the rate of mass transfer increased with increasing holdup for any combination of Re, Sc, n and α.

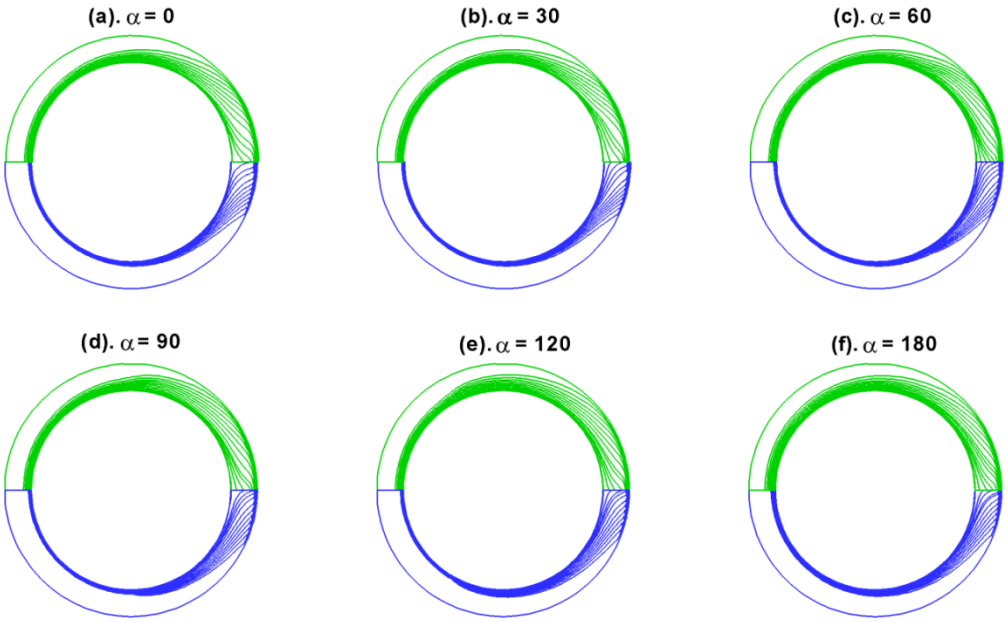

Figure 6.59: Concentration contours around contaminated bubble swarms of holdup = 0.5 in Newtonian fluids with *Re* = 20 (upper half) and *Re* = 200 (lower half) at *Sc* = 10.

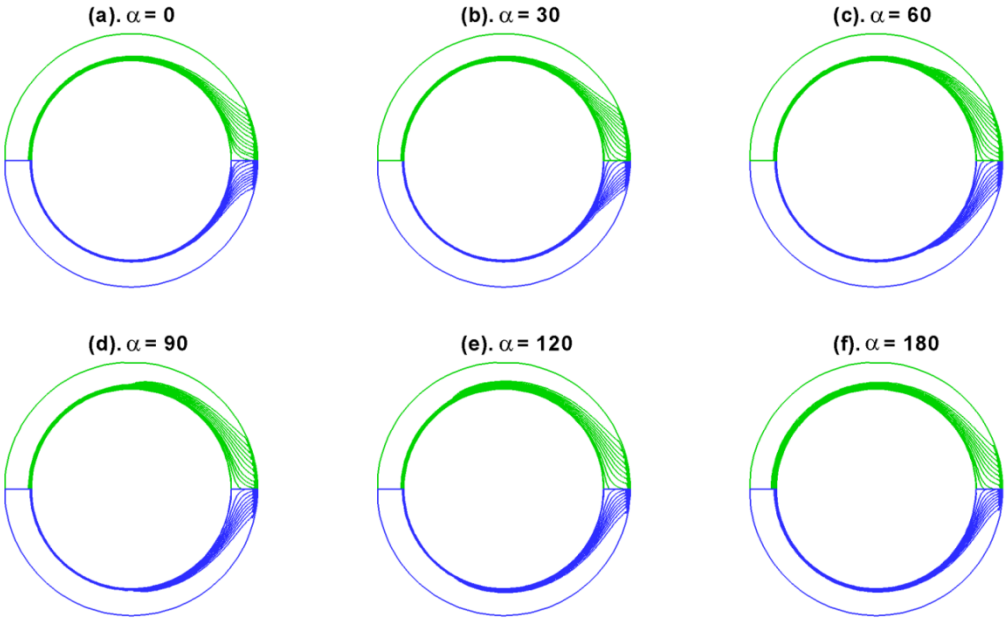

Figure 6.60: Concentration contours around contaminated bubble swarms of holdup = 0.5 in Newtonian fluids with *Re* = 20 (upper half) and *Re* = 200 (lower half) at *Sc* = 100.

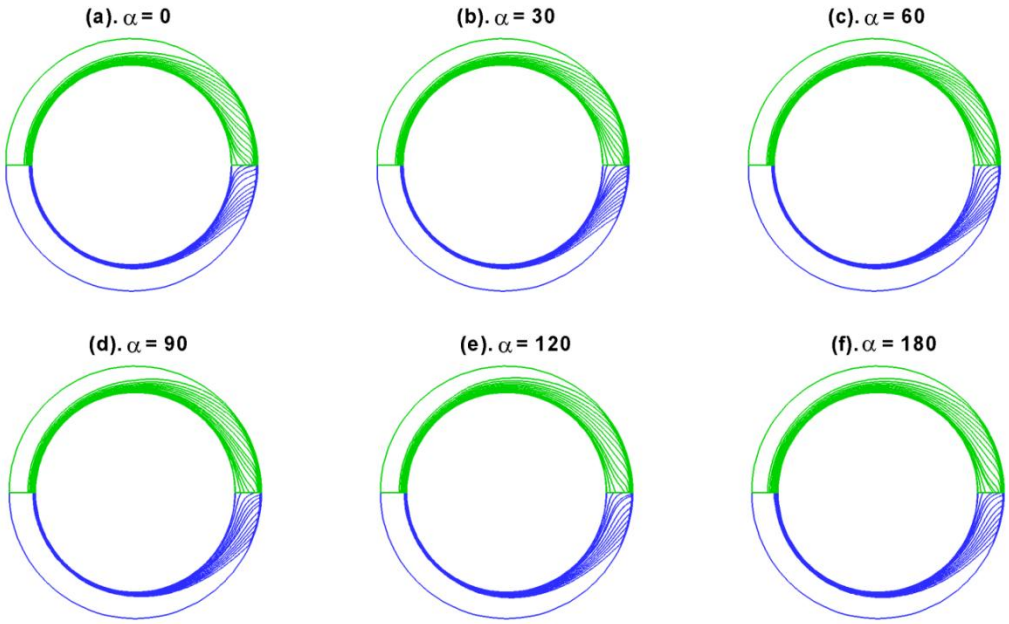

Figure 6.61: Concentration contours around contaminated bubble swarms of holdup = 0.5 in power-law fluid of n = 0.6 with Re = 20 (upper half) and Re = 200 (lower half) at Sc = 10.

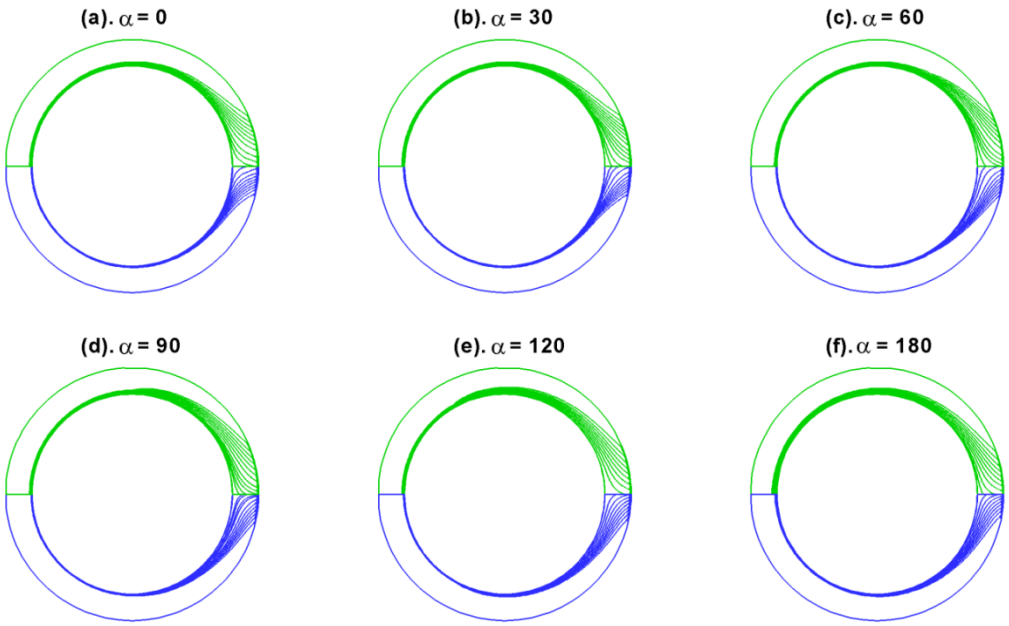

Figure 6.62: Concentration contours around contaminated bubble swarms of holdup = 0.5 in power-law fluid of n = 0.6 with Re = 20 (upper half) and Re = 200 (lower half) at Sc = 100.

6.6.2. Surface Sherwood number

Figure 6.63 shows the variation of the Sherwood number along the surface of target contaminated bubble contaminated bubble swarm of holdup = 0.1 in Newtonian (**Figures 6.63(a-b)**) and in power-law fluid of n = 0.6 (**Figures 6.63(c-d))** at Re = 50 for different values of the stagnant cap angle and Schmidt number. For clean bubbles, regardless of the value of power-law index and Schmidt number, the surface Sherwood number decreases from the front stagnation point to rear stagnation point because there is no flow recirculation at Re = 50 for bubble swarm of any holdup of present study. For fully contaminated bubbles, the surface Sherwood number decreases from the front stagnation point to the rear stagnation point, except for power-law fluids of n = 0.6 at Sc = 100 (**Figure 6.63d**). In this case, the surface Sherwood number increases from front the stagnation point to around $\theta \sim 30^{o}$, and decreases as traversing towards the rear stagnation point. For partially contaminated bubbles, the surface Sherwood number follows the surface Sh trends of the clean bubbles as traversing from front stagnation point to leading edge of stagnant cap, and then there is a sudden decrease in surface Sherwood number at the leading edge of the stagnant cap. This reduction is strong function of the Schmidt number and power-law index. As traversing from the leading edge of the stagnant cap to the rear stagnation point, the surface Sherwood number of partially contaminated bubbles follows the surface Sh trends of fully contaminated bubble trends. Furthermore, for fixed values of the cap angle and Schmidt number, as the power-law index decreases, the local value of the surface Sh increases (especially for large Sc) and the sudden decrement in the value of the surface Sh at the leading edge of the cap increases.

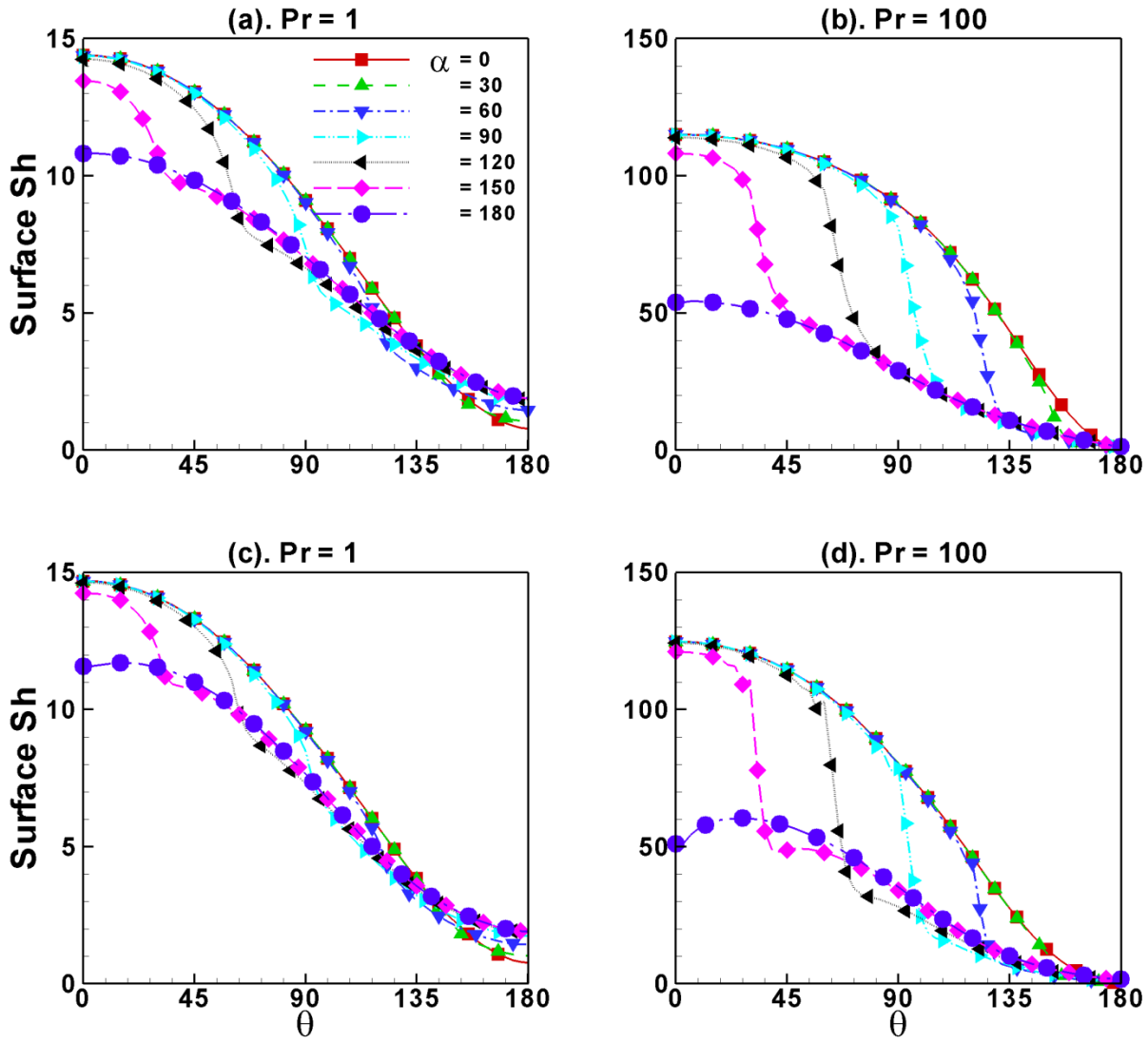

Figure 6.63: Surface Sherwood number around a target contaminated bubble in swarms of holdup = 0.1 at *Re* = 50 for *n* = 1 (a-b) and *n* = 0.6 (c-d).

Figure 6.64 shows the variation of the Sherwood number along the surface of contaminated bubble swarms of holdup = 0.5 in Newtonian (**Figures 6.64(a-b)**) and in power-law fluid of *n* = 0.6 (**Figures 6.64(c-d))** at *Re* = 50 for different values of stagnant cap angle and Schmidt number. Qualitatively similar trends observed as in the case of holdup 0.1 (**Figure 6.63**); however, the local value of Sherwood number increases with increasing holdup.

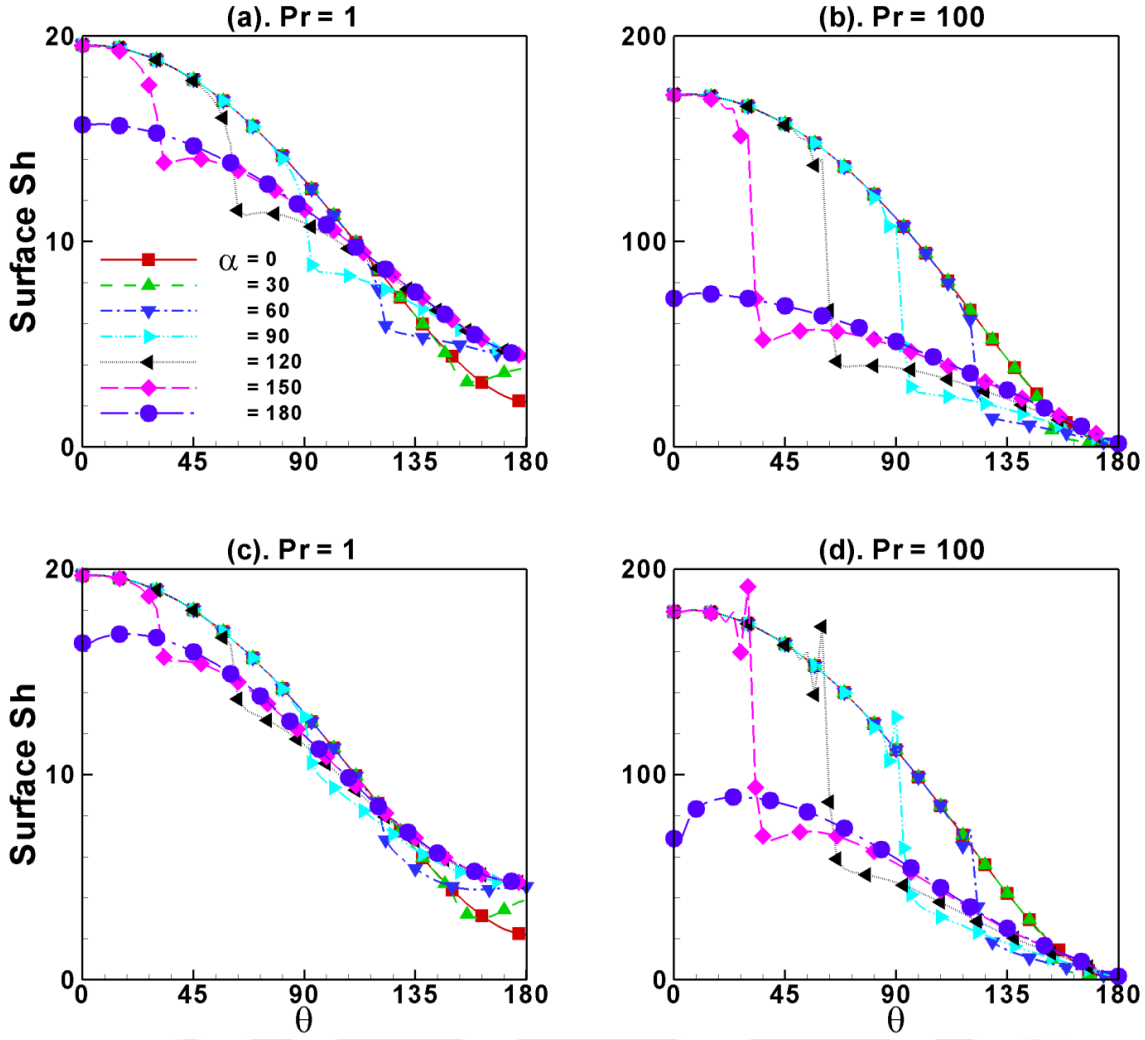

Figure 6.64: Surface Sherwood number around a target contaminated bubble in swarms of holdup = 0.5 at *Re* = 50 for *n* = 1 (a-b) and *n* = 0.6 (c-d).

6.6.3. Average Sherwood number

Figure 6.66 shows the variation of the average Sherwood numbers of contaminated bubble swarms of holdup = 0.1 (**Figure 6.66(a-c)**) and holdup = 0.5 (**Figure 6.66(d-f)**) for different Reynolds and Schmidt numbers in Newtonian fluids. The average Sherwood number increased with increasing Peclet number for all Reynolds numbers, cap angles and holdups. Further the

average Sherwood number decreases with the increase in the cap angle for all Reynolds numbers, Peclet numbers and holdups. This is due to convection near the bubble surface decreases as bubble surface becomes immobile (Takemura and Yabe, 1999). The average Sherwood number increased with increasing holdup because of increased hindrance for all Reynolds numbers, Peclet numbers and cap angles.

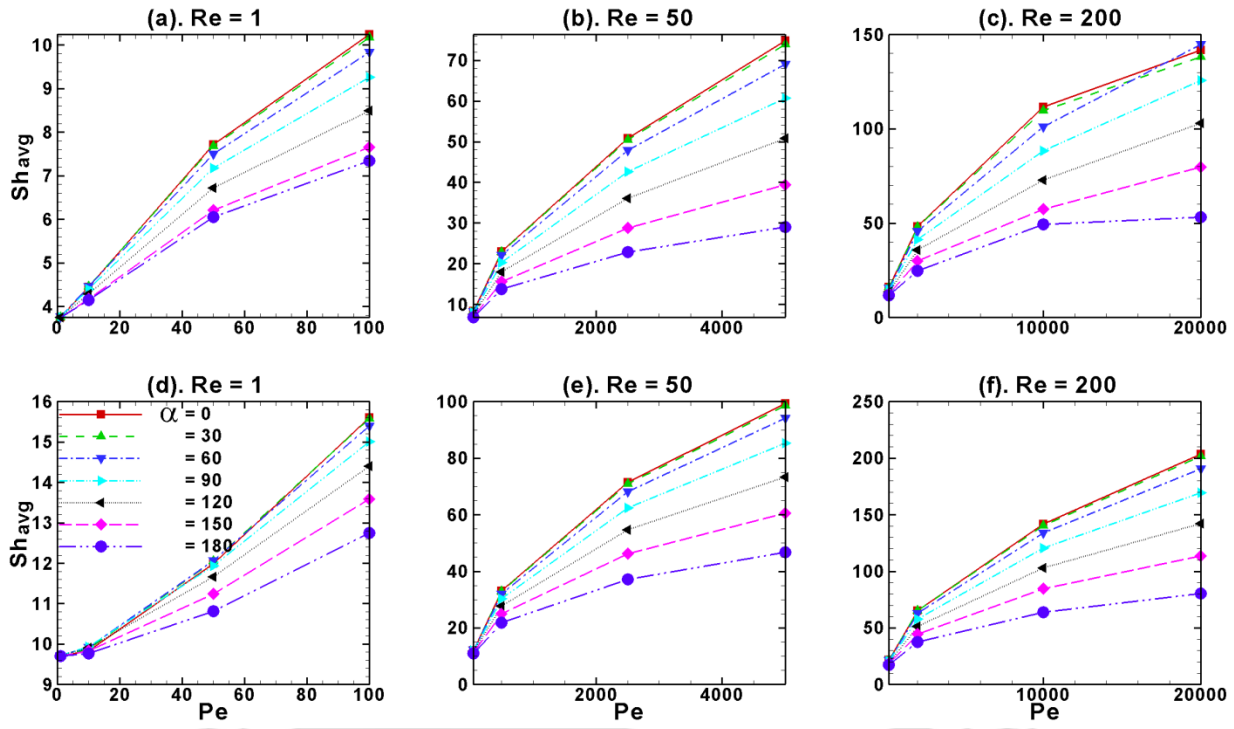

Figure 6.65: Average Sherwood number of bubble swarms in Newtonian liquids for holdup = 0.1 (a-c) and holdup = 0.5 (d-f).

Figures 6.66 and **6.67** shows the variation of average Sherwood number of contaminated bubble swarms of holdup = 0.1 (a-c) and holdup = 0.5 (d-f) in power-law fluid of n = 0.8 (**Figure 6.66**) and n = 0.6 (**Figure 6.67**). Qualitatively, the average Sherwood number trends with respect to Reynolds number, Peclet number, cap angle and holdup are same as in case of swarms in Newtonian fluid (**Figure 6.65)**. However, the average Sherwood number increased with

decreasing power-law indices for all Reynolds numbers, Peclet numbers, cap angles and holdups because of decreased concentration boundary layer.

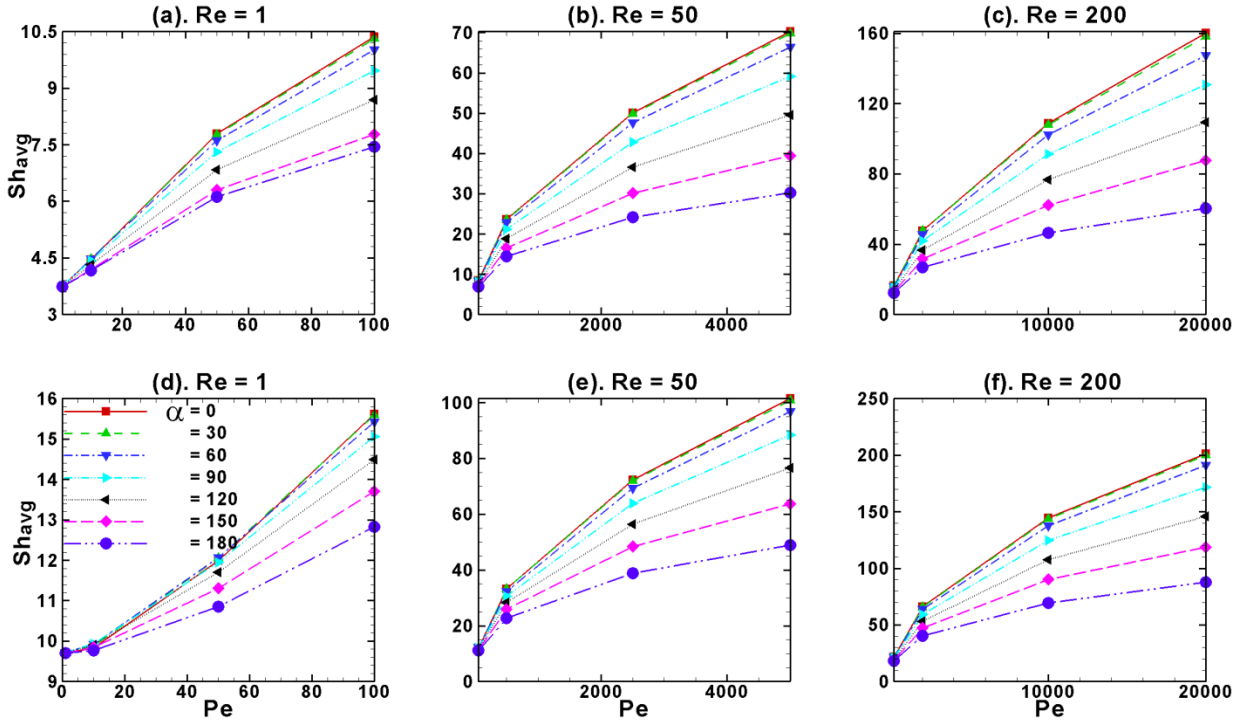

Figure 6.66: Average Sherwood number of bubble swarms in power-law liquid of n = 0.8 for holdup = 0.1 (a-c) and holdup = 0.5 (d-f).

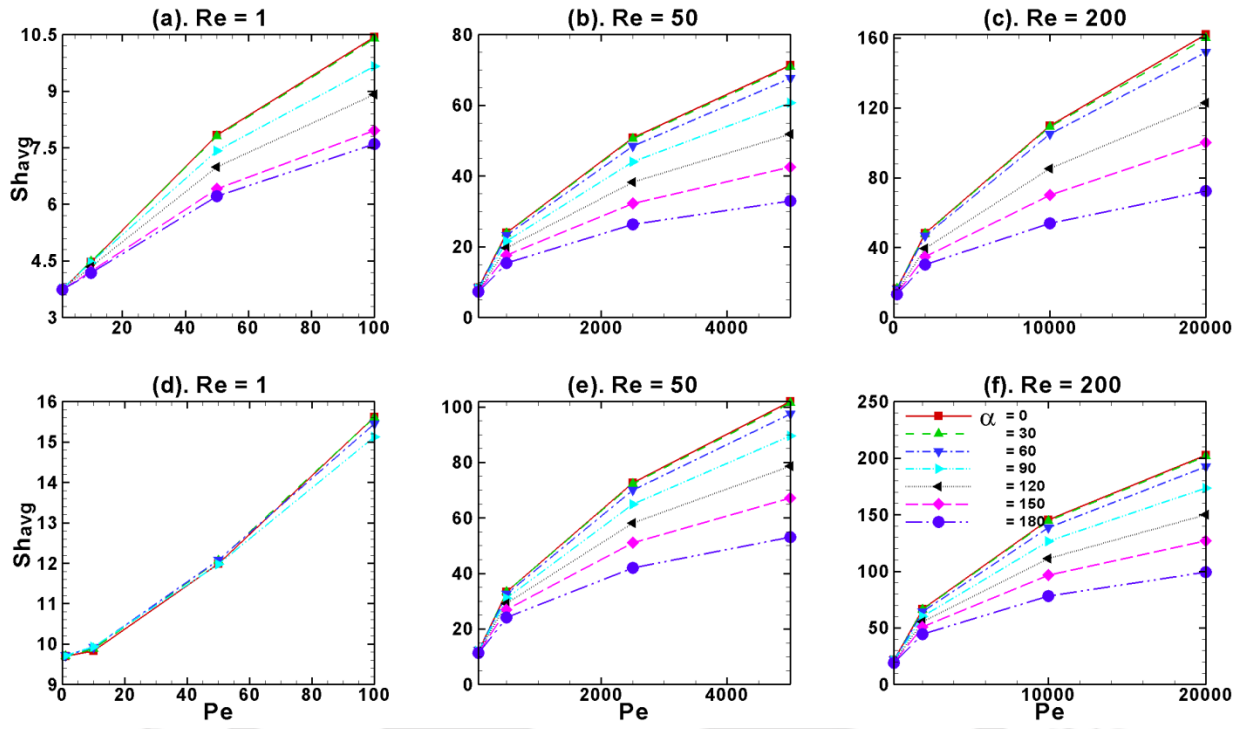

Figure 6.67: Average Sherwood number of bubble swarms in power-law liquid of n = 0.6 for holdup = 0.1 (a-c) and holdup = 0.5 (d-f).

Chapter 7

CONCLUSIONS AND FUTURE SCOPE

7.1. Conclusions

The drag behavior of unconfined contaminated single bubble in power-law fluids are studied using in-house solver and Ansys Fluent. For $Re \leq 20$, there is no flow separation for all cap angles and power-law index in the present range of investigation. For $Re \geq 50$, there is no flow separation for all values of power-law index provided the cap angle is $\leq 30°$. For $\alpha > 30°$ and $Re \geq 50$, the recirculation wake length increases and the separation angle moves forward (towards the front half of the bubble) with increasing Reynolds number; however, mixed trends observed with respect to power-law index and stagnant cap angle. For all values of the Reynolds number and stagnant cap angle, the sudden rise in surface pressure at the leading edge of the stagnant cap decreases with decreasing power-law index. On the other hand, the sudden rise in vorticity at the leading edge of the stagnant cap increases with decreasing power-law index. For $Re \geq 10$, the total drag coefficient increases with increasing cap angle and/or with increasing power-law index and/or with decreasing Reynolds numbers. A cross over Reynolds number (at $Re \approx 5$) is exist for drag coefficient versus Reynolds number behavior with respect to the power-law index for all degree of contamination. In other words, below the crossover Reynolds number, the drag coefficient increases with the decreasing power-law index while reverse trend is true for Reynolds numbers larger than the crossover Reynolds number. Further, the drag coefficient of contaminated bubble is found to increase with the increasing cap angle and/or with decreasing Reynolds number. For all values of the Reynolds number, the ratio of pressure and friction drag coefficient decreases with the increasing cap angle and/or with the increasing power-law index.

The heat transfer phenomenon of unconfined contaminated spherical bubbles in power-law liquids is numerically investigated using Ansys Fluent. Thickness of thermal boundary layer decreases with decreasing cap angle and/or power-law indices and/or increasing Reynolds numbers and/or Prandtl numbers. At Re = 200 for $\alpha \geq 60^{o}$, the distortion in isotherm contours becomes more intense with increasing Prandtl number and/or decreasing power-law indices. The surface Nu of contaminated bubbles follow the path of surface Nu of clean and fully contaminated bubble, respectively, along the mobile and immobile portions of the contaminated bubble surface with a sudden decrease in the value of the Nusselt number at the leading edge of the stagnant cap. This sudden decrease in surface Nu at the leading edge of the stagnant cap increases with the decreasing power-law index. The average Nusselt number of contaminated bubbles increases with the increasing Peclet number and/or with the decreasing cap angle and/or with the decreasing power-law index.

The momentum characteristics of the partially contaminated bubbles confined in tubes of different size are numerically investigated using Ansys Fluent over wide ranges of pertinent parameters. The size of the recirculation wake at the rear of the partially contaminated bubbles decreases with the decreasing wall factor (i.e., increasing wall retardation) and/or with the increasing power-law index and/or with the decreasing cap angle. The wall retardation effect on the surface pressure coefficient in highly shear-thinning fluids is large enough to suppress the sudden rise in the pressure coefficient at the leading edge of the spherical stagnant cap. However, the retardation effects could not suppress the sudden rise in the shear stress at the leading edge of the stagnant cap of the contaminated bubbles even in highly shear-thinning fluids. In the present case of the motion of confined bubbles there is no existence of the crossover Reynolds number in C_d versus Re curves with respect to the power-law index unlike in the case of the motion of

unconfined bubble. For all values of the Reynolds number, the drag ratio decreases with the increasing cap angle and/or with the increasing power-law index.

The wall retardation effect on heat transfer phenomena of contaminated single bubble in power-law fluids are studied using Ansys Fluent. At Re = 200 for $\alpha \geq 60^{o}$, the distortion of isotherm contour appeared because of recirculation wake formation becomes more intense with increasing Prandtl number and/or decreasing power-law indices. The average Nusselt number increases with increasing Reynolds number and/or Prandtl number and/or cap angle. The average Nusselt number increases with increasing wall retardation at moderate Reynolds and Prandtl numbers. Mixed trends observed with respect to power-law indices for different Reynolds numbers, Prandtl numbers and cap angles.

The rise of swarms of contaminated bubbles in power-law fluids has been studied using the in-house solver numerically over wide ranges of pertinent dimensionless parameters. For $\alpha \leq$ 30°, the recirculation wake is not observed for any combination of Reynolds number and the bubble holdup. The size of the recirculation wake is increased with increasing Reynolds number and/or decreasing bubble holdup and/or decreasing power-law indices and/or with the increasing cap angle. Regardless of values of the Reynolds number and stagnant cap angle, as the value of the holdup increases, the maximum value of the surface pressure coefficient at the leading edge of the stagnant cap decreases. On the other hand, for fixed value of bubble holdup, as the value of the Reynolds number increases, the rise in vorticity value at the leading edge of the stagnant cap increases. The drag coefficient of contaminated bubble swarms decreases with the decreasing bubble holdup and/or with the increasing power-law indices and/or with the decreasing cap angle and/or with the increasing Reynolds number. On the other hand, regardless of values of the bubble holdup, mixed trends observed on the effect of cap angle on the ratio

between pressure and friction drag coefficients for large values of the Reynolds numbers. The mass transfer phenomena of contaminated bubble swarms in power-law are studied using in-house solver. Concentration boundary layer becomes thinner with increasing Reynolds number and/or Schmidt number and/or decreasing power-law indices and/or cap angle. The reduction in surface Sh at leading edge of stagnant cap increases with increasing power-law index. The average Sherwood number increases with increasing Reynolds number and/or Schmidt number and/or bubble holdup and/or decreasing cap angle and/or power-law indices.

7.2. Scope for Future Work

- Momentum and mass transfer phenomena of contaminated spherical droplets in power-law fluids for confined and unconfined cases.
- Momentum and mass transfer phenomena of contaminated spherical bubbles and droplets in other non-Newtonian fluids.
- Momentum and mass transfer phenomena of ensembles of partially contaminated droplets in non-Newtonian fluids.
- Momentum and mass transfer phenomena of contaminated spherical bubbles and droplets by considering Marangoni effects.

REFERENCES

Abd-El-Rahman, M.K., Maes, A., Cauwenberg, P., Removal of heavy metal impurities from dredged river sediment, *Chem. Eng. Technol*., **22**, 707-712 (1999).

Acharya, A., Mashelkar R.A., Ulbrecht J., Flow of inelastic and viscoelastic fluid past a sphere, *Rheol. Acta*, **15**, 471-478 (1976).

Alves, S.S., Maia, C.I., Vasconcelos, J.M.T., Gas liquid mass transfer coefficient in stirred tanks interpreted through bubble contamination kinetics, *Chem. Eng. Process.*, **43**, 823-830 (2004).

Alves, S.S., Orvalha, S.P., Vasconcelos, J.M.T., Effect of bubble contamination on rise velocity and mass transfer, *Chem. Eng. Sci.*, **60**, 1-9 (2005).

Beitel, A., Heideger, W., Surfactant effects on mass transfer from drops subject to interfacial instability, *Chem. Eng. Sci.*, **26**, 711-717 (1971).

Bhavaraju, S.M., Mashelkar, R.A., Blanch, H.W., Bubble motion and mass transfer in non-Newtonian fluids: Part II. Swarms of bubbles in power-law fluid, *AIChE J*., **24**, 1070-1076 (1978).

Bird, R.B., Stewart, W.E., Lightfoot, E.N., *Transport Phenomena*, 2nd Edition, John Wiley, New York, (2002).

Boye-Christensen, G., Terjesen, S.G., On the action of surface active agents on mass transfer in liquid liquid-extraction, *Chem. Engng. Sci*., **9**, 225-241 (1959).

Butcher, T.A., Irvine, T.F., Use of the falling ball viscometer to obtain flow curves for inelastic non-Newtonian fluids, *J. Non-Newtonian Fluid Mech.*, **36**, 51-70 (1990).

Chhabra, R.P., Comiti, J., Machac, I., Flow of non-Newtonian fluids in fixed and fluidized beds, *Chem. Eng. Sci*., **56**, 1-27 (2001).

Chhabra, R.P., Raman, J.R., Slow non-Newtonian flow past an assemblage of rigid spheres, *Chem. Eng. Comm*., **27**, 23-46 (1984).

Chhabra, R.P., Comiti, J., Machac, I., Flow of non-Newtonian fluids in fixed and fluidized beds, *Chem. Eng. Sci*., **56**, 1-27 (2001).

Chhabra, R.P., Richardson, J.F., *Non-Newtonian flow and applied rheology*, Butterworth-Heinemann, Oxford, UK (2008).

Chhabra, R.P., *Bubles, drops and particles in Non-Newtonian fluids*, 2nd edition, CRC Press, Boca Raton, FL (2006).

Clift, R., Grace, J.R., Weber, M.E., *Bubbles, Drops and Particles*, Academic press, New York (1978).

Coutelieris, F.A., Kainourgiakis, M.E., Stubos, A.K., Low to moderate Peclet mass transport in assemblages of spherical particles for a realistic adsorption-reaction-desorption mechanism, *Powder Tech*., **159**, 173-179 (2005).

Cuenot, B., Magnaudet, J., Spennato, B., The effects of slightly soluble surfactants on the flow around a spherical bubble, *J. Fluid Mech.*, **339**, 25–53 (1997).

Cullen, E.J., Davidson, J.F., Absorption of gases in liquid jets, *Trans. Faraday Soc.*, **53**, 113-120 (1957).

D'Alessio, S.J.D., Pascal, J.P., Steady flow of a power law fluid past a cylinder, *Acta Mech.*, **117**, 87-100 (1996).

Dani, A., Cockx, A., Guiraud, P., Direct numerical simulation of mass transfer from spherical bubbles: the effect of interface contamination at low Reynolds numbers, *Int. J. Chem. Rector Eng.*, **4**, (2006).

Dani, A., Transfert de masse entre une bulle et un liquide: simulations numeriques directes et fluorescence induite par nappe laser, *These de doctorat de I'Institut National des Sciences appliquees de Toulouse*, France (2007).

Dani, A., Cockx, A., Guiraud, P., Mass transfer from single spherical bubble with the presence of chemical reaction: the effect of interface contamination at low Reynolds number. Proceedings of the COMSOL users conference, Grenoble, France (2007).

Davis, R.E., Acrivos, A., The influence of surfactants on the creeping motion of bubbles, *Engng Sci.*, **21**, 681-685 (1966).

Deckwer, W.D., *Bubble Column Reactors*, Wiley, New York (1992).

Dhole, S.D., Chhabra, R.P., Eswaran, V., Power-law fluid flow through beds of spheres at intermediate Reynolds numbers pressure in fixed and distended beds, *Chem. Eng. Res. Des*., **82**, 642-652 (2004).

Dhole, S.D., Chhabra, R.P., Eswaran, V., Flow of power-law fluids past a sphere at intermediate Reynolds numbers, *Ind. Eng. Chem. Res*., **45**, 4773-4781 (2006a).

Dhole, S.D., Chhabra, R.P., Eswaran, V., Forced convection heat transfer from a sphere to non-Newtonian power-law fluids, *AIChE J*., **52**, 3658-3667 (2006b).

Dhole, S.D., Chhabra, R.P., Eswaran, V., Drag of a spherical bubble rising in power-law fluids at intermediate Reynolds numbers, *Ind. Eng. Chem. Res*., **46**, 939-946 (2007a).

Dhole, S.D., Chhabra, R.P., Eswaran, V., Mass transfer from a spherical bubble rising in power-law fluids at intermediate Reynolds numbers, *Int. Commun. Heat Mass Transfer*, **34**, 971-978 (2007b).

Drelich, J., Lelinski, D., Hupka J., Miller, J.D., The role of gas bubbles in bitumen release during oil sand digestion, *Fuel*, **74**, 1150-1155 (1995).

El-Kaissy, M.M., Homsy, G.M., A theoretical study of pressure drop and transport in packed beds at intermediate Reynolds numbers, *Ind. Eng. Chem. Fundam*., **12**, 82-90 (1973).

Elzinga, E., Banchero, J., Some observations on the mechanics of drops in liquid–liquid systems, *AIChE J*., **7**, 394–399 (1961).

Escobar, F.H., Vega, L.J., Bonilla, L.F., Determination of well-drainage area for power-law fluids by transient pressure analysis, *CT&F-Ciencia*, **5**, 45-56 (2012).

Fdhila, R.B., Duineveld, P.C., The effect of surfactant on the rise of a spherical bubble at high Reynolds and Peclet number, *Phys. Fluids*, **8**, 310-321 (1996).

Frossling, N., Uber die verdunstung fallenden tropfen (evaporation of falling drops), *Gerlands Beitage Zur Geophysik*, **52**, 170-216 (1938).

Frumkin, A., Levich, V.G., On surfactants and interfacial motion, *Z. Fiz. Kbim.*, **21**, 1183-1204 (1947).

Gal-Or, B., Resnick, W., Mass transfer from gas bubbles in an agitated vessel with and without simultaneous chemical reaction, *Chem. Eng. Sci*., **19**, 653-663 (1964).

Gal-Or, B., Waslo, S., Hydrodynamics of an ensemble of drops (or bubbles) in the presence or absence of surfactants, *Chem. Eng. Sci*., **23**, 1431-1446 (1968).

Gal-Or, B., Yaron, I., Transient mass or heat transfer in ensembles of drops or bubbles translating at low Reynolds numbers, *AIChE J*., **19**, 200-202 (1973).

Garner, F.H., Skelland, A.H.P., Some factors affecting droplet behaviour in liquid–liquid systems, *Chem. Eng. Sci.*, **4**, 149–158 (1955).

Ghosal, S.K., Sanyal S.K., Dutta, S., *Introduction to Chemical Engineering*, Tata-McGraw Hill Publications, New Delhi (1993).

Graham, D.J., Jones, T.E.R., Settling and transport of spherical particles in power-law fluids at finite Reynolds number, *J. Non-Newtonian Fluid Mech.*, **54**, 465-488 (1994).

Griffith, R., The effect of surfactants on the terminal velocity of drops and particles, *Chem. Eng. Sci.*, **17**, 1057-1070 (1962).

Gummalam, S., Chhabra, R.P., Rising velocity of a swarm of spherical bubbles in a power-law non-Newtonian liquids, *Can. J. Chem. Eng*., **65**, 1004-1008 (1987).

Gummalam, S., Narayan, K.A., Chhabra, R.P., Rising velocity of a swarm of spherical bubbles through a non-Newtonian fluid: Effect of zero viscosity, *Int. J. Multiphase Flow*, **14**, 361-371 (1988).

Hadamard, J., Mouvement permanent lent d'une sphère liquide et visqueuse dans un liquide visqueux, *C. R. Acad. Sci. Paris*, **152**, 1735–1738 (1911).

Happel, J., Viscous flow in multiparticle systems: slow motion of fluids relative to beds of spherical particles, *AIChE J*., **4**, 197-201 (1958).

Happel, J., Brenner H., *Low Reynolds Number Hydrodynamics*, Martinus Nijhoff, Netherlands (1983).

Harlow, F.H., Welch, J.E., Numerical calculation of time-dependent viscous incompressible flow of fluid with free surfaces, *Phys. Fluids*, **8**, 2182-2188 (1965).

He, Z., Maldarelli, C., Dagan, Z., The size of stagnant caps of bulk soluble surfactant on the interfaces of translating fluid droplets, *J. Colloid Interface Sci.*, **146**, 442-451 (1991).

Higbie, R., The rate of absorption of pure gas into a still liquid during short periods of exposure, *Trans. Amer. Inst. Chem. Eng.*, **31**, 365-389 (1935).

Hirose, T., Moo-Young, M., Bubble drag and mass transfer in non-Newtonian fluids: Creeping flow with power-law fluids, *Can. J. Chem. Eng*., **47**, 265-267 (1969).

Horton, Y.J., Fritsch, I.R., Kintner, R., Experimental determination of circulation velocities inside drops, *Can. J. Chem. Eng.*, **43**, 143–146 (1965).

Hsu, J.P., Lee, E., Huang, Y.F., Electrophoresis of a concentrated dispersion of spherical particles in a non-Newtonian fluid, *Langmuir*, **20**, 2149-2156 (2004).

Hua, T.N., Ishii, T., Momentum transfer for multi-solid- particle power-law fluid systems at high Reynolds numbers, *J. Non-Newtonian Fluid Mech*., **9**, 301-319 (1981).

Huang, W., Kintner, R.C., Effects of surfactants on mass transfer inside drops, *AIChE J*.,**15**, 735–744 (1969).

Jaiswal, A.K., Sundararajan, T., Chhabra, R.P., Hydrodynamics of Newtonian fluid through assemblages of rigid spherical particles in intermediate Reynolds number regime, *Int. J. Eng. Sci.*, **29**, 693-708 (1991a).

Jaiswal, A.K., Sundararajan, T., Chhabra, R.P., Flow characteristics of settling suspensions and fluidized beds of spherical particles, *Chem. Eng. Comm*., **106**, 139-150 (1991b).

Jaiswal, A.K., Sundararajan, T., Chhabra, R.P., Flow of power-law liquids through particle assemblages at intermediate Reynolds numbers, *Can. J. Chem. Eng*., **69**, 1235-1241 (1992).

Jaiswal, A.K., Sundararajan, T., Chhabra, R.P., Hydrodynamics of creeping flow of power-law liquids through particle assemblages, *Int. J. Eng. Sci.*, **31**, 293-306 (1993).

Jaiswal, A.K., Sundararajan, T., Chhabra, R.P., Pressure drop for the flow of dilatant fluids through a fixed bed of spherical particles, *Can. J. Chem. Eng*., **72**, 352-353 (1994).

Jarzebski, A.B., Malinowski, J.J., Drag and mass transfer in multiple drop slow motion in power-law fluids, *Chem. Eng. Sci*., **41**, 2569-2573 (1986).

Jarzebski, A.B., Malinowski, J.J., Drag and mass transfer in slow non-Newtonian flows over an ensemble of Newtonian spherical drops or bubbles, *Chem. Eng. Comm*., **49**, 235-246 (1987a).

Jarzebski, A.B., Malinowski, J.J., Drag and mass transfer in creeping flow of a Carreau fluid over drops or bubbles, *Can. J. Chem. Eng*., **65**, 680-684 (1987b).

Kawase, Y., Ulbrecht, J.J., Drag and mass transfer in non-Newtonian flows through multi-particle systems at low Reynolds numbers, *Chem. Eng. Sci*., **36**, 1193-1202 (1981a).

Kawase, Y., Ulbrecht, J.J., Motion of and mass transfer from an assemblage of solid spheres moving in non-Newtonian fluids at high Reynolds numbers, *Chem. Eng. Comm*., **8**, 233-249 (1981b).

Kawase, Y., Ulbrecht, J.J., Sedimentation of particles in non-Newtonian fluids, *Chem. Eng. Comm*., **13**, 55-64 (1981c).

Kawase, Y., Ulbrecht, J.J., Mass and momentum transfer with non-Newtonian fluids in fluidized beds, *Chem. Eng. Comm*., **32**, 263-288 (1985).

Kishore, N., Chhabra, R.P., Eswaran, V., Sedimentation in emulsions of mono-size droplets at moderate Reynolds numbers, *Chem. Eng. Res. Des.*, **84**, 1180-1193 (2006).

Kishore, N., Chhabra, R.P., Eswaran, V., Mass transfer from ensembles of fluid spheres at moderate Reynolds and Peclet numbers, Chem. Eng. Res. Des., 85, 1203-1214 (2007).

Kishore, N., Chhabra, R.P., Eswaran, V., Drag on ensembles of fluid spheres translating in power-law liquids at moderate Reynolds numbers, *Chem. Eng. J.*, **139**, 224-235 (2008a).

Kishore, N., Chhabra, R.P., Eswaran, V., Bubble swarms in power-law liquids at moderate Reynolds numbers: drag and mass transfer, *Chem. Eng. Res. Des.*, **86**, 39-53 (2008b).

Kishore, N., Chhabra, R.P., Eswaran, V., Mass transfer from ensembles of fluid spheres to power-law liquids at moderate Reynolds and Peclet numbers, *Chem. Eng. Sci.*, 63, 2484-2499 (2008c)

Kishore, N., Dhole, S.D., Chhabra, R.P., Eswaran, V., Momentum and heat transfer phenomena for power-law liquids in assemblages of solid spheres of moderate to large void fractions, *Numer. Heat Transfer A*, **56**, 970-986 (2009).

Kishore, N., Gu, S., Wall effects on flow and drag phenomena of spheroid particles at moderate Reynolds numbers, *Ind. Eng. Chem. Res.*, **49**, 9486-9495 (2010).

Krzan, M., Malysa, K., Profiles of local velocities of bubbles in *n*-butanol, *n*-hexanol and *n*-nonanol solutions, *Coll. Surf. A*, **207**, 279-291 (2002).

Krzan, M., Lunkenheimer, K., Malysa, K., On the influence of the surfactant's polar group on the local and terminal velocities of bubbles, *Coll. Surf. A*, **250**, 431-441 (2004).

Krzan, M., Zawala, J., Malysa, K., Development of steady state adsorption distribution over interface of a bubble rising in solutions of n-alkanols (C_5, C_8) and n-alkyltrimethylammonium bromides (C_8, C_{12}, C_{16}), *Coll. Surf. A*, **298**, 42-51 (2007).

Kulkarni, A.A., Joshi, J.B., Bubble formation and bubbles rise velocity in gas-liquids systems: A review, *Ind. Eng. Chem. Res.*, **44**, 5873-5931 (2005).

Kuwabara, S., The forces experienced by randomly distributed parallel cylinders or spheres in a viscous flow at small Reynolds numbers, *J. Phys. Soc. Japan*, **14**, 527-532 (1959).

Leal, L.G., Vorticity transport and wake structure for bluff bodies at finite Reynolds numbers, *Phy. Fluids*, **A 1**, 124-131 (1989).

LeClair, B.P., Hamielec, A.E., Viscous flow through particle assemblages at intermediate Reynolds numbers, *Ind. Eng. Chem. Fundam.*, **7**, 542-549 (1968).

LeClair, B.P., Hamielec, A.E., Viscous flow through particle assemblages at intermediate Reynolds numbers-A cell model for transport in bubble swarms, *Can. J. Chem. Eng.*, **49**, 713-720 (1971).

Lee, E., Chu, J-W., Hsu, J.P., Electrophoretic mobility of a concentrated suspension of spherical particles, *J. Colloid Interf. Sci.*, **209**, 240-246 (1999).

Lee, E., Tai, C.S., Hsu, J.P., Chen, C.J., Electrophoresis in a carreau fluid at arbitrary zeta potentials, *Langmuir*, **20**, 7952-7959 (2004).

Leonard, B.P., A stable and accurate convective modeling procedure based on quadratic upstream interpolation, *Comp. Methods Appl. Mech. Engr.*,**19**, 59-98 (1979).

Leppinen, D.M., Renksizbulut, M., Haywood R.J., The effects of surfactants on droplet behaviour at intermediate Reynolds numbers-i. the numerical model and steady-state results, *Chem. Engng. Sci.*, **51**, 479-489 (1996a).

Leppinen, D.M., Renksizbulut, M., Haywood R.J., The effects of surfactants on droplet behaviour at intermediate Reynolds numbers-ii. transient deformation and evaporation, *Chem. Engng Sci.*, **51**, 491-501 (1996b).

Levich, V.G., *Physicochemical Hydrodynamics*, Prentice-Hall, Englewood Cliffs, NJ (1962).

Liao, Y., McLaughlin, J.B., Dissolution of a freely rising bubble in aqueous surfactant solutions, *Chem. Eng. Sci.*, **55**, 5831–5850 (2000).

Liao, Y., Wang, J., Nunge, R.J, McLaughlin J.B., Comments on 'Bubble motion in aqueous surfactant solutions, *J Colloid Interface Sci.*, **272**, 498–501 (2004).

Lindland, K., Terjesen, S., The effect of surface active agents on liquid-liquid mass transfer rates, *Chem. Engng. Sci*., **5**, 1-16 (1956).

Maceiras, R., Alves, S.S., Cancela, M.A., Alvarez, E., Effect of bubble contamination on gas liquid mass transfer coefficient on CO_2 absorption in amine solutions, *Chem. Eng. J.*, **137**, 422-427 (2008).

Madhavi, T., Golder, A.K., Samanta, A.N., Ray, S., Studies on bubble dynamics with mass transfer, *Chem. Eng. J.*, **128**, 95-104 (2007).

Manjunath, M., Chhabra, R.P., Free rise velocity of a swarm of spherical bubbles through a quiescent power-law liquid, *Int. J. Eng. Sci*., **30**, 871-878 (1992).

Manjunath, M., Tripathi, A., Chhabra, R.P., Sundararajan, Numerical simulation of the drag on a swarm of bubbles, *Int. J. Eng. Sci*., **32**, 927-933 (1994).

Mao, Z.S., Yang, C., Wang, Y., Effectiveness factor of a catalytic sphere in particle assemblage approached with a cell model, *Chem. Eng. Sci.*,**62**, 6475-6485 (2007).

Marucci, G., Rising velocity of a swarm of spherical bubbles, *Ind. Eng. Chem. Fundam*., **4**, 224-225 (1965).

McLaughlin, J.B., Numerical simulation of bubble motion in water, *J. Colloid Interf. Sci.*, **184**, 614–625 (1996).

Michaelides, E.E., *Particles, Bubbles and Drops: Their Motion, Heat and Mass Transfer*, World Scientific, Singapore (2006).

Mohan, V., Raghuraman, J., A theoretical study of pressure drop for non-Newtonian creeping flow past an assemblage of spheres, *AIChE J*., **22**, 259-264 (1976a).

Mohan, V., Raghuraman, J., Bounds on the drag for creeping flow of an Ellis fluid past an assemblage of spheres, *Int. J. Multiphase Flow*, **2**, 581-589 (1976b).

Nishimura, Y., Ishii, T., An analysis of transport phenomena for multi-solid particle systems at higher Reynolds numbers by a standard Karman-Pohlhausen method – I. Momentum transfer, *Chem. Eng. Sci*., **35**, 1195-1204 (1980a).

Nishimura, Y., Ishii, T., An analysis of transport phenomena for multi-solid particle systems at higher Reynolds numbers by a standard Karman-Pohlhausen method – II. Mass transfer, *Chem. Eng. Sci*., **35**, 1205-1209 (1980b).

Painmanakul, P., Loubiere, K., Hebrard, G., Mietton-Peuchot, M., Roustan, M., Effect of surfactants on liquid-side mass transfer coefficients, *Chem. Eng. Sci.*, **60**, 6480-6491 (2005).

Pfeffer, R., Heat and mass transport in multiparticle systems, *Ind. Eng. Chem. Fundam*., **3**, 380-383 (1964).

Palaparthi, R., Papageorgiou, D.T., Maldarelli C., Theory and experiments on the stagnant cap regime in the motion of spherical surfactant-laden bubbles, *J. Fluid Mech.*, **559**, 1-44 (2006).

Ponoth, S., McLaughlin, J.B., Numerical simulation of mass transfer for bubbles in water, *Chem. Eng. Sci*., **55**, 1237–1255 (2000).

Prasad, D., Narayan, K.A., Chhabra, R.P., Creeping fluid flow relative to an assemblage of composite spheres, *Int. J. Eng. Sci.*, **28**, 215-230 (1990).

Rajasekhar Reddy, C., Kishore, N., Wall retardation effects on flow and drag phenomena of confined spherical particles in shear-thickening fluids, *Ind. Eng. Chem. Res*., **51**, 16755-16762 (2012).

Rajasekhar Reddy, C., Kishore, N., Effects of wall confinement and power-law fluid viscosity on Nusselt number of confined spheres, *Chem. Eng. Technol*., **36**, 1568-1576 (2013).

Richardson, J.F., Zaki, W.N., The sedimentation of a suspension of uniform spheres under conditions of viscous flow, *Chem. Eng. Sci*., **3**, 65-73 (1954).

Rodrigue, D., De Kee, D., Chan Man Fong, C.F., An experimental study of the effect of surfactants on the free rise velocity of gas bubbles, *J. Non-Newt. Fluid Mech.*, **66**, 213-232 (1996).

Rodrigue, D., De Kee, D., Chan Man Fong, C.F., Bubble drag in contaminated non-Newtonian solutions, *Can. J. Chem. Eng.*,**75**, 794-796 (1997).

Rodrigue, D., De kee, D., Chan man Fong, C.F., The slow motion of a single gas bubble in non-Newtonian fluid containing surfactants, *J. Non-Newtonian Fluid Mech*., **86**, 211-227 (1999).

Ruckenstein, E., On mass transfer in the continuous phase from spherical bubbles and drops, *Chem. Eng. Sci*., **19**, 131-146 (1964).

Rybczynski, W., Uber die fortschreitende Bewegung einer flüssigen Kugel in einem zähen Medium, *Bull. Polish Acad. Sci. Krakow,* **A**, 40–46 (1911).

Ryskin, G., Leal, L.G., Numerical solution of free-boundary problems in fluid mechanics. Part 2: Buoyancy-driven motion of gas bubbles through a quiescent liquid, *J. Fluid Mech.*, **148**, 1-36 (1984).

Saboni, A., Alexandrova, S., Mory, M., Flow around a contaminated fluid sphere, *Int. J. Multiphase Flow.*, **36**, 503-512 (2010).

Saboni, A., Alexandrova, S., Karsheva, M., Gourdon, C., Mass transfer from a contaminated fluid sphere, *AIChE J*., **57**, 1684-1692 (2011).

Sadhal, S.S., Johnson, R.E., Stokes flow past bubbles and drops partially coated with thin films – exact solution, *J. Fluid Mech.*, **126**, 237–250 (1983).

Sardeing, R., Painmanakul, P., Hebrard, G., Effect of surfactants on liquid-side mass transfer coefficients in gas-liquid systems: A first step to modeling, *Chem. Eng. Sci.*, **61**, 6249-6260 (2006).

Sarrot, V., Capture De fines particules par des inclusions fluids, These de doctorat de I'Institut National des Sciences Appliquees de Toulouse, France (2006).

Satish, M.G., Zhu, J., Flow resistance and mass transfer in slow non-Newtonian flow through multiparticle systems, *J. Appl. Mech*., **59**, 431-437 (1992).

Savic, P., Circulation and distortion of liquid drops falling through a viscous medium, *Tech. Rep. MT-22. Natl. Res. Counc. Can., Div. Mech. Eng.*, (1953).

Shukla, R., Chhabra, R.P., Effect of non-Newtonian characteristics on convective liquid-solid heat transfer in packed and fluidized beds of spherical particles, *Can. J. Chem. Eng*., **82**, 1071-1075 (2004a).

Shukla, R., Dhole, S.D., Chhabra, R.P., Eswaran, V., Convective heat transfer for power-law fluids in packed and fluidized beds of spheres, *Chem. Eng. Sci*., **59**, 645-659 (2004b).

Skelland, A., Woo, S., Ramsay, G., Effect of surface active agents on drop size, terminal velocity and droplet oscillation in liquid-liquid systems, *Ind. Engng. Chem. Res*., **26**, 907-911 (1987).

Song, D., Gupta, R.K., Chhabra, R.P., Wall effects on a sphere falling in quiescent power law fluids in cylindrical tubes, *Ind. Eng. Chem. Res*., **48**, 5845-5856 (2009).

Song, D., Gupta, R.K., Chhabra, R.P., Effect of blockage on heat transfer from a sphere in power-law fluids, *Ind. Eng. Chem. Res*., **49**, 3849-3861 (2010).

Soo, S.L., *Multiphase fluid Dynamics*, Science press, Beijing, China (1990).

Sun, D., Zhu, J., Approximate solutions of non-Newtonian flows over a swarm of bubbles, *Int. J. Multiphase Flow*, **30**, 1271-1278 (2004).

Takemura, F., Yabe, A., Rising speed and dissolution rate of a carbon dioxide bubble in slightly contaminated water, *J. Fluid Mech.*, **378**, 319-334 (1999).

Takemura, F., Matsumoto, Y., Dissolution rate of spherical carbon dioxide bubbles in strong alkaline solutions, *Chem. Eng. Sci.*, **55**, 3907-3917 (2000).

Tripathi, A., Chhabra, R.P., Sundararajan, T., Power-law fluid flow over spheroidal particles, *Ind. Eng. Chem. Res.*, **33**, 403-410 (1994).

Tripathi, A., Chhabra, R.P., Drag on spheroidal particles in dilatant fluids, *AIChE J.*, **41**, 728-731 (1995).

Tzounakos, A., Karamanev, D.G., Margaritis, A., Bergougnou, Effect of the surfactant concentration on the rise of gas bubbles in power-law non-Newtonian liquids, *Ind. Eng. Chem. Res.*, **43**, 5790-5795 (2004).

Vasconcelos, J.M.T., Orvalho, S.P., Alves, S.S., Gas-liquid mass transfer to single bubbles: effect of surface contamination, *AIChE J*., **6**, 1145-1154 (2002).

Velez-Cordero, J.R., Zenit, R., Bubble cluster formation in shear-thinning inelastic bubbly columns, *J. Non-Newtonian Fluid Mech*., **166**, 32-41 (2011).

Waslo, S., Gal-Or, B., Boundary layer theory for mass and heat transfer in clouds of moving drops, bubbles or solid particles, *Chem. Eng. Sci.*, **26**, 829-838 (1971).

Wellek, R.M., Agarwal, A.K., Skelland, H.P., Shape of liquid drops moving in liquid media, *AIChE J*., **12**, 854-862 (1966).

Wham, R.M., Basaran, O.A., Byers, C.H., Wall effects on flow past solid spheres at finite Reynolds numbers, *Ind. Eng. Chem. Res*., **35**, 864-874 (1996).

Winnikow, S., Chao, B.T., Droplet motion in purified systems, *Phys. Fluids*, **9**, 50-61 (1966).

Winnikow, S., The heat and mass transfer from a fluid sphere at large Reynolds and Peclet numbers, *Can. J. Chem. Eng.*, **46**, 217-222 (1968).

Yang, J., Li H-F., Li, M., Lin J-M., Gas dispersion concentration of trace inorganic contaminants from fuel gas and analysis using head-column field-amplified sample stacking capillary electrophoresis, *Analyst*, **137**, 3710-3716 (2012).

Yaron, I., Gal-Or, B., Convective mass or heat transfer from size-distributed drops, bubbles or solid particles, *Int. J. Heat Mass Transf*., **14**, 727-737 (1971).

Yaron, I., Gal-Or, B., High Reynolds number fluid dynamics and heat and mass transfer in real concentrated particulate two-phase systems, *Int. J. Heat Mass Transf*., **16**, 887-895 (1973).

Yu, K., Cao, H., Qian, K., Sha, X., Chen, Y., Shear-thickening behavior of modified silica nanoparticles in polyethylene glycol, *J. Nanopart. Res.*, **14**, 747-745 (2012).

Zhang, Y., Finch, J., A note on single bubble motion in surfactant solutions, *J. Fluid Mech.*, **429**, 63-66 (2001).

Zhang, Y., McLaughlin, J., Finch, J., Bubble velocity profile and model of surfactant mass transfer to bubble surface, *Chem. Engng. Sci*., **56**, 6605-6616 (2001).

Zhang, Y., Sam, A., Finch, J., Temperature effect on single bubble velocity profile in water and surfactant solution, *Colloids Surf. A*, **223**, 45-54 (2003).

Zholkovskij, E.K., Koval'chuk, V.I., Dukhin, S.S., Miller, R., Dynamics of rear stagnant cap formation at low Reynolds numbers, *J. Colloid Interface Sci.*, **226**, 51-59 (2000).

Zholkovskiy, E.K., Masliyah, J.H., Shilov, V.N., Bhattacharjee, S., Electrokinetic phenomena in concentrated disperse systems: general problem formulation and spherical cell approach, *Adv. Colloid Interface Sci.*, **134-135**, 279-321 (2007a)

Zholkovskiy, E.K., Shilov, V.N., Masliyah, J.H., Bondarenko, M.P., Hydrodynamic cell model: General formulation and comparative analysis of different approaches, *Can. J. Chem. Eng.*, **85**, 701-725, (2007b).

Zhu, J., Drag and mass transfer for flow of a Carreau fluid past a swarm of Newtonian drops, *Int. J. Multiphase Flow*, **21**, 935-940 (1995).

Zhu, J., A note on slow non-Newtonian flow over an ensemble of spherical bubbles, *Chem. Eng. Sci.*, **56**, 2237-2241 (2001).

Zhu, J., Deng, W., Non-Newtonian flow past a swarm of Newtonian droplets, *Chem. Engng. Sci.*, **49**, 147-150 (1994).

Zhu, J. and Satish, M.G., Non-Newtonian effects on the drag of creeping flow through packed beds, *Int. J. Multiphase Flow*, **18**, 765-777 (1992).

APPENDIX A

Evaluation of Drag Coefficient

The drag force experienced by a spherical object translating in a fluid is given by the following expression:

$$F_d = \int_0^{\pi} \left[\left(-p^* + \tau_{rr}^* \right) \cos\theta + \tau_{r\theta}^* \left(-\sin\theta \right) \right] 2\pi R^2 \sin\theta d\theta \tag{A-1}$$

The drag coefficient is defined as

$$C_d = \frac{F_d}{(1/2)\rho U_o^2 \pi R^2} \tag{A-2}$$

The normalization parameters are

$$p \to \frac{p^*}{\rho U_o^2}; \quad \tau_{xy} \to \frac{\tau_{xy}^*}{\eta_{app}\left(U_o / R\right)}; \quad \text{where} \quad x, y = r, \theta, \phi$$

Therefore, the drag coefficient can now be simplified as follows

$$C_d = \int_0^{\pi} \left(-2p \sin 2\theta \right) d\theta + 4 \int_0^{\pi} \left[\frac{\tau_{rr}\left(\eta_{app} U_o / R\right) \cos\theta \sin\theta}{\rho U_o^2} - \frac{\tau_{r\theta}\left(\eta_{app} U_o / R\right) \sin^2\theta}{\rho U_o^2} \right] d\theta$$

$$C_d = \int_0^{\pi} \left(-2p \sin 2\theta \right) d\theta + 4 \left(\frac{\eta_{app}}{\rho U_o R} \right) \int_0^{\pi} \left[\tau_{rr} \cos\theta \sin\theta - \tau_{r\theta} \sin^2\theta \right] d\theta \tag{A-3}$$

For power-law fluids

$$\left(\frac{\eta_{app}}{\rho U_o R} \right) = \frac{m\left(U_o / R\right)^{n-1}}{\rho U_o R} = \frac{m}{\rho U_o^{2-n} R^n} = 2^n \left[\frac{m}{\rho U_o^{2-n} \left(2R\right)^n} \right] = \frac{2^n}{\mathrm{Re}_{pl}} \tag{A-4}$$

$$C_d = \int_0^{\pi} \left(-2p\sin 2\theta\right) d\theta + 4\left(\frac{2^n}{\mathrm{Re}_{pl}}\right)\int_0^{\pi}\left[\tau_{rr}\cos\theta\sin\theta - \tau_{r\theta}\sin^2\theta\right]d\theta$$

$$C_d = \int_0^{\pi} \left(-2p\sin 2\theta\right) d\theta + \left(\frac{2^{n+2}}{\mathrm{Re}_{pl}}\right)\int_0^{\pi}\left[\tau_{rr}\cos\theta\sin\theta - \tau_{r\theta}\sin^2\theta\right]d\theta \qquad \text{(A-5)}$$

where

$$\tau_{rr} = 2\eta\varepsilon_{r\theta} = \eta\left[\frac{1}{r}\frac{\partial v_r}{\partial\theta} + \frac{\partial v_\theta}{\partial r} - \frac{v_\theta}{r}\right]$$

$$C_d = \int_0^{\pi} \left(-2p\sin 2\theta\right)_{|r=1} d\theta + \frac{2^{n+2}}{\mathrm{Re}_{pl}}\int_0^{\pi}\left(\eta\left[\left(\frac{\partial v_r}{\partial r}\right)\sin 2\theta - \left(\frac{1}{r}\frac{\partial v_r}{\partial\theta} + \frac{\partial v_\theta}{\partial r} - \frac{v_\theta}{r}\right)\sin^2\theta\right]\right)_{|r=1} d\theta \qquad \text{(A-6)}$$

In the right hand side of the above expression, the first and second integr4ents represent the respective pressure and frictional components of the drag coefficient.

APPENDIX B

Evaluation of Sherwood Number

Equating the mass transfer by diffusion and by convection at the interface, gives the following dimensional relation:

$$-D_o\frac{\partial c^*}{\partial r^*} = k_c\left(C^* - C_o^*\right) \qquad \text{(A-7)}$$

The radial distances are normalized by drop radius (R) and the concentration difference (C^*-C_o^*) by (C_s^*-C_o^*). Therefore, the normalization of above equation leads to the following expression

$$-D_o \frac{\left(C_s^* - C_o^*\right)}{R} \frac{\partial C}{\partial r} = k_c \left(C_s^* - C_o^*\right) \tag{A-8}$$

this gives rise to

$$\frac{k_c R}{D_o} = -\left[\frac{\partial C}{\partial r}\right] \tag{A-9}$$

Therefore,

$$Sh_\theta = \frac{k_c (2R)}{D_o} = -2\left[\frac{\partial C}{\partial r}\right] \tag{A-10}$$

Now, the surface average Sherwood number can be obtained as follows:

$$Sh_{avg} = \frac{1}{4\pi R^2} \int_0^\pi Sh_\theta \left[2\pi R^2\right] \sin\theta d\theta = \frac{1}{2} \int_0^\pi Sh_\theta \sin\theta d\theta \tag{A-11}$$

APPENDIX -C

The r- and θ-components of momentum equations, respectively, can be written as follows:

$$\frac{\partial v_r}{\partial t} + [CONVR] = -\frac{\partial p}{\partial r} + [DIFF - R] + [NON - R] \tag{B-1}$$

$$\frac{\partial v_\theta}{\partial t} + [CONV\theta] = -\frac{1}{r}\frac{\partial p}{\partial \theta} + [DIFF - \theta] + [NON - \theta] \tag{B-2}$$

Discretization of Governing Equations

Discretization of r-component of Momentum Equation

Since for r-component of momentum equation (i, j+1/2) is the centre of the v_r-control volume, the individual terms of equation (B-1) can be discretized as follows:

$$CONVR = \left[\frac{1}{r^2}\frac{\partial (v_r{}^2 r^2)}{\partial r} + \frac{1}{r\sin\theta}\frac{\partial (v_r v_\theta \sin\theta)}{\partial \theta} - \frac{v_\theta{}^2}{r}\right]$$

$$\left[\frac{1}{r^2}\frac{\partial\left(v_r{}^2 r^2\right)}{\partial r}\right]_{(i,j+1/2)} = \frac{\left(v_{ravg}v_{rup}r^2\right)_{i,j+1} - \left(v_{ravg}v_{rup}r^2\right)_{i,j}}{r_{j+1/2}{}^2 \Delta r_{j+1/2}}$$

where

$$v_{ravg}(i,j+1) = \frac{v_r(i,j+1/2) + v_r(i,j+3/2)}{2}$$

$$v_{ravg}(i,j) = \frac{v_r(i,j-1/2) + v_r(i,j+1/2)}{2}$$

if $v_{ravg}(i,j+1) \geq 0$ then

$$v_{rup} = \frac{3}{8}v_r(i,j+1) + \frac{3}{4}v_r(i,j) - \frac{1}{8}v_r(i,j-1)$$

else

$$v_{rup} = \frac{3}{8}v_r(i,j) + \frac{3}{4}v_r(i,j+1) - \frac{1}{8}v_r(i,j+2)$$

if $v_{ravg}(i,j) \geq 0$ then

$$v_{rup} = \frac{3}{8}v_r(i,j) + \frac{3}{4}v_r(i,j-1) - \frac{1}{8}v_r(i,j-2)$$

else

$$v_{rup}(i,j) = \frac{3}{8}v_r(i,j-1) + \frac{3}{4}v_r(i,j) - \frac{1}{8}v_r(i,j+1)$$

$$\left[\frac{1}{r\sin\theta}\frac{\partial\left(v_r v_\theta \sin\theta\right)}{\partial\theta}\right]_{(i,j+1/2)} = \frac{\left(v_{rup}v_{\theta avg}\sin\theta\right)_{i+1/2,j+1/2} - \left(v_{rup}v_{\theta avg}\sin\theta\right)_{i-1/2,j+1/2}}{r_{j+1/2}\sin\theta_i d\theta}$$

$$v_{\theta avg}(i+1/2, j+1/2) = \frac{v_\theta(i+1/2, j) + v_\theta(i+1/2, j+1)}{2}$$

$$v_{\theta avg}(i-1/2, j+1/2) = \frac{v_\theta(i-1/2, j) + v_\theta(i-1/2, j+1)}{2}$$

If $v_{\theta avg}$ (i+1/2,j+1/2) ≥ 0 then

$$v_{rup} = \frac{3}{8}v_r(i+1, j) + \frac{3}{4}v_r(i, j) - \frac{1}{8}v_r(i-1, j)$$

else

$$v_{rup} = \frac{3}{8}v_r(i, j) + \frac{3}{4}v_r(i+1, j) - \frac{1}{8}v_r(i+2, j)$$

if $v_{\theta avg}$ (i-1/2,j+1/2) ≥ 0 then

$$v_{rup} = \frac{3}{8}v_r(i, j) + \frac{3}{4}v_r(i-1, j) - \frac{1}{8}v_r(i-2, j)$$

else

$$v_{rup} = \frac{3}{8}v_r(i-1, j) + \frac{3}{4}v_r(i, j) - \frac{1}{8}v_r(i+1, j)$$

$$\left[\frac{v_\theta{}^2}{r}\right]_{i,j+1/2} = \frac{\left[v_\theta(i-1/2, j+1) + v_\theta(i+1/2, j+1) + v_\theta(i-1/2, j) + v_\theta(i+1/2, j)\right]^2}{16 r_{j+1/2}}$$

$$-\left[\frac{\partial p}{\partial r}\right]_{i,j+1/2} = -\left(\frac{p(i, j+1) - p(i, j)}{\Delta r}\right)$$

$$DIFFR = \frac{2^n \eta}{Re}\left[\frac{1}{r^2}\frac{\partial^2(r^2 v_r)}{\partial r^2} + \frac{1}{r^2 \sin\theta}\frac{\partial\left(\sin\theta \dfrac{\partial v_r}{\partial \theta}\right)}{\partial \theta}\right]$$

$$\left[\frac{1}{r^2}\frac{\partial^2\left(r^2 v_r\right)}{\partial r^2}\right]_{i,j+1/2} = \frac{1}{r_{j+1/2}{}^2}\left[\frac{\dfrac{\partial}{\partial r}\left(r^2 v_r\right)_{i,j+1} - \dfrac{\partial}{\partial r}\left(r^2 v_r\right)_{i,j}}{\Delta r}\right]$$

where

$$\frac{\partial}{\partial r}\left(r^2 v_r\right)_{i,j+1} = \frac{r^2{}_{j+3/2} v_{ri,j+3/2} - r^2{}_{j+1/2} v_{ri,j+1/2}}{\Delta r}$$

$$\frac{\partial}{\partial r}\left(r^2 v_r\right)_{i,j} = \frac{r^2{}_{j+1/2} v_{ri,j+1/2} - r^2{}_{j-1/2} v_{ri,j-1/2}}{\Delta r}$$

$$\left[\frac{1}{r^2\sin\theta}\frac{\partial}{\partial\theta}\left(\sin\theta\frac{\partial v_r}{\partial\theta}\right)\right]_{i,j+1/2} = \frac{1}{r^2_{j+1/2}\sin\theta_i}\left[\frac{\left(\sin\theta\frac{\partial v_r}{\partial\theta}\right)_{i+1/2,j+1/2} - \left(\sin\theta\frac{\partial v_r}{\partial\theta}\right)_{i-1/2,j+1/2}}{\Delta\theta}\right]$$

where

$$\left(\sin\theta\frac{\partial v_r}{\partial\theta}\right)_{i+1/2,j+1/2} = \sin\theta_{i+1/2}\left(\frac{v_r(i+1,j+1/2)-v_r(i,j+1/2)}{\Delta\theta}\right)$$

$$\left(\sin\theta\frac{\partial v_r}{\partial\theta}\right)_{i-1/2,j+1/2} = \sin\theta_{i-1/2}\left(\frac{v_r(i,j+1/2)-v_r(i-1,j+1/2)}{\Delta\theta}\right)$$

$$\eta(i,j+1/2) = \frac{\eta(i,j)+\eta(i,j+1)}{2}$$

$$NONR = \frac{2^{(n+1)}}{Re}\left[\varepsilon_{rr}\frac{\partial\eta}{\partial r} + \frac{\varepsilon_{r\theta}}{r}\frac{\partial\eta}{\partial\theta}\right]$$

where

$$\varepsilon_{rr} = \left(\frac{\partial v_r}{\partial r}\right)_{i,j+1/2} = \frac{v_r(i,j+3/2)-v_r(i,j-1/2)}{2\Delta r}$$

$$\varepsilon_{r\theta} = \frac{1}{2}\left(\frac{1}{r}\frac{\partial v_r}{\partial\theta} + \frac{\partial v_\theta}{\partial r} - \frac{v_\theta}{r}\right)_{i,j+1/2}$$

$$\left(\frac{1}{r}\frac{\partial v_r}{\partial\theta}\right)_{i,j+1/2} = \left(\frac{1}{r_{j+1/2}}\right)\left[\frac{v_r(i+1,j+1/2)-v_r(i-1,j+1/2)}{2\Delta\theta}\right]$$

$$\left(\frac{\partial v_\theta}{\partial r}\right)_{i,j+1/2} = \left[\frac{v_\theta(i,j+1)-v_\theta(i,j)}{\Delta r}\right]$$

$$= \left[\frac{v_\theta(i+1/2,j+1)+v_\theta(i-1/2,j+1)-\left(v_\theta(i+1/2,j)+v_\theta(i-1/2,j)\right)}{2\Delta r}\right]$$

$$\left(\frac{v_\theta}{r}\right)_{i,j+1/2} = \left[\frac{v_\theta(i+1/2,j+1)+v_\theta(i-1/2,j+1)-\left(v_\theta(i+1/2,j)+v_\theta(i-1/2,j)\right)}{4r_{j+1/2}}\right]$$

$$\left(\frac{\partial \eta}{\partial \theta}\right)_{i,j+1/2} = \left[\frac{\eta(i+1, j+1/2) - \eta(i-1, j+1/2)}{2\Delta\theta}\right]$$

$$= \left[\frac{\eta(i+1, j) + \eta(i+1, j+1) - \left(\eta(i-1, j) + \eta(i-1, j+1)\right)}{4\Delta\theta}\right]$$

$$\left(\frac{\partial \eta}{\partial r}\right)_{i,j+1/2} = \left[\frac{\eta(i, j+1) - \eta(i, j)}{\Delta r}\right]$$

Discretization of θ-component of Momentum Equation

Since for θ-component of momentum equation (i+1/2,j) is the centre of the vΘ-control volume, equation (B-2) can be discretized as follows:

$$CONV\theta = \left[\frac{1}{r^2}\frac{\partial\left(r^2 v_r v_\theta\right)}{\partial r} + \frac{1}{r\sin\theta}\frac{\partial\left(v_\theta{}^2 \sin\theta\right)}{\partial\theta} + \frac{v_r v_\theta}{r}\right]$$

$$\left[\frac{1}{r^2}\frac{\partial\left(r^2 v_r v_\theta\right)}{\partial r}\right]_{i+1/2,j} = \left[\frac{\left(r^2 v_{ravg} v_{\theta up}\right)_{i+1/2,j+1/2} - \left(r^2 v_{ravg} v_{\theta up}\right)_{i+1/2,j-1/2}}{r_j{}^2 \Delta r}\right]$$

where

$$v_{ravg}\left(i+1/2, j+1/2\right) = \frac{v_r\left(i, j+1/2\right) + v_r\left(i+1, j+1/2\right)}{2}$$

$$v_{ravg}\left(i+1/2, j-1/2\right) = \frac{v_r\left(i, j-1/2\right) + v_r\left(i+1, j-1/2\right)}{2}$$

if $v_{ravg}(i+1/2,j+1/2) \geq 0$ then

$$v_{\theta up} = \frac{3}{8}v_\theta(i, j+1) + \frac{3}{4}v_\theta(i, j) - \frac{1}{8}v_\theta(i, j-1)$$

else

$$v_{\theta up} = \frac{3}{8}v_\theta(i, j) + \frac{3}{4}v_\theta(i, j+1) - \frac{1}{8}v_\theta(i, j+2)$$

if $v_{ravg}(i+1/2,j-1/2) \geq 0$ then

$$v_{\theta up} = \frac{3}{8}v_\theta(i,j) + \frac{3}{4}v_\theta(i,j-1) - \frac{1}{8}v_\theta(i,j-2)$$

else

$$v_{\theta up} = \frac{3}{8}v_\theta(i,j-1) + \frac{3}{4}v_\theta(i,j) - \frac{1}{8}v_\theta(i,j+1)$$

$$\left[\frac{1}{r\sin\theta}\frac{\partial\left(v_\theta{}^2\sin\theta\right)}{\partial\theta}\right]_{i+1/2,j} = \left(\frac{1}{r_j\sin\theta_i}\right)\left[\frac{\left(v_{\theta avg}v_{\theta up}\sin\theta\right)_{i+1,j} - \left(v_{\theta avg}v_{\theta up}\sin\theta\right)_{i,j}}{\Delta\theta}\right]$$

where

$$v_{\theta avg}(i+1,j) = \frac{v_\theta(i+3/2,j) + v_\theta(i+1/2,j)}{2}$$

$$v_{\theta avg}(i,j) = \frac{v_\theta(i+1/2,j) + v_\theta(i-1/2,j)}{2}$$

if $v_{\theta avg}(i+1,j) \geq 0$ then

$$v_{\theta up} = \frac{3}{8}v_\theta(i+1,j) + \frac{3}{4}v_\theta(i,j) - \frac{1}{8}v_\theta(i-1,j)$$

else

$$v_{\theta up} = \frac{3}{8}v_\theta(i,j) + \frac{3}{4}v_\theta(i+1,j) - \frac{1}{8}v_\theta(i+2,j)$$

if $v_{\theta avg}(i,j) \geq 0$ then

$$v_{\theta up} = \frac{3}{8}v_\theta(i,j) + \frac{3}{4}v_\theta(i-1,j) - \frac{1}{8}v_\theta(i-2,j)$$

else

$$v_{\theta up} = \frac{3}{8}v_\theta(i-1,j) + \frac{3}{4}v_\theta(i,j) - \frac{1}{8}v_\theta(i+1,j)$$

$$\left[\frac{v_r v_\theta}{r}\right]_{i+1/2,j} = \left[\frac{v_r(i,j+1/2) + v_r(i+1,j+1/2) + v_r(i,j-1/2) + v_r(i+1,j-1/2)}{4}\right]\left(\frac{v_\theta(i+1/2,j)}{r_j}\right)$$

$$\left(-\frac{1}{r}\frac{\partial p}{\partial \theta}\right)_{i+1/2,j} = -\left(\frac{1}{r_j}\right)\left[\frac{p(i+1,j)-p(i,j)}{\Delta\theta}\right]$$

$$DIFF\theta = \frac{2^n\eta}{Re}\left[\frac{1}{r^2}\frac{\partial}{\partial r}\left(r^2\frac{\partial v\theta}{\partial r}\right)+\frac{1}{r^2}\frac{\partial}{\partial\theta}\left(\frac{1}{\sin\theta}\frac{\partial}{\partial\theta}(v_\theta\sin\theta\right)+\frac{2}{r^2}\frac{\partial v_r}{\partial\theta}\right]$$

$$\left[\frac{1}{r^2}\frac{\partial}{\partial r}\left(r^2\frac{\partial v_\theta}{\partial r}\right)\right]_{i+1/2,j} = \left(\frac{1}{r_j^{\,2}}\right)\left[\frac{\left(r^2\frac{\partial v_\theta}{\partial r}\right)_{i+1/2,j+1/2}-\left(r^2\frac{\partial v_\theta}{\partial r}\right)_{i+1/2,j-1/2}}{\Delta r}\right]$$

where

$$\left(r^2\frac{\partial v_\theta}{\partial r}\right)_{i+1/2,j+1/2} = \left(r^2{}_{j+1/2}\right)\left[\frac{v_\theta(i+1/2,j+1)-v_\theta(i+1/2,j)}{\Delta r}\right]$$

$$\left(r^2\frac{\partial v_\theta}{\partial r}\right)_{i+1/2,j-1/2} = \left(r^2{}_{j-1/2}\right)\left[\frac{v_\theta(i+1/2,j)-v_\theta(i+1/2,j-1)}{\Delta r}\right]$$

$$\left[\frac{1}{r^2}\frac{\partial}{\partial\theta}\left(\frac{1}{\sin\theta}\frac{\partial}{\partial\theta}(v_\theta\sin\theta)\right)\right]_{i+1/2,j} = \left(\frac{1}{r_j^{\,2}}\right)\left[\frac{\left(\frac{1}{\sin\theta}\frac{\partial}{\partial\theta}(v_\theta\sin\theta)\right)_{i+1,j}-\left(\frac{1}{\sin\theta}\frac{\partial}{\partial\theta}(v_\theta\sin\theta)\right)_{i,j}}{\Delta\theta}\right]$$

where

$$\left[\frac{1}{\sin\theta}\frac{\partial}{\partial\theta}(v_\theta\sin\theta)\right]_{i+1,j} = \left(\frac{1}{\sin\theta_{i+1}}\right)\left[\frac{v_\theta(i+3/2,j)\sin\theta_{i+3/2}-v_\theta(i+1/2,j)\sin\theta_{i+1/2}}{\Delta\theta}\right]$$

$$\left[\frac{1}{\sin\theta}\frac{\partial}{\partial\theta}(v_\theta\sin\theta)\right]_{i,j} = \left(\frac{1}{\sin\theta_i}\right)\left[\frac{v_\theta(i+1/2,j)\sin\theta_{i+1/2}-v_\theta(i-1/2,j)\sin\theta_{i-1/2}}{\Delta\theta}\right]$$

$$\left[\frac{2}{r^2}\frac{\partial v_r}{\partial\theta}\right]_{i+1/2,j} = \left(\frac{2}{r_j^{\,2}}\right)\left[\frac{v_r(i+1,j)-v_r(i,j)}{\Delta\theta}\right]$$

$$= \left(\frac{2}{r_j^{\,2}}\right)\left[\frac{\left(v_r(i+1,j+1/2)+v_r(i+1,j-1/2)\right)-\left(v_r(i,j+1/2)+v_r(i,j-1/2)\right)}{2\Delta\theta}\right]$$

$$\eta(i+1/2,\, j) = \left[\frac{\eta(i+1,\, j)+\eta(i,\, j)}{2}\right]$$

$$NON\theta = \frac{2^{(n+1)}}{Re}\left[\varepsilon_{r\theta}\frac{\partial\eta}{\partial r}+\frac{\varepsilon_{\theta\theta}}{r}\frac{\partial\eta}{\partial\theta}\right]$$

where

$$\varepsilon_{r\theta} = \frac{1}{2}\left(\frac{1}{r}\frac{\partial v_r}{\partial\theta}+\frac{\partial v_\theta}{\partial r}-\frac{v_\theta}{r}\right)_{i+1/2,\,j}$$

$$\left(\frac{1}{r}\frac{\partial v_r}{\partial\theta}\right)_{i+1/2,\,j} = \left(\frac{1}{r_j}\right)\left[\frac{v_r(i+1,\, j)-v_r(i-1,\, j)}{2\Delta\theta}\right]$$

$$= \left(\frac{1}{r_j}\right)\left[\frac{\left(v_r(i+1,\, j+1/2)+v_r(i+1,\, j-1/2)\right)-\left(v_r(i-1,\, j+1/2)+v_r(i-1,\, j-1/2)\right)}{4\Delta\theta}\right]$$

$$\left(\frac{\partial v_\theta}{\partial r}\right)_{i+1/2,\,j} = \left[\frac{v_\theta(i+1/2,\, j+1)-v_\theta(i+1/2,\, j-1)}{2\Delta r}\right]$$

$$\left(\frac{v_\theta}{r}\right)_{i+1/2,\,j} = \frac{v_\theta(i+1/2,\, j)}{r_j}$$

$$\varepsilon_{\theta\theta} = \left[\frac{v_r}{r}+\frac{1}{r}\frac{\partial v_\theta}{\partial\theta}\right]_{i+1/2,\,j}$$

$$\left(\frac{v_r}{r}\right)_{i+1/2,\,j} = \left(\frac{1}{r_j}\right)\left[\frac{v_r(i+1,\, j+1/2)+v_r(i+1,\, j-1/2)+v_r(i,\, j+1/2)+v_r(i,\, j-1/2)}{4}\right]$$

$$\left(\frac{1}{r}\frac{\partial v_\theta}{\partial\theta}\right)_{i+1/2,\,j} = \left(\frac{1}{r_j}\right)\left[\frac{v_\theta(i+3/2,\, j)-v_\theta(i-1/2,\, j)}{2\Delta\theta}\right]$$

$$\left(\frac{\partial\eta}{\partial r}\right)_{i+1/2,\,j} = \left[\frac{\eta(i,\, j+1)+\eta(i+1,\, j+1)-\eta(i,\, j-1)-\eta(i+1,\, j-1)}{4\Delta r}\right]$$

$$\left(\frac{\partial\eta}{\partial\theta}\right)_{i+1/2,\,j} = \frac{\eta(i+1,\, j)-\eta(i,\, j)}{\Delta\theta}$$

Discretization of Continuity Equation

$$\left[\frac{1}{r^2}\frac{\partial\left(r^2 v_r\right)}{\partial r}+\frac{1}{r\sin\theta}\frac{\partial\left(v_\theta \sin\theta\right)}{\partial\theta}\right]_{i,j}=0$$

$$\left[\frac{1}{r^2}\frac{\partial\left(r^2 v_r\right)}{\partial r}\right]_{i,j}=\left[\frac{\left(r^2 v_r\right)_{i,j+1}-\left(r^2 v_r\right)_{i,j-1}}{r_j^{\,2}\left(2\Delta r\right)}\right]=\left[\frac{\left(r_{j+1}{}^2 v_r(i,j+1)\right)-\left(r_{j-1}{}^2 v_r(i,j-1)\right)}{r_j^{\,2}\left(2\Delta r\right)}\right]$$

$$\left[\frac{1}{r\sin\theta}\frac{\partial\left(v_\theta\sin\theta\right)}{\partial\theta}\right]_{i,j}=\left(\frac{1}{r_j\sin\theta_i}\right)\left[\frac{\left(v_\theta\sin\theta\right)_{i+1,j}-\left(v_\theta\sin\theta\right)_{i-1,j}}{2\Delta\theta}\right]$$

$$=\left(\frac{1}{r_j\sin\theta_i}\right)\left[\frac{\left(\sin\theta_{i+1}v_\theta(i+1,j)\right)-\left(\sin\theta_{i-1}v_\theta(i-1,j)\right)}{2\Delta\theta}\right]$$

Discretization of Power-law Fluid Viscosity Equation

$$\eta=\left[2\Pi_\varepsilon\right]^{(n-1)/2}$$

where

$$\Pi_\varepsilon=\varepsilon_{rr}{}^2+\varepsilon_{\theta\theta}{}^2+\varepsilon_{\phi\phi}{}^2+2\varepsilon_{r\theta}{}^2$$

The centre of control volume of the viscosity is (i,j) and it can be discretized as follows:

$$\varepsilon_{rr}=\left(\frac{\partial v_r}{\partial r}\right)_{i,j}=\frac{v_r(i,j+1/2)-v_r(i,j-1/2)}{\Delta r}$$

$$\varepsilon_{\theta\theta}=\left[\frac{v_r}{r}+\frac{1}{r}\frac{\partial v_\theta}{\partial\theta}\right]_{i,j}$$

$$\left(\frac{v_r}{r}\right)_{i,j}=\left(\frac{1}{r_j}\right)\left[\frac{v_r(i,j+1/2)+v_r(i,j-1/2)}{2}\right]$$

$$\left(\frac{1}{r}\frac{\partial v_\theta}{\partial\theta}\right)_{i,j}=\left(\frac{1}{r_j}\right)\left[\frac{v_\theta(i+1/2,j)-v_\theta(i-1/2,j)}{\Delta\theta}\right]$$

$$\varepsilon_{\phi\phi}=\left(\frac{v_r+v_\theta\cot\theta}{r}\right)_{i,j}$$

$$= \left(\frac{\left(v_r(i, j+1/2) + v_r(i, j-1/2)\right) + \left(v_\theta(i+1/2, j) + v_\theta(i-1/2, j)\right)\cot\theta_i}{2r_j} \right)$$

$$\varepsilon_{r\theta} = \frac{1}{2}\left(\frac{1}{r}\frac{\partial v_r}{\partial \theta} + \frac{\partial v_\theta}{\partial r} - \frac{v_\theta}{r} \right)_{i,j}$$

$$\left(\frac{1}{r}\frac{\partial v_r}{\partial \theta} \right)_{i,j} = \left(\frac{1}{r_j} \right)\left[\frac{v_r(i+1, j+1/2) - v_r(i-1, j+1/2)}{2\Delta\theta} \right]$$

$$= \left(\frac{1}{r_j} \right)\left[\frac{\left(v_r(i+1, j+1/2) + v_r(i+1, j-1/2)\right) - \left(v_r(i-1, j+1/2) + v_r(i-1, j-1/2)\right)}{4\Delta\theta} \right]$$

$$\left(\frac{\partial v_\theta}{\partial r} \right)_{i,j} = \left[\frac{\left(v_\theta(i+1/2, j+1) + v_\theta(i-1/2, j+1)\right) - \left(v_\theta(i+1/2, j-1) - v_\theta(i-1/2, j-1)\right)}{4\Delta r} \right]$$

$$\left(\frac{v_\theta}{r} \right)_{i,j} = \frac{v_\theta(i+1/2, j) + v_\theta(i-1/2, j)}{2r_j}$$

Discretization of Pressure Correction Equation

This equation is discretized by taking centre (i, j). Let

$$D_{i,j} = \nabla . V^*$$

$$\nabla^2 p' = \frac{\nabla . V^*}{\Delta t} - \nabla^2\left(\nabla . V^*\right)$$

where

$$D_{i,j} = \left[\frac{1}{r^2}\frac{\partial\left(r^2 v_r^*\right)}{\partial r} + \frac{1}{r\sin\theta}\frac{\partial\left(v_\theta^* \sin\theta\right)}{\partial \theta} \right]_{i,j}$$

and

$$\left(\nabla^2 p'\right)_{i,j} = \left[\frac{1}{r^2}\frac{\partial}{\partial r}\left(r^2 \frac{\partial p'}{\partial r} \right) + \frac{1}{r^2\sin\theta}\frac{\partial}{\partial \theta}\left(\sin\theta \frac{\partial p'}{\partial \theta} \right) \right]_{i,j}$$

Discretizing *Di,j* we get

$$\left[\frac{1}{r^2}\frac{\partial\left(r^2 v_r^{\,*}\right)}{\partial r}\right]_{i,j} = \left[\frac{\left(r^2 v_r^{\,*}\right)_{i,j+1/2} - \left(r^2 v_r^{\,*}\right)_{i,j-1/2}}{r_j^{\,2}\Delta r}\right]$$

$$= \left[\frac{\left(r_{j+1}^{\,2} v_r^{\,*}(i, j+1/2)\right) - \left(r_{j-1}^{\,2} v_r^{\,*}(i, j-1/2)\right)}{r_j^{\,2}\Delta r}\right]$$

$$= \left[\frac{\left(r_{j+1}^{\,2} v_r^{\,*}(i, j+1/2)\right) - \left(r_{j-1}^{\,2} v_r^{\,*}(i, j-1/2)\right)}{r_j^{\,2}\Delta r}\right]$$

$$\left[\frac{1}{r\sin\theta}\frac{\partial\left(v_\theta^{\,*}\sin\theta\right)}{\partial\theta}\right]_{i,j} = \left[\frac{\left(v_\theta^{\,*}\sin\theta\right)_{i+1/2,j} - \left(v_\theta^{\,*}\sin\theta\right)_{i-1/2,j}}{\left(r_j\sin\theta_i\right)(\Delta\theta)}\right]$$

$$= \left(\frac{1}{r_j\sin\theta_i}\right)\left[\frac{\left(\sin\theta_{i+1/2} v_\theta^{\,*}(i+1/2, j)\right) - \left(\sin\theta_{i-1/2} v_\theta^{\,*}(i-1/2, j)\right)}{\Delta\theta}\right]$$

Discretizing $\left(\nabla^2 p'\right)_{i,j}$ we get

$$\left[\frac{1}{r^2}\frac{\partial}{\partial r}\left(r^2\frac{\partial p'}{\partial r}\right)\right]_{i,j} = \left[\frac{\left(r^2\frac{\partial p'}{\partial r}\right)_{i,j+1/2} - \left(r^2\frac{\partial p'}{\partial r}\right)_{i,j-1/2}}{r_j^{\,2}\Delta r}\right]$$

where

$$\left(r^2\frac{\partial p'}{\partial r}\right)_{i,j+1/2} = r_{j+1/2}^{\,2}\left[\frac{p'(i, j+1) - p'(i, j)}{\Delta r}\right]$$

$$\left(r^2\frac{\partial p'}{\partial r}\right)_{i,j-1/2} = r_{j-1/2}^{\,2}\left[\frac{p'(i, j) - p'(i, j-1)}{\Delta r}\right]$$

$$\left[\frac{1}{r^2\sin\theta}\frac{\partial}{\partial\theta}\left(\sin\theta\frac{\partial p'}{\partial\theta}\right)\right]_{i,j} = \left[\frac{\left(\sin\theta\frac{\partial p'}{\partial\theta}\right)_{i+1/2,j} - \left(\sin\theta\frac{\partial p'}{\partial\theta}\right)_{i-1/2,j}}{r_j^{\,2}\sin\theta_i\Delta\theta}\right]$$

where

$$\left(\sin\theta\frac{\partial p'}{\partial\theta}\right)_{i+1/2,j}=\sin\theta_{i+1/2}\left[\frac{p'(i+1,j)-p'(i,j)}{\Delta\theta}\right]$$

$$\left(\sin\theta\frac{\partial p'}{\partial\theta}\right)_{i-1/2,j}=\sin\theta_{i-1/2}\left[\frac{p'(i,j)-p'(i-1,j)}{\Delta\theta}\right]$$

Discretization of Vorticity Equation

The vorticity in spherical coordinates can be calculated using the formula given below:

$$\omega_{r\theta}=\frac{\partial v_\theta}{\partial r}+\frac{v_\theta}{r}-\frac{1}{r}\frac{\partial v_r}{\partial\theta} \qquad \text{(B-4)}$$

The above equation is discretized using the central difference scheme with (i+1/2, j+1/2) as centre of the control volume:

$$\omega_{r\theta}(i+1/2,j+1/2)=\frac{v_\theta(i+1/2,j+1)-v_\theta(i+1/2,j-1)}{2\Delta r}+\frac{v_\theta(i+1/2,j+1)+v_\theta(i+1/2,j)}{2r_{j+1/2}}$$

$$-\frac{1}{r_{j+1/2}}\frac{v_r(i+1,j+1/2)-v_r(i,j+1/2)}{\Delta\theta}$$

Henceforth $\omega_{r\theta}$ will be presented as ω.

Discretization of Stream Function Expression

The stream function in spherical coordinates can be calculated using the following expression:

$$E^2(\psi)=\omega r\sin\theta \qquad \text{(B-5)}$$

where

$$E^2(\psi)=\frac{\partial^2\psi}{\partial r^2}+\frac{\sin\theta}{r^2}\frac{\partial}{\partial\theta}\left(\frac{1}{\sin\theta}\frac{\partial\psi}{\partial\theta}\right)$$

and

$$v_r = \frac{-1}{r^2 \sin\theta}\frac{\partial \psi}{\partial \theta}; \qquad v_\theta = \frac{1}{r \sin\theta}\frac{\partial \psi}{\partial r}$$

Discretizing $\left[E^2(\psi)\right]_{i+1/2,\, j+1/2}$ we get

$$\left[\frac{\partial^2 \psi}{\partial r^2}\right]_{i+1/2,\, j+1/2} = \left[\frac{\psi(i+1/2,\, j+3/2) - 2.0\psi(i+1/2,\, j+1/2) + \psi(i+1/2,\, j-1/2)}{\Delta r^2}\right]$$

$$\left[\frac{\partial}{\partial \theta}\left(\frac{1}{\sin\theta}\frac{\partial \psi}{\partial \theta}\right)\right]_{i+1/2,\, j+1/2} = \left[\frac{\psi(i+3/2,\, j+1/2) - \psi(i-1/2,\, j+1/2)}{\Delta\theta^2 \sin\theta_{i+1/2}} + \frac{\psi(i+1/2,\, j+1/2) - \psi(i-3/2,\, j+1/2)}{\Delta\theta^2 \sin\theta_{i-1/2}}\right]$$

Discretization of Species Continuity Equation

The Dimensionless mass transfer equation for the continuous phase in its conservative form can be written as follows:

$$\frac{\partial C}{\partial t} + \frac{1}{r^2}\frac{\partial}{\partial r}\left[r^2 v_{r,o} C\right] + \frac{1}{r \sin\theta}\frac{\partial}{\partial \theta}\left[v_{\theta,o} C \sin\theta\right] = \frac{2}{Pe}\left[\frac{1}{r^2}\frac{\partial}{\partial r}\left(r^2 \frac{\partial C}{\partial r}\right) + \frac{1}{r^2 \sin\theta}\frac{\partial}{\partial \theta}\left(\sin\theta \frac{\partial C}{\partial \theta}\right)\right] \tag{B-6}$$

The temporal term is discretized as

$$\frac{\partial C}{\partial t} = \frac{C(i,j)^{ts+1} - C(i,j)^{ts}}{\Delta t}$$

The convective terms have been discretized using the QUICK scheme as follows:

$$\frac{1}{r^2}\frac{\partial}{\partial r}\left[r^2 v_{r,o} C\right]_{i,j} = \frac{\left(r^2 v_{r,o} C_{up}\right)_{i,\, j+1/2} - \left(r^2 v_{r,o} C_{up}\right)_{i,\, j-1/2}}{r^2(j)\Delta r}$$

If

$$v_{r,o}(i,\, j+1/2) \geq 0$$

then

$$C_{up}(i, j+1/2) = \frac{3}{8}C(i, j+1) + \frac{3}{4}C(i, j) - \frac{1}{8}C(i, j-1)$$

else

$$C_{up}(i, j+1/2) = \frac{3}{8}C(i, j) + \frac{3}{4}C(i, j+1) - \frac{1}{8}C(i, j+2)$$

If

$$v_{r,o}(i, j-1/2) \geq 0$$

then

$$C_{up}(i, j-1/2) = \frac{3}{8}C(i, j) + \frac{3}{4}C(i, j-1) - \frac{1}{8}C(i, j-2)$$

else

$$C_{up}(i, j-1/2) = \frac{3}{8}C(i, j-1) + \frac{3}{4}C(i, j) - \frac{1}{8}C(i, j+1)$$

$$\frac{1}{r\sin\theta}\frac{\partial}{\partial\theta}\left[v_{\theta,o}C\sin\theta\right]_{i,j} = \frac{\left(v_{\theta,o}C_{up}\sin\theta\right)_{i+1/2,j} - \left(v_{\theta,o}C_{up}\sin\theta\right)_{i-1/2,j}}{r(j)\sin\theta_i\Delta\theta}$$

If

$$v_{\theta,o}(i+1/2, j) \geq 0$$

then

$$C_{up}(i+1/2, j) = \frac{3}{8}C(i+1, j) + \frac{3}{4}C(i, j) - \frac{1}{8}C(i-1, j)$$

else

$$C_{up}(i+1/2, j) = \frac{3}{8}C(i, j) + \frac{3}{4}C(i+1, j) - \frac{1}{8}C(i+2, j)$$

If

$$v_{\theta,o}\left(i-1/2,\, j\right)\geq 0$$

then

$$C_{up}\left(i-1/2,\, j\right)=\frac{3}{8}C\left(i,\, j\right)+\frac{3}{4}C\left(i-1,\, j\right)-\frac{1}{8}C\left(i-2,\, j\right)$$

else

$$C_{up}\left(i-1/2,\, j\right)=\frac{3}{8}C\left(i-1,\, j\right)+\frac{3}{4}C\left(i,\, j\right)-\frac{1}{8}C\left(i+1,\, j\right)$$

The diffusive terms have been discretized using second order central differencing scheme as follows:

$$\left[\frac{1}{r^2}\frac{\partial}{\partial r}\left(r^2\frac{\partial C}{\partial r}\right)\right]_{i,j}=\frac{\left(r^2\frac{\partial C}{\partial r}\right)_{i,j+1/2}-\left(r^2\frac{\partial C}{\partial r}\right)_{i,j-1/2}}{r^2\left(j\right)\Delta r}$$

$$=\frac{r^2\left(j+1/2\right)\left[C\left(i,\, j+1\right)-C(i,\, j)\right]-r^2\left(j-1/2\right)\left[C\left(i,\, j\right)-C\left(i,\, j-1\right)\right]}{r^2\left(j\right)\Delta r^2}$$

$$\left[\frac{1}{r^2\sin\theta}\frac{\partial}{\partial\theta}\left(\sin\theta\frac{\partial C}{\partial\theta}\right)\right]_{i,j}=\frac{\left(\sin\theta\frac{\partial C}{\partial\theta}\right)_{i+1/2,j}-\left(\sin\theta\frac{\partial C}{\partial\theta}\right)_{i-1/2,j}}{r^2\left(j\right)\sin\theta_i\Delta\theta}$$

$$=\frac{\sin\theta\left(i+1/2\right)\left[C\left(i+1,\, j\right)-C(i,\, j)\right]-\sin\theta\left(i-1/2\right)\left[C\left(i,\, j\right)-C\left(i-1,\, j\right)\right]}{r^2\left(j\right)\sin\theta_i\Delta\theta^2}$$

RESEARCH OUTPUT

1. Venkata Swamy Nalajala, Raj. P. Chhabra, Nanda Kishore, **"**Effect of Surfactants on Rise Velocity of Bubble Swarms at Moderate Reynolds Numbers", *Chemical Engineering Research and Design, 92* (**2013**) 1016-1026.

2. Venkata Swamy Nalajala, Nanda Kishore, "Drag of Contaminated Bubbles in Power-law Fluids", *Colloids and Surfaces A: Physicochemical and Engineering Aspects* A, *443* **(2014)** 240-248.

3. Nanda Kishore, Venkata Swamy Nalajala, Raj. P. Chhabra, **"**Effects of Contamination and Shear-thinning Fluid Viscosity on Drag Behavior of Spherical Bubbles", *Industrial and Engineering Chemistry Research, 52* **(2013)** 6049-6056.

4. Venkata Swamy Nalajala, Nanda Kishore, "Heat Transfer Phenomenon of Spherical Bubbles in Contaminated Power-law Liquids", *Chemical Engineering & Technology*, 37 **(2014)** 1757-1764.

5. Venkata Swamy Nalajala, Nanda Kishore, "Effects of Wall Retardation and Surfactant-laden Power-law Fluid Viscosity on Momentum Transfer Characteristics of Partially Contaminated Bubbles", *International Journal of Mineral Processing*, (Under Revision).

6. Venkata Swamy Nalajala, Nanda Kishore, "Effects of Wall Retardation and Surfactant-laden Power-law Fluid Viscosity on Heat Transfer Characteristics of Partially Contaminated Bubbles", Manuscript under preparation.

7. Venkata Swamy Nalajala, Nanda Kishore, "Mass Transfer Phenomena of Contaminated Bubble Swarms in Power-law Fluids", Manuscript under preparation.

8. Venkata Swamy Nalajala, Nanda Kishore, Harsaraj Biswanath, "Effect of Contamination on Rise Velocity of Bubble Swarms in Power-law Fluids", *FMFP*, Kanpur (2014).